

EXPERIMENTAL INVESTIGATION AND MODELING OF TIME RESOLVED  
THRUST OF A FLAPPING WING AIRCRAFT

A Dissertation

Submitted to the Graduate School  
of the University of Notre Dame  
in Partial Fulfillment of the Requirements  
for the Degree of

Doctor of Philosophy

by

Thomas B. Apker,

---

Thomas C. Corke, Director

Graduate Program in Aerospace and Mechanical Engineering

Notre Dame, Indiana

December 2009

EXPERIMENTAL INVESTIGATION AND MODELING OF TIME RESOLVED  
THRUST OF A FLAPPING WING AIRCRAFT

Abstract

by

Thomas B. Apker

This work presents a novel method of measuring the unsteady thrust of a hovering flapping wing vehicle and the development of phenomenological models to simulate it. The measurements were taken using a balance beam with the flapping wings mounted at one end and a counterweight plus an accelerometer mounted at the other. The thrust axis of the flapping wings was mounted vertically, and the counterweight was adjusted to balance the weight and average thrust of the flapping wings. An accelerometer mounted above the counterweight measured the unsteady thrust. This method decoupled the force sensing element from the mass of the flapping wings, as opposed to standard force sensors that use a linear spring. This study showed that the spectral content of the flapping wings extended to 15 times the flapping frequency, well above the resonant frequency of the mass-spring-damper system formed by a load cell and flapping mechanism. High speed video of the wings was used to determine the motion of the flexible structure. This motion was used to develop phenomenological linear models of flapping wing thrust generation. The results show that this approach to linear modeling produces a system of equations that can be used for flight dynamics simulation and controller design.

This dissertation is dedicated to caffeine, capsaicin and most of all Kirstin.

## CONTENTS

FIGURES . . . . .	vi
TABLES . . . . .	xv
ACKNOWLEDGMENTS . . . . .	xvi
CHAPTER 1: INTRODUCTION . . . . .	1
1.1 Experimental background . . . . .	2
1.1.1 Insect flight studies . . . . .	2
1.1.2 Avian and mammalian flight . . . . .	4
1.1.3 Mechanical flight experiments . . . . .	6
1.2 Aerodynamic modeling . . . . .	7
1.2.1 Thin airfoil theory . . . . .	8
1.2.2 Panel methods . . . . .	9
1.2.3 Lifting line theories . . . . .	10
1.3 Structural modeling . . . . .	12
1.4 Piezoelectric wing membranes . . . . .	13
1.4.1 Sensing . . . . .	14
1.4.2 Acceleration measurement . . . . .	14
1.4.3 Pressure measurement . . . . .	15
1.4.4 Deflection measurements . . . . .	16
1.4.5 Energy harvesting . . . . .	16
1.5 Flow control . . . . .	17
1.5.1 Applications . . . . .	17
1.5.2 Modeling . . . . .	18
1.6 Flight dynamics modeling . . . . .	19
1.7 Summary and open issues . . . . .	20
1.7.1 How we reached TRL-3 . . . . .	20
1.7.2 How to reach TRL-4 . . . . .	21
CHAPTER 2: EXPERIMENTAL METHODS . . . . .	23
2.1 Force measurement system . . . . .	23
2.1.1 Measurement system dynamic modeling . . . . .	23
2.1.2 Force measurement system . . . . .	25

2.1.3	Wing design and construction . . . . .	26
2.1.4	Flapping mechanism . . . . .	29
2.1.5	Balance beam deflection measurement . . . . .	31
2.1.6	Accelerometer selection and mounting . . . . .	31
2.1.7	Balance beam design . . . . .	32
2.1.8	Data collection procedure . . . . .	33
2.2	Structure deformation measurements . . . . .	34
2.2.1	Mechanism, Camera and Lighting Setup . . . . .	34
2.2.2	Image collection procedure . . . . .	36
CHAPTER 3: Force Measurement . . . . .		37
3.1	Introduction . . . . .	37
3.2	Data Analysis . . . . .	38
3.3	Results and Discussion . . . . .	41
3.3.1	Average force measurements . . . . .	41
3.3.2	Time-resolved force measurement . . . . .	48
3.3.3	Flapping thrust frequency content . . . . .	64
3.4	Chapter Summary . . . . .	64
CHAPTER 4: STRUCTURE DEFORMATION MEASUREMENTS . . . . .		71
4.1	Image Analysis . . . . .	71
4.1.1	Determining Phase Angle . . . . .	71
4.1.2	Wing Motion and Angle of attack . . . . .	75
4.1.3	Determine angle of attack . . . . .	80
4.2	Results and discussion . . . . .	83
4.2.1	Stiff Wing . . . . .	83
4.2.2	Flexible Wing . . . . .	93
4.2.3	Drumhead Wing . . . . .	103
4.3	Chapter Summary . . . . .	113
CHAPTER 5: MODELING AND SIMULATION . . . . .		116
5.1	Purpose and Objective . . . . .	116
5.2	Aerodynamics functional form . . . . .	116
5.3	Linear model . . . . .	119
5.4	System Identification . . . . .	120
5.4.1	Filter time series to remove high frequency noise . . . . .	121
5.4.2	Determining $\dot{\Gamma}$ . . . . .	126
5.4.3	Find $\dot{h}$ along the wing . . . . .	126
5.4.4	Construct long time series . . . . .	129
5.5	Model Generation . . . . .	132
5.5.1	Stiff Wing . . . . .	132
5.5.2	Flexible Wing . . . . .	139
5.5.3	Drumhead Wing . . . . .	154
5.6	Model trend analysis . . . . .	163
5.6.1	Stiff wing . . . . .	170
5.6.2	Flexible wing . . . . .	170

5.6.3	Drumhead wing . . . . .	181
5.7	Chapter discussion . . . . .	181
CHAPTER 6: Conclusion and Future Work . . . . .		187
6.1	Conclusions . . . . .	187
6.2	Future Work . . . . .	190
6.2.1	Clap and Fling . . . . .	190
6.2.2	Fluid dynamics measurements . . . . .	190
6.2.3	Wing membrane strain measurements . . . . .	191
6.2.4	Gust and cross-wind response . . . . .	191
6.2.5	Three axis measurements . . . . .	191
APPENDIX A: FLUID MEASUREMENTS . . . . .		192
A.1	Purpose and Objective . . . . .	192
A.1.1	Thrust Measurement . . . . .	192
A.1.2	Fundamental Physics . . . . .	193
A.2	Experimental setup . . . . .	194
A.3	Image collection procedure . . . . .	197
A.4	Problems Encountered . . . . .	198
A.4.1	Incomplete Vector Fields . . . . .	198
A.5	Specular reflection mitigation attempts . . . . .	198
A.6	Successful measurements . . . . .	200

## FIGURES

2.1	Schematic of the standard load cell force transducer. The large mass of the flapping mechanism lowers the natural frequency of the system to well below the frequency content of the flapping aerodynamics. . . .	24
2.2	Expected flapping wing thrust time series generated using phase-averaged data from Lehmann, <i>et al.</i> and assuming a flapping rate of $10Hz$ [32] . . . . .	24
2.3	Power spectral density of the force signal generated by a dynamically scaled flapping wing model showing significant frequency content up to 12 times the flapping rate . . . . .	25
2.4	Photograph of the assembled balance beam mechanism. . . . .	26
2.5	Schematic of the electrical system used in the experiment . . . . .	27
2.6	Schematic view of the planform and support structures of the wings used in this study . . . . .	27
2.7	Photograph of the stiffest wing with structural details noted. Mass = 5.85g . . . . .	28
2.8	Photograph of the most flexible wing with structural details noted. Mass = 4.79g . . . . .	28
2.9	Photograph of the drumhead wing with structural details noted. Mass = 5.56g . . . . .	29
2.10	Photograph of the flapping mechanism, a Cybird gearbox, and brushed DC motor used to drive it for this experiment. . . . .	30
2.11	Schematic view of the operation of the reflective optical tachometer. . . . .	30
2.12	Diagram showing how the vertical displacement of the beam was used to find the angle $\theta$ . . . . .	31
2.13	Photograph of the accelerometer mounted on the test stand with sensitive axis in the vertical direction. . . . .	32
2.14	Photograph of the balance beams used in this experiment. The shorter beam is shown with ball bearing mounted at the rotation point. . . . .	33

2.15	Top-view of the arrangement of camera, flapping mechanism and spotlight as seen from above during the structure deformation measurements . . . . .	35
2.16	One of the frames captured during high speed flapping of the stiff wing	35
2.17	Electrical schematic of the optical deflection measurement system . .	36
3.1	A schematic view of the instrumented balance beam used to measure the flapping wing forces and moments . . . . .	39
3.2	Diagram showing how the measured vertical displacement of the balance beam was used to measure the angle $\theta$ . . . . .	41
3.3	The average thrust generated by the stiff wing. . . . .	42
3.4	Log-log plot of the data presented in Figure 3.3. . . . .	43
3.5	The average thrust generated by the flexible wing. . . . .	44
3.6	Log-log plot of the data presented in Figure 3.5. . . . .	45
3.7	The average thrust generated by the drumhead wing. . . . .	46
3.8	Log-log plot of the data presented in figure 3.7. . . . .	47
3.9	Time resolved thrust generated by the stiff wing at a flapping frequency of 11.5Hz . . . . .	48
3.10	Time resolved thrust generated by the flexible wing at a flapping frequency of 12Hz . . . . .	49
3.11	Time resolved thrust generated by the drumhead wing at a flapping frequency of 11.5Hz . . . . .	50
3.12	Plot of the phase resolved thrust of the stiff wing at 11.5Hz . . . . .	51
3.13	Plot of the phase resolved thrust of the stiff wing at 10Hz . . . . .	52
3.14	Plot of the phase resolved thrust of the stiff wing at 9Hz . . . . .	53
3.15	Plot of the phase angle of the peak thrust generated by the stiff wing at the flapping rates tested. . . . .	54
3.16	Plot of the peak thrust generated by the stiff wing at the flapping frequencies tested . . . . .	55
3.17	Plot of the phase resolved thrust of the flexible wing at 12Hz. . . . .	56
3.18	Plot of the phase resolved thrust of the flexible wing at 11Hz. . . . .	57
3.19	Plot of the phase resolved thrust of the flexible wing at 9Hz. . . . .	58
3.20	Peak thrust generated by the flexible wing as a function of frequency.	59

3.21	Plot of the phase angle of the peak thrust generated by the flexible wing at the flapping rates tested. . . . .	60
3.22	Plot of the phase resolved thrust of the drumhead wing at 11.5Hz. . .	61
3.23	Plot of the phase resolved thrust of the drumhead wing at 10Hz. . . .	62
3.24	Plot of the phase resolved thrust of the drumhead wing at 10Hz. . . .	63
3.25	Peak thrust generated by the drumhead wing as a function of flapping frequency. . . . .	65
3.26	Phase angle of the peak thrust generated by the drumhead wing vs. flapping frequency. . . . .	66
3.27	Spectra of frequency content of the thrust time series for the stiff wing.	67
3.28	Spectra of frequency content of the thrust time series for the flexible wing. . . . .	68
3.29	Spectra of frequency content of the thrust time series for the drumhead wing. . . . .	69
4.1	Schematic of the flapping mechanism with drive wheel and connection point highlighted. . . . .	72
4.2	Close up view of the drive wheel from the first frame in a series. The center (star), $\phi = 0$ (diamond) and location of the connection (x) are highlighted. . . . .	73
4.3	Close up view of the drive wheel from the 100 <sup>th</sup> frame in a series. The center (star), $\phi = 0$ (diamond) and location of the connection (x) are highlighted. . . . .	74
4.4	Close up view of the drive wheel from the 2000 <sup>th</sup> frame in a series showing the initial guess (x), and corrected estimate of $\phi$ (open circle).	76
4.5	Plot of the measured phase angle versus frame number with a linear fit. . . . .	77
4.6	The output of the Prewitt edge detection filter for an image of the flexible wing. . . . .	79
4.7	Schematic view of the leading edge edge search algorithm. The box with the most edge points determines the flapping angle. . . . .	80
4.8	Image of a wing with its leading edge highlighted by a line of open circles. . . . .	81
4.9	Orthographic and cut-away views of the angle of attack of the wing. .	82
4.10	Schematic view of the trailing edge location algorithm. . . . .	83

4.11	Example of the trailing edge location algorithm applied to the image shown in Figure 4.8. The selected trailing edge points are highlight with stars. . . . .	84
4.12	Angle of attack near the wing root of the stiff wing at the 11Hz flapping frequency. . . . .	85
4.13	Angle of attack near the wing root of the stiff wing at the 10.5Hz flapping frequency. . . . .	86
4.14	Angle of attack near the wing root of the stiff wing at the 9.5Hz . . .	87
4.15	Angle of attack near the wing tip of the stiff wing at the 11Hz flapping frequency. . . . .	88
4.16	Angle of attack near the wing tip of the stiff wing at the 10.5Hz flapping frequency. . . . .	89
4.17	Angle of attack near the wing tip of the stiff wing at the 9.5Hz . . . .	90
4.18	Peak angle of attack of the root of the wing as function of the flapping frequency for the stiff wing. . . . .	91
4.19	Phase angle of the peak angle of attack of the root of the stiff wing versus flapping frequency. . . . .	92
4.20	Maximum angle of attack of the tip of the wing versus flapping frequency for the stiff wing. . . . .	93
4.21	Phase angle of the peak tip angle of attack for the stiff wing. . . . .	94
4.22	Angle of attack near the root of the flexible wing at the 11.5Hz flapping frequency. . . . .	95
4.23	Angle of attack near the root of the flexible wing at the 11Hz flapping frequency. . . . .	96
4.24	Angle of attack near the root of the flexible wing at the 10Hz flapping frequency. . . . .	97
4.25	Angle of attack near the tip of the flexible wing at the 11.5Hz flapping frequency. . . . .	98
4.26	Angle of attack near the tip of the flexible wing at the 11Hz flapping frequency. . . . .	99
4.27	Angle of attack near the tip of the flexible wing at the 10Hz flapping frequency. . . . .	100
4.28	Peak angle of attack of the root of the wing as function of the flapping frequency for the flexible wing. . . . .	101
4.29	Phase angle of the peak angle of attack of the root of the flexible wing versus flapping frequency. . . . .	102

4.30	Maximum angle of attack of the tip of the wing versus flapping frequency for the flexible wing. . . . .	103
4.31	Phase angle of the peak tip angle of attack for the flexible wing. . . . .	104
4.32	Angle of attack near the root of the drumhead wing at the 11Hz flapping frequency. . . . .	105
4.33	Angle of attack near the root of the drumhead wing at the 10.5Hz . . . . .	106
4.34	Angle of attack near the root of the drumhead wing at the 8Hz flapping frequency. . . . .	107
4.35	Angle of attack near the tip of the drumhead wing at the 11Hz flapping frequency. . . . .	108
4.36	Angle of attack near the tip of the drumhead wing at the 10.5Hz . . . . .	109
4.37	Angle of attack near the tip of the drumhead wing at the 8Hz flapping frequency. . . . .	110
4.38	Peak angle of attack of the root of the wing as function of the flapping frequency of the drumhead wing. . . . .	111
4.39	Phase angle of the peak angle of attack of the root of the drumhead wing versus flapping frequency. . . . .	112
4.40	Maximum angle of attack of the tip of the wing versus flapping frequency of the drumhead wing. . . . .	113
4.41	Phase angle of the peak tip angle of attack of the drumhead wing. . . . .	114
5.1	Schematic illustration of the angle of attack and plunge rate inputs for a blade element theory model. . . . .	118
5.2	Block diagram showing how the matrices generated by least square prediction error are used to compute the thrust given aerodynamic inputs. . . . .	122
5.3	Plot of the unfiltered and filtered phase averaged thrust for the stiff wing at an 11Hz flapping frequency. . . . .	123
5.4	Plot of the unfiltered and filtered phase averaged wing root deflection for the stiff wing at an 11Hz flapping frequency. . . . .	124
5.5	Plots of the unfiltered and filtered phase averaged deflection of the wing tip of the stiff wing at an 11Hz flapping frequency. . . . .	125
5.6	Plot of the simplified time series and spline fit for the stiff wing at an 11Hz flapping frequency. . . . .	127
5.7	Plot of $\dot{\Gamma}(t)$ for the time series in Figure 5.6. . . . .	128

5.8	Diagram showing how $\alpha$ and $\dot{h}$ were computed. . . . .	129
5.9	Estimate of $\alpha_{tip}(t)$ and $\alpha_{root}(t)$ for the stiff wing at a flapping frequency of 11Hz. . . . .	130
5.10	Estimate of $\dot{h}_{tip}(t)$ and $\dot{h}_{root}(t)$ for the stiff wing at a flapping frequency of 11Hz. . . . .	131
5.11	Comparison between the linear model and measured thrust for the stiff wing at a flapping frequency of 11Hz. . . . .	133
5.12	Comparison between the linear model and measured thrust for the stiff wing at a flapping frequency of 10.5Hz. . . . .	134
5.13	Comparison between the linear model and measured thrust for the stiff wing at flapping frequency 9.5Hz. . . . .	135
5.14	Comparison between the linear model and measured thrust for the stiff wing at a flapping frequency of 8Hz. . . . .	136
5.15	Comparison between the linear model and measured thrust for the stiff wing a flapping frequency of 6Hz. . . . .	137
5.16	Normalize mean-squared error in the model estimated thrust for the stiff wing as a function of flapping frequency. . . . .	138
5.17	Comparison between the measured thrust and predicted thrust at flapping frequency of 10.5Hz for the model coefficients estimated for the stiff wing at an 11Hz flapping frequency. . . . .	140
5.18	Comparison between the measured thrust and predicted thrust at flapping frequency 9.5Hz for the model coefficients estimated for the stiff wing at an 11Hz flapping frequency. . . . .	141
5.19	Comparison between the measured thrust and predicted thrust at a flapping frequency of 8Hz for the model coefficients estimated for the stiff wing at an 11Hz flapping frequency. . . . .	142
5.20	Comparison between the measured thrust and predicted thrust at a flapping frequency of 6Hz for the model coefficients estimated for the stiff wing at an 11Hz flapping frequency. . . . .	143
5.21	Normalized mean-squared error in the model estimate of the thrust for the stiff wing obtained using the 11Hz flapping model coefficients for conditions of the other flapping frequencies. . . . .	144
5.22	Plot of the data presented in Figure 5.21 above 8Hz. . . . .	145
5.23	Input $\alpha(t)$ for the flexible wing at a flapping frequency of 11.5Hz. . .	146
5.24	Input $\dot{h}(t)$ for the flexible wing at a flapping frequency of 11.5Hz. . .	147

5.25	Comparison of the linear model and measured thrust for the flexible wing data at flapping frequency 11.5Hz. . . . .	148
5.26	Comparison of the linear model and measured thrust for the flexible wing at a flapping frequency of 11Hz. . . . .	149
5.27	Comparison of the linear model and measured thrust for the flexible wing at a flapping frequency of 10Hz. . . . .	150
5.28	Comparison of the linear model and measured thrust for the flexible wing data at a flapping frequency of 8.5Hz. . . . .	151
5.29	Comparison of the linear model and measured thrust for the flexible wing data at a flapping frequency of 6Hz. . . . .	152
5.30	Normalized mean square prediction error versus flapping frequency for the flexible wing. . . . .	153
5.31	Comparison between the measured thrust and predicted thrust at a flapping frequency of 11Hz using the model coefficient's for the flexible wing at an 11.5Hz flapping frequency. . . . .	154
5.32	Comparison between the measured thrust and predicted thrust at a flapping frequency of 10Hz using the model coefficient's for the flexible wing at an 11.5Hz flapping frequency. . . . .	155
5.33	Comparison of measured thrust and predicted thrust at a flapping frequency of 8.5Hz using the model coefficients for the flexible wing at an 11.5Hz flapping frequency. . . . .	156
5.34	Comparison of measured thrust and predicted thrust at flapping frequency of 6Hz using the model coefficients for the flexible wing at an 11.5Hz flapping frequency. . . . .	157
5.35	Normalized mean-squared error in the model estimate of the thrust for the flexible wing obtained using the 11.5Hz flapping model coefficients for conditions at the other flapping frequencies. . . . .	158
5.36	Plot of the data presented in Figure 5.35 above 8Hz. . . . .	159
5.37	Estimates of $\alpha$ for the drumhead wing at an 11Hz flapping frequency.	160
5.38	Estimates of $\dot{h}$ for the drumhead wing at an 11Hz flapping frequency.	161
5.39	Comparison between the linear model output thrust, $T(t)$ , and the measured thrust for the drumhead wing at a flapping frequency of 11Hz. . . . .	162
5.40	Estimate of $\alpha$ for the drumhead wing at a flapping frequency of 10.5Hz.	163
5.41	Estimate of $\dot{h}(t)$ for the drumhead wing at a flapping frequency of 10.5Hz. . . . .	164

5.42	Comparison between the linear model and the measured thrust for the drumhead wing at a flapping frequency of 10.5Hz. . . . .	165
5.43	Comparison between the linear model and the measured thrust for the drumhead wing at a flapping frequency of 9.5Hz. . . . .	166
5.44	Comparison between the linear model and the measured thrust for the drumhead wing at a flapping frequency of 8.5Hz. . . . .	167
5.45	Comparison between the linear model and the measured thrust for the drumhead wing at a flapping frequency of 6Hz. . . . .	168
5.46	Normalized mean square error in the estimate of the thrust for the drumhead wing as a function of flapping frequency. . . . .	169
5.47	Histogram of power law relationship observed between mean thrust and flapping frequency in Zdunich <i>et al.</i> [70], Wu <i>et al.</i> [67] and the wings used in this study. . . . .	171
5.48	Plot of the model estimate of mean thrust for the stiff wing. . . . .	172
5.49	Log-log plot of the mean thrust presented in Figure 5.48 after a constant was added to each point to make the minimum value $10^{-6}$ . . . . .	173
5.50	Plot of the model estimate of maximum thrust for the stiff wing. . . . .	174
5.51	Log-log plot of the maximum thrust presented in Figure 5.50 . . . . .	175
5.52	Block diagram showing a decoupled mean, $\bar{T}$ , and unsteady, $\hat{T}$ , thrust model. . . . .	176
5.53	Plot of the model estimate of mean thrust for the flexible wing. . . . .	177
5.54	Log-log plot of the mean thrust presented in Figure 5.53. . . . .	178
5.55	Plot of the model estimate of maximum thrust for the flexible wing. . . . .	179
5.56	Log-log plot of the maximum thrust presented in Figure 5.55 . . . . .	180
5.57	Plot of the model estimate of mean thrust for the drumhead wing. . . . .	182
5.58	Log-log plot of the mean thrust presented in Figure 5.57 after a constant was added to each point to make the minimum value $10^{-6}$ . . . . .	183
5.59	Plot of the model estimate of maximum thrust for the drumhead wing. . . . .	184
5.60	Log-log plot of the maximum thrust presented in Figure 5.59 . . . . .	185
A.1	Schematic of the control volume planned for force measurement. Flow symmetry is assumed based on the literature. . . . .	192
A.2	Diagram showing arrangement of PIV camera, laser and flapping mechanism. . . . .	194

A.3	Photograph of the camera and laser mounted outside the measurement box . . . . .	195
A.4	Circuit diagram of the experiment . . . . .	197
A.5	Images captured by the PIV camera with the laser at low power showing specular reflections off the wing. The top image shows the reflection off black and rhodamine paint, the bottom matte black fabric	199
A.6	Phase-averaged flow images at two phase angles showing a vortex dominated flow. . . . .	201
A.7	Measurements of the flow immediately after the wing has passed on its downward plunge. . . . .	202

## TABLES

3.1	Values used in this analysis . . . . .	39
-----	--	----

## ACKNOWLEDGMENTS

I would like to thank Dr. Mark Minor of the University of Utah and his student Erik Johnson for showing me their balance-beam force measurement technique that proved the critical component of this research.

## CHAPTER 1

### INTRODUCTION

This work seeks to find a means of producing a low order model of mechanical flapping wing flight in hover. It will study the flow environment in the neighborhood of the flapping wings to determine what kind of aerodynamic model is appropriate, measure the steady and unsteady components of the forces produced and determine, based on observations of the structure, how to best model the relationship between aerodynamic thrust and wing motion.

The goal of this effort is to produce a simulation that can, in real time, accurately predict the flight dynamics of a vehicle whose primary propulsion comes from the periodic flapping of its wings. It will accomplish this using the minimum number of parameters necessary to estimate aerodynamic forces and moments in hover and related maneuvers. It will also help define the design space of hovering flapping wing vehicles to determine what types of control actuators, aerodynamic or mass-displacement, are most effective.

The results of this work will be useful in the design of flight dynamics simulators for training of ornithopter pilots and developing control laws for autonomous ornithopters, including “hardware in the loop” simulation, similar to the Real Flight radio controlled aircraft training software [53] and simulation work done at Georgia Tech [21], respectively. Such simulations have also been useful for automating aircraft design and mission planning systems. This software will also prove useful in the

design of future flapping wing vehicles by allowing the development of optimization routines based on the performance estimates generated by the simulation.

## 1.1 Experimental background

There have been countless studies over the last several decades exploring the fluid phenomena associated with flapping wing flight. In general, these can be broken down into insect, avian, and mechanical. The insect studies tend to follow the model of Lehmann, Sane and Dickinson [32] or Willmott, Ellington and Thomas [66], using liquids such as mineral oil or water to allow larger mechanisms to recreate the complicated movements of a flapping insect, or a tethered insect in air. Birds and bats are more difficult to study, as their wings are composed of a complicated arrangement of muscle, bone, skin and feathers, and so the study of their flight mechanisms tends to focus on high speed imaging, particle image velocimetry (PIV) and oxygen sensors to determine wing motion, fluid motion and energy consumption, respectively [52]. Mechanical flapping flight is currently being studied in relatively few places, with a heavy emphasis on clamped wind tunnel models for analysis and flying prototypes to conduct flight performance studies [19]. For the purposes of this document, computational fluid dynamics (CFD) is treated as an experimental tool, as it provides data about flow structures and properties without requiring the researcher to explicitly predict them.

### 1.1.1 Insect flight studies

In many ways, insects represent the best model for development of very small flapping wing vehicles. Their wings are solid plates driven through root-centered plunging and twisting by relatively few muscles and an energy storing carapace [69]. The ongoing Micromechanical Flying Insect (MFI) project is looking to develop a piezoelectrically actuated system that behaves in this manner [8]. Insect

flight research can be further subdivided into two major groups, clap and fling, or small insect studies, and conventional flapping, typically with larger insects such as dragonflies and large flies.

“Clap and fling” was first studied in detail by Wies-Fough while investigating hovering flight of small wasps [34]. More recently, these results were confirmed in numerical simulations by Miller and Peskin [42] and Sun and Yu [60], showing a strong correlation of bound vorticity between the wings and aerodynamic loads. It has been observed that clap and fling produces approximately 17% more aerodynamic force per unit muscle mass than conventional, unclapped flapping based on observations of small flies in flight. Biologists have observed this mechanism used when an insect needs an extra burst of aerodynamic force, such as during aggressive maneuvers [42], or when trying to escape a tether [66].

Mechanical difficulties generally prevent studies of insect-like clap and fling in air on any platform other than a real insect or a CFD model of one. Several studies have attempted to overcome this constraint by immersing mechanical wings in a liquid with larger kinematic viscosity, thus allowing a larger mechanism to have the same effective Reynolds number. Lehmann, *et al.* [32] performed an experiment on fruit-fly shaped wings immersed in mineral oil. Their results showed that clapping and flinging add a significant increase in lift and a smaller increase in drag at the beginning of the “fling” cycle.

Numerical studies of the effects of clap and fling are becoming more common as computer speeds continue to increase and our knowledge of the kinematics of the process evolves. Miller and Peskin [42] performed several numerical experiments of 2D wings clapping together in an effectively infinite fluid. Their results showed that for Reynolds numbers up to 128, based on average wing speed, there was a reduction in average aerodynamic coefficients for clap and fling fliers, and that the benefits

of clap and fling are very large for the smallest fliers. Sun and Yu [60] conducted a similar 2D study that showed a strong correlation between the presence of large vortical structures and aerodynamic loads using an innovative dynamic meshing scheme.

Clap and fling aerodynamics in live insects was studied by Willmott, Ellington and Thomas [66] on a tethered hawkmoth. Using stereo cameras and strobe lights, they were able to clearly illuminate smoke tracers caught in the vortex wake of the moth, providing clear evidence of the aerodynamic model proposed by Wies-Fogh .

There have also been several studies of non-clapping wings, such as large flies and dragonflies. Work on dragonflies has focused largely on mapping the motion of their wings or testing flapping motions using their wings or man-made wings patterned after them. One example is a CFD study by Tang, *et al.* [63] which found that optimal lift in hover occurred when the wings ended each half period aligned vertically, as this allows for more significant wake capture.

Mokhtar, *et al.* conducted a numeric study of the effect of adding flow control to a 2D airfoil based on a dragonfly wing undergoing a figure-8 flapping motion. They showed that adding leading edge suction improved lift by increasing the strength of the leading edge vortex by as much as a factor of two [44].

### 1.1.2 Avian and mammalian flight

In terms of moving parts per unit volume, birds and bats are probably the most complicated flying machines on Earth and so make poor subjects to guide the design of mechanical fliers that cannot take advantage of muscle and bone structures. However, they are remarkably efficient in the regimes of greatest interest to those interested in urban surveillance. As such, they have been extensively studied in the past decade in the hope of learning how they connect their many sensors and

actuators in hover, forward and maneuvering flight.

One relatively simple study that can give substantial physical intuition into the realm of realizable MAV configurations is to compare multiple bird species wing area, flight speed, flapping rate, and other design parameters. Shyy, Berg and Ljungqvist [57] present an interesting and detailed explanation of scaling laws found in birds, bats and insects and applied them to the design space of the DARPA-defined micro air vehicle. Based on their observations of wing loading, flapping rate and vehicle mass, they conclude that the optimal MAV could have a mass of 50g and flap at 10Hz. Additionally, they provide a means of determining the power required to accelerate a flapping wing and data on the effects of flexible membranes on fixed-wing lift generation. Ho, *et al.* described similar scaling laws in their study of the design space of flapping wings [19].

The motions of bird wings reflect the full range of the mechanical possibilities achievable by their combinations of muscle, joints and bone. As one might expect, they use these to achieve optimum configurations for various flight regimes such as long-endurance glide, landing and high-speed dive [1]. Interestingly, this points out that a flapping wing aircraft also can be a morphing wing glider.

In addition to studying power consumption and wing motion in flight, several researchers have applied flow visualization and PIV to study the wake produced by these flying creatures. Rayner describes four distinct wake shapes based on the wing geometry and flapping motion. These include ladder shaped, with each rung having the same direction of circulation applicable mostly to small insects; ladder shaped with rungs that reverse their circulation with each half cycle, typically seen with larger insects and small ornithopters; ring-shaped vortecies shed each half cycle by small birds and larger ornithopters; and permanently attached wingtip vortexes [52].

### 1.1.3 Mechanical flight experiments

Mechanical flight studies can generally be divided into two categories, (1) fixed bench-top and wind tunnel experiments and (2) flight tests. In the case of (1), all of the tools at the experimental fluid dynamicist are available and have been applied to the body and the fluid nearby. For (2), all of the aerodynamic components are necessarily included, including changes in speed and angle of attack due to the period loading of the wings, but it is difficult to collect flight data beyond handling qualities, range and endurance. To date, the only flight data collected from an ornithopter was published by Krashanitsa *et al.* [27] which showed that a relatively large conventional ornithopter behaves much like a conventional fixed wing aircraft.

In addition to a thorough review of the literature involving scaling laws, the results of several experiments related to the development of small ornithopter wings was reported by Ho, *et al.* [19]. They discovered several key factors in the design of small flapping wing. Most importantly for spanwise rigid wings, lift and thrust coefficients increase with decreasing advance ratio, and that flexible membranes and MEMS check-valves result in more efficient thrust production by minimizing the negative peaks in the thrust curve [19]. Shyy, Berg and Ljungqvist [57] also presented results showing how flexible membranes lead to improvements in lift production in Clarky-Y airfoils at low Reynolds numbers.

A detailed analysis of the wake of a thick (NACA 0030) flapping foil was undertaken by Parker, von Ellenrider and Soria that revealed a complicated pair of leading and trailing edge vortical structures shed every half period in response to plunging motion in a low-speed mean flow [48].

There is a growing interest in flapping wing aircraft that hover, which has inspired several researchers to investigate clamped models in quiescent air. Tarascio *et al.* [62] constructed a small mechanism with a rectangular wing in a pin joint

that allowed it to move freely between angles of attack of  $15^\circ$ ,  $30^\circ$  and  $45^\circ$ . Wing speeds were chosen such that the device was quickly driven to its stops and held in place by airflow through out most of the flap cycle. Using this mechanism, typical of many micro air vehicle flappers, they observed a wake structure consisting of a recirculation region near the stroke reversal points, starting vortices shed with each stroke reversal and turbulent eddies throughout the stroke cycle. They also appeared to show the “necking-down” wake predicted by actuator disk theory.

Publications involving mechanical flapping wing flight are limited to largely subjective pilot reports [11]. Additionally, the ornithopter subsection of the International Micro Air Vehicle Competition rewards primarily small size, followed by endurance and finally maneuverability, while fixed wing vehicles face strict rules for vehicle autonomy and ground crew interaction [40].

Extending the work of Cylinder, Srull and Kellogg [10], Kellogg, *et al.* [25] describe an alternative approach to mechanical flapping that attempts to make better use of the tools available to human engineers than the conventional ornithopter configuration. They discussed free-flight tests of several small vehicles that made use of a combination of fixed foils, clapping wings and reversing camber wings to produce thrust and lift, a concept they call “aerial swimming.” Their most successful design features a pair of camber-reversing, clapping foils at the front and rear of the airframe, which they describe as being steerable in flight via radio control and capable of crawling across level ground.

## 1.2 Aerodynamic modeling

For the purposes stated above, there are three major approaches to the modeling of unsteady aerodynamics. The oldest, classical approach involves computing the lift on two dimensional segments using thin airfoil theory or conformal mapping. Also,

there are several varieties of lifting line theory, generally based on Theodorsen-like functions, that attempt to compute the lift on segments of the wing based on their motion. Finally, as faster computers increase the amount of computation that can be done in “real-time”, it becomes possible to model vehicles using panel methods.

### 1.2.1 Thin airfoil theory

Nearly all studies of unsteady aerodynamic forces cite Sears’ dissertation, or at least cite a paper that cites it. The reason is that he and his advisor, von Karman, derived an analytical expression for the pressure distribution around an airfoil subject to a sinusoidally varying angle of attack [55]. However, the method he developed relies on multiple Bessel functions for each relatively small segment, and as such is not practical for real time simulations.

However, a number of authors have considered the problem of conformally mapping a circle undergoing period movement into a flat plate flapping at the same rate. Yu and Tong [68] use this technique to demonstrate the utility of stroke asymmetry using conformal mapping of a flapping airfoil going through several different versions of asymmetric downstrokes. They showed that different ratios of upstroke and downstroke speed and angle of attack lead to more powerful or efficient force generation for different flight regimes. Minotti [43] developed a two dimensional, inviscid model for a flapping airfoil in hover. Like most thin airfoil models, it assumed a combination of quasi-steady thin airfoil theory, wake recapture and added, or virtual, mass effects. However, his paper explicitly lays out the conformal mapping transformation, giving explicit relationships for the bound and leading edge vortex circulation, as well as the forces generated by the airfoil.

### 1.2.2 Panel methods

As desktop computers become capable of hundreds of mega-flops, panel methods become a realistic way of simulating flapping flight in real time without the constraints of models that imposed conditions on the mean flow for validity. The most obvious singularity method to use is the vortex lattice method, as the literature is full of information related to the placement and motion of shed vorticity near flapping wings.

In addition to the number and spacing of panels, the most important implementation detail of an unsteady vortex lattice method is the position of the wake. Konstadinopoulos *et al.* [26] take the method proposed in Katz and Plotkin [24] farther by including the effects of vorticity shed from the leading edge of a delta wing, and from the sides of a square subjected to slow rotation about its streamwise axis. They continued adding elements until the wake effect on the wing panels fell below a threshold, resulting in a relatively long grid that bore a striking resemblance to flow visualization of the scenarios presented.

More recently, Fritz and Long [17] explained how to implement an unsteady vortex lattice method for unsteady wing aerodynamics using the C++ programming language. The central observation was that one should use vortex rings. They suggested a profile of 15 spanwise by 5 chordwise, and a vortex wake shed from these rings to compute the steady and unsteady components of lift. They also suggest that if the run times are not fast enough, the algorithm was highly parallelizable, allowing the researcher to farm out the expensive computations to the local supercomputer and use a desktop to display the results. The authors included equations relating panel circulation to panel forces. This is most useful for thin wings such as those that would work for micro air vehicles. They showed how to compute the pressure jump across a panel, allowing simple decomposition into lift and thrust based on

the equations in Katz and Plotkin’s book [24]. Aside from this, the paper compares its code to Theodorsen theory for a pitching and plunging airfoil to verify that it produced good results. The final sections include wake portraits and lift plots. The results showed fertile ground for improving wake models to provide higher fidelity and reduce run time.

### 1.2.3 Lifting line theories

The original aerodynamic work that is relevant to the problem of single degree of freedom ornithopter propulsion was done by Theodorsen while investigating aeroelastic flutter. His frequency domain analysis focused on the coupling between angle of attack changes due to the wing motion and the aerodynamic loads on the airfoil. Since his time, there have been numerous studies devoted to the topic of lift generated by an airfoil section based on a frequency domain analysis of the motion. The primary advantage of these methods for real-time simulations over thin airfoil theory and panel methods is execution time, although they tend to make assumptions about the periodicity of the flow that may not be valid in free flight.

In 1936, Garrick [18] investigated the realm of flapping foil propulsion assuming synchronized pitching, plunging and aileron flapping assuming inviscid flow and no leading edge vortex. The equations were developed in great detail, and he concluded that for high Reynolds numbers, slower flapping is more efficient, provided the wing motion is purely normal to the direction of flight.

The mid-1990’s saw a revival of sorts for these methods, with two papers that focused on applying them to different scenarios. By assuming sinusoidal flapping and relatively low advance ratio, DeLaurier [12] developed an aerodynamic model based on modified Theodorsen functions and empirical relations for wake recapture. Further, he assumed that leading edge suction from a thick airfoil is the primary

means of producing thrust. As such, his model does not apply to MAVs, but is useful for investigating the possibility of larger-scale flapping vehicles. Extending the analysis in his previous work, DeLaurier explains a mechanism for computing the aeroelastic deflections of a flapping wing. Effectively, he assumes that spanwise and twist deflections have the same period as the root flapping with a phase and amplitude determined by structural stiffness. Without this assumption, the result of integrating the presented equations is an unstable system, but the assumptions match experimental data well [13]. Later, a student of his, Larijani, developed the nonlinear equations, including damping, that represent a stable set of equations for the aeroelastic performance developed in the other DeLaurier papers [12, 13]. This paper extends that work a bit by adding damping as a result of material stretching to the original equations to cancel out the unbounded flexure and twisting observed with the standard set. It also covers how to add the effects of stall. This method predicts that all of the aeroelastic motion settles into a sinusoidal pattern, even with the stall during part of the flapping cycle [29].

Jumper and Hugo [23] develop a panel-type method for unsteady lift with more theoretical backing than DeLaurier’s work. Their results were for solid wings, and so the method should work for the “aerial swimming” platforms developed by Kellogg, *et al.* [25]. Instead of simply assuming a singularity on each panel, it attempted to compute the unsteady circulation and unsteady wake given the time history of the motion of the wing. As there are no explicit limits on the allowable motions, this model offers an interesting and possibly highly efficient and effective wing model. Anderson, Pesavento and Wang [3] developed a lifting line model of a flat plate falling and fluttering. They explicitly determined the aerodynamic forces and moments by treating the falling plate as a rapidly pitching 2D airfoil with end effects, and presented experimental comparisons.

### 1.3 Structural modeling

For root-flapping ornithopters, the deflection of the wings in flight must be tracked as part of the vehicle state. As such, it is important to find a good way to represent the motion of the wing accurately with as few states as possible. DeLaurier [12] proposed that a wing could be broken up into strips, each with its own twist and vertical deflection. This model produced remarkably accurate results for a  $2m$  span ornithopter wing. However, this means that the simulation must track four states for each wing section used in the aerodynamic model, and decoupling sections of the structure that are bound together tightly.

Most aeroelastic simulations follow the example of Preidikman [51], and use a finite element method (FEM) code, to determine the structure's response to forcing found with either a computational fluid dynamics (CFD) or vortex lattice method (VLM) simulation. Despite its much greater computational complexity, this method may provide the most accurate model of tractable order by reducing the problem to an eigenvalue decomposition of the system's fundamental matrix,  $A$ , transforming from the full set of FEM states,  $\vec{x}$ , into a more convenient transformed space  $\vec{\zeta}$ , according to Eq. 1.2. The vast majority of the energy of any vibrating structure is contained in relatively few modes, reducing the number of states to be tracked from several thousand for a properly fine mesh, down to two or three relevant states. This method also decouples the structure and aerodynamic models, placing the aerodynamics in the forcing term  $\vec{u}$  in Eq. 1.1 and 1.3, and allowing a linear transform of the filter states to serve as the input to any aerodynamic model.

$$\dot{\vec{x}} = A\vec{x} + B\vec{u} \tag{1.1}$$

$$\vec{x} = M\vec{\zeta} \tag{1.2}$$

$$\dot{\vec{\zeta}} = M^{-1}AM\vec{\zeta} + M^{-1}B\vec{u} \quad (1.3)$$

Generating a finite element model of a small composite structure requires detailed knowledge of the fiber to resin ratio as well as the properties of the fibers and the resin. In addition, the interface between the composite structure and membrane must be modeled accurately. This type of analysis has been performed for the tightly controlled “dry lay-up” process using pre-impregnated fibers and a well established membrane attachment process developed at the University of Florida [20]. They were able to tune a model to predict the peak displacement of a flexible latex membrane glued to the frame subjected to steady air loads simulating level flight of a fixed-wing micro air vehicle. This study did not observe large deflections of the composite structure, and so avoided the need to model the viscoelastic response of the epoxy resin [58]. This viscoelastic character of carbon fiber composites may be enough to violate the assumptions underlying the transformation in Eq. 1.2 [29].

#### 1.4 Piezoelectric wing membranes

Piezoelectric materials respond to changes in strain by generating a time-varying charge across its capacitive elements. Numerous devices take advantage of this property to detect acceleration and rotational motion by placing either a beam or a tuning fork made from a piezoelectric crystal. Piezoelectric films are frequently used in microphones, producing a current proportional to the change in pressure across the microphone.

For most sensing applications, the output current is too small to power the sensor and its accompanying amplifiers and signal conditioners. However, interest in low power, persistent sensor networks has led to the development of circuits to harvest and analytical models to maximize utilization of the alternating current generated by these materials as they undergo unsteady loads.

### 1.4.1 Sensing

Piezoelectric materials have been used in accelerometers, pressure sensors and as strain gages on vibrating beams. This review considers using them simultaneously for all three, as the wings will be accelerating, driven by unsteady air loads and continuously flexing. Each of these induce a time varying strain at each point on the wing. Assuming the membrane's response is linear up to its elastic limits, the measurement model is simply a matter of projecting the estimations of the three components onto the wing's measurement space[46]. This does have some interesting consequences for the design of the wing, however, as the sampled area must have conductive material covering both sides of the membrane, and traces that do not overlap to carry the signal back to the processor. In general, the equations in this section will have to be integrated over the area sampled.

### 1.4.2 Acceleration measurement

The local acceleration of a point on the wing can be found using the standard equation for a point acceleration in a rotating frame, Eq. 1.4, multiplied by the mass,  $m$ , divided by the stiffness,  $k$ , of the membrane covered by the electrodes. However, Usherwood, *et al.* [64] observed that is it not necessary to filter out the acceleration signals of small pressure sensors on the wing of a pigeon. In practice, this term may be washed out by the pressure and deflection portions, but it is useful to include it until that has been demonstrated. The acceleration  $a_m$ , of the measured point  $r_m$  is a function of the vehicle's acceleration  $a_v$ , the instantaneous flapping rate  $\omega_{wing}$ , and the velocity and acceleration of the structure at that point,  $a_s$  and  $v_s$ , respectively, and found by transforming the modal space of Eq. 1.3 back into physical space.

$$a_m = a_v + a_s + \omega_{wing} \times (\omega_{wing} \times r_m) + 2\omega_{wing} \times v_s; S(t) = \nu_a \dot{a}_m \quad (1.4)$$

The actual signal,  $S(t)$ , measured by the microprocessor will be the time rate of change of this acceleration times a constant  $\nu_a$  that accounts for the mass, stiffness and electrical properties. Given that  $\omega_{wing}$  drops to zero twice per flapping cycle and that the change in acceleration is smallest when the wing is moving fastest, and thus producing the most aerodynamic force, it is easy to see how this term can be neglected.

### 1.4.3 Pressure measurement

Piezoelectric materials generally respond to changing loads, and so are particularly useful as microphones. Here the pressure loads are generally changing faster than the flapping frequency in response to wing harmonics and unsteady flow movement. Estimating the signal depends on computing the change in load on a particular point, using the computed normal force and pitching moment of a strip to estimate the pressure distribution using Eq. 1.5. The predicted signal is then computed by estimating a derivative using the difference the current and previous lift estimate  $L(t)$  divided by the time step  $dt$ . For panel methods, the pressure difference at a given point is computed as part of the standard force and moment calculations. However, for lifting line methods, the pressure distribution is implicitly integrated over the chord, and so the measurement model requires a term  $\nu_p$  that accounts for the sensor's position and the current state of the wing structure.

$$S(t) = \nu_p(r_m, \vec{\zeta})(L(t) - L(t - dt))/dt \quad (1.5)$$

#### 1.4.4 Deflection measurements

The relationship between strain rate and piezoelectric response was shown by Lee and O’Sullivan to be Eq. 1.6[30]. The signal due to the deflection of the whole wing, rather than local strains induced by local pressure or acceleration, is a strong function of the strains,  $\epsilon_1$ ,  $\epsilon_2$  and  $\epsilon_6$  in the polling, normal to the polling and shear directions, respectively, and the associated piezoelectric constants,  $e_{31}$ ,  $e_{32}$  and  $e_{36}$  in those directions. This effect must be integrated over the area of the sensor  $A$ , while a scaling factor  $\nu_\epsilon$  accounts for how this current signal is interpreted by a voltage-sensing microprocessor.

$$S_\epsilon = \nu_\epsilon \int_A \left( e_{31} \frac{\partial \epsilon_1(\vec{\zeta})}{\partial t} + e_{32} \frac{\partial \epsilon_2(\vec{\zeta})}{\partial t} + e_{36} \frac{\partial \epsilon_6(\vec{\zeta})}{\partial t} \right) dx dy \quad (1.6)$$

The relationship between  $\vec{\zeta}$  and local strain rate based on the large scale structural deformation can be found in Bandyopadhyay.[7]

#### 1.4.5 Energy harvesting

The nature of the capacitive, strain induced current requires a fair amount of creativity in the circuit designed to harvest energy from it. Like most resistor-capacitor circuits, there is an optimal average resistance that should be supplied by the load, and modern research seeks to more finely tune the process of converting the AC signal to DC with a focus on battery charging.

The most basic method of harvesting energy is a simple diode rectifier. This essentially changes the alternating sign of the piezoelectric voltage into its absolute value, but fails to optimize the process of charging a battery. Lefevre, *et al.* [31] compared four different approaches to piezoelectric energy harvesting, the most efficient being Parallel Synchronized Switch Harvesting on Inductor (SSHI). The way this works is an inductor and switch are placed in parallel with a piezoelectric

element and diode rectifier. The switch is closed briefly at peak displacement in order to grab the charge that has built up on the piezoelectric capacitor. This sets up an  $L - C$  circuit that is designed to have a period much shorter than the mechanical period, and is broken at half an electrical period. The result is a nearly constant voltage to the rectifier, and power harvesting up to 800% greater than a simple rectifier circuit.

More recently, Erika, *et al.* [15] described a means of designing and modeling a piezoelectric unimorph harvester for remote power supplies. They supplied a model for the ratio of voltage to bending moment with a resistive load, and concluded that this model works at the resonance frequency of the deflecting disk. The important point to note from this is the need to design the energy harvesting membrane such that its resonance is close to the expected forcing frequency.

## 1.5 Flow control

As mentioned above, insects, bats and birds employ a variety of complicated wing motions and other kinetic features, such as small hairs, flexible skin and feathers to manages the flow over their wings. With the current mechanical state of the art limiting humans to single degree of freedom flapping and aeroelastic wings, solid state and micro electromechanical systems (MEMS) provide a means to reproduce the flow effects of these more complicated movements and structures. This review will focus on the solid state single dielectric barrier discharge (SDBD) plasma actuator. This section will briefly discuss SDBD plasma actuator applications and their modeling.

### 1.5.1 Applications

Post [50] applied a plasma actuator to the leading edge of an airfoil oscillating in pitch, demonstrating that the actuator can delay stall and speed reattachment,

leading to a thirteen percent increase in cycle integrated lift using the “smart actuation” technique. This study demonstrated the effectiveness of feed-forward control of a dynamic stall vortex.

As mentioned above, one of the major research efforts currently underway involves finding a means of implementing feedback flow control on a flapping wing to maximize the lift production.

One of the central difficulties in applying feedback flow control to flight vehicles is that despite substantial progress in open-loop flow control, there has been no significant research into the implications of vehicle motion in response to flow control on the effectiveness of that control. An interdisciplinary team from the Georgia Institute of Technology began to address this question by applying model-inverse adaptive control to an airfoil section with trapped vorticity actuators on the pressure and suction side of the trailing edge[28].

### 1.5.2 Modeling

Yu and Tong [68] use a conformal mapping scheme to demonstrate how to use stroke asymmetry as a means of flow control for insect flight, demonstrating that an asymmetric stroke is more effective at generating lift and thrust than equally long up and downstrokes. While not technically a flow control mechanism, this does provide a possible means of designing control laws for the motors that drive the wings that would achieve the same effect.

Orlov developed a model for the distribution of the electric-field induced body force from a single DBD actuator, although it requires an empirical “scaling factor” to use in flow simulations [47]. While one can manipulate the magnetic field to control plasma-heavy flows, too much energy is required to perform magnet-based flow control in air according to simulations and plasma tunnel experiments conducted

by Shang, *et al.* [56].

## 1.6 Flight dynamics modeling

Three groups developed flapping wing flight dynamics models, each using a very different approach. The oldest was developed by the ornithopter group at the University of Toronto under DeLaurier as a simulator for their manned ornithopter. They use an aerodynamics model based on a look-up table that takes the vehicle motion as an input and interpolates between the nearest data points in a database collected from wind tunnel studies [16]. The rest of the vehicle was modeled using standard techniques for fixed wing aircraft.

DeLaurier was involved with another group that developed a clap-fling vehicle capable of hover and transition to forward flight. They describe using a wing aerodynamic model that uses a very simple single-vortex model of wing circulation that sheds a point vortex with circulation equivalent to the computed difference between the current and previous time step's vorticity, as determined by a function fit to experimental data. This singularity model was also used to model the flow over the aerodynamic control surfaces. Early flight tests suggested that this model was acceptable in hover, but did not accurately capture the flow over the control surfaces during transition to forward flight [70].

The Dickinson Lab at the California Institute of Technology developed a flight dynamics simulation of a fruit fly using a panel method based on conventional unsteady aerodynamics that assumes the flow is locally two dimensional. The “steady” component of the model uses data collected by rotating a scaled model of a fly wing in linseed oil to determine the lift and thrust components. The rest of the flight dynamics are computed using standard rigid body mechanics equations [14].

## 1.7 Summary and open issues

On the NASA Technical Readiness Level (TRL) scale, flapping wing aircraft have roughly reached level three, “proof of concept.” There are some flyable prototypes, mostly ornithopters capable of forward flight, one of them autonomous, and one manually controlled vehicle capable of hover. There has been significant fundamental fluids research investigating the conditions in which flapping wings are the optimal propulsion mechanism. Scaling laws based on preliminary vehicle and animal flight data provide a good start for exploring the design space of feasible flapping wing aircraft.

However, developing a functional prototype, *i.e.* an autonomous, hovering flapping wing vehicle that can carry a small surveillance payload, requires a more methodical approach to examining the behaviors of flapping wings in hover. Specifically, for a given wing geometry, there are four fundamental questions that need to be answered:

1. What fluid dynamics assumptions can or must be included in a flapping wing flight dynamics model?
2. What are the time-resolved forces and moments generated by flapping wings in air?
3. What is the bandwidth and magnitude required of controls, sensors and navigation filters to maintain a stable hover?
4. What effect does changing the wing structure or motion of the wing have on this force generation?

### 1.7.1 How we reached TRL-3

The early basic science work was done by Wies-Fogh [65], who discovered the clap-fling mechanism for very small insects. Lighthill [34] conducted experiments and produced an excellent summary of the early work on unsteady aerodynamics as it applies to flapping wing vehicles. Numerous bird, bat and insect studies since have

provided a plethora of information about the fluid and mechanical constraints in which flapping wing aircraft operate. Together, these efforts brought the technology to TRL-1, basic science.

Scaling studies for micro air vehicles based on bird and insect data conducted by Ho, *et al.* [19] and Liu [35] began the process of reaching TRL-2 by examining the likely payload, range and size constraints a flapping wing micro air vehicle would encounter. Numerous studies into flapping mechanism design and various wing shapes fleshed out these broad parameters into specific parameters vehicle designers could chose between to optimize speed, range or maneuverability.

The flapping wing component of the annual International Micro Air Vehicle Competition, led to a large number of vehicles, complete with detailed design reports, being produced, providing practical experience and academic knowledge of realistic flight vehicles. A team at the University of Arizona took this a step further and automated a camera-carrying ornithopter, proving that it can be done. Combined with the hovering vehicle prototype developed under a DARPA contract, it is safe to say that the technology has reached TRL-3, proof of concept.

#### 1.7.2 How to reach TRL-4

The goal of this effort is to develop the path towards TRL-4 through experiments and analysis to provide answers to the questions above.

Chapter 2 presents a novel method of measuring the unsteady flapping wing forces in a hover and the wing motions associated with those forces to provide information needed for Questions 1 through 4. The most important lesson of all of the attempts at modeling flapping wing force production is that all models are inherently empirical.

Chapter 3 covers the results of the force measurement experiments. These are

important for both understanding the fundamental physics of flapping wing flight and advancing understanding of flapping wing flight dynamics. Stabilizing a vehicle in hover will likely require at the very least an empirically derived process model for an on-line state estimator such as a Kalman filter, and any attempt at flight simulation must have an update rate greater than the Nyquist frequency of the flapping wing aerodynamics.

Chapter 4 presents measurements of the structural deformation to provide information towards the answers to Questions 1 and 4. Specifically, it seeks to determine if the structure can be modeled simply enough to include its dynamics in the equations of motion of the vehicle, or should it be handled by a look-up table based on flight conditions. Whether as a simplified structure model or look up table, it will determine the inputs to the flapping wing aerodynamic model.

Chapter 5 combines the information collected in the previous chapters to directly answer Question 1 by investigating the results of applying the appropriate model estimation techniques to the data.

This work concludes with a brief summary of the answers to questions 1-4 and a description of further efforts required to build, simulate and automate a hovering, flapping wing aircraft.

## CHAPTER 2

### EXPERIMENTAL METHODS

#### 2.1 Force measurement system

##### 2.1.1 Measurement system dynamic modeling

The typical system used to measure flapping wing thrust force is a load cell or cantilever beam with strain gages that measure the displacement of a linear spring. This is illustrated in Figure 2.1. Equation 2.1 is a simplified model of the relationship between the measured displacement,  $x$ , and thrust force,  $T$ , as a function of time,  $t$ , given a flapping mechanism mass of  $m_m$  and spring constant,  $k$ . The first vibration mode frequency,  $f_n$ , of this type of sensor is given by Eq. 2.2.

$$m_m \ddot{x} = xk + \dot{x}b + T(t) \quad (2.1)$$

$$f_n \approx \sqrt{\frac{k}{m}} \quad (2.2)$$

This system is not a force sensor, but a displacement sensor whose frequency response depends on the mass of the flapping mechanism. When  $T(t)$  has frequency content near or greater than  $f_n$ , the output of a load cell will be dominated by oscillations at that frequency, as shown in results from Wu *et al.* [67]. This is critically important for unsteady force measurements.

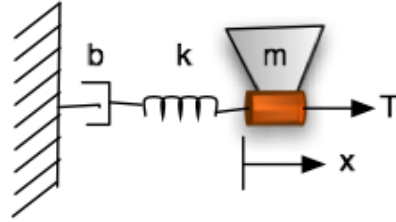


Figure 2.1. Schematic of the standard load cell force transducer. The large mass of the flapping mechanism lowers the natural frequency of the system to well below the frequency content of the flapping aerodynamics.

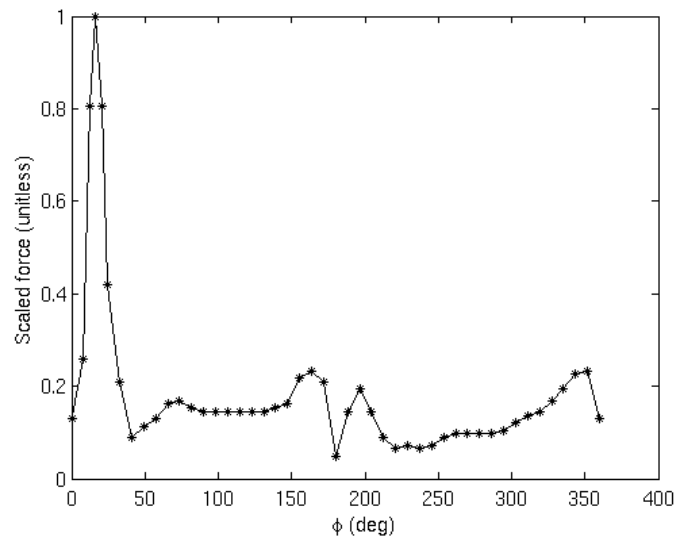


Figure 2.2. Expected flapping wing thrust time series generated using phase-averaged data from Lehmann, *et al.* and assuming a flapping rate of  $10Hz$  [32]

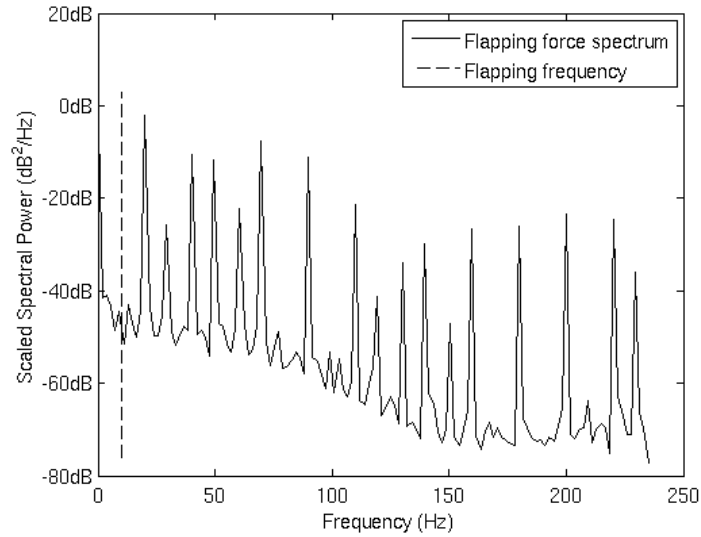


Figure 2.3. Power spectral density of the force signal generated by a dynamically scaled flapping wing model showing significant frequency content up to 12 times the flapping rate

The phase-averaged thrust force measured by Lehmann *et al.* [32] was used as a starting point to make a synthetic time series. This is shown in Figure 2.2. The spectra of the flapping time series shown in Figure 2.3 indicates that the frequency content of the aerodynamic load extends out to twelve times the flapping frequency. Thus, a system whose first vibration mode frequency is only two or three times greater than the flapping rate will not be able to faithfully represent the time-resolved force signal.

### 2.1.2 Force measurement system

The balance beam system shown in Figure 2.4 has two significant advantages over conventional load cells: (1) it separates the sensing element's properties from the force generation mechanism and (2) it provides a much better simulation of a real hovering vehicle by allowing the mechanism to move slightly in a vertical plane.

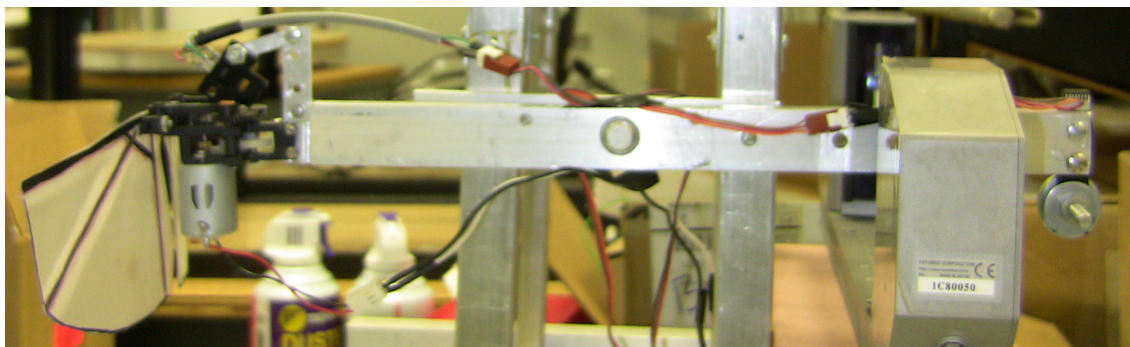


Figure 2.4. Photograph of the assembled balance beam mechanism.

The first advantage allows time resolved force measurements because accelerometers are available with a wide variety of sensitivity and bandwidth. The second advantage results in measurements that are more useful to researchers interested in flapping wing flight mechanics. Figure 2.5 shows a complete electrical schematic, the components of which are discussed in detail below.

### 2.1.3 Wing design and construction

Three pairs of wings were built for for this study based on the planform shown in Figure 2.6. They consisted of an aluminum screw plate used to attach the wing to the gearbox, a carbon fiber structure and a polyvinylidene fluoride (PVDF) skin. The screw plate allowed the custom-made wings to mount to the gearbox as a solid connection that guaranteed the wing root could not rotate relative to the mechanism. The carbon fiber frame was made using a wet lay up process and was vacuum cured in a warm oven. The frame and PVDF skin were bonded using cyanoacrylate glue.

Figure 2.7 shows the stiffest wing tested. It had three layers on the inboard stiffener, two layers on the batten and one on the crossbar. Including the aluminum screw plates, this pair of wings had a total mass of 5.85g.

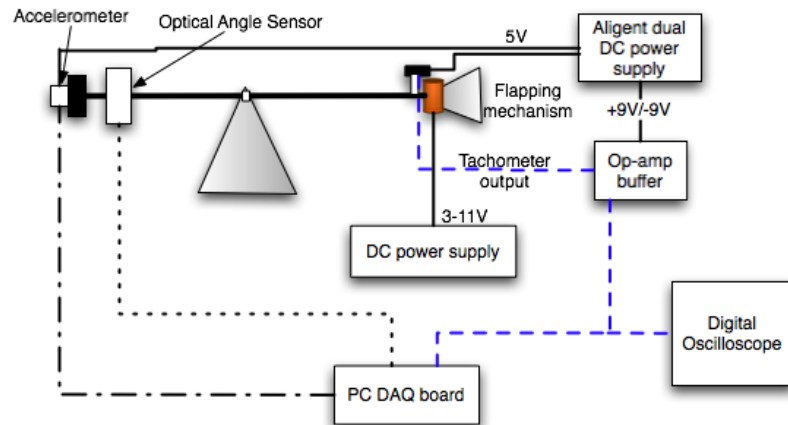


Figure 2.5. Schematic of the electrical system used in the experiment

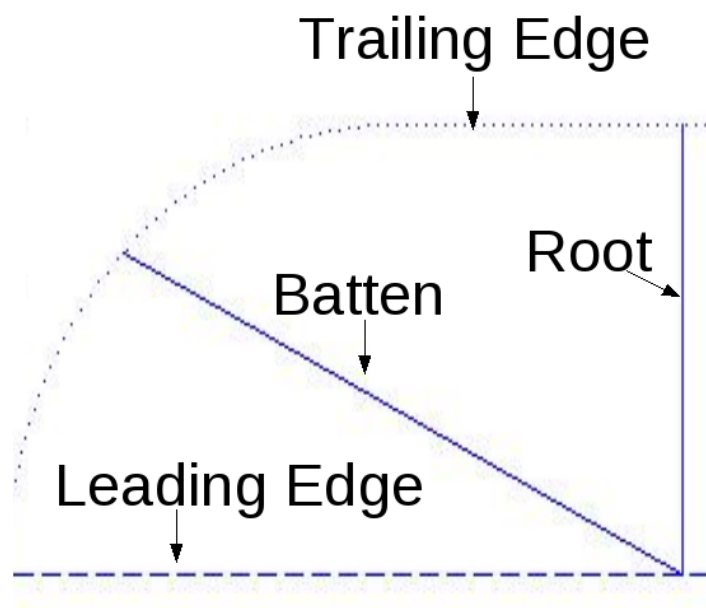


Figure 2.6. Schematic view of the planform and support structures of the wings used in this study

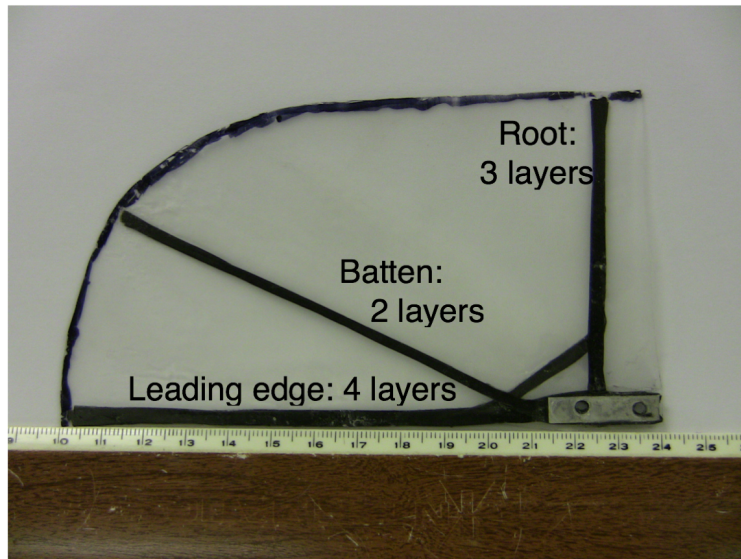


Figure 2.7. Photograph of the stiffest wing with structural details noted. Mass = 5.85g

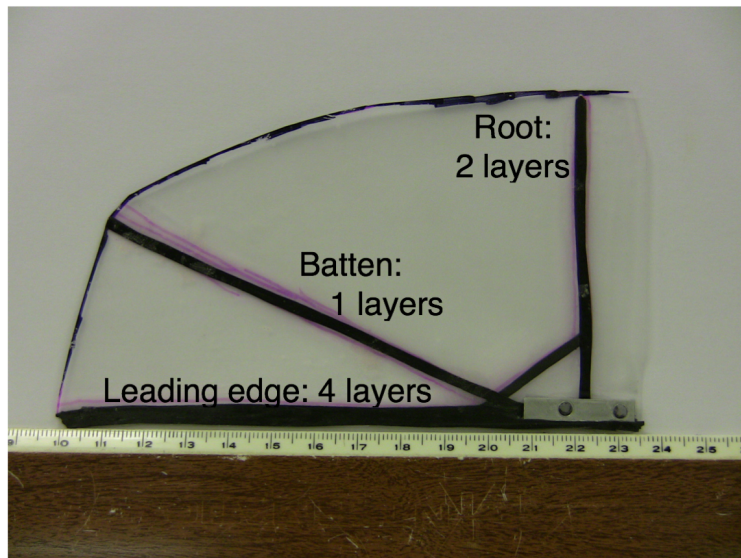


Figure 2.8. Photograph of the most flexible wing with structural details noted. Mass = 4.79g

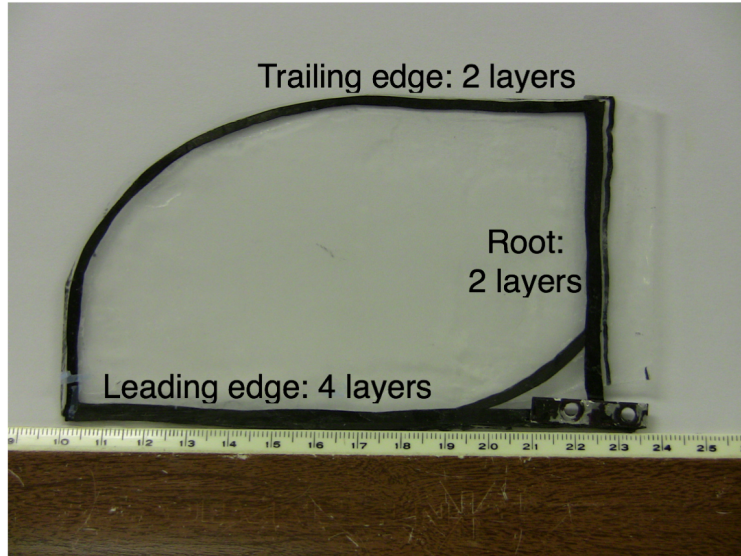


Figure 2.9. Photograph of the drumhead wing with structural details noted. Mass = 5.56g

Figure 2.8 shows the most flexible wing tested. It had two layers on the inboard stiffener, one layer on the batten and one on the crossbar. Including the aluminum screw plates, the most flexible wings had a total mass of 4.79g.

Figure 2.9 shows the drumhead wing. It had two layers on the inboard stiffener, two layers along the trailing edge and one on the crossbar. This drumhead arrangement placed more mass farther from the axis of rotation and thus produced a significantly different timing of pitching of the wing relative to the flap cycle. The pair of drumhead wings had a total mass of 5.56g.

#### 2.1.4 Flapping mechanism

Figure 2.10 shows the Cybird commercial gearbox driven by a Great Planes Speed 280 motor that was used to flap the wings. The motor was powered using a radio control aircraft electronic speed control (ESC) powered by a Tenma 72-630A power supply. The Tenma power supply replaced the battery that would

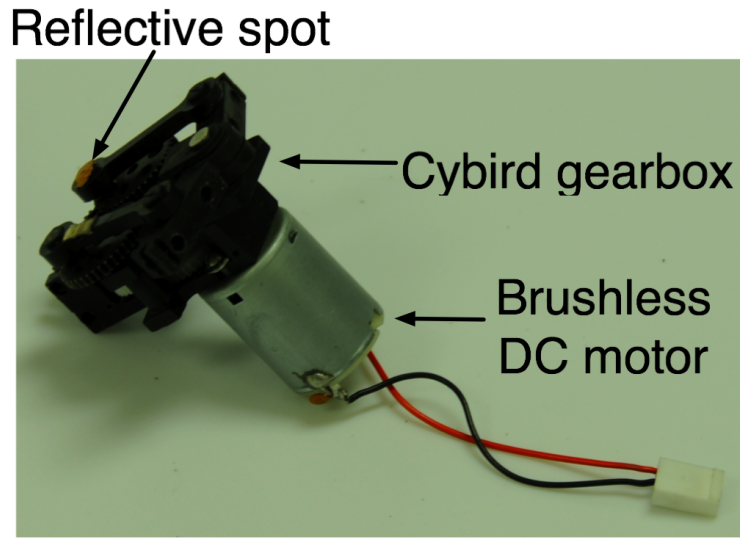


Figure 2.10. Photograph of the flapping mechanism, a Cybird gearbox, and brushed DC motor used to drive it for this experiment.

normally accompany the ESC in an RC aircraft. The ESC received standard RC pulse width modulated (PWM) control signals from a Pololu serial servo controller (SSC). The SSC received its commands from a Linux desktop that also hosted the data acquisition electronics.

Figure 2.11 shows how an optical sensor was used as a tachometer that measured the passage of a reflective element on the mechanism. This produced a pulse that

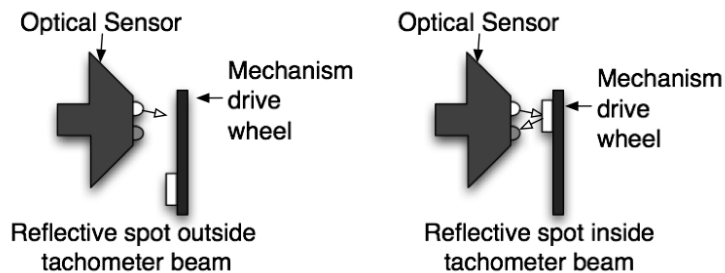


Figure 2.11. Schematic view of the operation of the reflective optical tachometer.

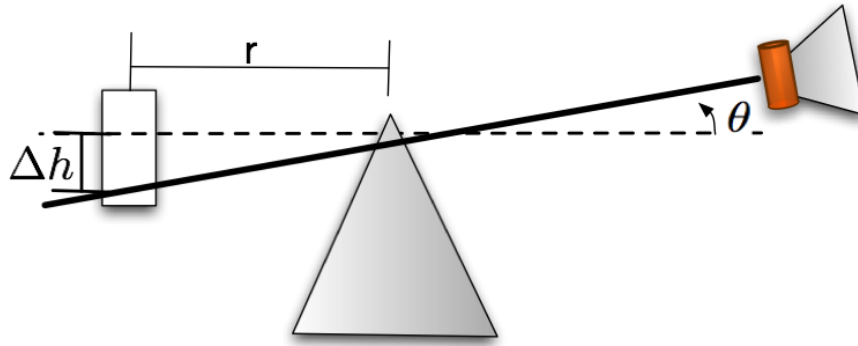


Figure 2.12. Diagram showing how the vertical displacement of the beam was used to find the angle  $\theta$ .

began at a phase angle  $\phi = 110^\circ$  on each passage, allowing both measurement of the flapping rate and phase averaging of the data.

#### 2.1.5 Balance beam deflection measurement

The angle of the balance beam relative to the horizontal plane  $\theta$  was important both for determining the counterweight by showing when the beam was level and for processing the accelerometer data. In this experiment it was measured using a Keyence optical displacement sensor that measured the distance between the bottom of the balance beam and a reference height. This is shown schematically in Figure 3.2.

#### 2.1.6 Accelerometer selection and mounting

The unsteady part of the aerodynamic load was measured using an accelerometer mounted above the counterweight. The accelerometer was a Freescale MMA1270EG with a single sensitive axis orthogonal to the plane of its surface mount. It was able to measure accelerations between  $\pm 28\text{m/s}^2$  ( $\pm 2.5$  times acceleration due to gravity) over a frequency range from from 0 – 1kHz. Figure 2.13 shows how it was mounted

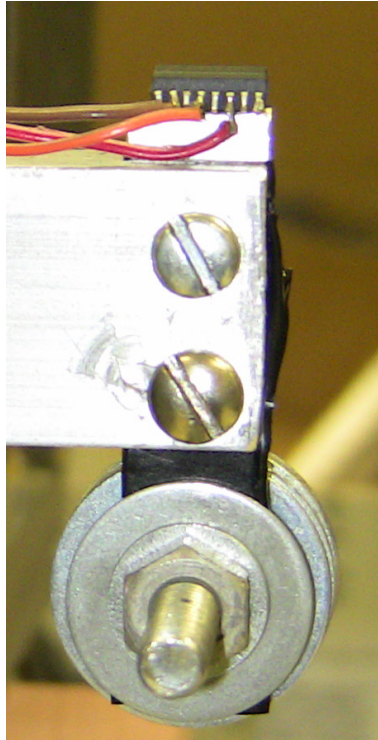


Figure 2.13. Photograph of the accelerometer mounted on the test stand with sensitive axis in the vertical direction.

above the counterweight during experiments. This placed the accelerometer as far from the axis of rotation as possible, with its sensitive axis perpendicular to the balance beam. The counterweight itself consisted of a quarter inch bolt on which washers were secured. This provided an adjustable and rigid counterweight.

#### 2.1.7 Balance beam design

The balance beams were constructed from aluminum bars as shown in Figure 2.14. They rotated about a quarter inch shaft that passed through a ball bearing sleeve located near the center. The flapping mechanism mounted to one side of the beam. That end of the beam had been milled thinner to attach the mechanism. A slot was milled into the other side to hold the accelerometer and counterweight.

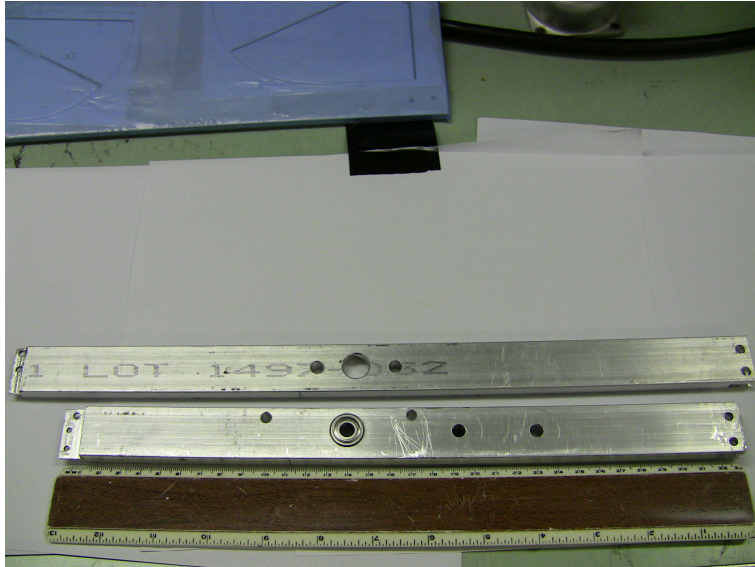


Figure 2.14. Photograph of the balance beams used in this experiment. The shorter beam is shown with ball bearing mounted at the rotation point.

A second longer beam was built to confirm the assumption that the system was measuring the thrust force generated by the wings. Its length was longer, resulting in a larger moment of inertia and thus smaller net acceleration than the shorter beam.

#### 2.1.8 Data collection procedure

Data collection involved three distinct steps: (1) setting the motor speed, (2) adjusting the counterweight to level the beam, and (3) collecting acceleration, displacement and tachometer time series as well as the weight of the counterweight.

Step (1) was accomplished with a small program written to convert Linux command line arguments into RS-232 signals that could be read by the SSC. Generally, there was a settling time of approximately 10s between the sending of the command and the mechanism's arriving at its new speed. This also included the time required for the pendulum part of the beam dynamics to damp out to a low amplitude,

long-period oscillation.

Step (2) involved adding or removing metal washers and nuts from the 1/4" bolt attached to the end of the beam. This method was labor intensive, but provided a finely adjustable mass that could be firmly attached to the beam. The counterweight hung below the center-line to insure the system center of gravity stayed below its axis of rotation. This resulted in a small change to  $l_p$  and thus the oscillation frequency of the pendulum. However, it was never faster than on the order of  $1Hz$ , well below the flapping frequency.

Step (3) used a PowerDAQ analog to digital (A/D) board with three single-ended inputs to measure the accelerometer, deflection and tachometer time series. It was controlled using the vendor-provided drivers and a custom program that ran from the Linux command line. The counterweight's mass was measured using an electronic balance after the electronic data was collected. A shell script was written to insure that these steps were done in the correct order and that the generated data files were handled properly.

## 2.2 Structure deformation measurements

### 2.2.1 Mechanism, Camera and Lighting Setup

A schematic of the arrangement the camera, spot light and flapping mechanism is shown in Figure 2.15. The flapping mechanism was mounted on the short beam shown in Figure 2.14. The driving electronics are the same, but no motion sensors were used. A white board placed behind the wings provided a relatively contrast-free background. The best results for lighting were obtained by placing the light source off to the side and bouncing it off the background such that the wings are easily detected shadows. An example of an image obtained by this setup is shown in Figure 2.16.

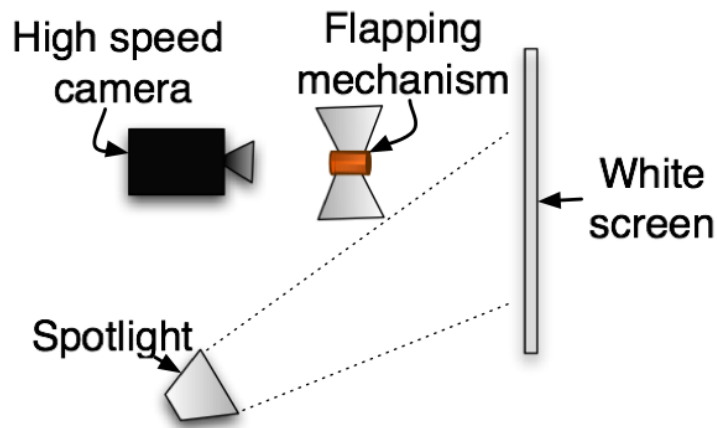


Figure 2.15. Top-view of the arrangement of camera, flapping mechanism and spotlight as seen from above during the structure deformation measurements



Figure 2.16. One of the frames captured during high speed flapping of the stiff wing

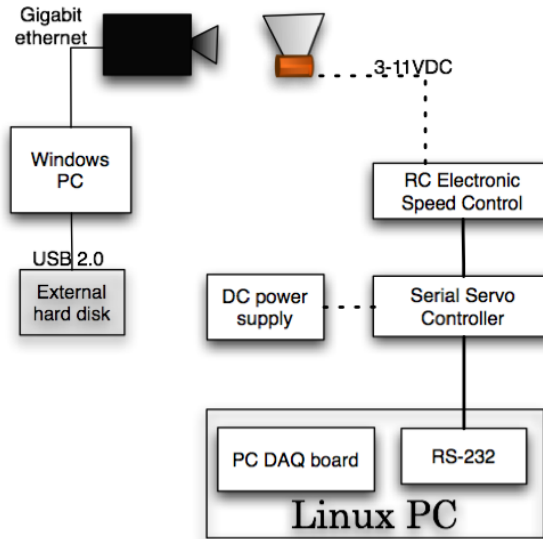


Figure 2.17. Electrical schematic of the optical deflection measurement system

Measurements were taken with a high speed digital camera at a frame rate of 2kHz. This matched the sampling rate of the force measurement system. Each sequence consisted of 5,457 frames, each with a resolution of  $1024 \times 1024$  pixels per image. An electrical schematic of this system is shown in Figure 2.17.

### 2.2.2 Image collection procedure

Images were collected at five flapping rates for each of the three wings described above. The camera was configured to fill its internal memory buffer, resulting in 5,457 frames collected over 2.7s. This resulted in a minimum of 10 flap periods at the slowest flapping rate, and up to 33 complete periods at the highest flapping frequency.

## CHAPTER 3

### Force Measurement

#### 3.1 Introduction

The objective of this study was to examine the time-resolved forces generated by mechanical flapping wings in hover. This is useful for generating insight into the fundamental physics of flapping wing flight, designing flight dynamics models (FDMs), and finding control laws for micro air vehicles (MAVs).

The standard ornithopter uses a pair of wings hinged at the root and flapped about a single axis. This approach has been used for over a century in order to propel mechanical flapping wings that use wing flexing to achieve a pitch-plunge profile, that in turn generates thrust [45]. There has been substantial progress in the design of mechanisms that mimic the complex motions of hummingbird and insect wing flapping, but these mechanisms add weight and complexity to vehicle systems, and for now exist only as bench top models [9]. Another popular flapping mechanism involves clapping pairs of wings together that mimic the “clap and fling” mechanism used by small insects to boost their efficiency [70]. In short, for all man made flapping vehicles in use today, the flexible wing is a critical component in the force generation. Since a combination of aerodynamic and inertial loads causes the wings to take on a shape trajectory, quantifying this is critical for designing flapping vehicles.

Previous efforts to measure flapping wing forces have used scaled models in a

heavier fluid such as oil or water, or have attempted to interpret the output of a spring scale [19, 14, 61]. The problem with these models is the difficulty of dynamically scaling both fluid and structural components. As a result the complicated fluid-structure interaction is generally neglected, thus producing substantially different results from tests conducted in air. Additionally, the heavier fluid essentially acts as a larger second order low-pass filter. Both effects limit the detectable bandwidth of the flapping system, which gives the impression of less high-frequency content than is actually present in the force time series, and potentially leads to inadequate update rates in the design of simulations and control systems.

Force measurements in air typically use a strain-gage load cell or cantilever beam that behaves like a spring scale. As discussed further in the next section, this technique is useful for measuring the average force [39]. Wu *et al.* [67] developed a flapping mechanism and camera system to simultaneously measure the small forces generated by the flapping wings and their deformation. They encountered significant problems with “ringing” in the force measurement device. They ultimately assumed that the heavily filtered strain gage output represented the true force measurement.

### 3.2 Data Analysis

The mean thrust,  $\bar{T}$ , is balanced by an adjustable counterweight,  $m_c$ . The magnitude of the acceleration is determined by the angular acceleration of the beam,  $\ddot{\theta}$ , which in turn depends on the moment of inertia of the whole beam,  $I$ . The mass and moment arm of the counterweight,  $l_c$ ; the mass and moment of arm of the flapping mechanism  $l_m$  and  $m_m$  respectively, and the mass and moment arm of the wings themselves  $l_w(t)$  and  $m_w$ . These dimensions are enumerated in Table 3.1.

$$I\ddot{\theta} = l_c m_c g + l_b m_b g + l_w T(t) - l_w m_w g - l_m m_m g - \sin \theta m_t l_p g, \quad (3.1)$$

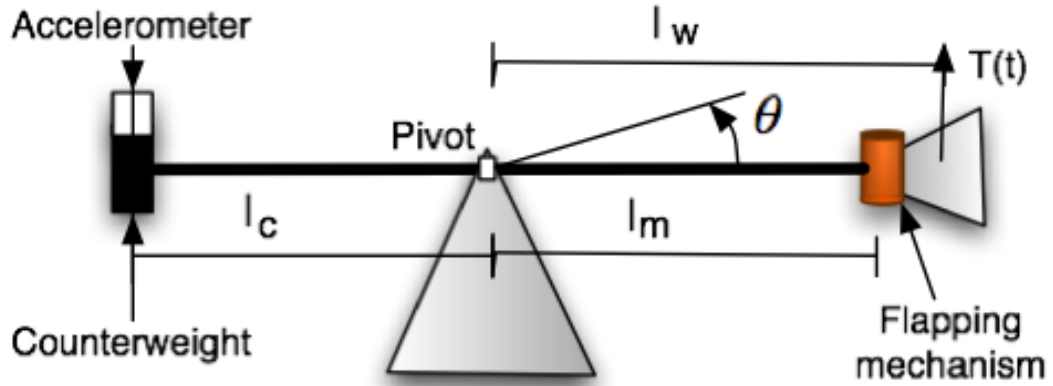


Figure 3.1. A schematic view of the instrumented balance beam used to measure the flapping wing forces and moments

Table 3.1

Values used in this analysis

Beam	$l_m$	$l_c$	$l_b$	$m_b$	$l_w$	$m_m$	$l_p$
Short	17cm	18cm	3.00cm	272cm	19cm	97 g	1.5cm
Long	21cm	19cm	1.6cm	236.5 g	23cm	97 g	1.5cm

$$\bar{T} = (\bar{l}_w m_w g + l_m m_m g - l_b m_b g - l_c m_c g) / l_w, \quad (3.2)$$

$$\hat{T} = I \ddot{\theta} + \sin \theta m_t l_p g. \quad (3.3)$$

As shown in Equations 3.1-3.3, accelerometers do not directly measure the generated thrust, only the changes from the mean thrust  $\hat{T}$ . The unsteady thrust component  $\hat{T}$  was measured using an accelerometer mounted above the counterweight. The voltage generated by the accelerometer,  $V_a$  was a combination of the acceleration at the point above the counterweight and the alignment of the sensitive axis with gravity. The acceleration was determined using the equation for the

acceleration of a point on a rotating body in Meriam and Kraige [41]. The gravity influence is based on the properties of accelerometers described in Chapter 1 of Sevens and Lewis [59]. The voltage generated is related to these physical factors through a scaling factor  $k_a$  as shown derived in Equations 3.4-3.6. Equation 3.4 describes the relationship between linear acceleration, alignment with local gravity, and the voltage measured by the device. Equation 3.5 relates the linear acceleration of a point on a rigid rotating body to the angular acceleration of the body given its distance from the point of rotation. Equation 3.6 combines these two to produce an estimate of the voltage time series generated by the accelerometer.

$$V_a = -k_a * (\ddot{x}_a + \cos \theta g) \quad (3.4)$$

$$\ddot{x}_a = l_c \ddot{\theta} \quad (3.5)$$

$$V_a = -k_a * (\ddot{\theta} l_c + \cos \theta g) \quad (3.6)$$

The voltage time series from the accelerometer was processed in three steps to compute  $\hat{T}(t)$ . First, the raw voltage from the accelerometer was converted to the nongravitational specific force. The second step involved removing the effect of gravity using the measurement of the beam's angle to determine the relationship between the axis of sensitivity and the local gravity vector. The third step was to use Equation 3.8 to determine  $\ddot{\theta}$ . With  $\ddot{\theta}$  and Equation 3.7, it was possible to solve for  $\hat{T}$ . The total thrust was then the sum of the average and unsteady components.

$$I \ddot{\theta} = \hat{T}(t) l_w - \sin \theta m_t l_p g \quad (3.7)$$

$$\ddot{\theta} = \frac{(-V_a/k_a - g \cos(\theta))}{l_c} \quad (3.8)$$

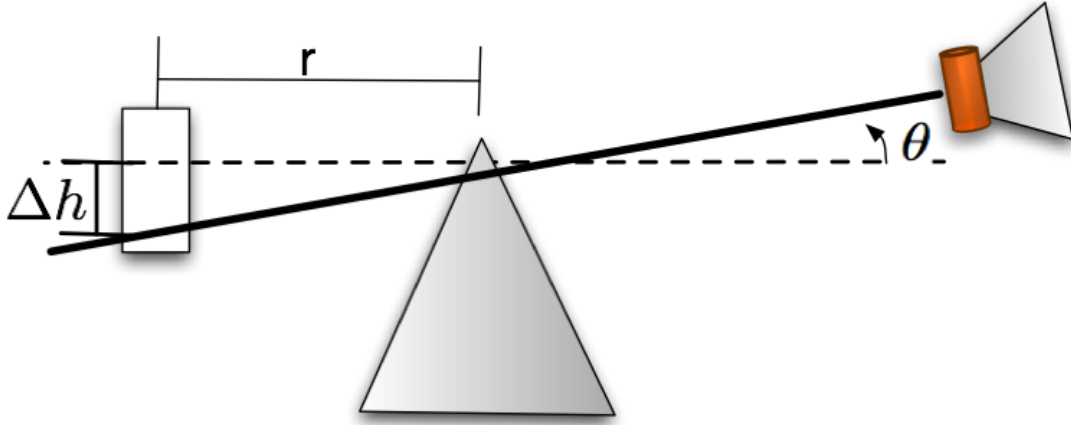


Figure 3.2. Diagram showing how the measured vertical displacement of the balance beam was used to measure the angle  $\theta$ .

The angle  $\theta$  was important both for determining the counterweight by showing when the beam was level and for processing the accelerometer data. In this experiment,  $\theta$  was measured using a Keyence optical displacement sensor. This is an industrial sensor typically used for process control, but it provides a very fast and accurate non-contact measurement of the height of the bottom of the beam as shown in Figure 3.2. The angle  $\theta$  is related to the measurement by Equation 3.9, where  $r$  is the horizontal distance from the axis of rotation to the measurement system

$$\theta = \arctan \frac{\Delta h}{r}. \quad (3.9)$$

### 3.3 Results and Discussion

#### 3.3.1 Average force measurements

Figures 3.3-3.7 show the average thrust force generated over the range of flapping frequencies tested using both the short and long beams. In each case, the measure-

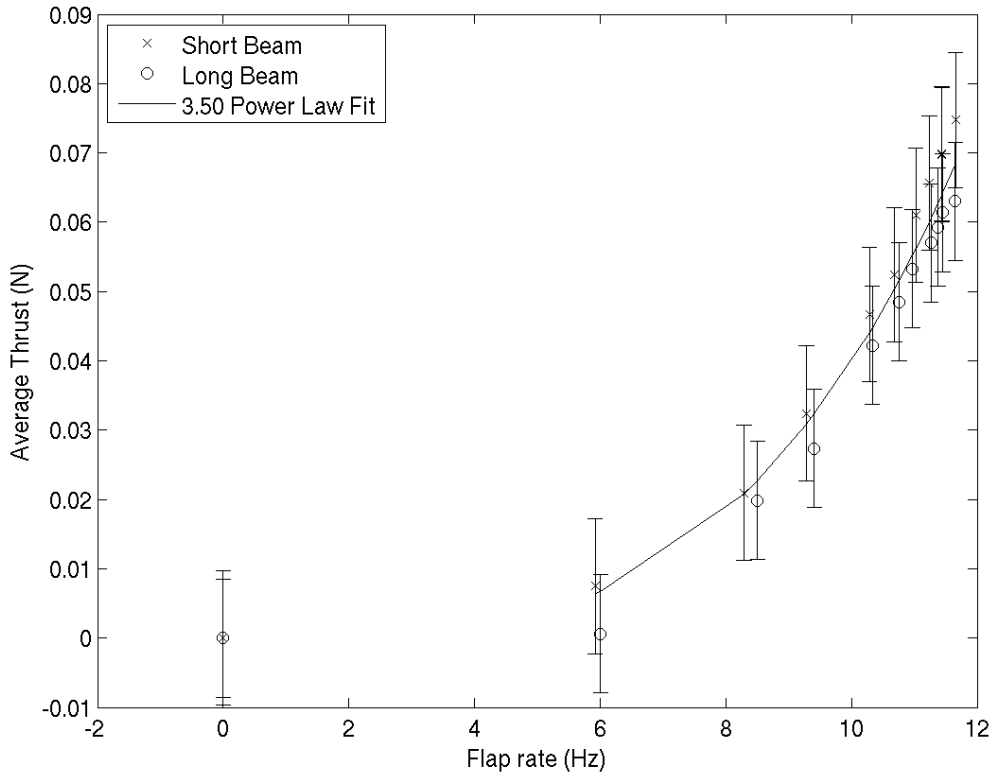


Figure 3.3. The average thrust generated by the stiff wing.

ments from the two beam are repeatable with the experimental uncertainty. This confirms that the balance beam is measuring a thrust force as shown in Figure 3.1 and modeled by Equation 3.2.

The stiff wing average thrust is shown in Figure 3.3. A log-log plot of thrust versus flap rate is shown in Figure 3.4, demonstrating the average thrust increases with the flapping frequency to the 3.5 power. This is very similar to the 3.3 power observed in data collected by Wu, *et al.* [67] for a similar wing design.

The average thrust versus flapping frequency for the flexible is shown in Figure 3.5. A log-log plot of thrust versus flapping frequency is shown in Figure 3.6. This shows that the flexible wing average force increased with flapping frequency to the

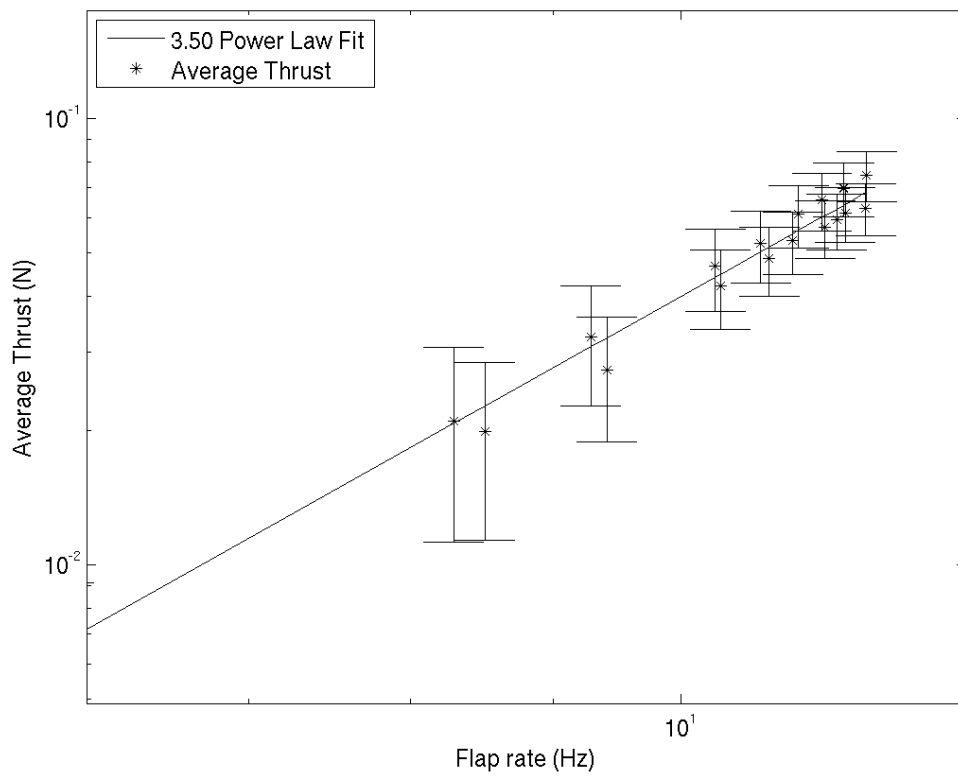


Figure 3.4. Log-log plot of the data presented in Figure 3.3.

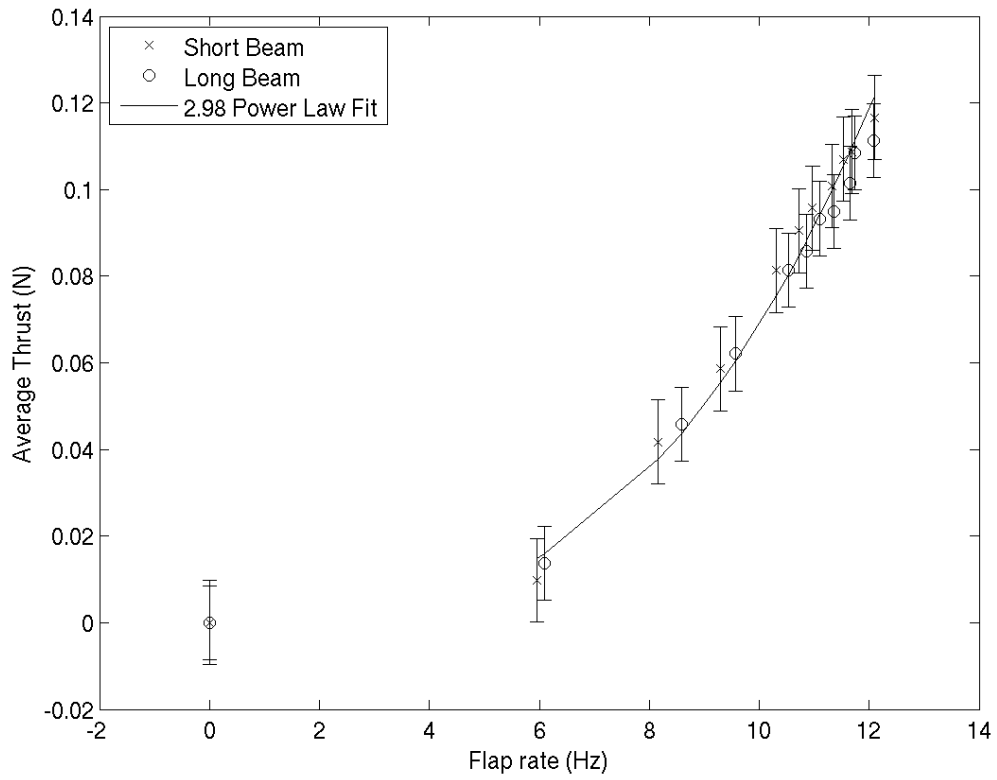


Figure 3.5. The average thrust generated by the flexible wing.

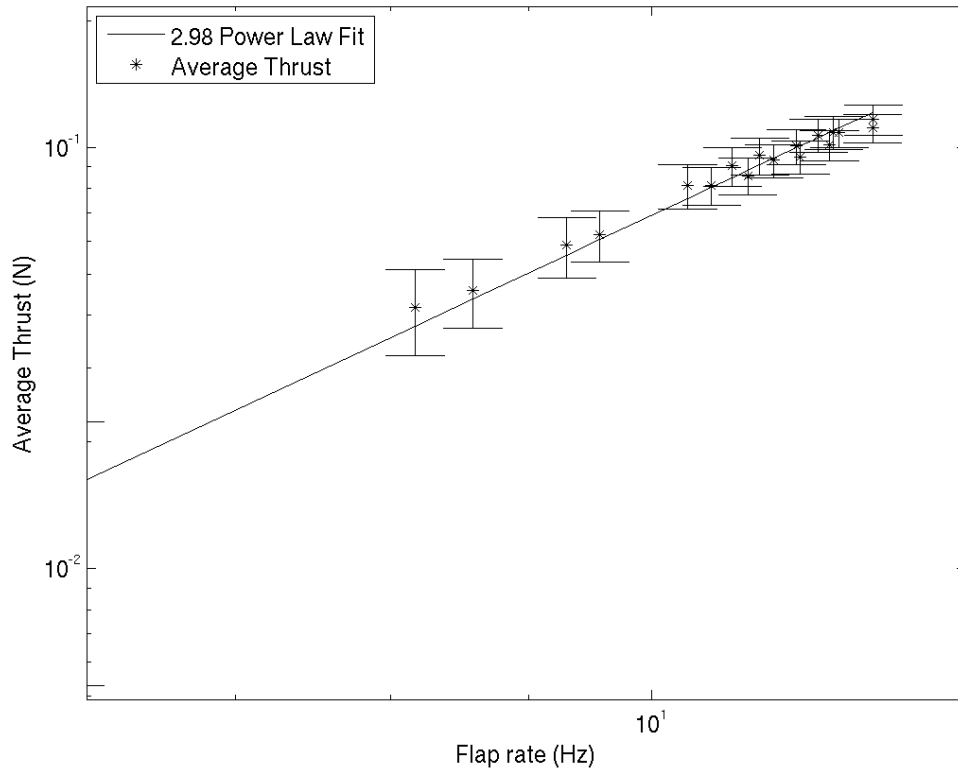


Figure 3.6. Log-log plot of the data presented in Figure 3.5.

2.98 power. However, the flexible wing generated more thrust than the stiff wing.

The average thrust for the drumhead wing is shown in Figure 3.7. The log-log plot of these data is shown in Figure 3.8. The drumhead wing produced considerably more thrust than the stiff wing at all flapping frequencies. This implies that a less stiff root, and consequently greater deflection due to wing acceleration, is beneficial for thrust production. The drumhead wing produced as much thrust as the flexible wing.

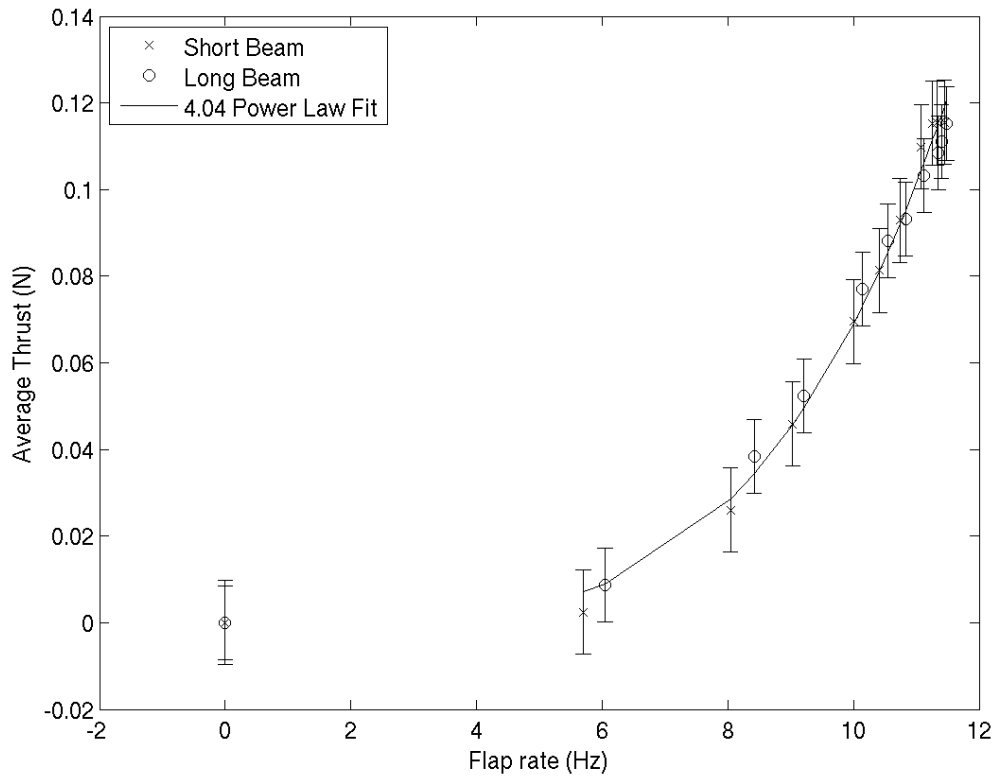


Figure 3.7. The average thrust generated by the drumhead wing.

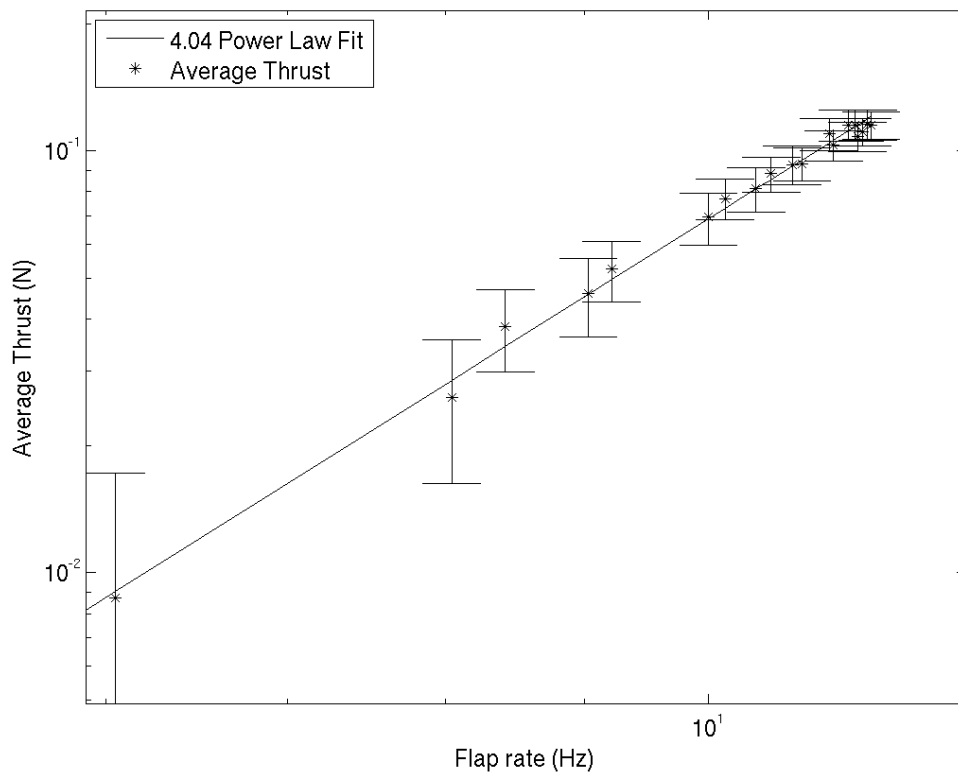


Figure 3.8. Log-log plot of the data presented in figure 3.7.

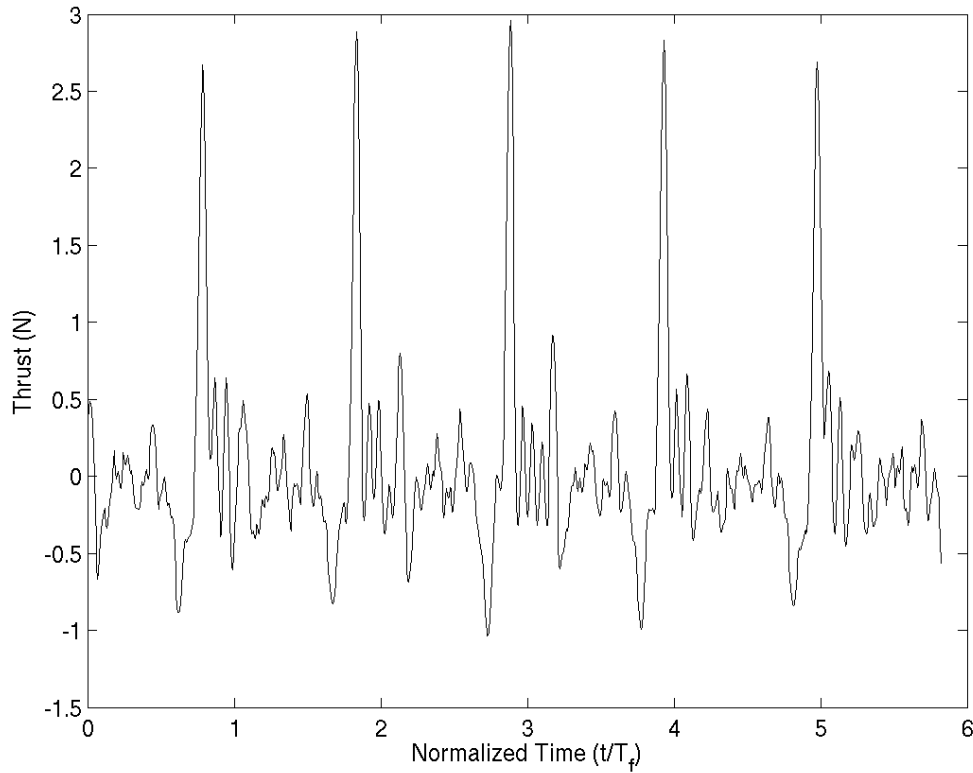


Figure 3.9. Time resolved thrust generated by the stiff wing at a flapping frequency of 11.5Hz

### 3.3.2 Time-resolved force measurement

Figures 3.9-3.11 show time-resolved thrust measurements for the stiff, flexible, and drumhead wings, respectively, at the highest flapping frequency tested. They show that the flapping thrust generation is a highly periodic process with respect to the flapping rate. This fact allowed the data sets to be phase-averaged for further analysis.

Figures 3.12 through 3.14 show the phased averaged thrust time series for the stiff wing at three flapping frequencies. This shows similarities to the data collected by Lehmann, *et al.* [32]. Most notable is the large peak in the thrust shortly

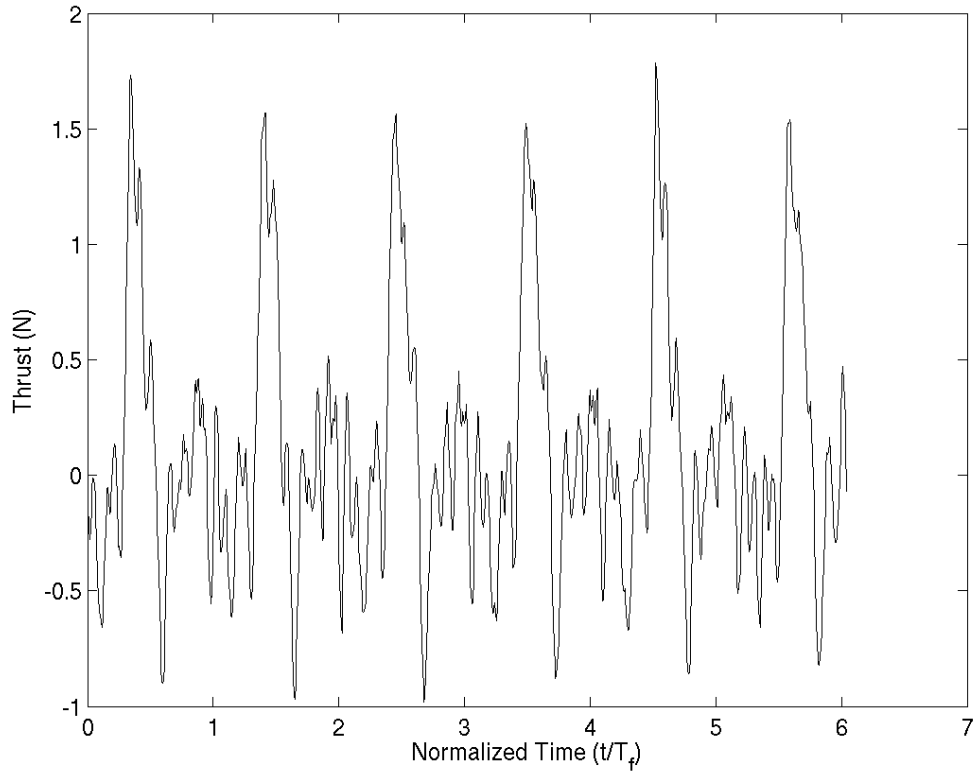


Figure 3.10. Time resolved thrust generated by the flexible wing at a flapping frequency of 12Hz

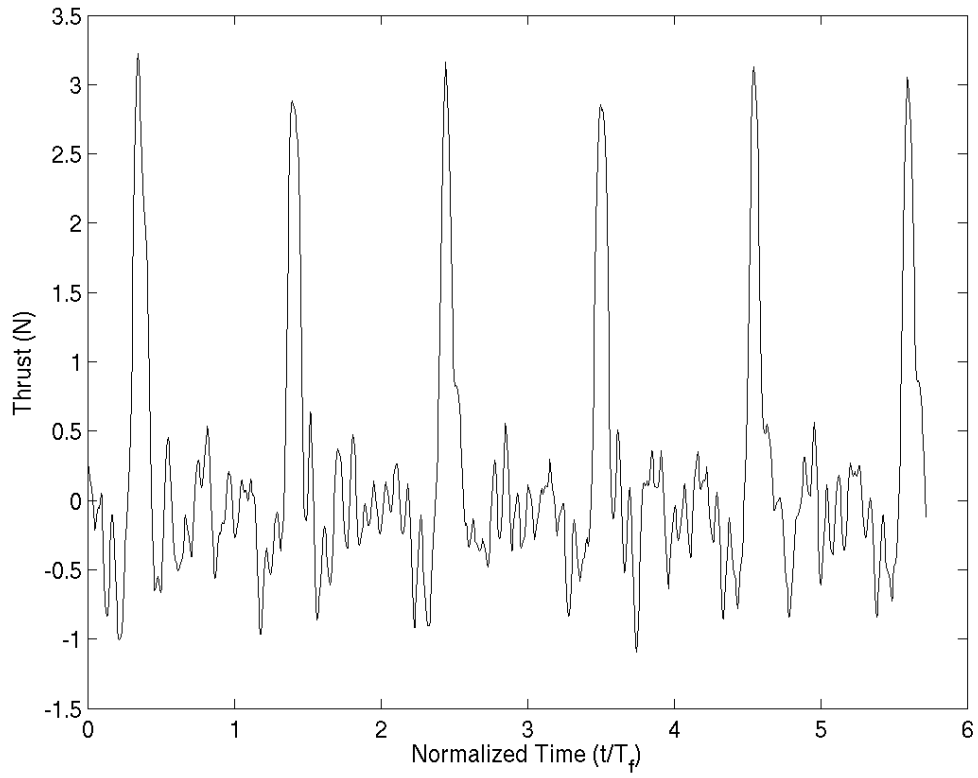


Figure 3.11. Time resolved thrust generated by the drumhead wing at a flapping frequency of 11.5Hz

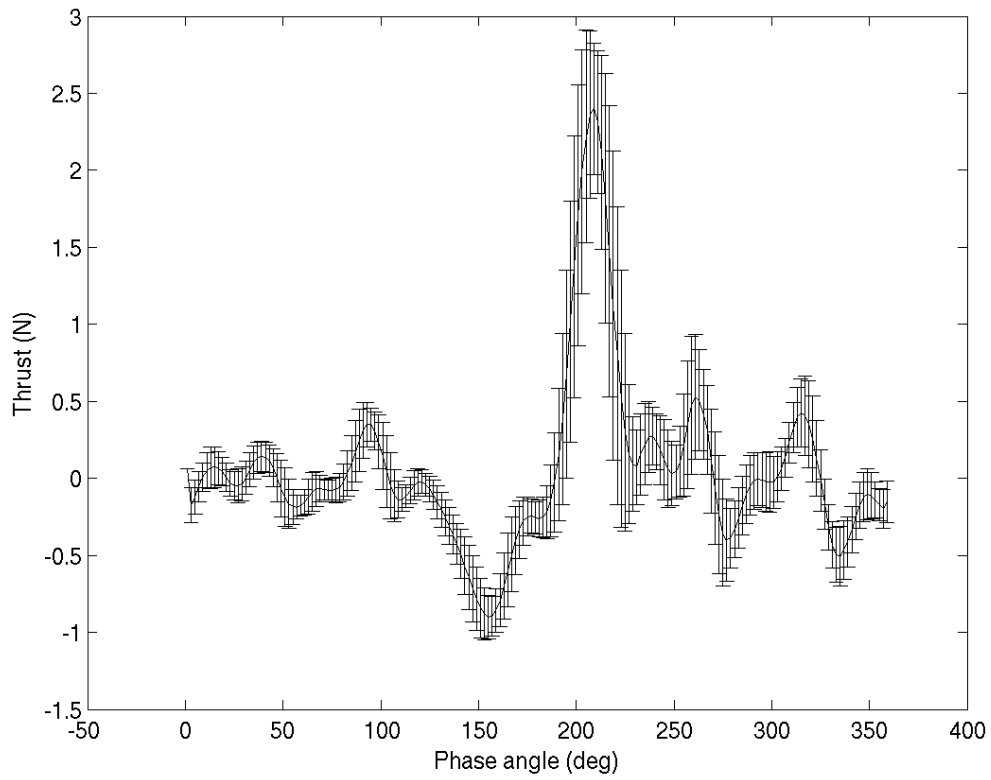


Figure 3.12. Plot of the phase resolved thrust of the stiff wing at  $11.5Hz$

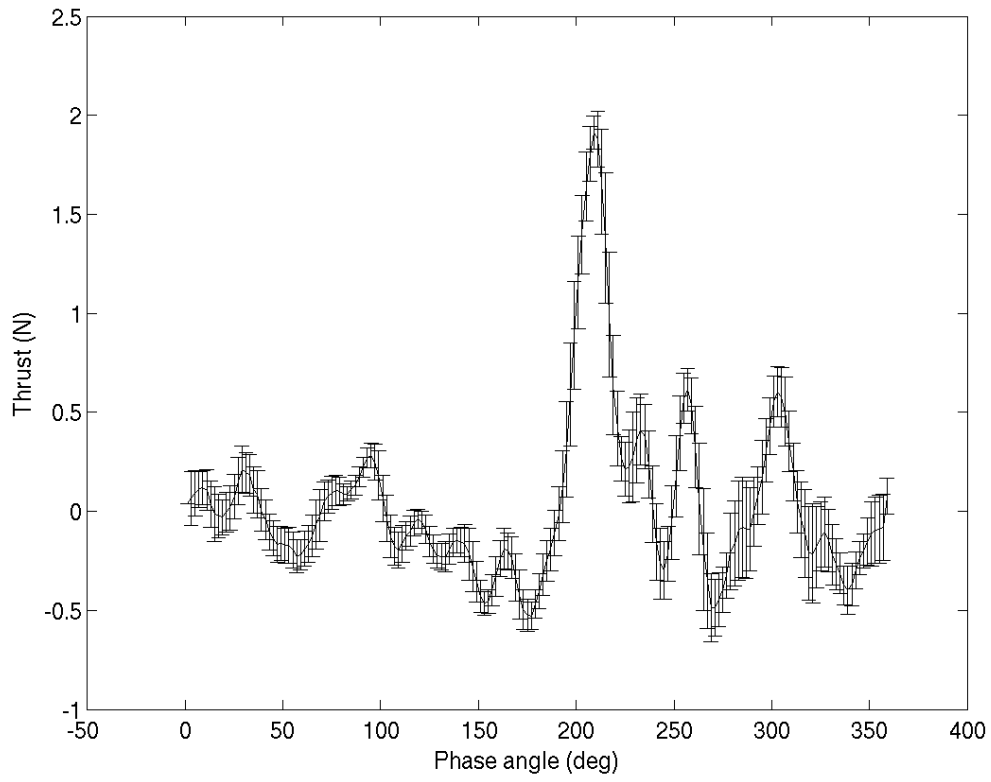


Figure 3.13. Plot of the phase resolved thrust of the stiff wing at  $10Hz$

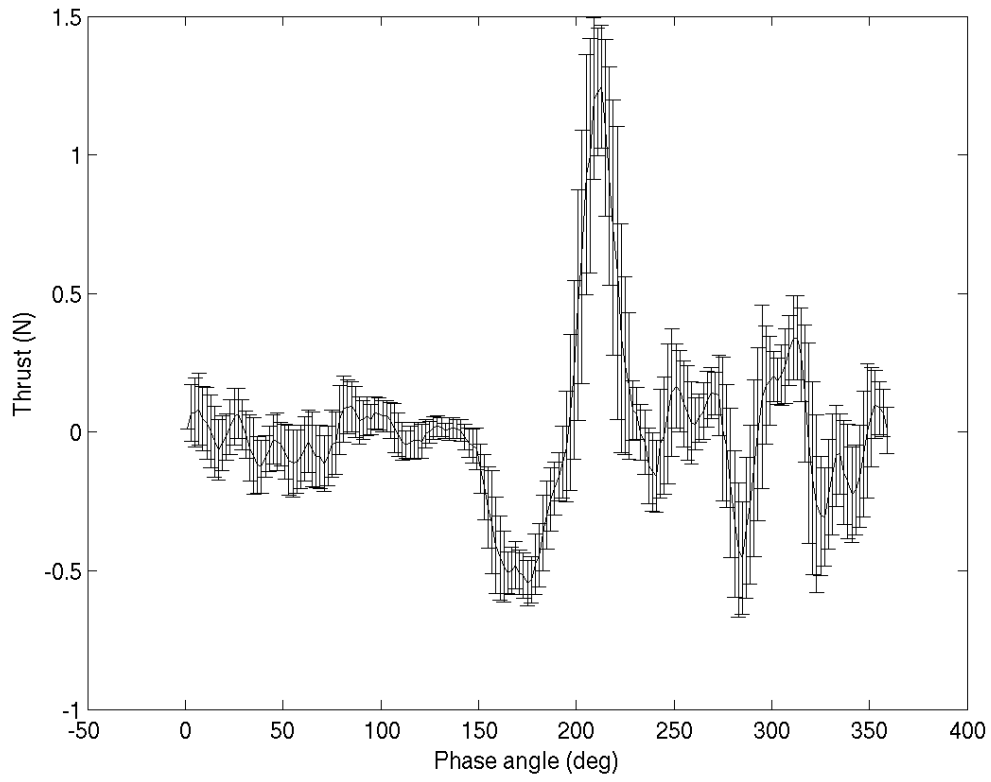


Figure 3.14. Plot of the phase resolved thrust of the stiff wing at  $9Hz$

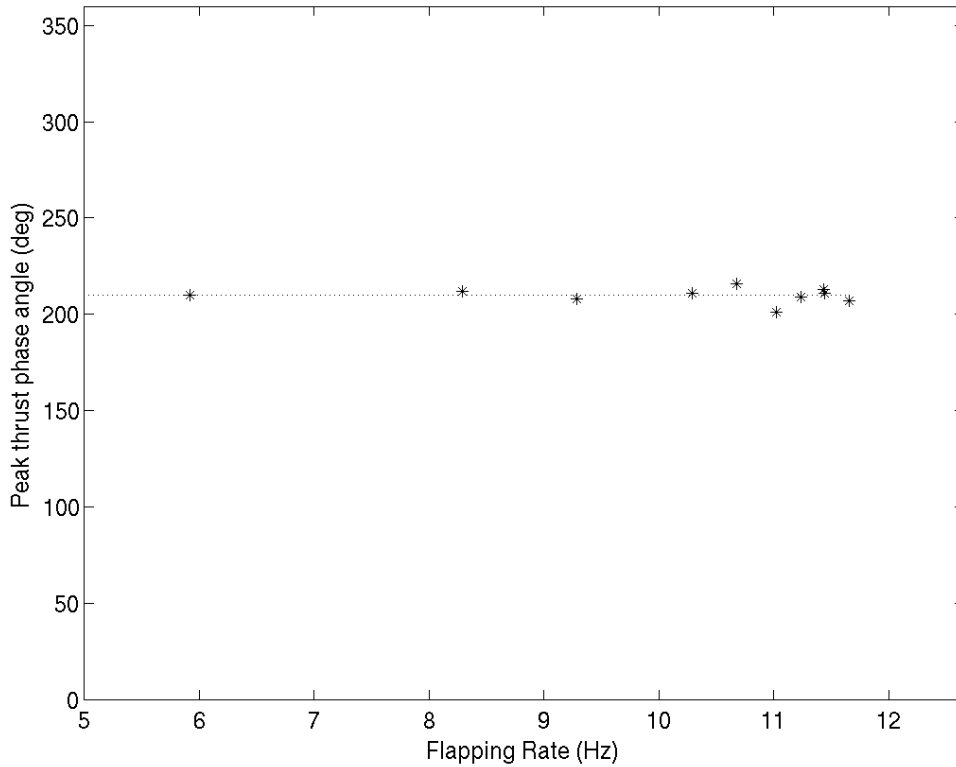


Figure 3.15. Plot of the phase angle of the peak thrust generated by the stiff wing at the flapping rates tested.

after the beginning of the downstroke, and followed by small oscillations afterward. Differences in these three curves relate to differences in vortex formation and vortex shedding as the wing transitions from a flow dominated by a starting vortex at high frequencies to a quasi-steady condition at slower flapping rates as described by Jones and Babinsky [22].

Figure 3.15 shows a plot of the phase angle of the peak thrust generated by the stiff wing versus flapping frequency. This shows that the phase angle of the peak of the peak thrust is approximately constant at  $\phi = 210^\circ$ , indicating thrust generation can be treated as a linear process relative to the flapping rate. The peak thrust

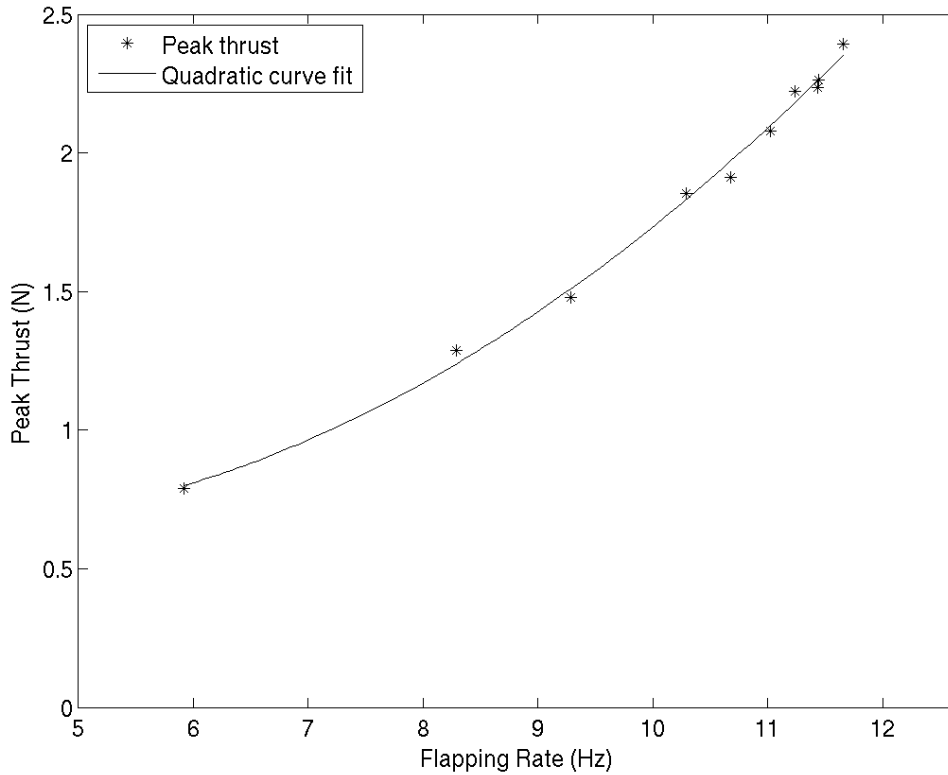


Figure 3.16. Plot of the peak thrust generated by the stiff wing at the flapping frequencies tested

generated during each flapping cycle can be fit very well by a quadratic function of the flapping frequency, as shown in Figure 3.16. The square of the flapping frequency is equivalent to the square of the maximum tip speed as computed by Equation 3.10. This fact suggests that the force generation process is at least qualitatively similar to that of rotors and propellers[33].

$$v_{tip} = (b/2)f_f 2\pi \quad (3.10)$$

The phase averaged thrust for the flexible wings at three different frequencies are

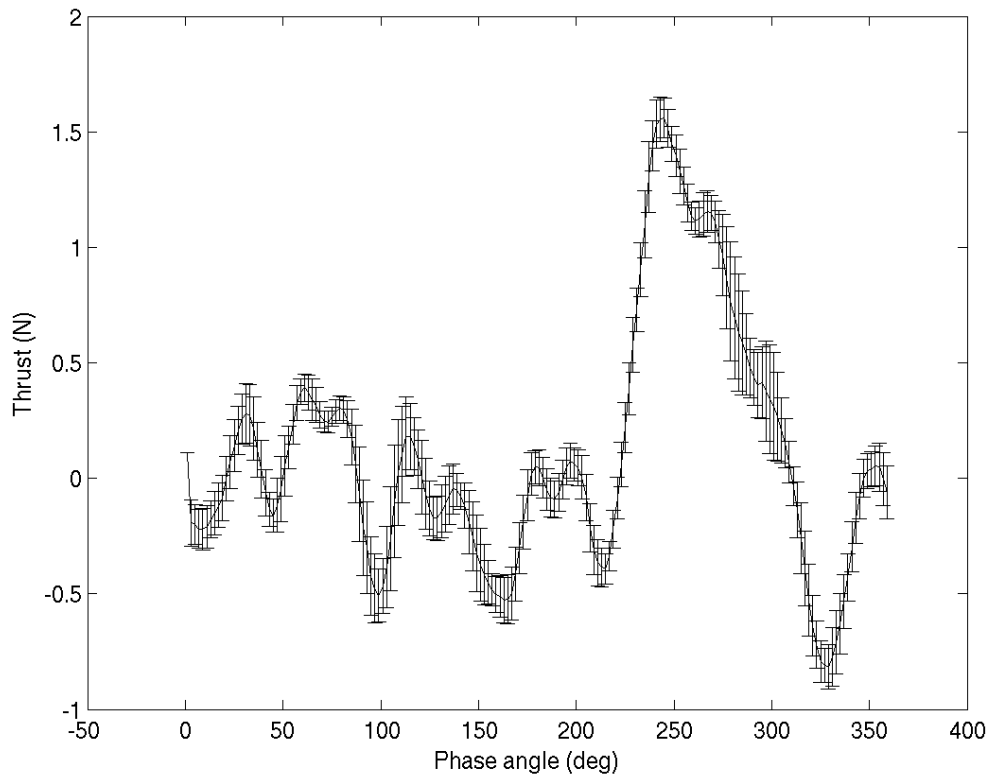


Figure 3.17. Plot of the phase resolved thrust of the flexible wing at  $12Hz$ .

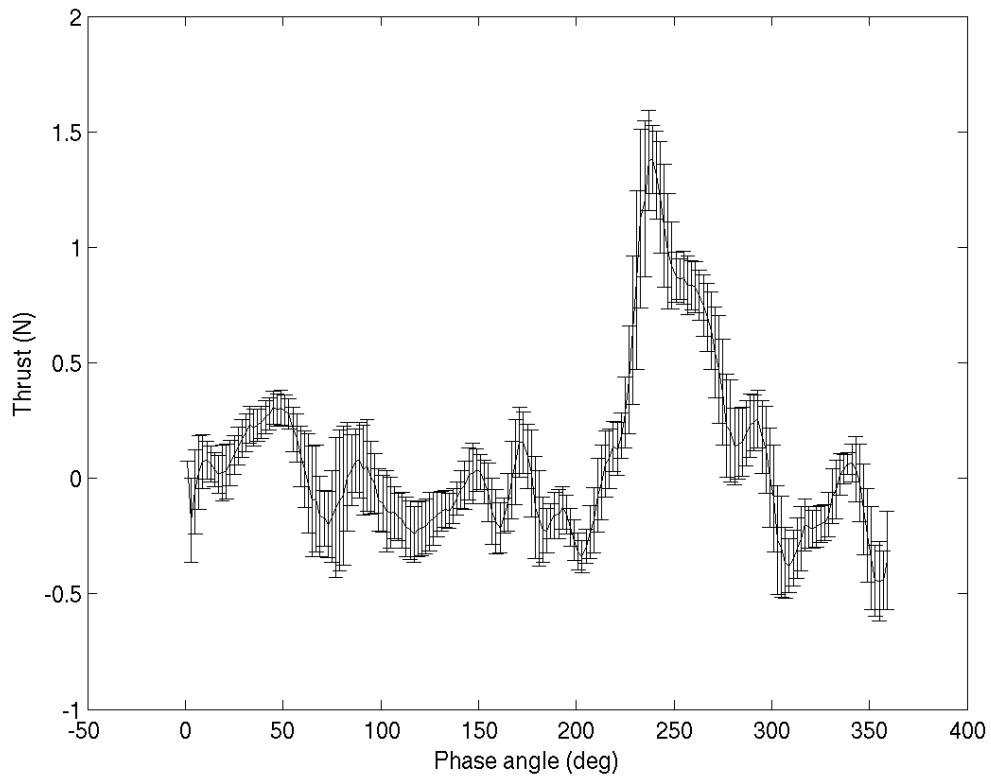


Figure 3.18. Plot of the phase resolved thrust of the flexible wing at  $11Hz$ .

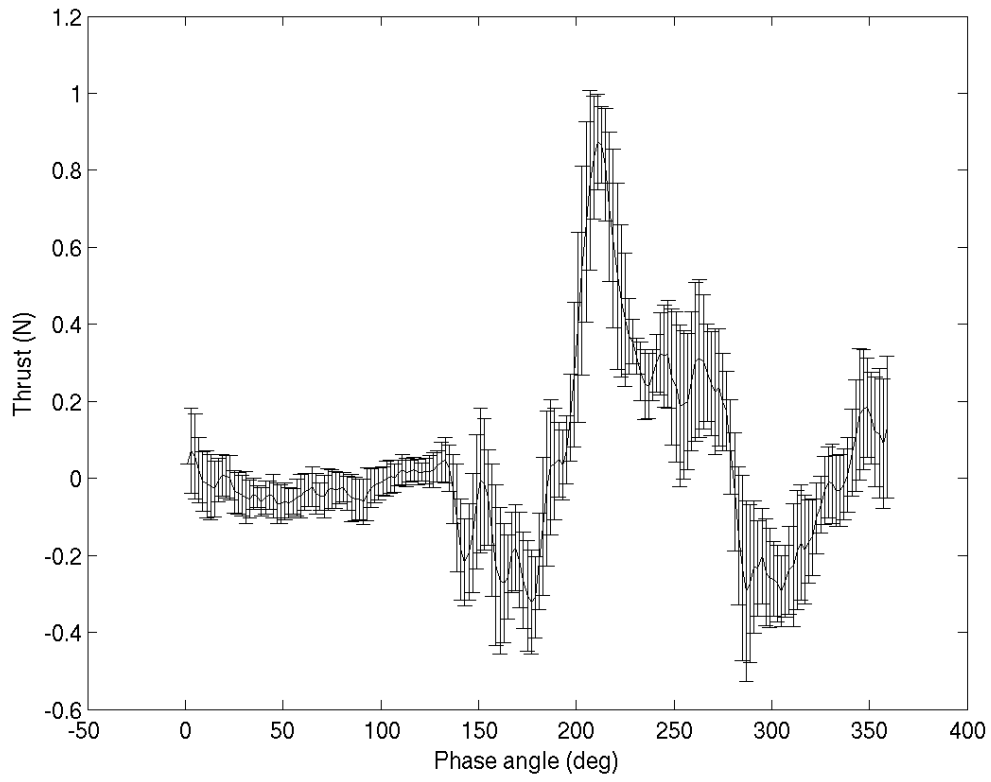


Figure 3.19. Plot of the phase resolved thrust of the flexible wing at  $9Hz$ .

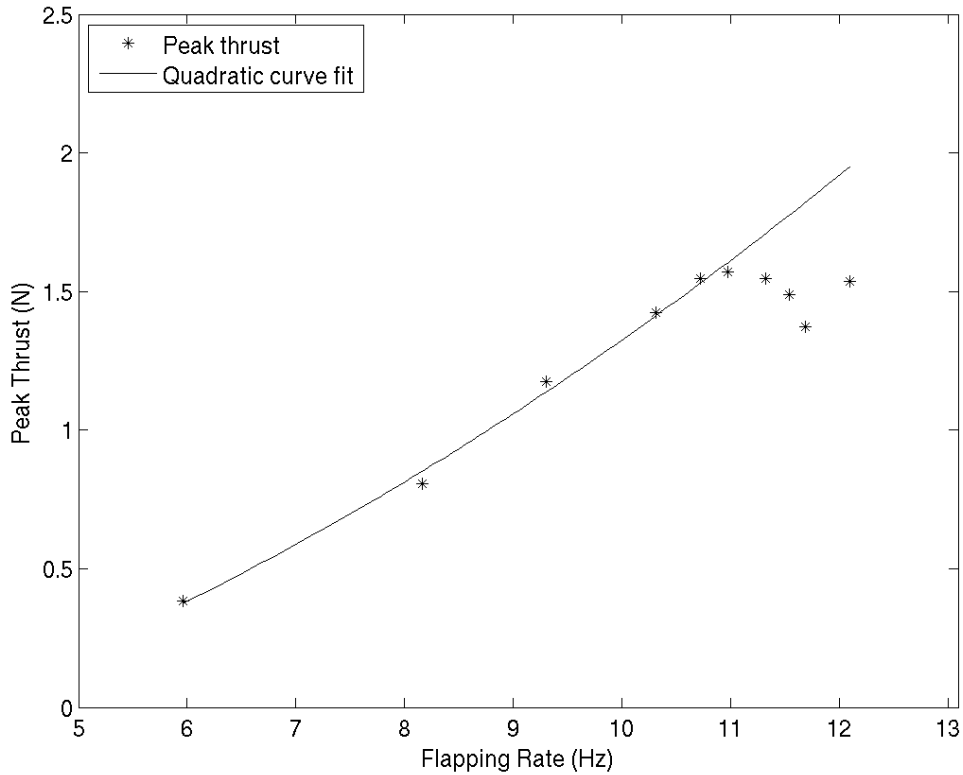


Figure 3.20. Peak thrust generated by the flexible wing as a function of frequency.

shown in Figures 3.17 through 3.19. As with the stiff wing, it exhibited a prominent peak in the thrust shortly after the beginning of the downstroke. However, the instantaneous thrust peak was broader with the flexible wing.

The peak thrust value is plotted versus the flapping frequency in Figure 3.20. This shows that the peak thrust scales as  $f_f^2$  like the stiff wing. However, it appears that the peak thrust saturates at flapping frequencies above 10Hz. The phase angle of the peak thrust versus flapping rate is shown in Figure 3.21. In this case it occurs at  $\phi = 240^\circ$  which is slight later than with the stiff wing. It still suggests that the thrust generation is a linear process.

The phase averaged thrust for the drumhead wing at different frequencies is

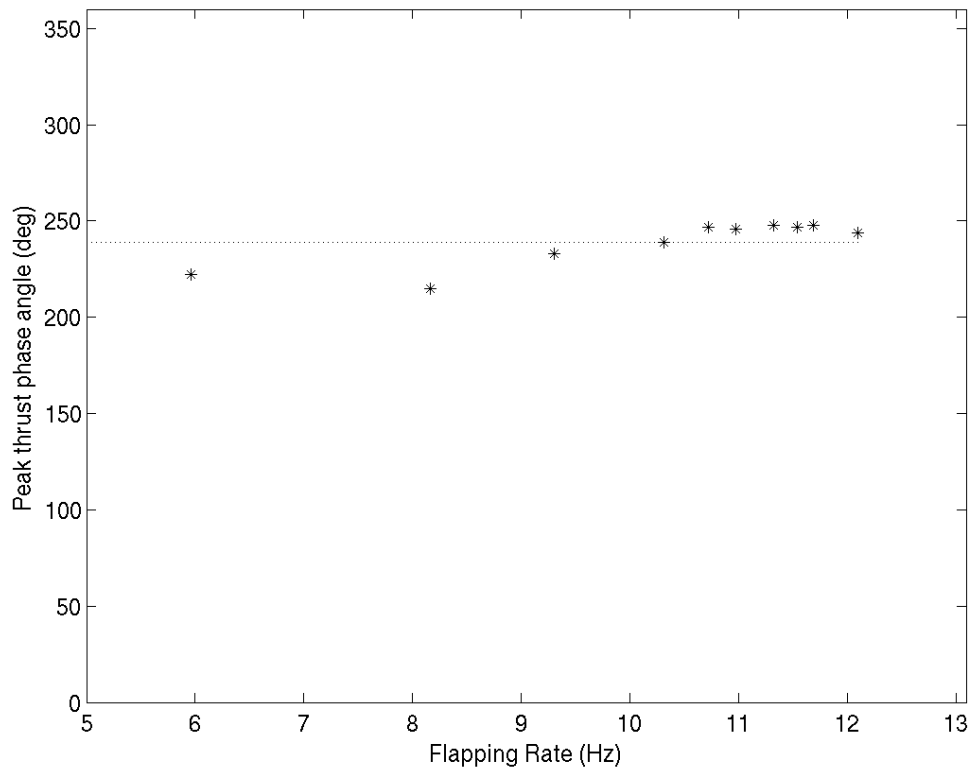


Figure 3.21. Plot of the phase angle of the peak thrust generated by the flexible wing at the flapping rates tested.

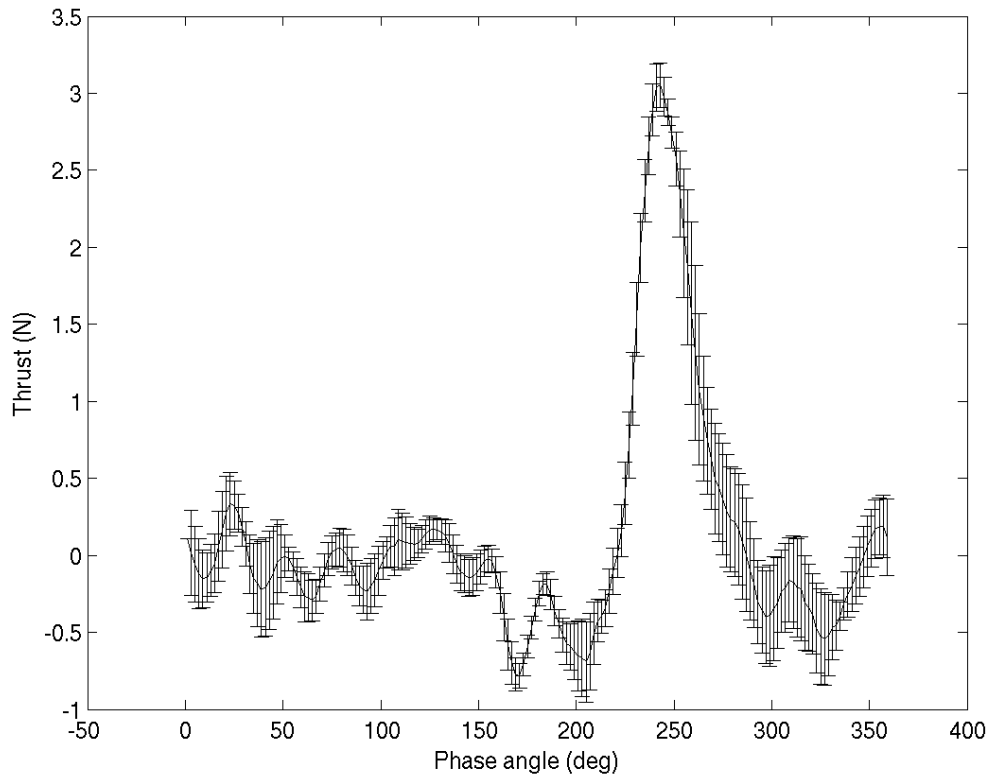


Figure 3.22. Plot of the phase resolved thrust of the drumhead wing at 11.5Hz.

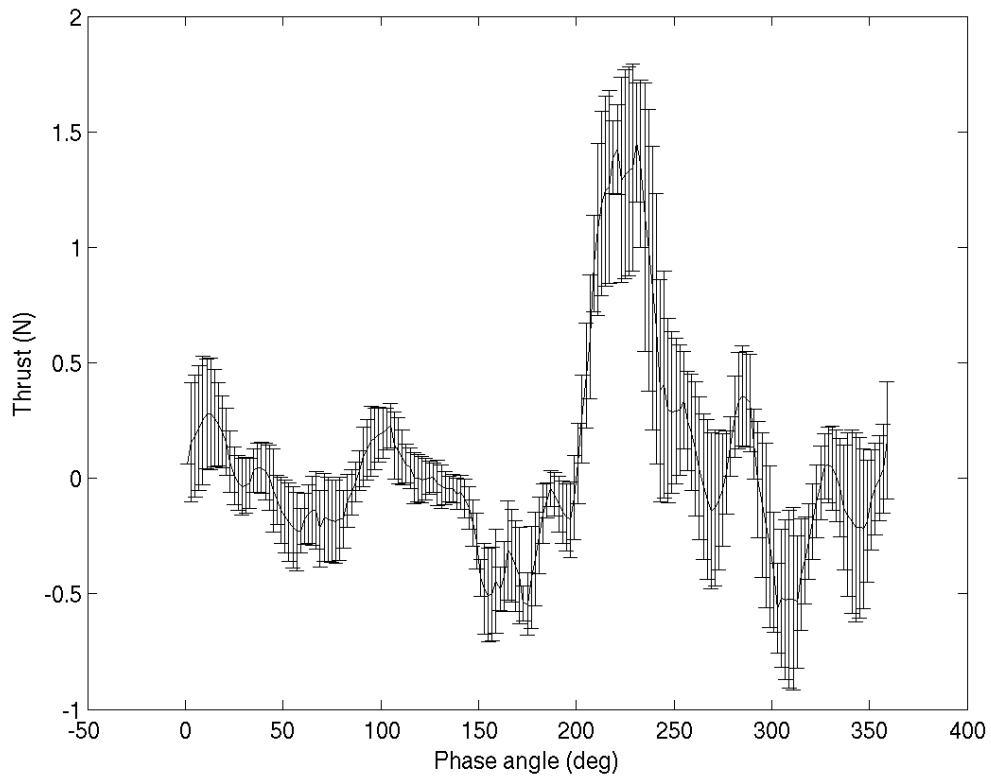


Figure 3.23. Plot of the phase resolved thrust of the drumhead wing at 10Hz.

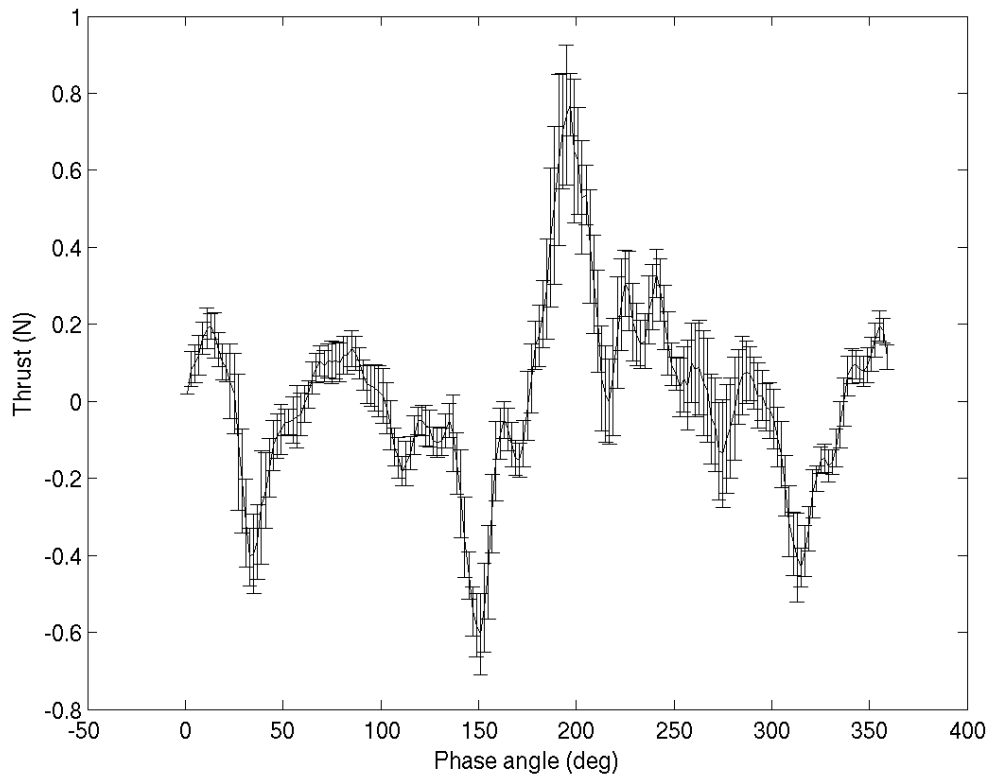


Figure 3.24. Plot of the phase resolved thrust of the drumhead wing at 10Hz.

shown in Figures 3.22 through 3.24. While the drumhead wing, like the other two wings, has a dominant peak in its thrust curve, the shape of this peak changes substantially with the flapping frequency. The peak thrust increases steadily over the range of flapping frequencies tested as shown in Figure 3.25. Figure 3.25 shows the magnitude of the peak thrust as a function of flapping frequency. Like the other wings, the peak thrust increases as the square of the flapping frequency. In contrast to the flexible wing, the drumhead wing does not saturate at the higher frequencies. The flapping phase angle of the peak thrust for the drumhead wing as a function of flapping frequency is presented in Figure 3.26. As with the other wings, the phase angle is constant at all frequencies.

### 3.3.3 Flapping thrust frequency content

The most significant challenge in this study was finding a means of measuring the time-resolved flapping wing forces given their high bandwidth and small magnitude relative to the weight of the flapping mechanism. To investigate this the spectral density was computed for the thrust time series for each of the wings. These spectra are shown in Figures 3.27 through 3.29. Here the frequency axis has been normalized by the flapping frequency. This indicates that significant energy exists at as much as fifteen times the flapping frequency.

## 3.4 Chapter Summary

The goal of this portion of the research was to gain a better understanding of the behavior of flapping wing aircraft in hover. The experimental setup proved effective in measuring the time-resolved thrust forces. It revealed differences in the thrust produced by wings of different stiffness. In particular it showed that wing structures that cannot easily twist tend to have a relatively sharp thrust peak in their flapping cycle compared to flexible wings. The flexible wings, in contrast to

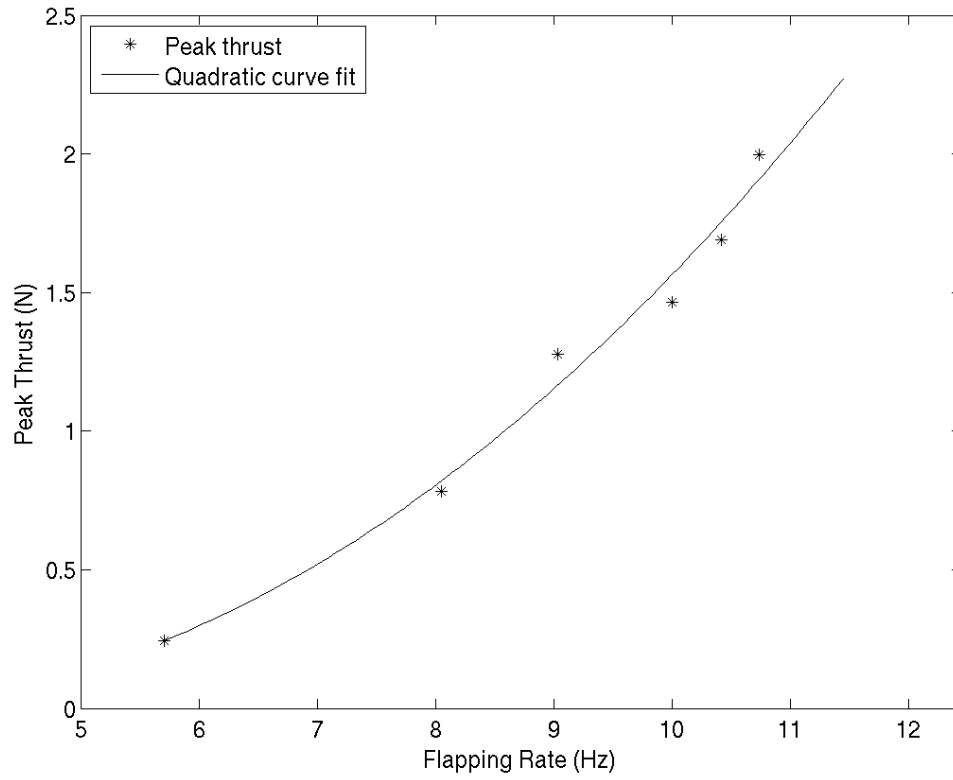


Figure 3.25. Peak thrust generated by the drumhead wing as a function of flapping frequency.

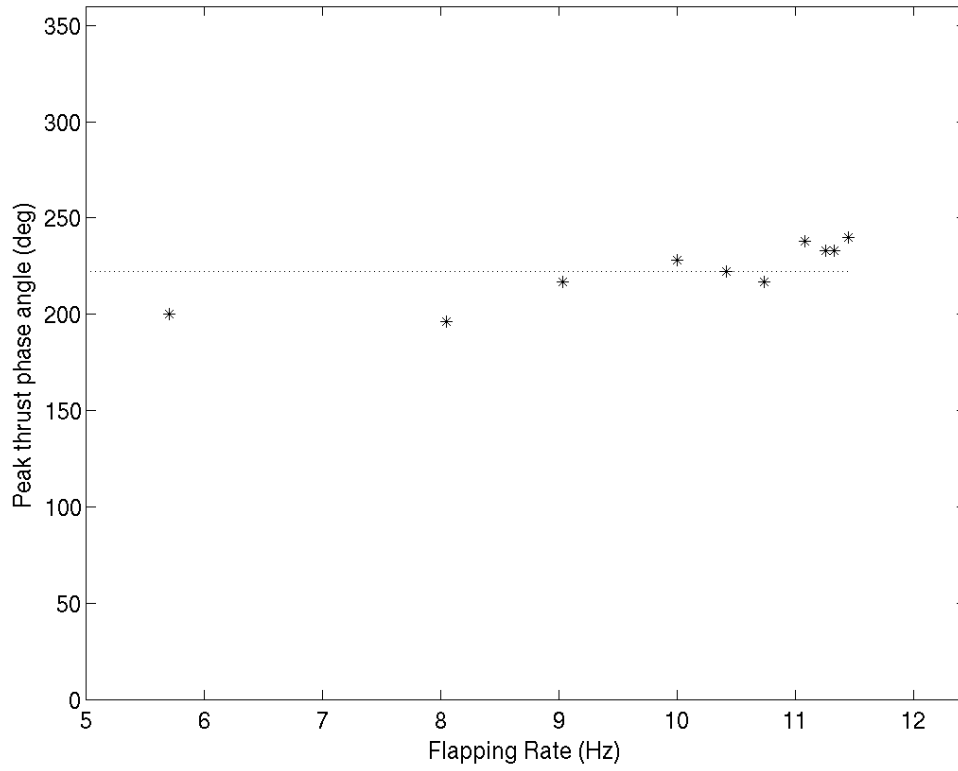


Figure 3.26. Phase angle of the peak thrust generated by the drumhead wing vs. flapping frequency.

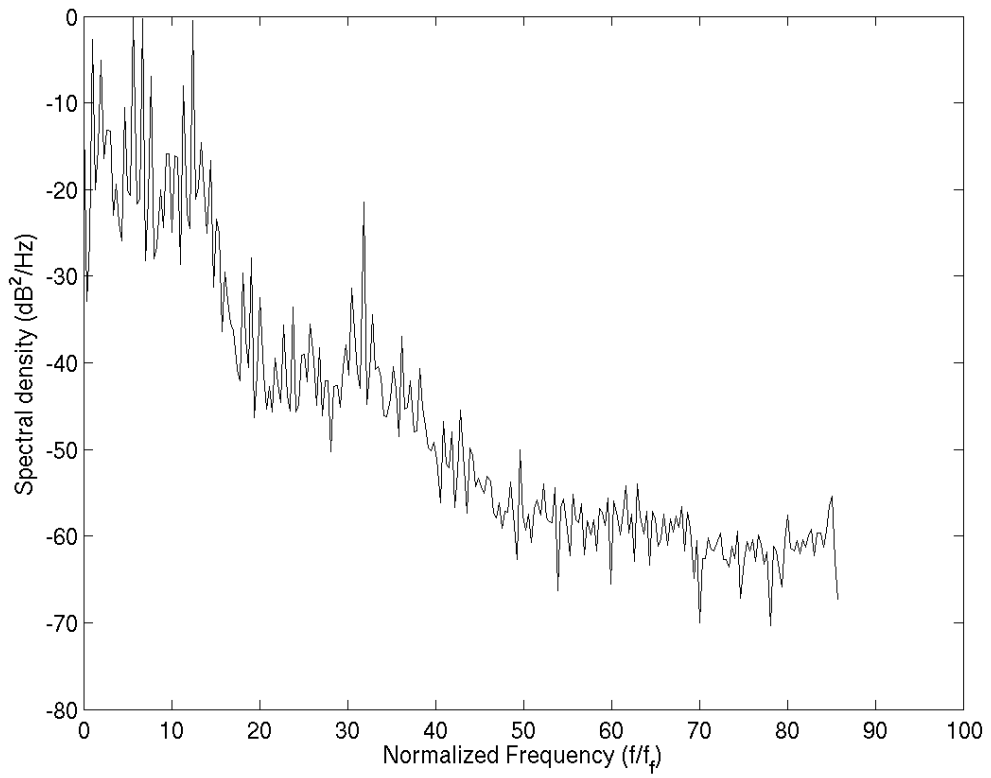


Figure 3.27. Spectra of frequency content of the thrust time series for the stiff wing.

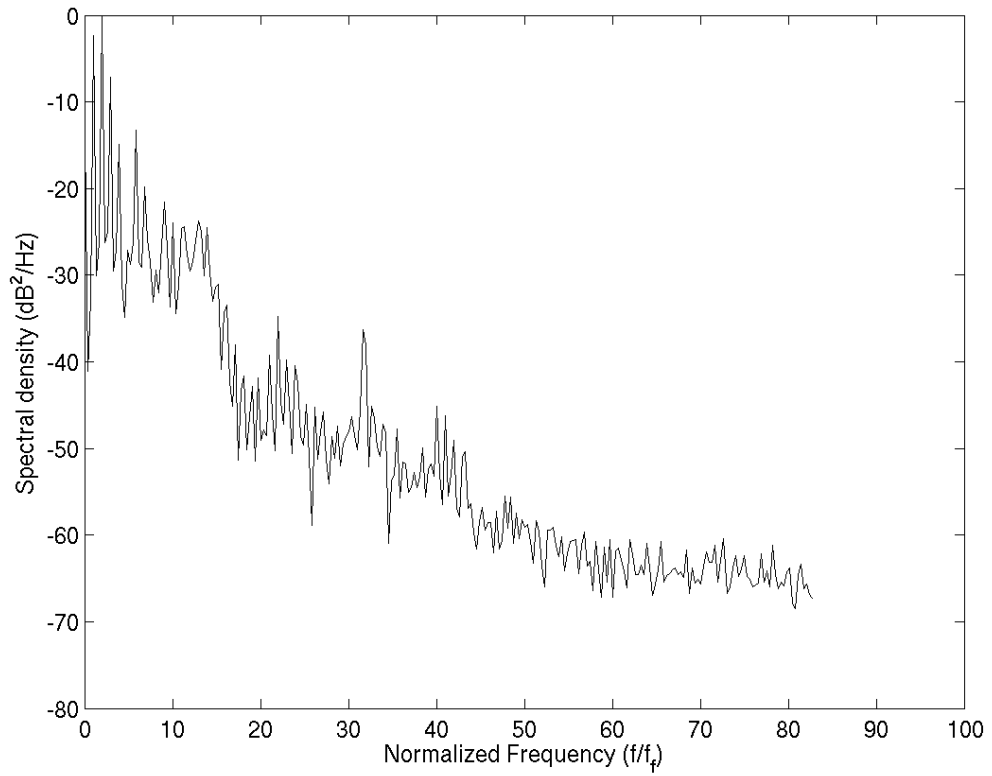


Figure 3.28. Spectra of frequency content of the thrust time series for the flexible wing.

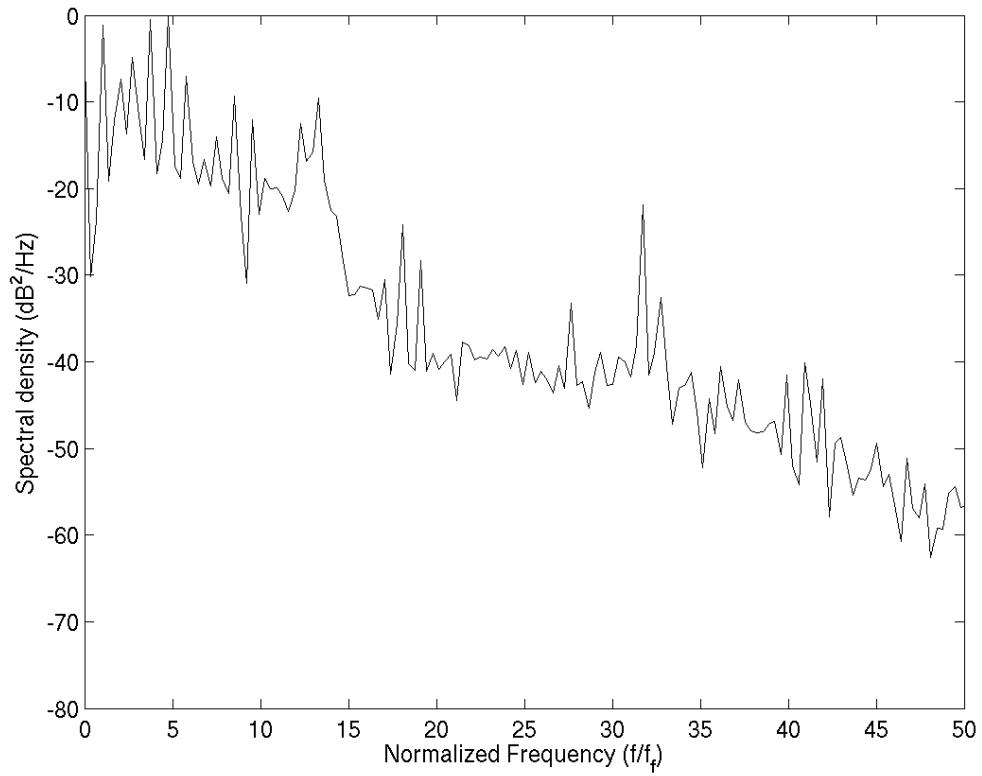


Figure 3.29. Spectra of frequency content of the thrust time series for the drumhead wing.

stiff wings, smoothly “washed out” in response to peak aerodynamic loads.

There was significant frequency content in the aerodynamic force generation out to 15 times the flapping frequency. As a result, simulations of flapping wing flight and on-board state estimators need to have bandwidths of at least 30 times the flapping frequency to avoid aliasing.

## CHAPTER 4

### STRUCTURE DEFORMATION MEASUREMENTS

As presented in Chapter 3, different wing stiffnesses produced different thrust time series. This chapter will examine the motion of the wings during the flapping cycle to attempt to correlate its effect on the generated flapping wing thrust.

#### 4.1 Image Analysis

The captured image sequences were processed to find four quantities, the phase angle of the flapping mechanism, the the flapping angle relative to a horizontal plane, and the deflection of the trailing edge of the wing relative to a stiff leading edge defined at two points.

##### 4.1.1 Determining Phase Angle

Figure 4.1 shows a schematic of the flapping mechanism that includes the drive wheel and connection between drive wheel and link to the flapping wing. The flapping phase angle was based on the position of the connection point relative to  $\phi = 0$ , the beginning of the upstroke, which was at the bottom of the drive wheel as seen in the collected images. These measurements replaced the tachometer used for force measurements in Chapter 3 and was used for determining the phase angle and flapping rate of the wing's motion.

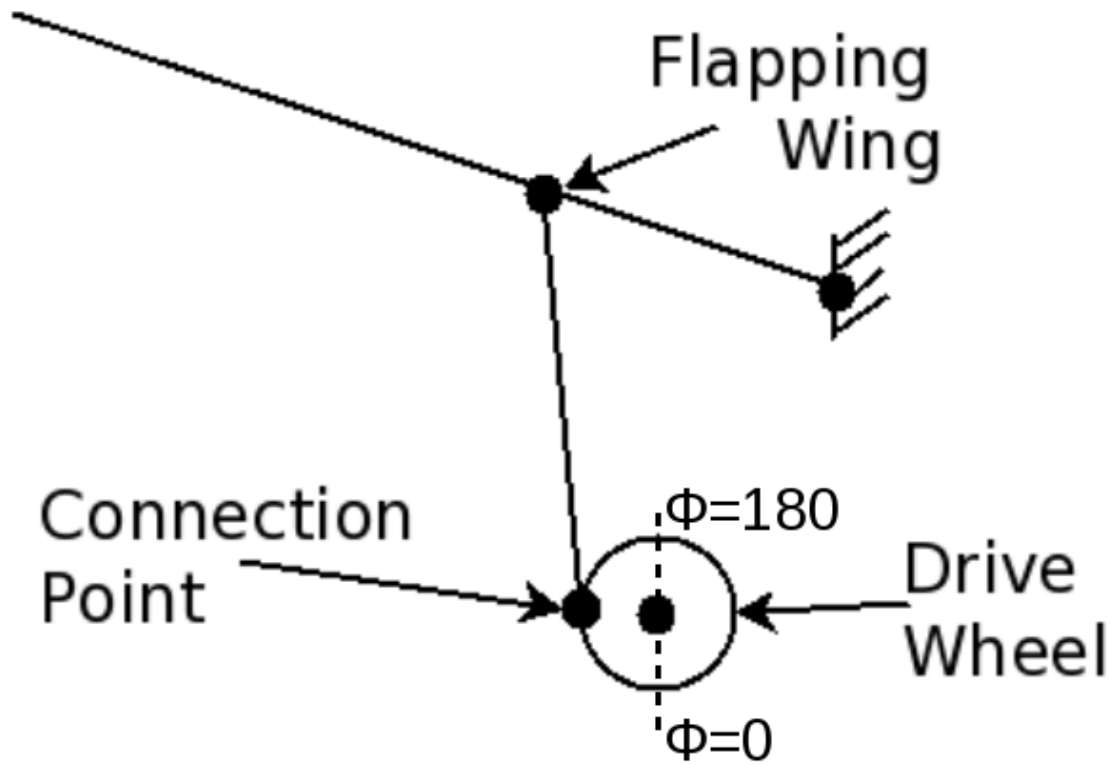


Figure 4.1. Schematic of the flapping mechanism with drive wheel and connection point highlighted.

The phase angle measurement was implemented by manually inspecting the images for the location of the center of the drive wheel, and then locating the connection point in several subsequent frames. Figure 4.2 shows this technique applied to the first frame in the sequence of images collected using the flexible wing at an 11.5Hz flapping frequency.

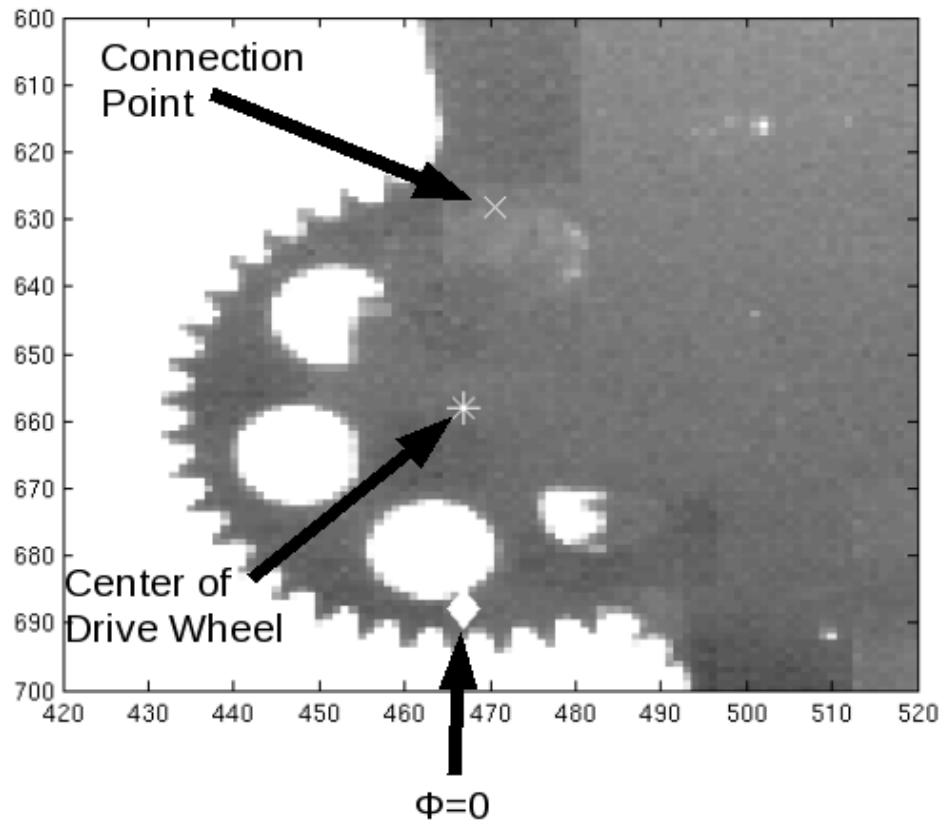


Figure 4.2. Close up view of the drive wheel from the first frame in a series. The center (star),  $\phi = 0$  (diamond) and location of the connection (x) are highlighted.

The process was repeated at frame number 100, providing two measurements of the phase angle in a single rotation, since the shortest period observed with the

tachometer was  $83ms$ , corresponding to 166 frames at 2kHz. Figure 4.3 shows the location of the connection point in the  $100^{th}$  frame of the sequence collected. These two measurements were used to estimate the phase angle of formulation as a function of flapping frequency given in Equation 4.1 as function of frame number  $f_n$ . Based on this the accuracy of the connection point position is within three degrees of its true position.

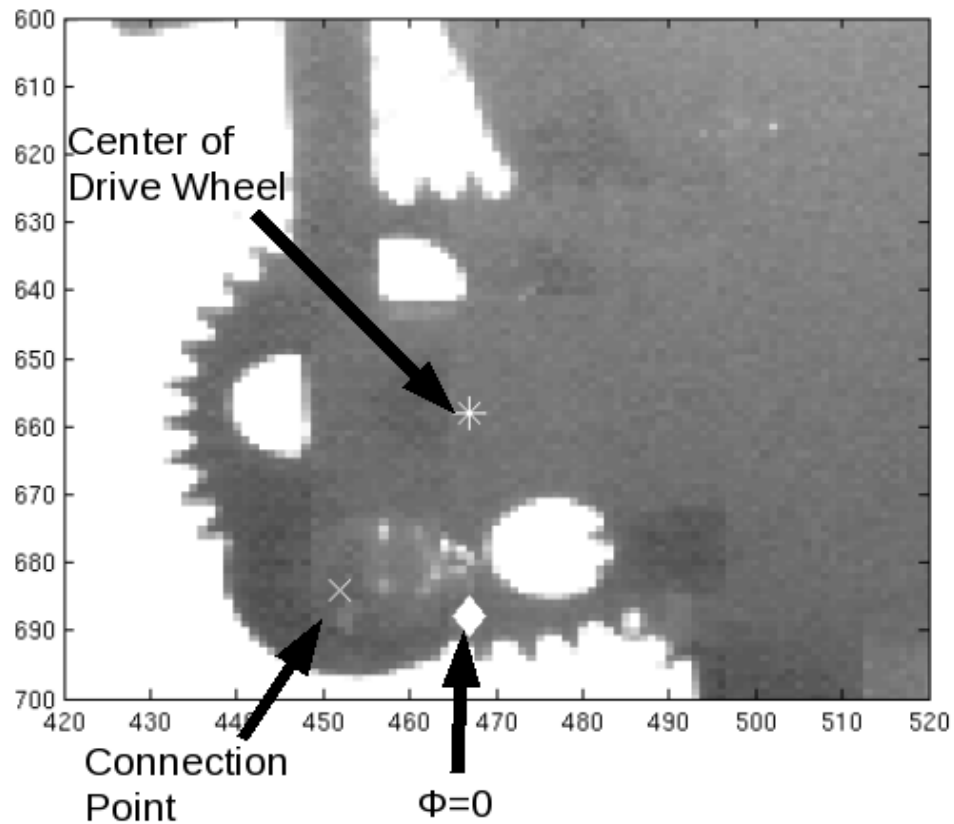


Figure 4.3. Close up view of the drive wheel from the  $100^{th}$  frame in a series. The center (star),  $\phi = 0$  (diamond) and location of the connection (x) are highlighted.

$$\phi_{est}(f_n) = f_n(\phi(100) - \phi(1))/(99) + \phi(1) \quad (4.1)$$

$$\phi_{true} = \phi_{est}(f_n) + \phi_{corr}(f_n) \quad (4.2)$$

The true phase angle in later images is the sum of the initial estimate  $\phi_{est}$  and a manual correction factor  $\phi_{corr}$ , as given in Equation 4.2. This approach was necessary because with  $\phi$  accurate to within  $3^\circ$  in any frame, the slope of any two point line could only be accurate to within  $6^\circ$  divided by the distance between the points. The extrapolation was used to ensure that the measurement of  $\phi$  included previous complete rotations.

Figure 4.4 shows a close up the drive wheel from the same series with both  $\phi_{est}$  and two estimates of  $\phi_{true}$  for frame number 2000. The circle in the center of the connection represents a plot of  $\phi_{true}$ , the circle slightly below it depicts a previous guess. A small correction was used to determine the difference between the initial estimate of  $\phi(f_n)$  and the true phase angle in each frame.

Figure 4.5 shows a plot of  $\phi_{true}$  versus time for the flexible wing at a flapping frequency of 11.5Hz. The good linear fit to the points confirms that the flapping frequency was constant. Therefore it is possible to use this linear estimate of  $\phi$  as a reference to phase-average the data in the following sections instead of determining it in each frame.

#### 4.1.2 Wing Motion and Angle of attack

The individual images were analyzed for three quantities, the flapping angle  $\Gamma(\phi)$ , near-root deflection  $\delta_{root}(\phi)$  and near tip angle of attack  $\delta_{tip}(\phi)$ . The spanwise bending was very small relative to these quantities. The analysis proceeded in 3 steps:

1. Use a non-directional edge detection scheme to find the edges of the wing in each frame

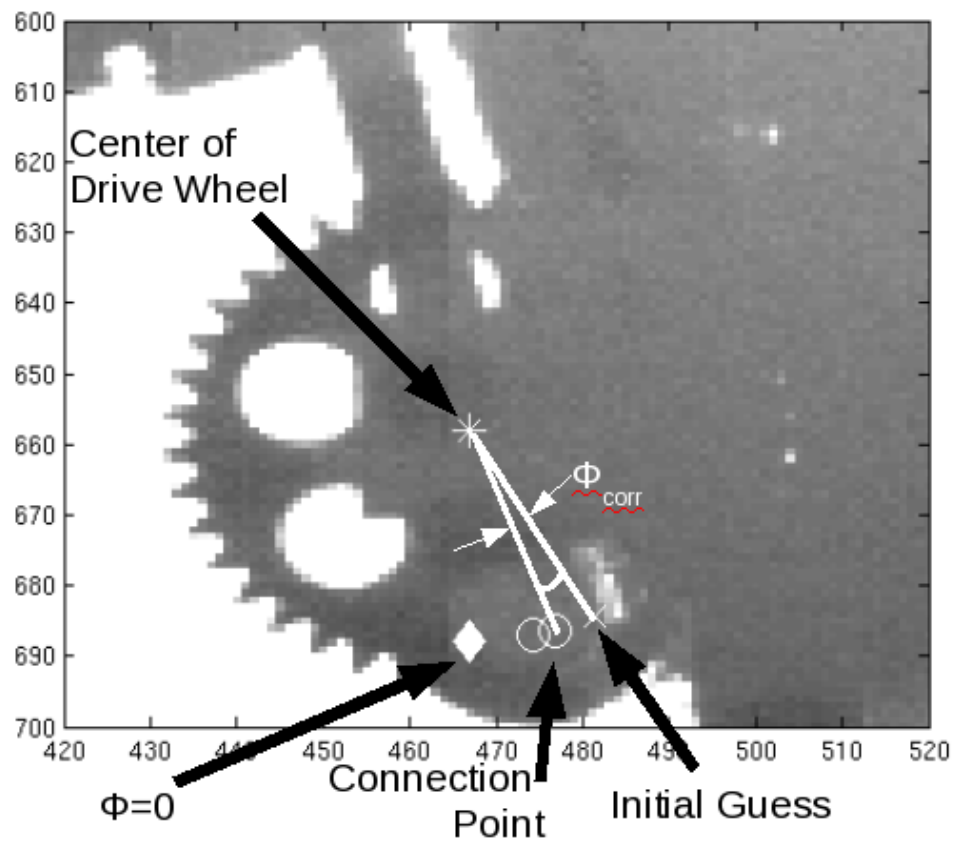


Figure 4.4. Close up view of the drive wheel from the 2000<sup>th</sup> frame in a series showing the initial guess (x), and corrected estimate of  $\phi$  (open circle).

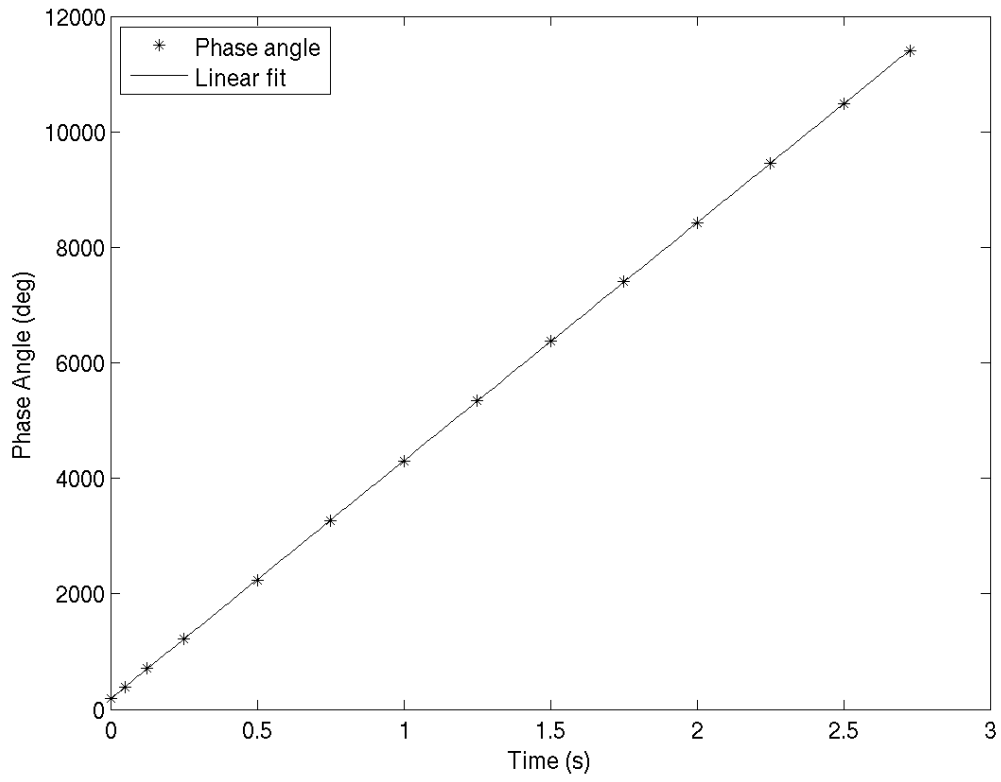


Figure 4.5. Plot of the measured phase angle versus frame number with a linear fit.

2. Find the leading edge of each wing in the frame
3. Search along a line perpendicular to the leading edge for the location of the trailing edge

The first step made use of the Prewitt edge detection filter. This is a non-directional edge detection algorithm that convolves eight edge detection kernels with the image and sums the result point by point. Points with values above a threshold set to be two standard deviations above the mean for the image were returned as edges. Figure 4.6 shows the output from this filter when applied to an image of the flexible wing.

Finding the flapping angle  $\Gamma(\phi)$  required finding the leading edge of the wing. This was implemented by finding a line in the image that passed through the root point that contained the largest number of edge points. This is illustrated in Figure 4.7 which shows a schematic of the search for the leading edge in an image. The search algorithm defined a rectangle covering the wing root and tip. The number of edge points in each rectangle was computed, and the rectangle with the largest number of edge points was determined to be the leading edge. Figure 4.8 shows an image with the estimated leading edge overlaid with a line of open circles.

The final step was to find the angle of attack of the trailing edge relative to the leading edge. Figure 4.9 shows an orthographic and cutaway view of the deflected wing. The two trailing edge measurements,  $\delta_{root}(\phi)$  and  $\delta_{tip}(\phi)$ , are highlighted in the front and side views. Figure 4.10 shows a schematic of the search areas used to find the trailing edge. These search areas are perpendicular to the leading edge detected in the previous step. The wing edge points farthest from the leading edge were assumed to be on the trailing edge. Figure 4.11 shows the results of this algorithm applied to the image used to generate Figure 4.8. The number of pixels between the leading and trailing edge defines the distances  $\delta_{root}(\phi)$  and  $\delta_{tip}(\phi)$  based



Figure 4.6. The output of the Prewitt edge detection filter for an image of the flexible wing.

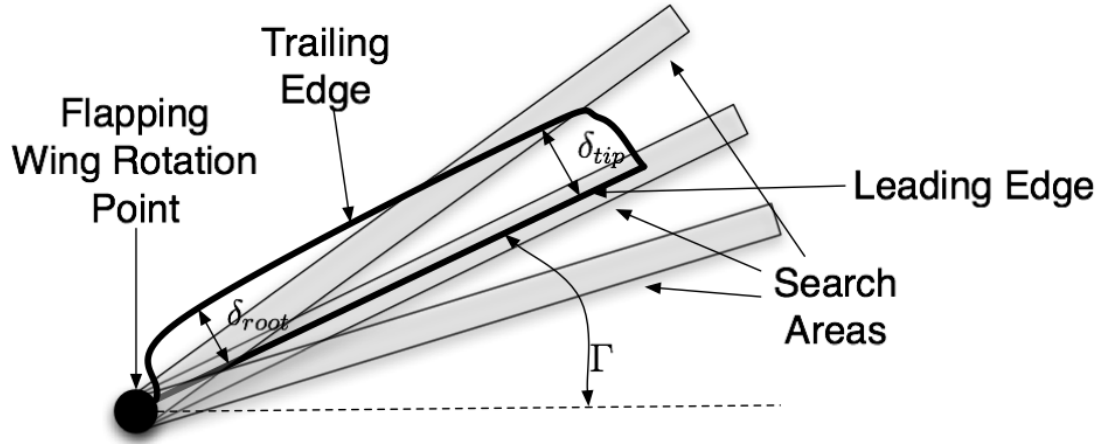


Figure 4.7. Schematic view of the leading edge edge search algorithm. The box with the most edge points determines the flapping angle.

on the relationship between pixel size and physical distance. As shown in Figure 4.9, the measurements of  $\delta_{root}(\phi)$  and  $\delta_{tip}(\phi)$  are analogous to the angle of attack of the wings during the flapping cycle.

#### 4.1.3 Determine angle of attack

The calculation of the angle of attack,  $\alpha$ , was straightforward. Equation 4.3 shows the computation for  $\alpha_{root}(t)$  at the point where the root deflection was measured, and based on the root chord  $c_{root}$ . Equation 4.4 shows the similar calculation for  $\alpha_{tip}$ .

$$\alpha_{root} = \arcsin \frac{\delta_{root}}{c_{root}} \quad (4.3)$$

$$\alpha_{tip} = \arcsin \frac{\delta_{tip}}{c_{tip}} \quad (4.4)$$

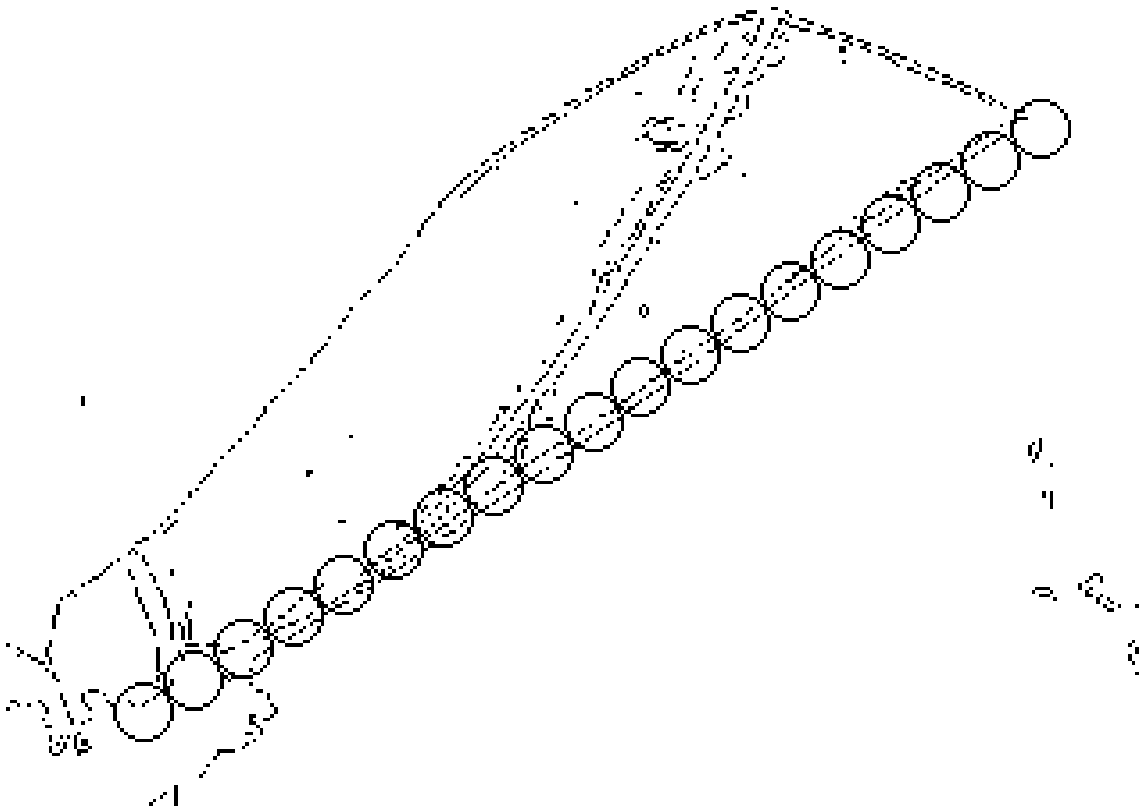


Figure 4.8. Image of a wing with its leading edge highlighted by a line of open circles.

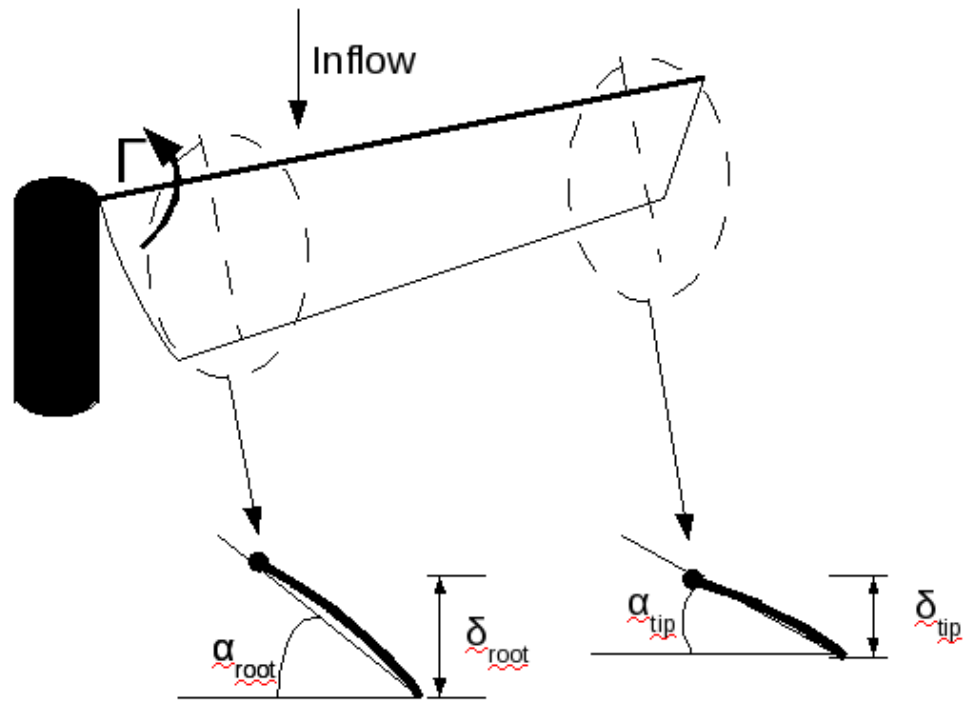


Figure 4.9. Orthographic and cut-away views of the angle of attack of the wing.

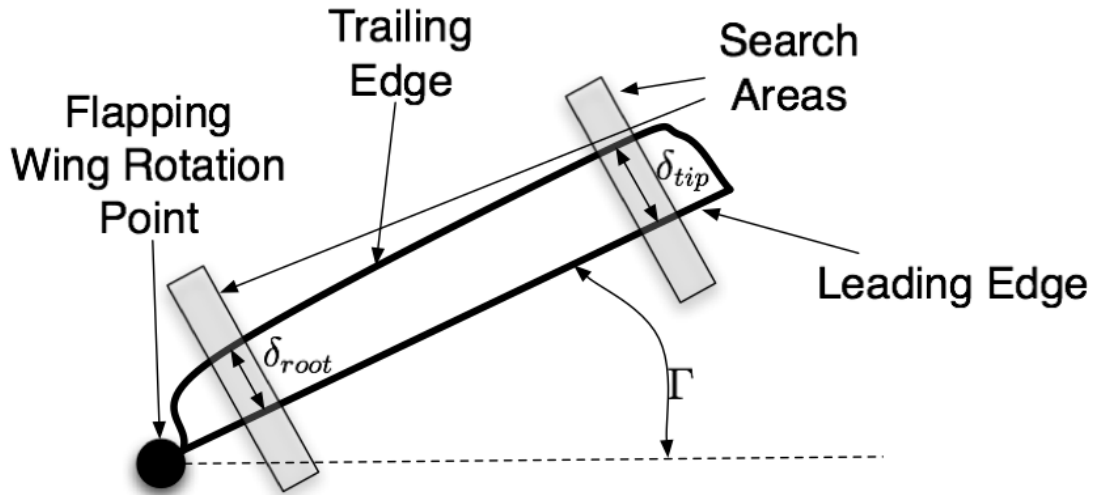


Figure 4.10. Schematic view of the trailing edge location algorithm.

## 4.2 Results and discussion

### 4.2.1 Stiff Wing

Figures 4.12 through 4.14 and 4.15 through 4.17 show the angle of attack of the wing root and tip as function of the flapping phase angle for the stiff wing. The maximum flapping angle  $\Gamma(\phi)$  corresponded to  $\phi = 180^\circ$ . The bars represent uncertainty in the angle of attack due to the pixel size propagated through the edge detection and search algorithms.

The membrane on top of the wings was stronger in tension than compression. This resulted in the wings having generated greater stiffness against downward motion. Therefore the largest wing angle of attack occurred at the beginning of the downstroke where the wing structure deflected in the upward direction. This is seen as a peak in the angle of attack at  $\phi \approx 180^\circ$ . The width of this angle of attack peak is comparable to the width of the thrust peak for this case that was shown in Figures 3.12 through 3.14.

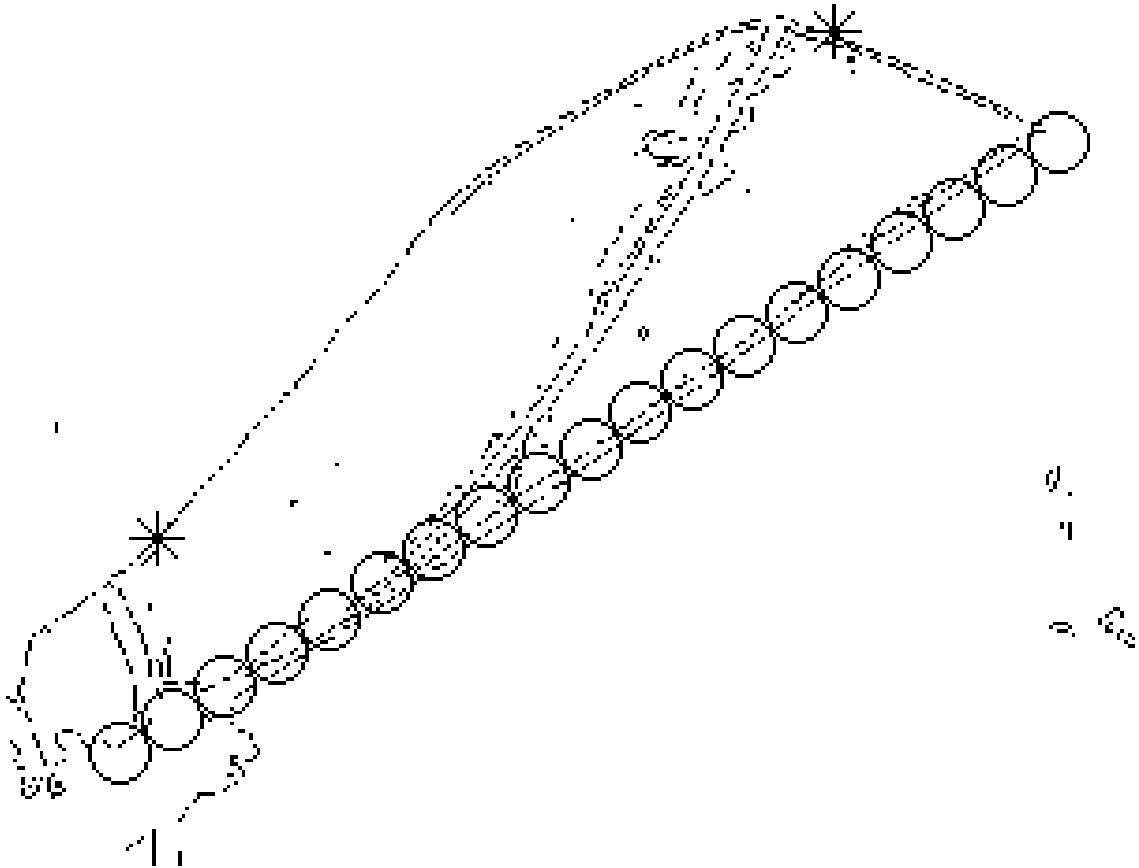


Figure 4.11. Example of the trailing edge location algorithm applied to the image shown in Figure 4.8. The selected trailing edge points are highlight with stars.

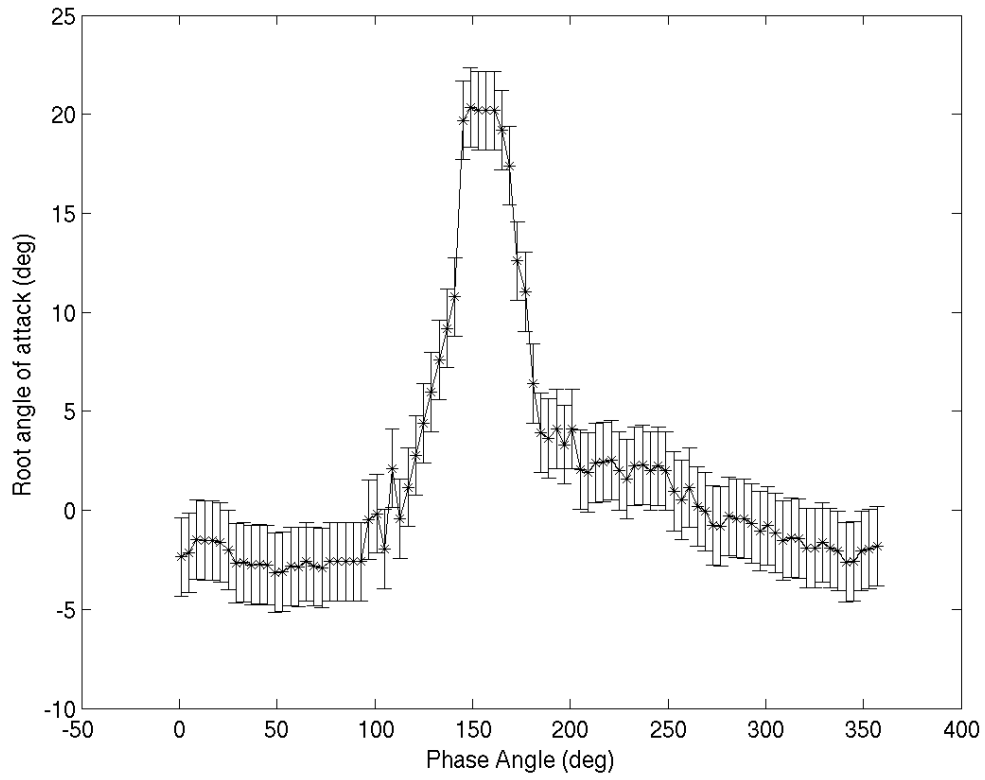


Figure 4.12. Angle of attack near the wing root of the stiff wing at the 11Hz flapping frequency.

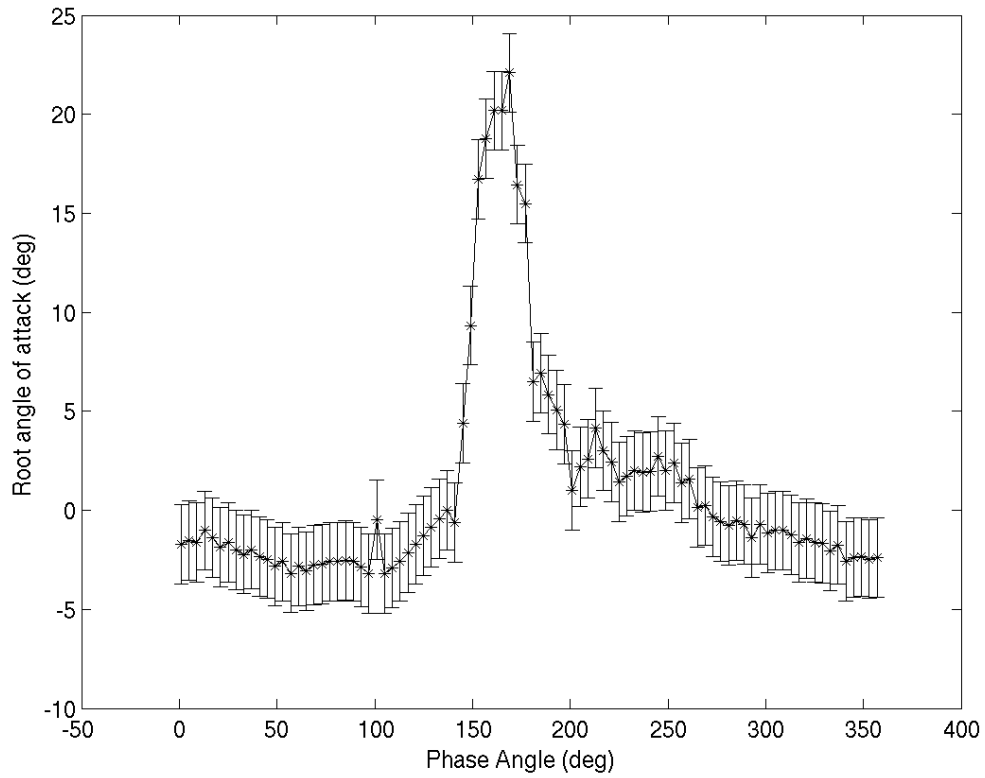


Figure 4.13. Angle of attack near the wing root of the stiff wing at the 10.5Hz flapping frequency.

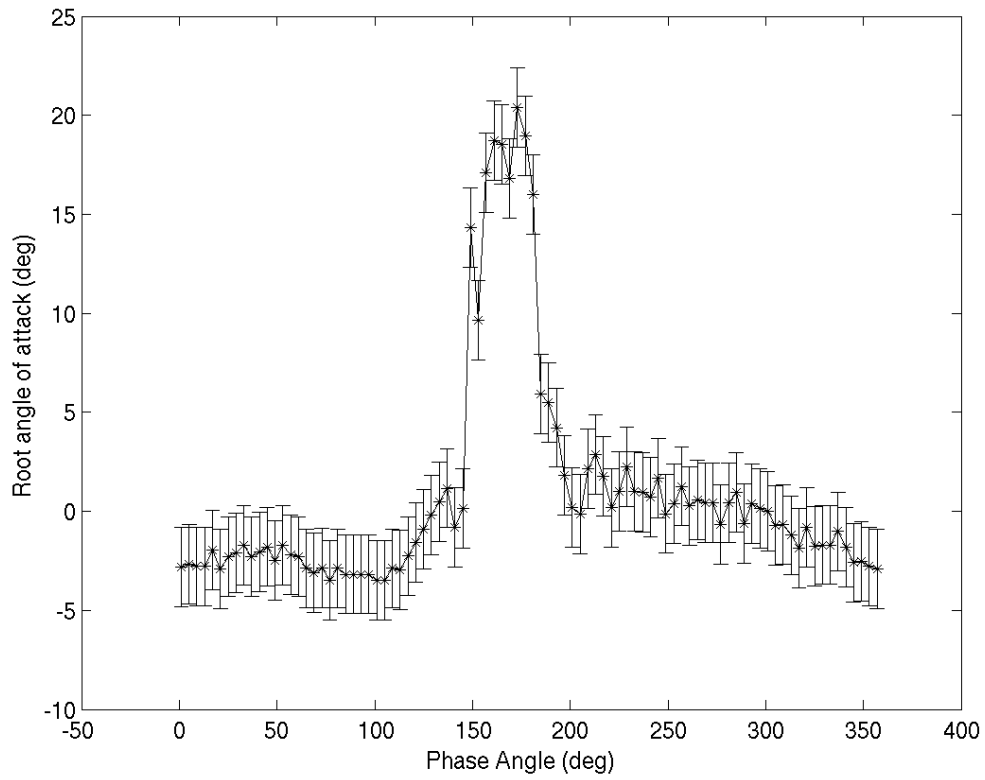


Figure 4.14. Angle of attack near the wing root of the stiff wing at the 9.5Hz

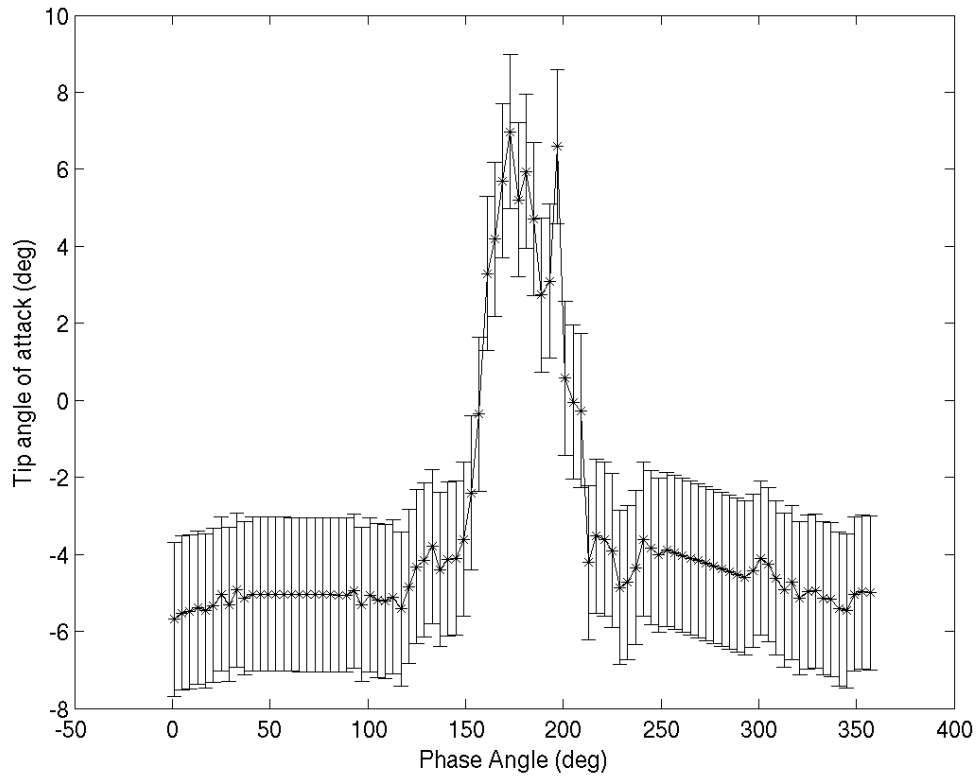


Figure 4.15. Angle of attack near the wing tip of the stiff wing at the 11Hz flapping frequency.

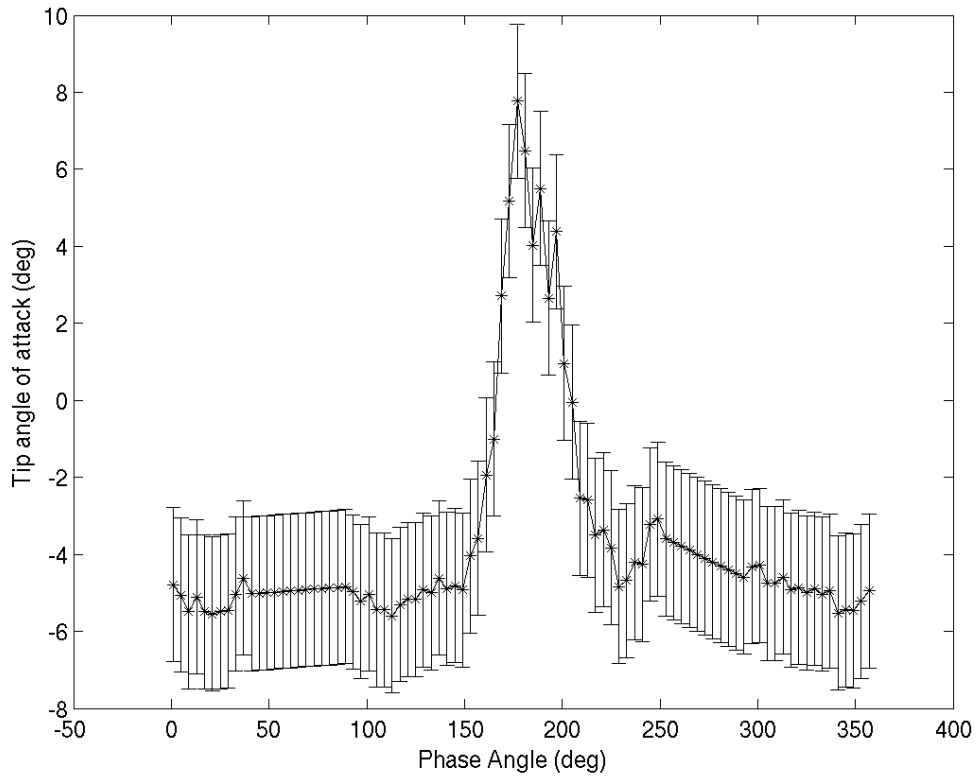


Figure 4.16. Angle of attack near the wing tip of the stiff wing at the 10.5Hz flapping frequency.

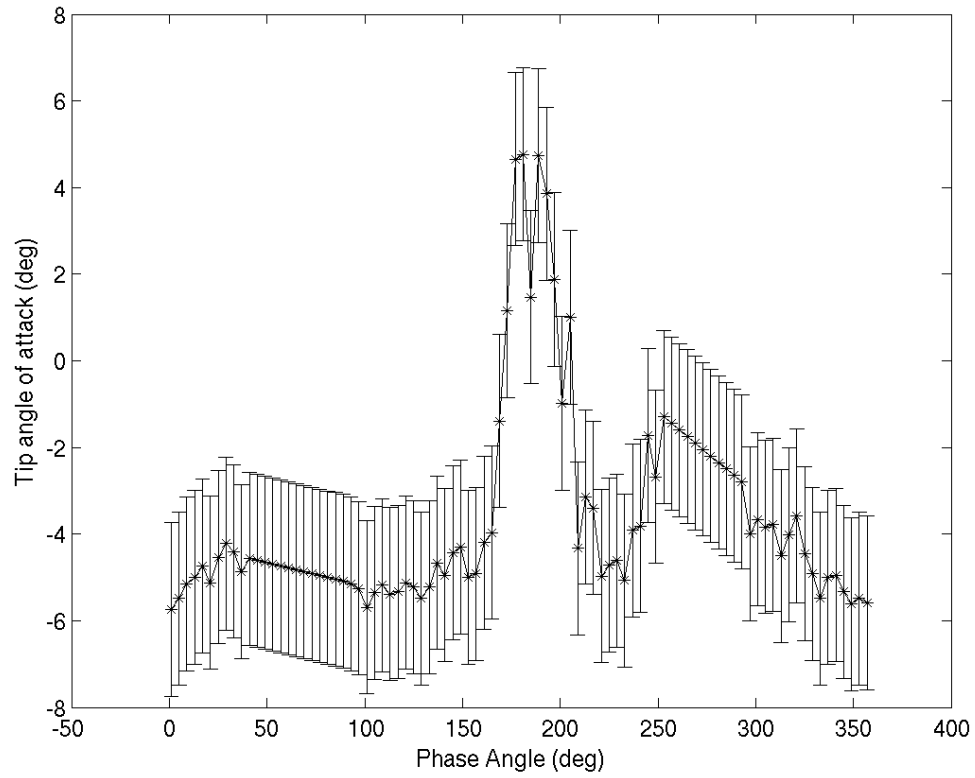


Figure 4.17. Angle of attack near the wing tip of the stiff wing at the 9.5Hz

Figure 4.18 shows the peak angle of attack at the root of the wing as function of the flapping frequency for the stiff wing. Figure 4.19 shows the flapping phase angle where the peak angle of attack occurs. There appears to be a frequency dependence on the angle of attack at the root that has a maximum at approximately 9.5Hz flapping frequency. At all frequencies, the peak angle of attack occurs near a phase angle of  $180^\circ$ , where the acceleration due to the flapping motion is at a maximum.

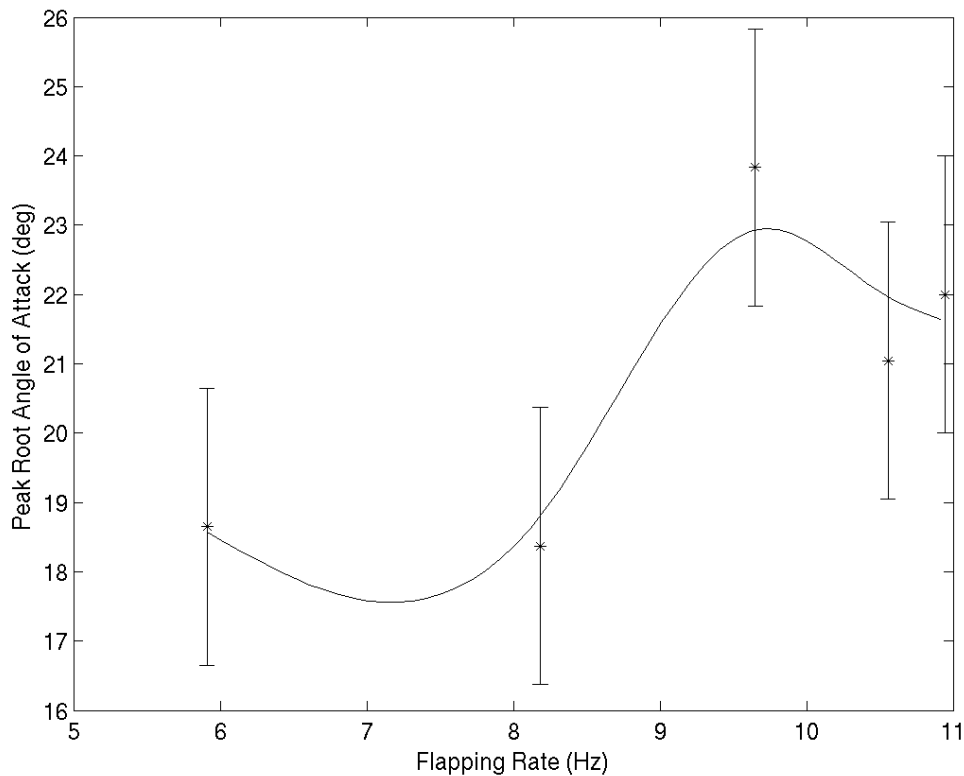


Figure 4.18. Peak angle of attack of the root of the wing as function of the flapping frequency for the stiff wing.

Figure 4.20 shows the maximum angle of attack of the wing tip versus flapping frequency for the stiff wing. The phase angle where the peak tip angle of attack was a maximum is shown in Figure 4.21. We observe that the largest angle of attack

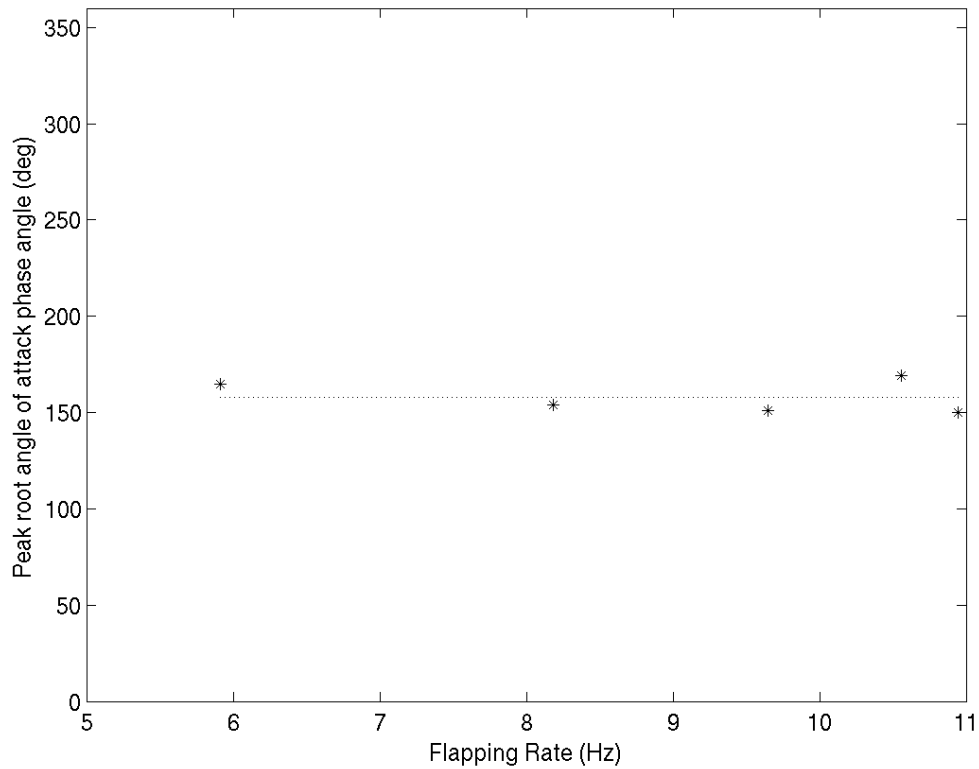


Figure 4.19. Phase angle of the peak angle of attack of the root of the stiff wing versus flapping frequency.

occurs at approximately 10.5Hz versus 9.5Hz at the root. We also note a significant change in phase angle of the maximum above the 6Hz flapping frequency. This might suggest that there is a different physical process that is causing the angle of attack at the lower flapping frequencies compared to the higher flapping frequencies.

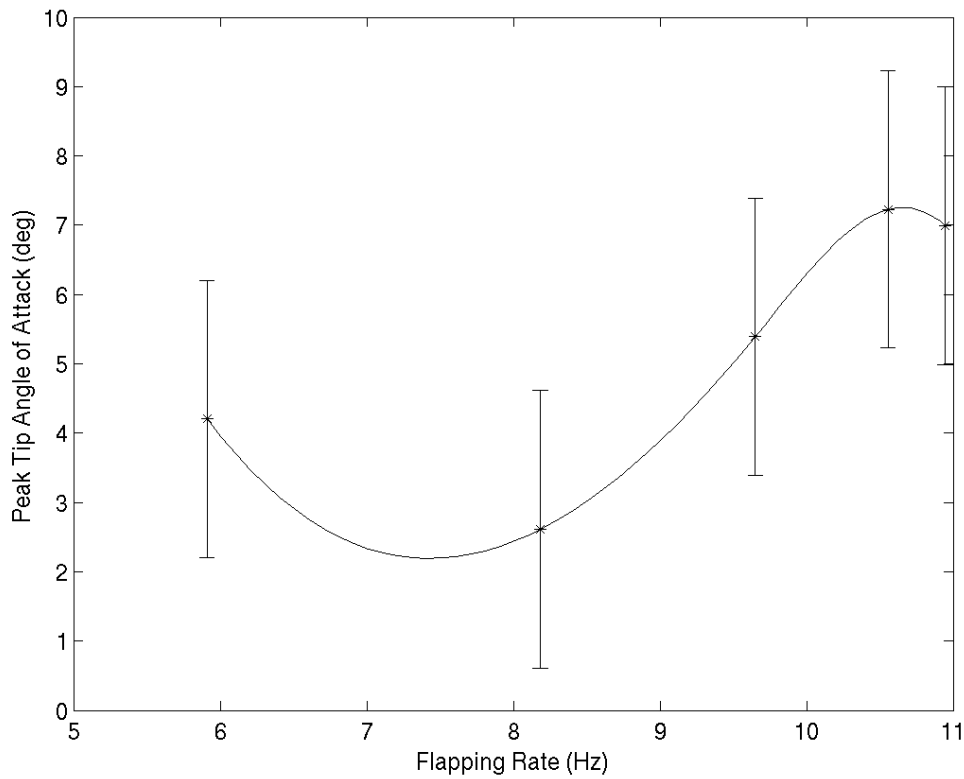


Figure 4.20. Maximum angle of attack of the tip of the wing versus flapping frequency for the stiff wing.

#### 4.2.2 Flexible Wing

The wing root angle of attack of the flexible wing versus the flapping phase angle phase angle is shown in Figures 4.22 through 4.24. The wing tip angle of attack for the flexible wing is shown in Figures 4.25 through 4.27. We note that

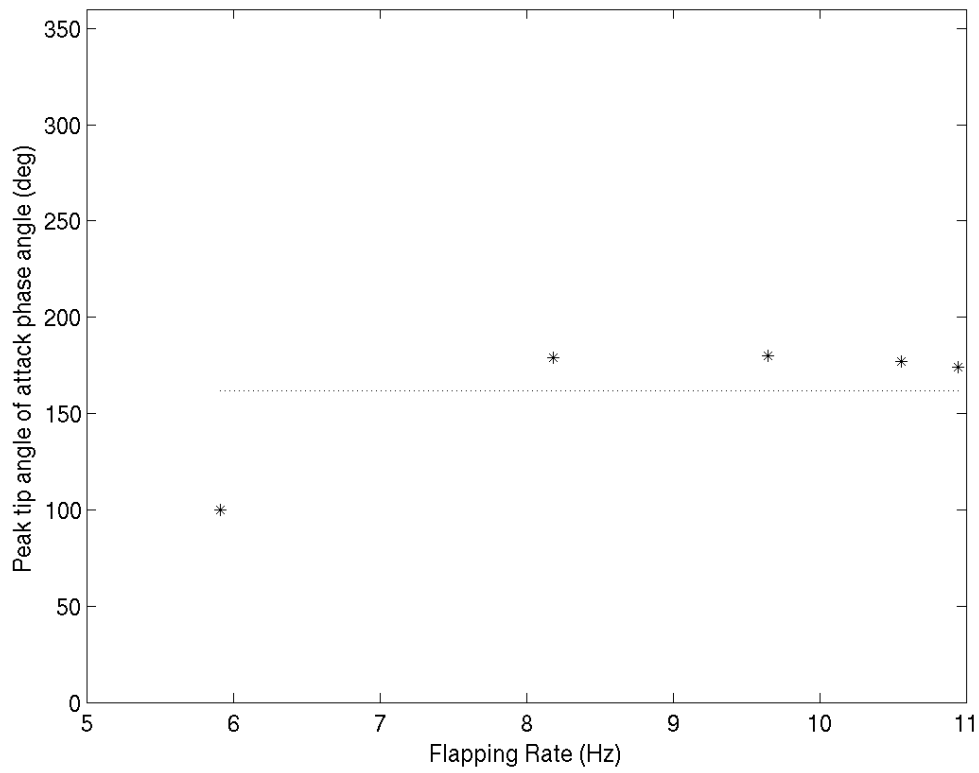


Figure 4.21. Phase angle of the peak tip angle of attack for the stiff wing.

the magnitude of both angles of attack for the flexible wing is larger than that of the the stiff wing. In addition, the peak in the angle of attack is considerably broader indicating a larger degree of wing twist over a larger portion of the flapping cycle. This correlates with the higher overall thrust measured for the flexible wing in Chapter 3. We note that although the overall thrust was higher, the maximum thrust was lower with the flexible wing.

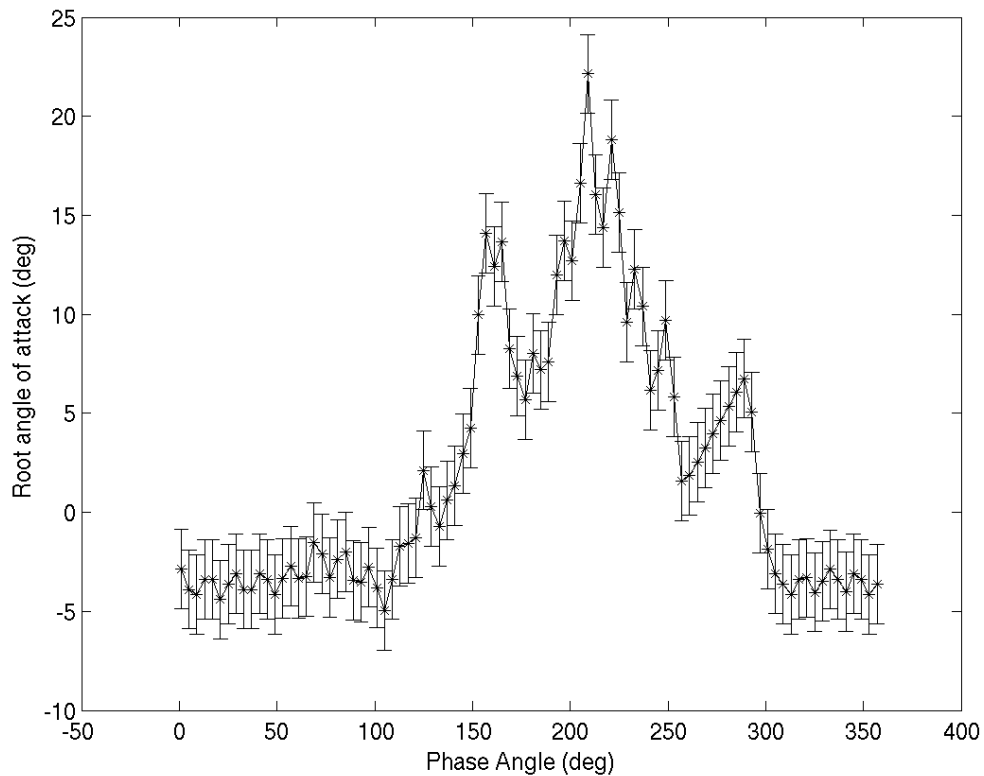


Figure 4.22. Angle of attack near the root of the flexible wing at the 11.5Hz flapping frequency.

Figure 4.28 shows the peak angle of attack of the wing root as function of the flapping frequency. The phase angle where this peak angle of attack occurs is shown in Figure 4.29. The peak angle of attack has a broad maximum centered at approx-

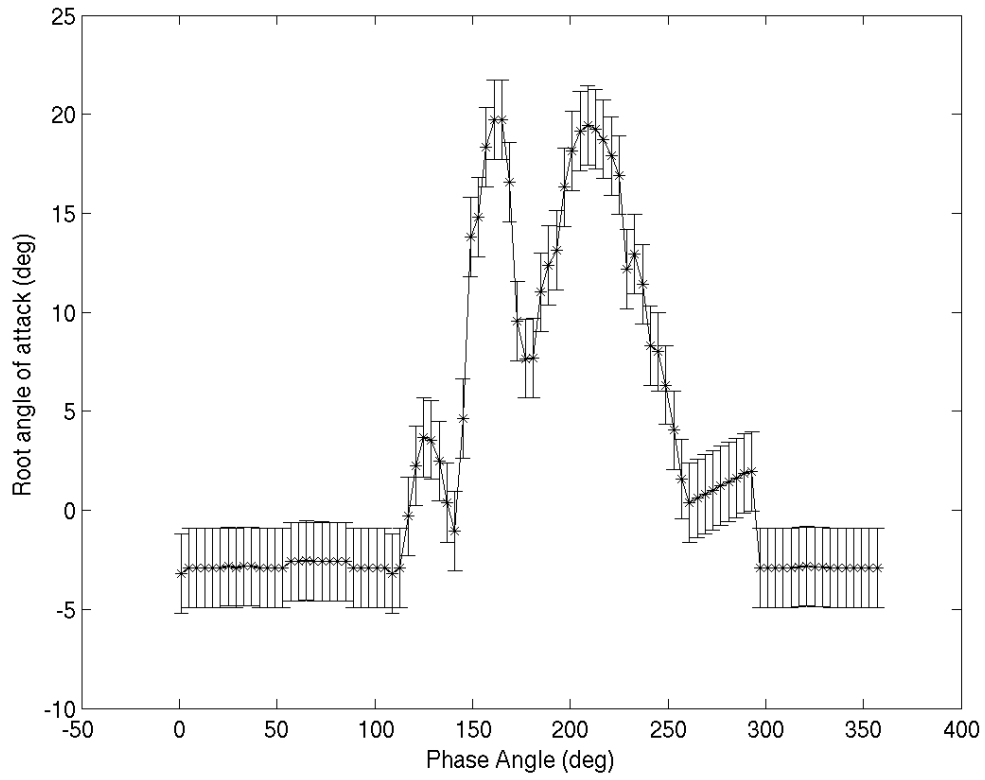


Figure 4.23. Angle of attack near the root of the flexible wing at the 11Hz flapping frequency.

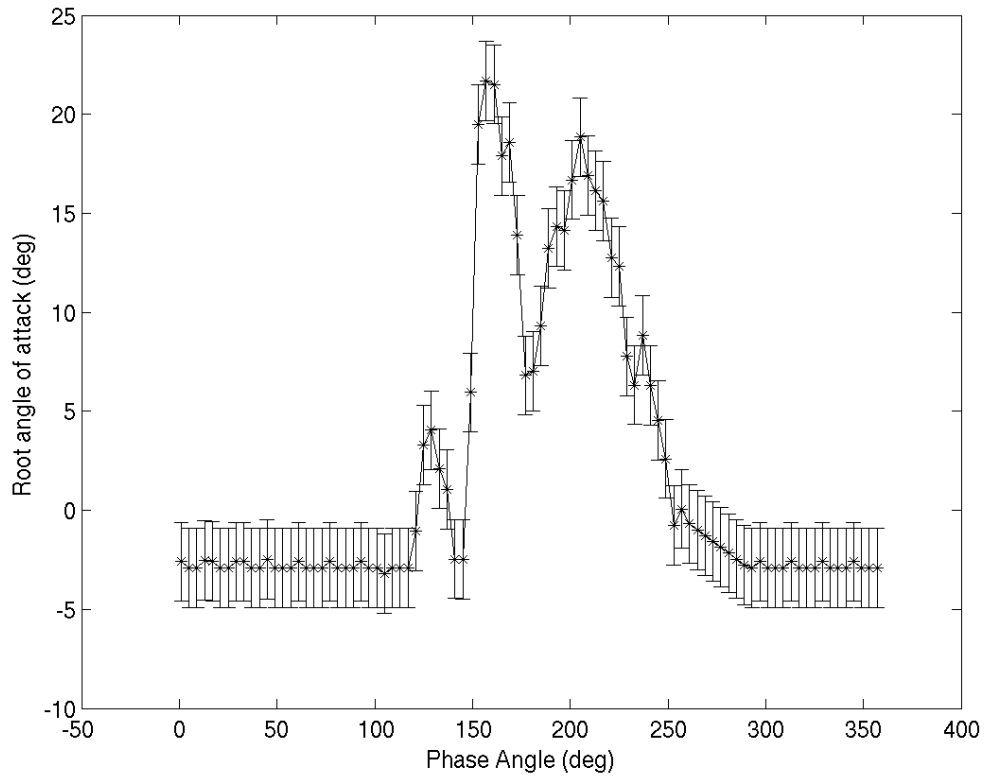


Figure 4.24. Angle of attack near the root of the flexible wing at the 10Hz flapping frequency.

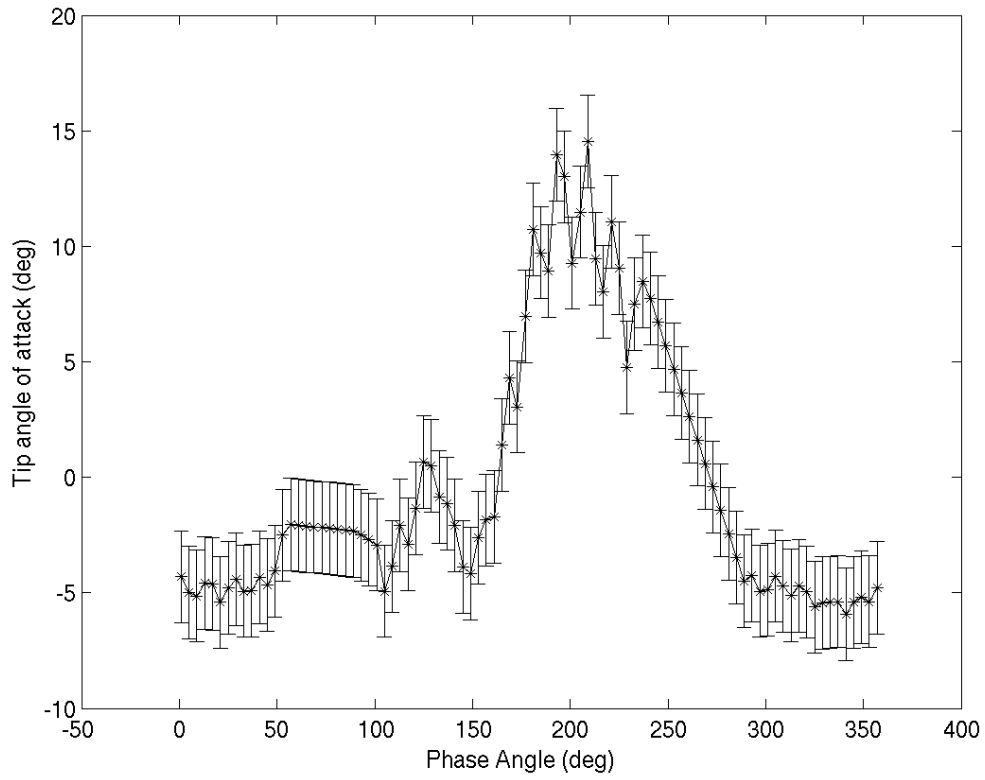


Figure 4.25. Angle of attack near the tip of the flexible wing at the 11.5Hz flapping frequency.

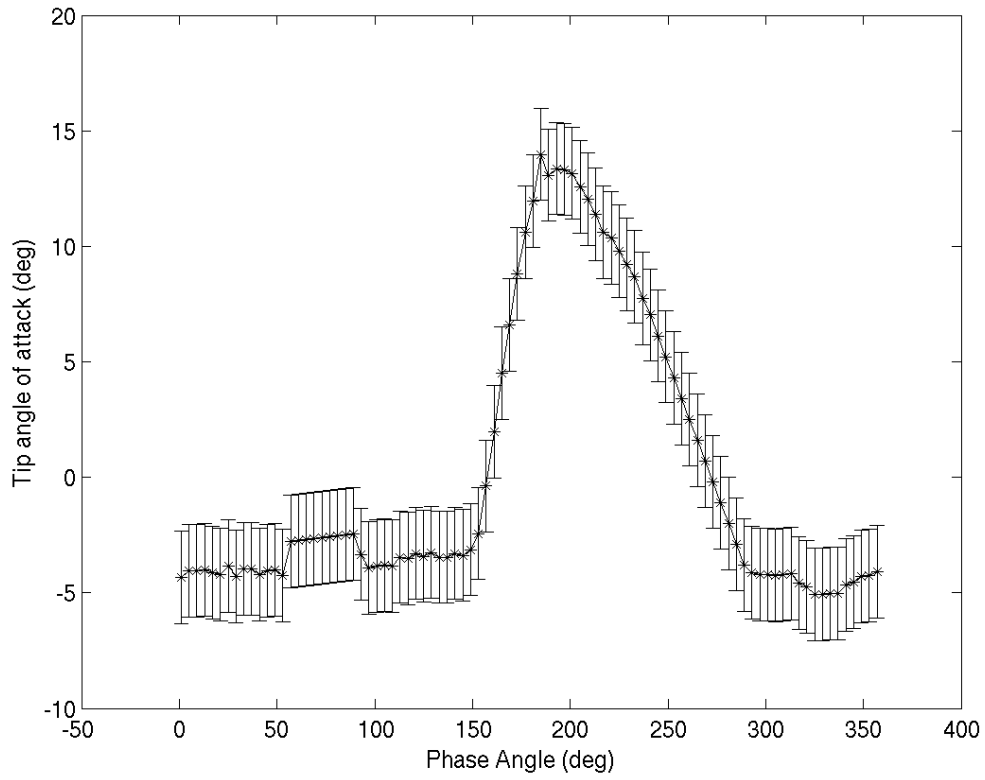


Figure 4.26. Angle of attack near the tip of the flexible wing at the 11Hz flapping frequency.

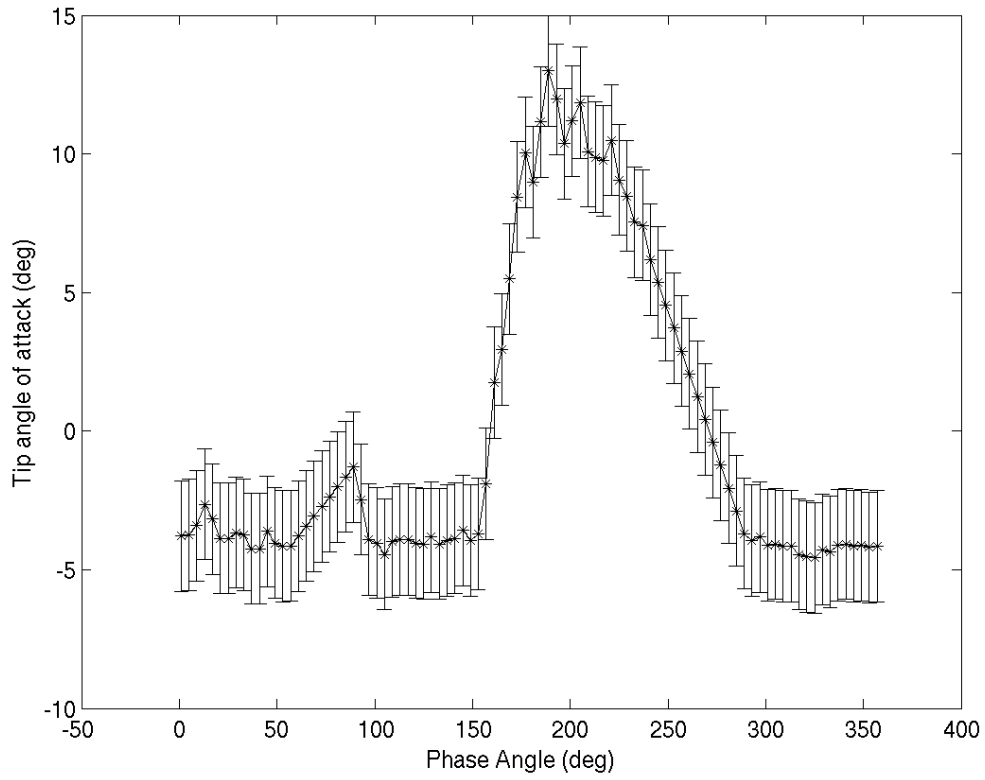


Figure 4.27. Angle of attack near the tip of the flexible wing at the 10Hz flapping frequency.

imately 11Hz flapping frequency. This is higher than the 9.8Hz frequency for the root location of the stiff wing. The phase angle of the maximum angle of attack of the wing root is constant, with the possible exception of the 11.5Hz frequency.

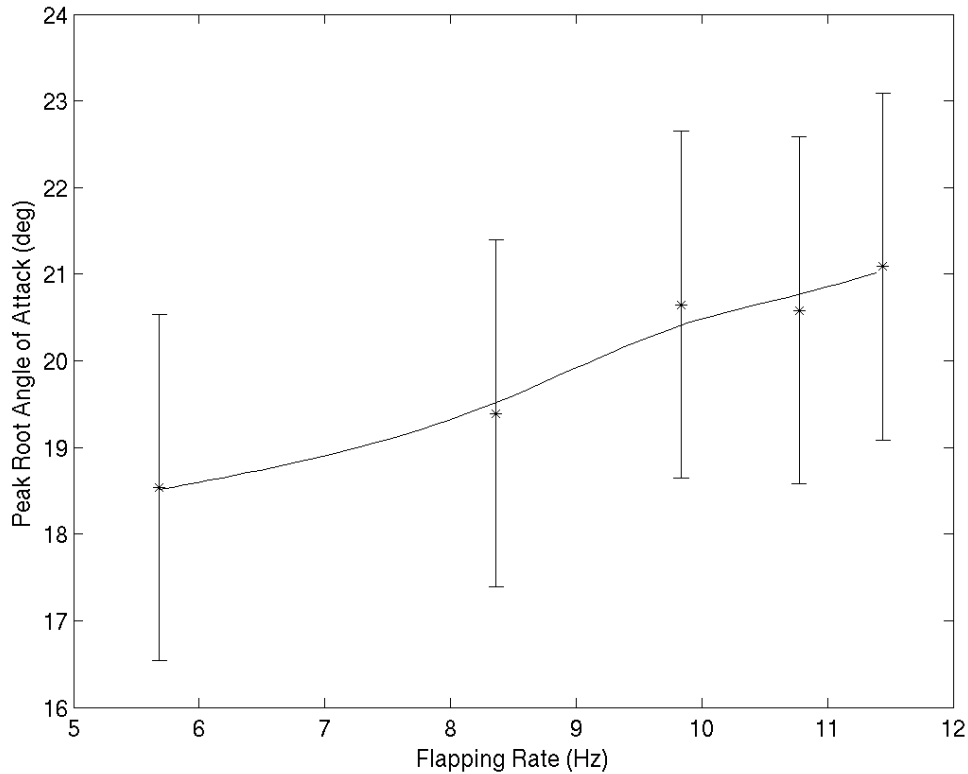


Figure 4.28. Peak angle of attack of the root of the wing as function of the flapping frequency for the flexible wing.

The maximum angle of attack of the wing tip versus flapping frequency is shown in Figure 4.30. The phase angle of the maximum tip angle of attack is shown in Figure 4.31. The maximum tip angle of attack has a peak at a flapping frequency centered at the 10.5Hz flapping frequency. This is similar to the wing root angle of attack. The flapping phase of the maximum tip angle of attack is again nearly constant with flapping frequency, similar to the wing root. In this case there is still

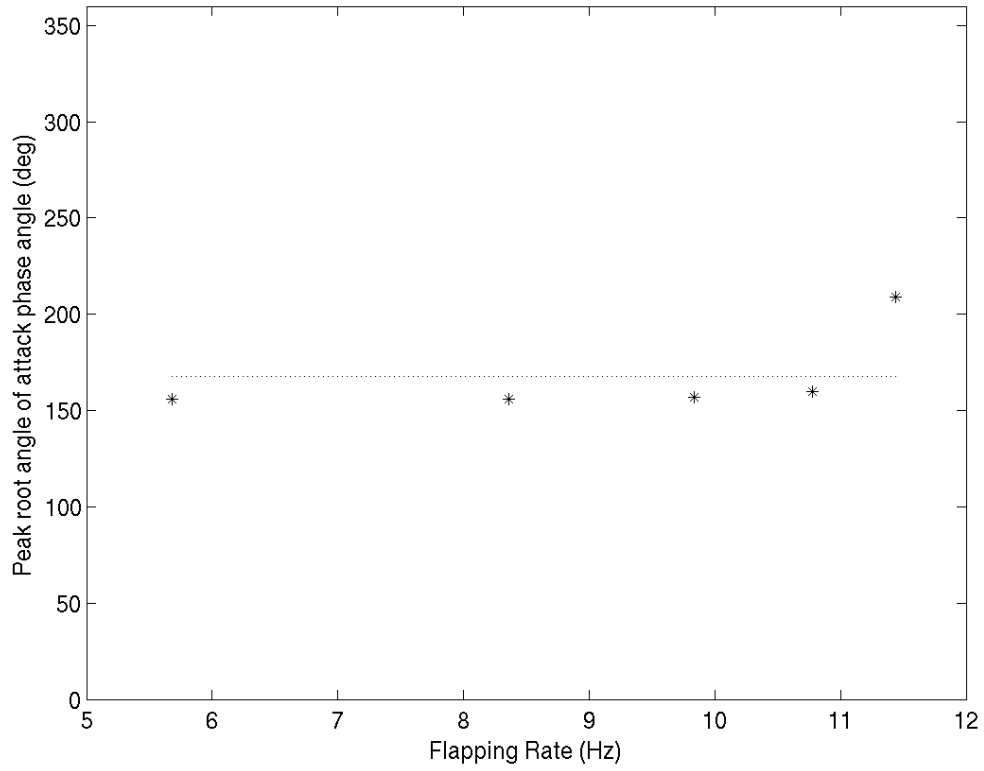


Figure 4.29. Phase angle of the peak angle of attack of the root of the flexible wing versus flapping frequency.

considerable wing twist between root and tip with the flexible wing.

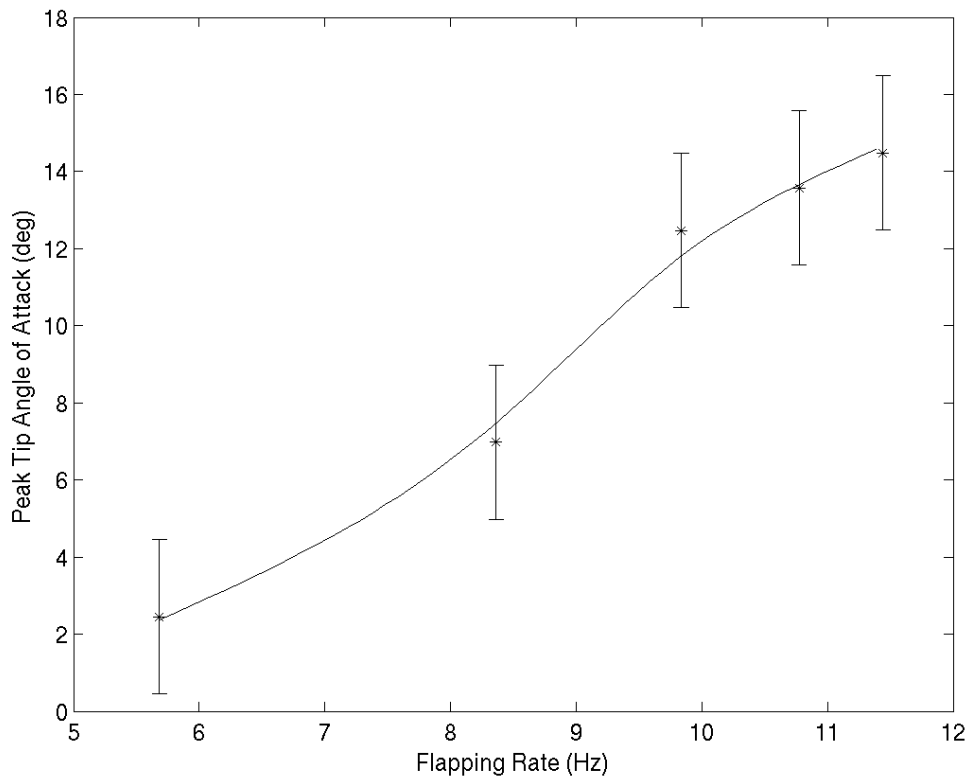


Figure 4.30. Maximum angle of attack of the tip of the wing versus flapping frequency for the flexible wing.

### 4.2.3 Drumhead Wing

The wing root angle of attack of the drumhead wing as a function of the flapping phase angle is shown in Figures 4.32 through 4.34. Figures 4.35 through 4.37 show the angle of attack of the drumhead wing tip as a function of the flapping phase angle. Here we observe that the magnitude of the angles of attack of the drumhead wing is larger than that of the stiff wing and comparable to the flexible wing. We note that the drumhead wing has the the largest maximum thrust compared to the

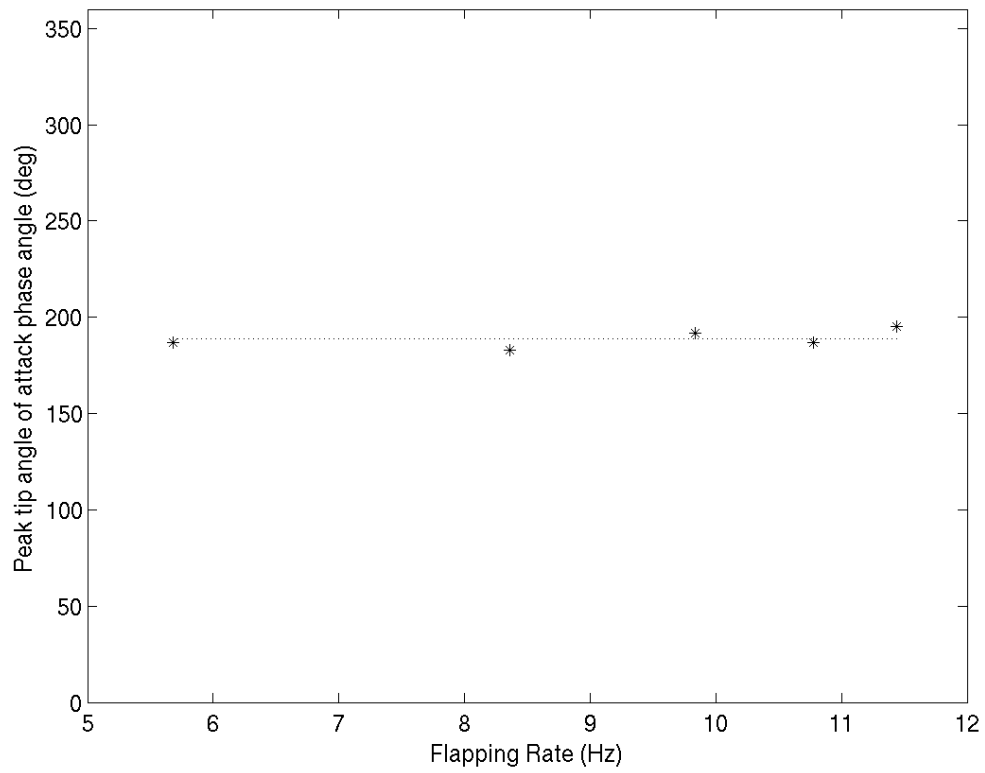


Figure 4.31. Phase angle of the peak tip angle of attack for the flexible wing.

other wings.

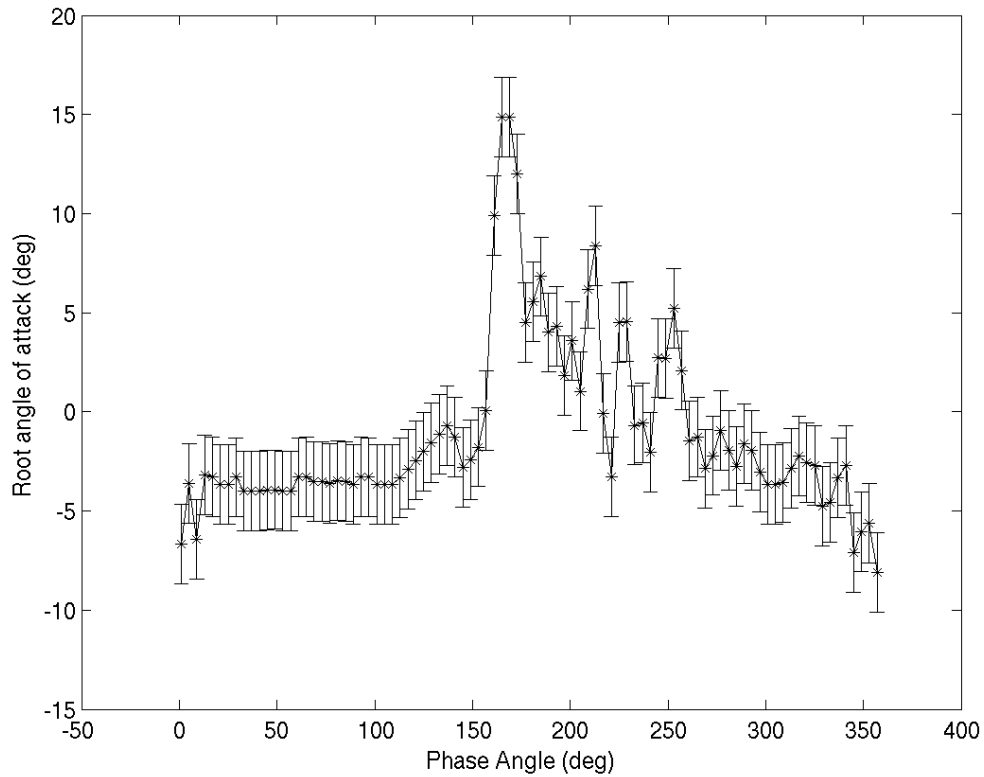


Figure 4.32. Angle of attack near the root of the drumhead wing at the 11Hz flapping frequency.

The peak angle of attack of the wing root as function of the flapping frequency is shown in Figure 4.38. The phase angle of this peak angle of attack is shown in Figure 4.39. The maximum wing root angle of attack has a peak at approximately 9.5Hz, which is comparable to the stiff wing. The flapping phase angle where the maximum angle of attack occurs is constant for all frequencies. This is more comparable to the flexible wing.

The maximum angle of attack of the wing tip versus the flapping frequency is shown in Figure 4.40. The flapping phase angle of the peak tip angles of attack are

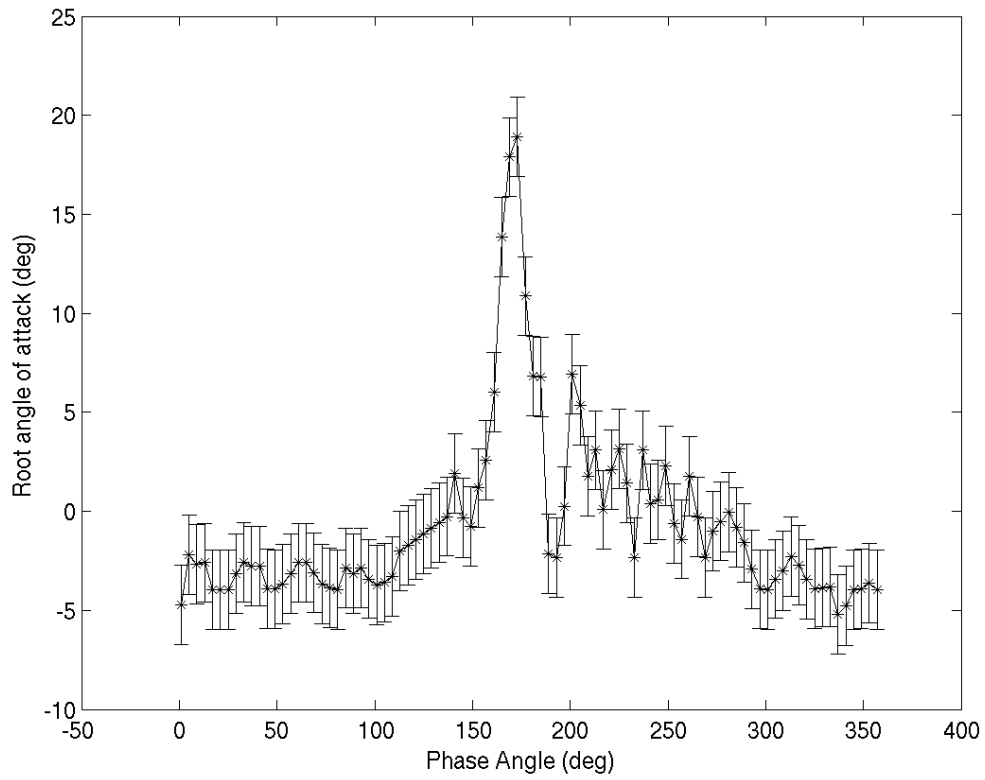


Figure 4.33. Angle of attack near the root of the drumhead wing at the 10.5Hz

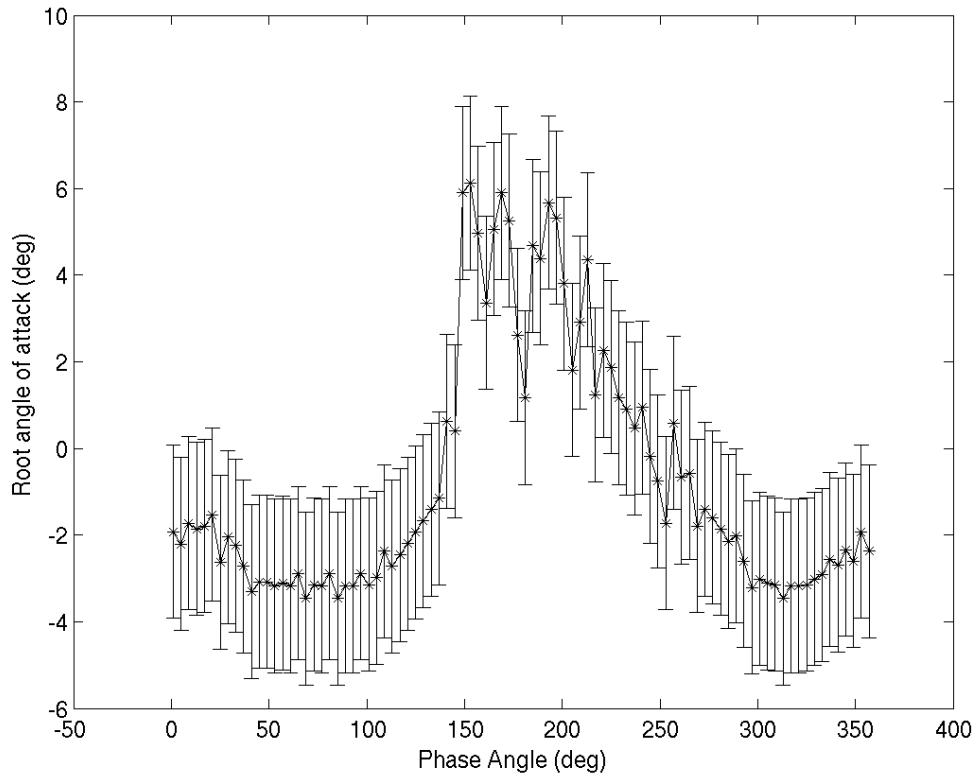


Figure 4.34. Angle of attack near the root of the drumhead wing at the 8Hz flapping frequency.

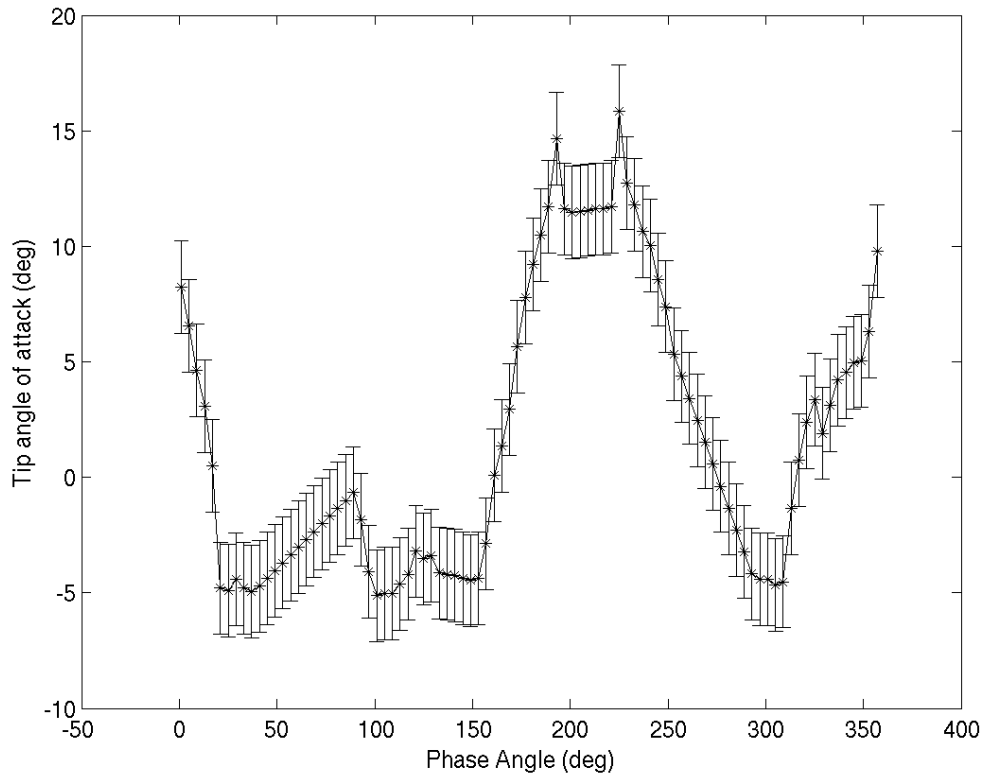


Figure 4.35. Angle of attack near the tip of the drumhead wing at the 11Hz flapping frequency.

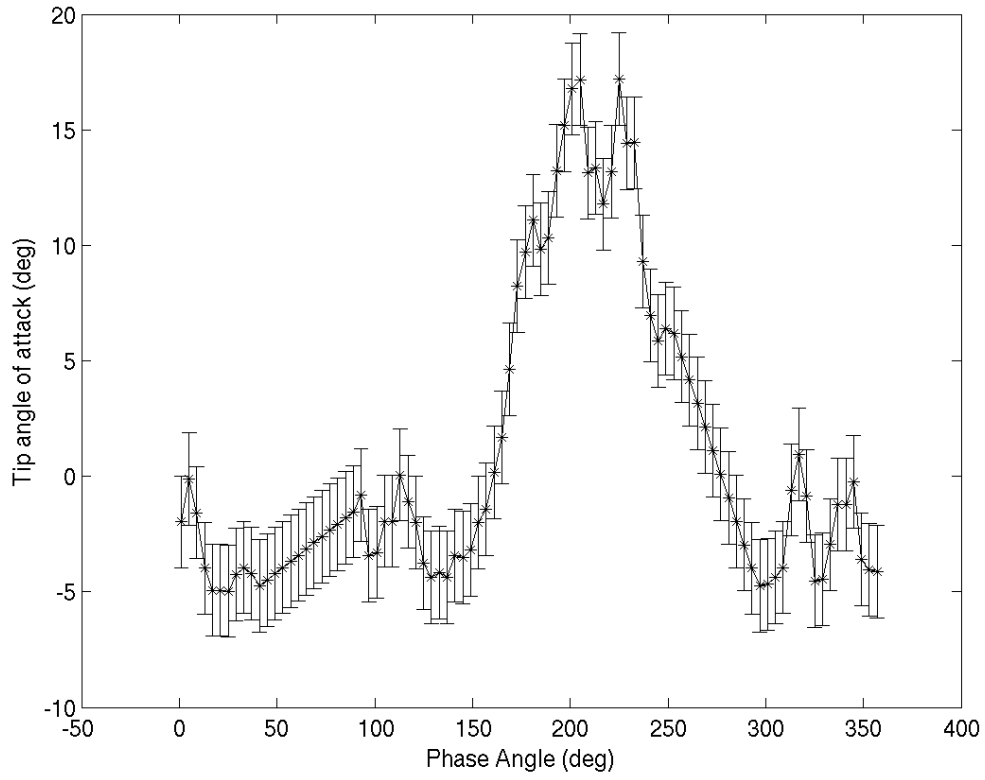


Figure 4.36. Angle of attack near the tip of the drumhead wing at the 10.5Hz

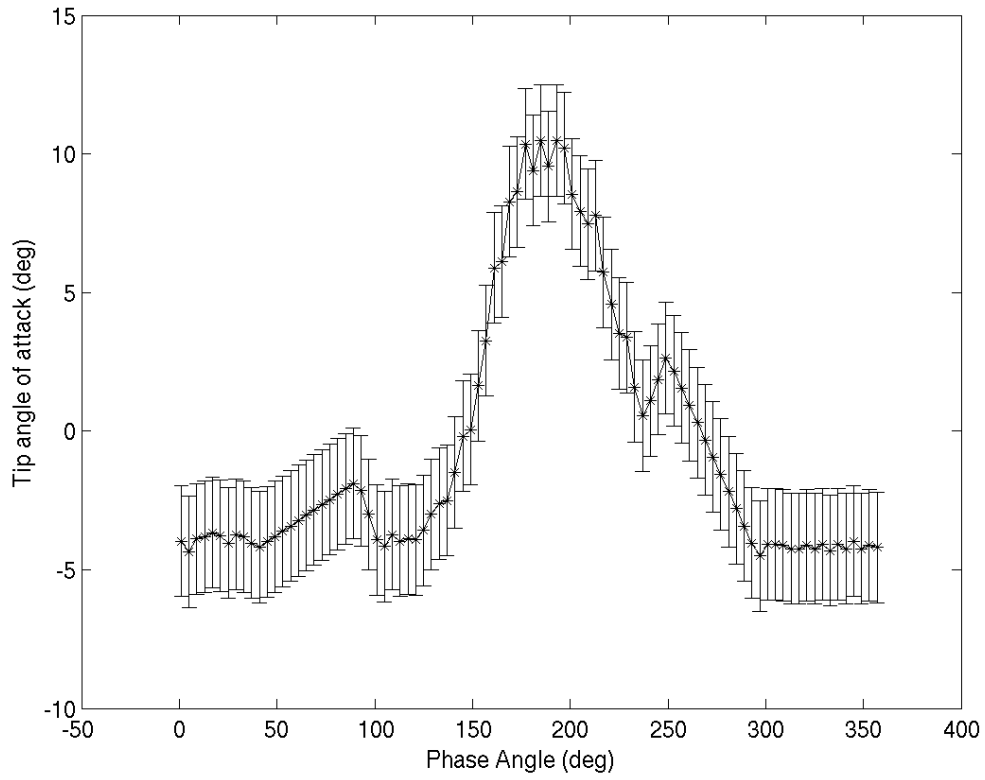


Figure 4.37. Angle of attack near the tip of the drumhead wing at the 8Hz flapping frequency.

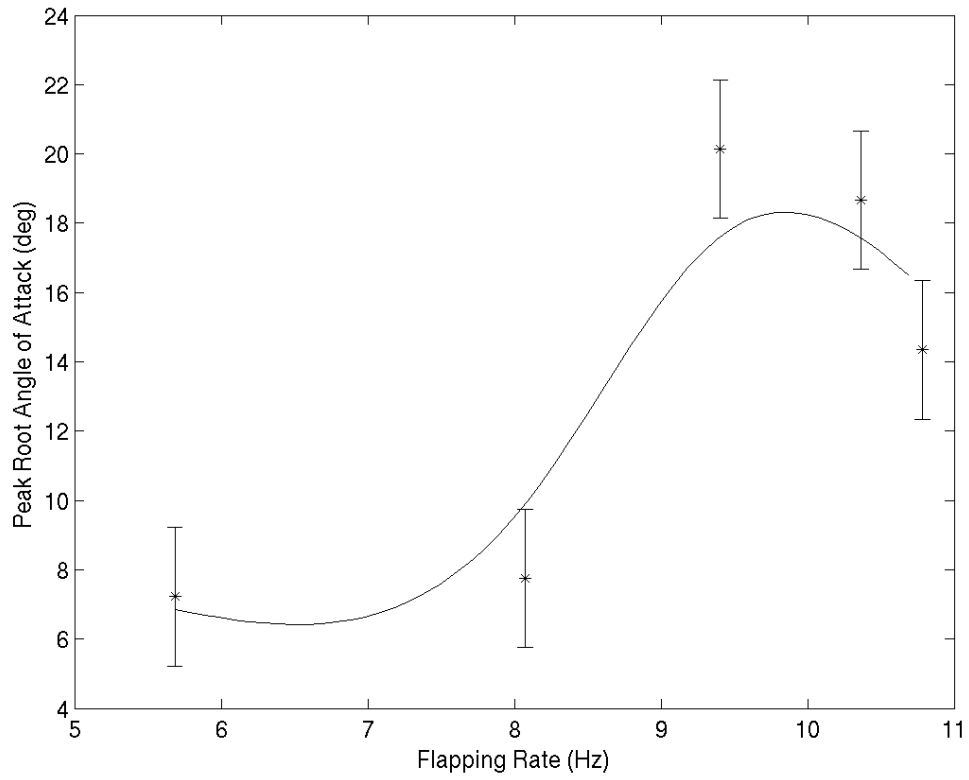


Figure 4.38. Peak angle of attack of the root of the wing as function of the flapping frequency of the drumhead wing.

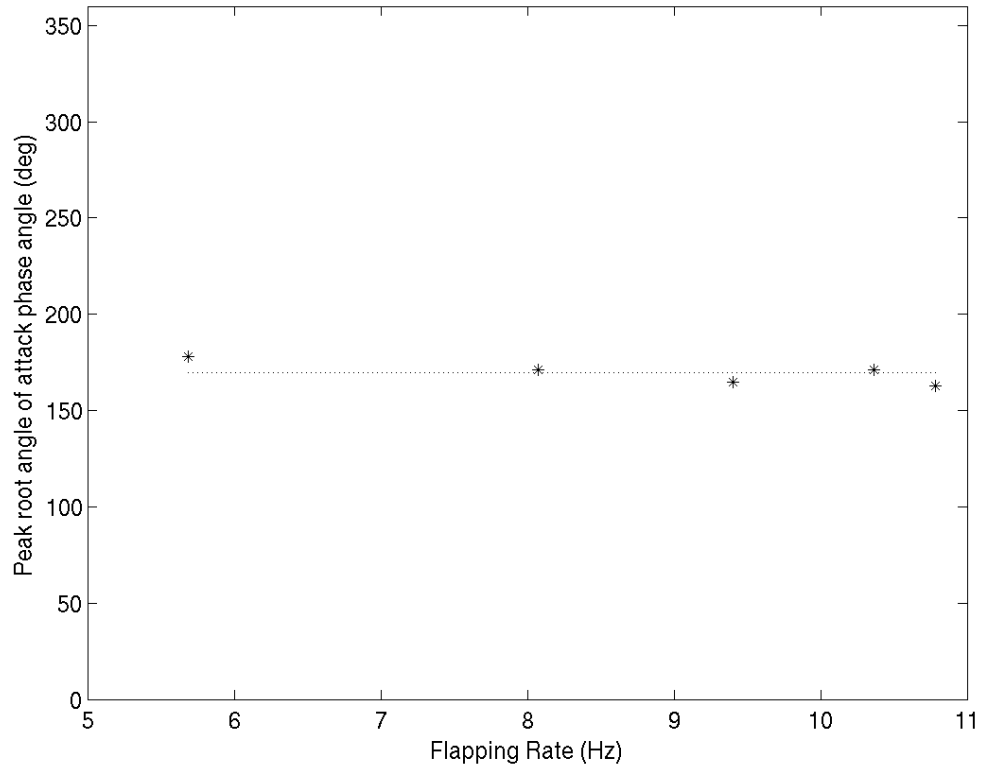


Figure 4.39. Phase angle of the peak angle of attack of the root of the drumhead wing versus flapping frequency.

shown in Figure 4.41. This indicates that the maximum angle of attack occurs at approximately 10.5Hz flapping frequency. This is comparable to the flexible wing. The phase angle of the maximum wing tip angle of attack is constant with frequency and comparable to all the other wings.

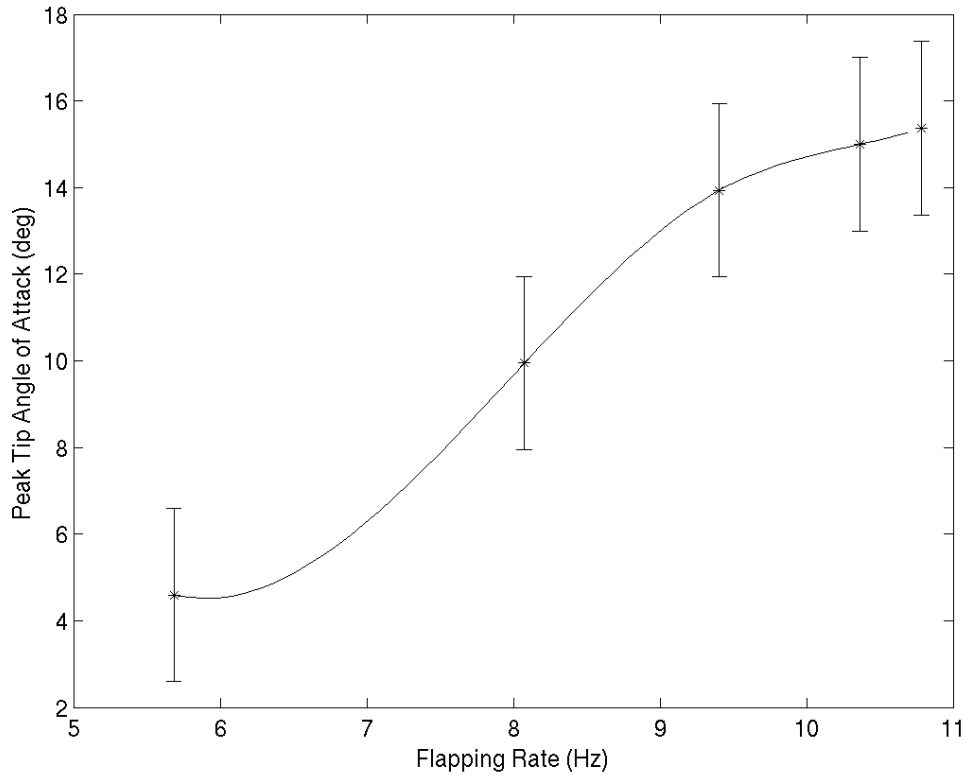


Figure 4.40. Maximum angle of attack of the tip of the wing versus flapping frequency of the drumhead wing.

### 4.3 Chapter Summary

The object of the results presented in this chapter was to determine the structural response of the different wing structures in flapping motion. These data, along with the thrust measurements presented in Chapter 3, can be combined to determine the

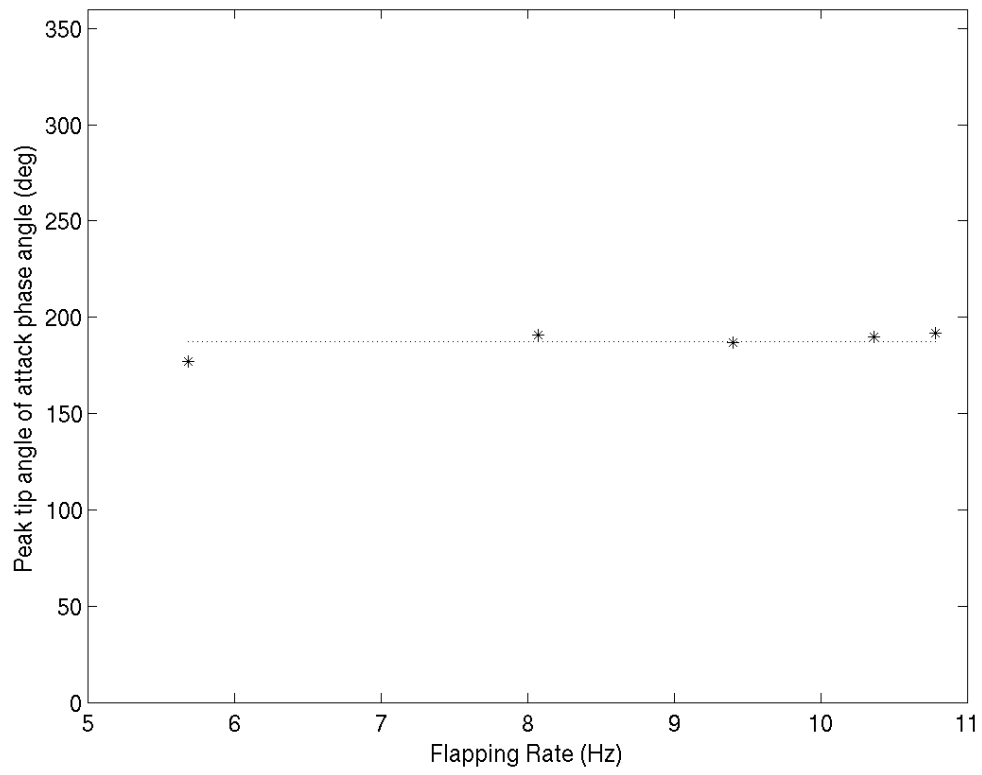


Figure 4.41. Phase angle of the peak tip angle of attack of the drumhead wing.

relationship between the structural deformation and aerodynamic thrust generation.

## CHAPTER 5

### MODELING AND SIMULATION

#### 5.1 Purpose and Objective

This chapter explores the fundamental physical properties of flapping wing thrust production by examining the functional relationship between the motion and deflection of the wings, and the thrust they produce. Estimates of the form of this functional relationship will be made based on what is known about the fluid dynamics of this situation.

The goal of this effort is to produce a phenomenological model that can provide insight into the underlying physics of flapping wing flight. It will also be useful for the design of autonomous flapping wing vehicles.

#### 5.2 Aerodynamics functional form

Three facts about flapping wing aerodynamics are well established in the literature. First, the flow is highly three dimensional, with significant spanwise components [61, 19]. Second, there are both quasi-steady and completely unsteady periods in each flapping half-cycle [2, 22]. Third, the flow is vortex-dominated [4, 66].

Linear models have been derived for situations involving unsteady, vortex dominated flow that use empirical corrections to linear inviscid aerodynamics for blade element theory models of helicopter rotors [33]. This approach has been applied to flapping wings as well by DeLaurier [11]. Both of these assume that the flow is

two dimensional over the wing, neglecting spanwise interactions. Functionally, they compute the circulation,  $\gamma$ , about each wing segment as a function of plunge rate,  $\dot{h}$ , and angle of attack,  $\alpha$ , and a linearized aerodynamic model,  $A$ , and then use a linear transformation,  $C$ , to compute the force,  $\vec{F}$ , generated by the wing in a given direction. A state space representation of this system is shown in Equations 5.2 and 5.3. This results in block diagonal matrices, where each block represents an independent wing segment. Figure 5.1 shows a diagram of a wing or rotor broken into segments for this type of analysis. Note that that it is assumed that one section does not interact with other segments.

$$\vec{u} = [\dot{h}\alpha] \quad (5.1)$$

$$\dot{\gamma} = A\gamma + B\vec{u} \quad (5.2)$$

$$\vec{F} = C\gamma \quad (5.3)$$

Ansari *et al.* [4] and Philips *et al.* [49] showed that it is possible to produce flapping wing aerodynamic models by assuming locally 2D flow and applying significant case-specific corrections. Both of these approaches potentially important spanwise flow effects and require significant effort by the modeler to assign values for any change in wing geometry or flapping motion.

Results from Swanton *et al.* [61] and Sallstrom and Ukeileythe [54], however, show that spanwise flow has important effects on flapping wing aerodynamics. This suggests that it may be possible to produce a three dimension linear model that assumes the wing segments interact. Instead of computing an internal fluid state like circulation about a wing segment in isolation, it should be possible to define the internal fluid state at the wing as a function of the fluid state at other points on the wing. Practically, this would mean replacing the off-diagonal zeros in the matrix  $A$

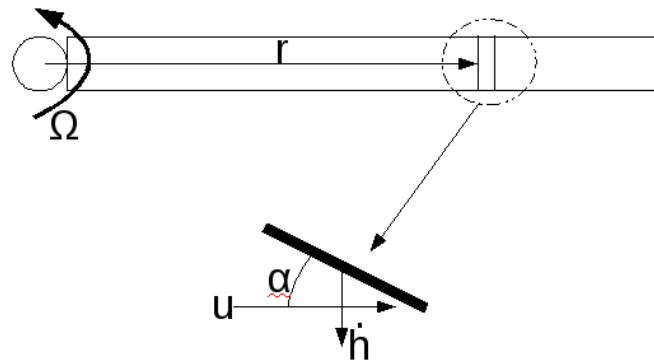


Figure 5.1. Schematic illustration of the angle of attack and plunge rate inputs for a blade element theory model.

in Equation 5.2 with non-zero parameters.

The ability to generate a linear model of flapping wing force generation without reference to wake geometry would imply that the fundamental aerodynamics depend more heavily on spanwise flow interaction than the structure of the wake. Inviscid CFD models are essentially linear approximations of the fluid, and eigenvector or proper orthogonal decomposition (POD) forms of these solutions are used to gain insight into the fundamental fluid dynamics. A low-order linear model of flapping wing aerodynamics could serve the same purpose. Additionally, the ability to use mathematical tools such as parameter estimation and system identification to develop flapping wing aerodynamic models would remove the need for complicated, case specific empirical corrections based on wake measurements.

### 5.3 Linear model

The results from Chapter 4 suggest that the structural deformation of the flapping wings were primarily driven by inertial loads on the wing, rather than aerodynamic loads. This makes it appropriate to use the structural deformation to define the inputs to a linear aerodynamic model. In this way the motion of the structure determines the aerodynamic forces.

For this analysis, we assume the existence of a smooth nonlinear function,  $F(\delta, \dot{\Gamma})$ , relating the deflection of the wing,  $\delta$ , and flapping angle rate,  $\dot{\Gamma}$ , of the wing to the thrust. This is given by Equation 5.4. By assuming this function is smooth, we expect to be able to find a linear approximation to  $F(\delta, \dot{\Gamma})$  at any combination of flapping frequency and structure deformation. This linear approximation is given in Equations 5.5 and 5.6. Here  $x$  represents the internal fluid states,  $A$  is the system matrix for this linearized fluid model,  $B$  is a linear transform between the model inputs,  $x$ , and fluid states  $u$ , and  $C$  is a linear transform relating

the fluid states to the thrust,  $T$ .

$$T = F(\delta, \dot{\Gamma}) \quad (5.4)$$

$$\dot{x} = Ax + Bu \quad (5.5)$$

$$T = Cx \quad (5.6)$$

#### 5.4 System Identification

Because the approximate form of the model is known, but nothing is known about its structure, this was an appropriate use of black box state space modeling techniques. A discrete time version of this parametrization is shown in Equations 5.7 and 5.8. The algorithm computes the elements of the  $A$ ,  $B$ , and  $C$  given the measurements of the system inputs, which in this case are wing deformation and motion; the system output, which is the thrust; and the number of states,  $n_x$ . These elements are determined such that the mean squared error of the prediction is minimized [37]. Six states were used to generate the models presented in this chapter. Fewer states resulted in less accurate models, and more states resulted in numerical instability.

$$x(\tau + \Delta\tau) = Ax(\tau) + Bu(\tau) \quad (5.7)$$

$$y(\tau) = Cx(\tau) \quad (5.8)$$

For this analysis, it was also necessary to specify that the eigenvalues of  $A$  had magnitude that was less than 1. This guaranteed a stable model. The study used the `n4sid` function in Matlab with stability enforced to implement this procedure. The generated models were converted from discrete to continuous time using the algorithm described by Ljung [37]. The inputs in this case are the deflection of

the wing structure from the previous chapter. By assuming that the deflection is periodic, the phase averaged values were used to generate smooth long time series. The block diagram for this technique is shown in Figure 5.2, where the output is the thrust  $T$ .

Because the system is periodic, the analysis was done using a non-dimensional time based on the flapping phase angle,  $\phi$ . Getting from the force and deflection measurements to an approximate system model required two broad steps, each of which contained several internal steps. The first broad step involved preparation of the time series to be estimated. This involved the following steps:

1. filtering the time series to remove high frequency noise,
2. determining the time derivative of the flap angle,  $\dot{\Gamma}$ ,
3. determining the aerodynamic inputs  $\dot{h}$  and  $\alpha$ ,
4. constructing long time series of the aerodynamic inputs,  $\dot{h}(t)$  and  $\alpha(t)$ , and thrust,  $T(t)$ .

#### 5.4.1 Filter time series to remove high frequency noise

The phase averaged time series contained some high-frequency noise. Therefore it was necessary to smooth them so that they could be used in the system identification algorithm. An effective tool for this was a seven point moving average filter whose width corresponded to 3.8% of the flapping cycle. The start and end of the time series were zero padded to half the filter width to provide the appropriate start-up and ending for filtering the time series. After filtering, periodicity was enforced by making the first and last points in the filtered signal equal each other. Figures 5.3 through 5.5 show a sample comparison between the unfiltered and filtered time series of the wing root and tip deflection and thrust for the stiff wing at a flapping frequency of 11Hz.

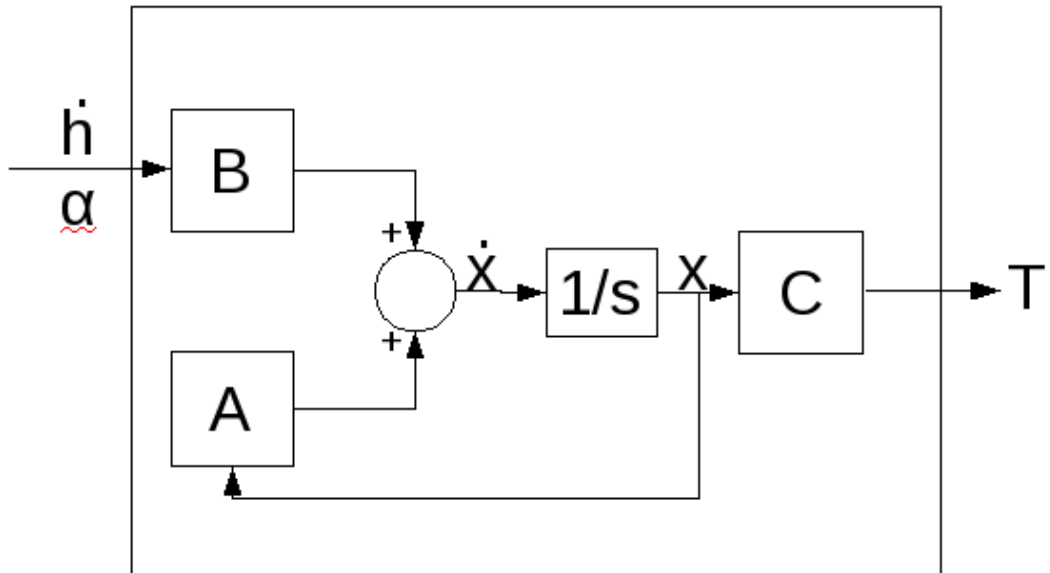


Figure 5.2. Block diagram showing how the matrices generated by least square prediction error are used to compute the thrust given aerodynamic inputs.

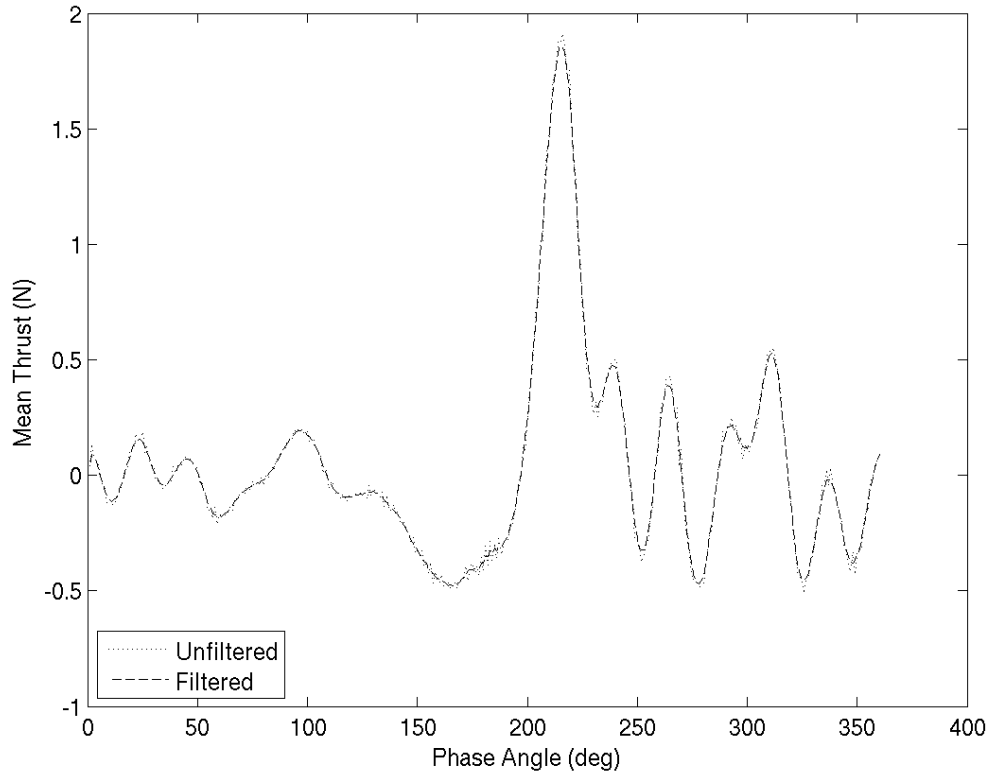


Figure 5.3. Plot of the unfiltered and filtered phase averaged thrust for the stiff wing at an 11Hz flapping frequency.

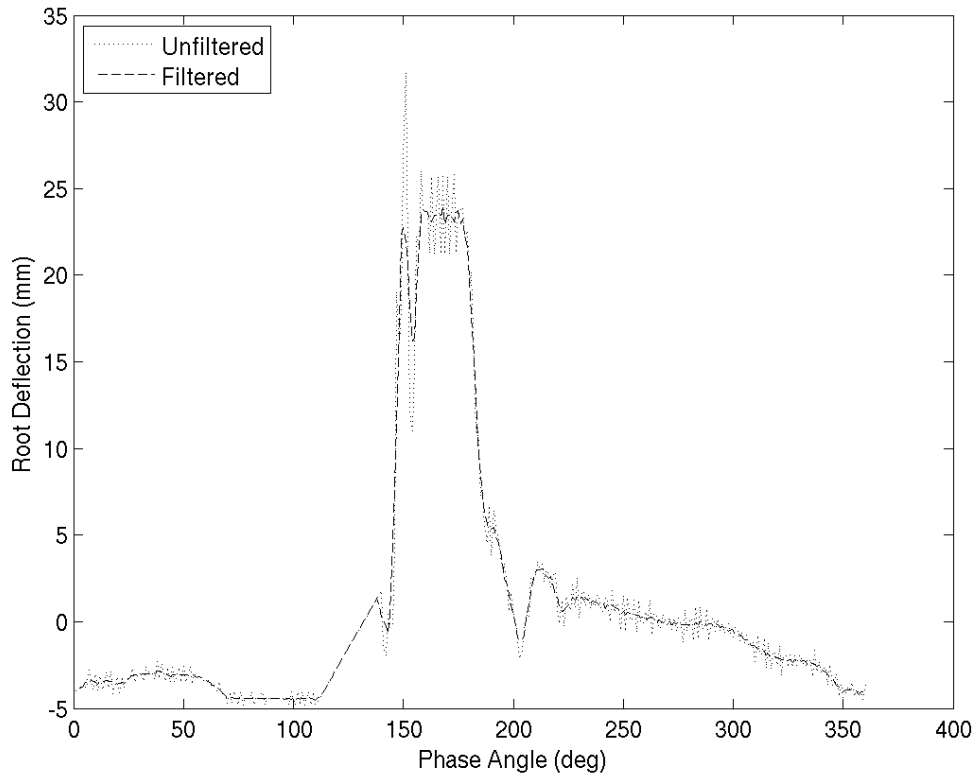


Figure 5.4. Plot of the unfiltered and filtered phase averaged wing root deflection for the stiff wing at an 11Hz flapping frequency.

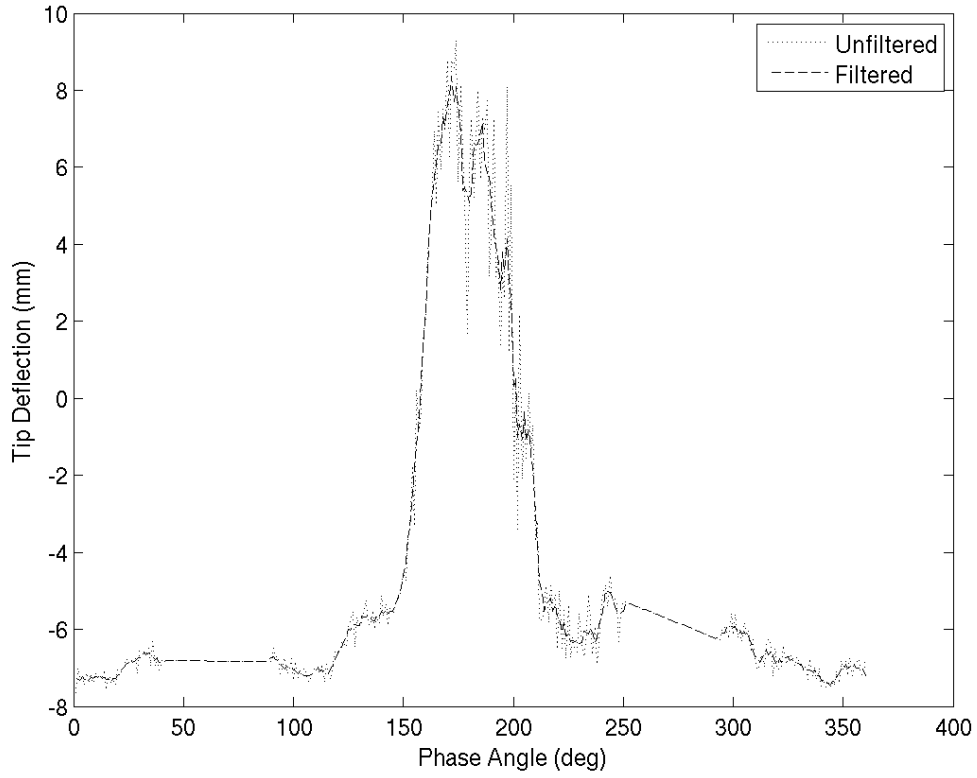


Figure 5.5. Plots of the unfiltered and filtered phase averaged deflection of the wing tip of the stiff wing at an 11Hz flapping frequency.

### 5.4.2 Determining $\dot{\Gamma}$

While the flapping angle,  $\Gamma(t)$ , was directly determined in Chapter 4, its time derivative,  $\dot{\Gamma}(t)$ , is the most relevant aerodynamic quantity, since it largely defines the plunge rate. Determining  $\dot{\Gamma}(t)$  involved estimating the time derivative of a real data series, which is a non-trivial process given its inherent noise. This was accomplished in three steps:

1. simplify the time series of  $\Gamma(t)$  by only selecting points corresponding to every  $10^\circ$  of the flapping phase angle,
2. generate a spline fit to  $\Gamma(t)$ ,
3. determine the time derivative  $\dot{\Gamma}(t)$  based on the spline function.

An example of the simplified time series  $\Gamma(t)$  and its spline fit is shown in Figure 5.6 for the stiff wing at an 11Hz flapping frequency. The correspond  $\dot{\Gamma}(t)$  time series is shown in Figure 5.7.

### 5.4.3 Find $\dot{h}$ along the wing

Most simplified aerodynamic models assume a chord-wise flow along the wings, relative to which they pitch and plunge [11, 70, 18]. Conservation of momentum theory stipulates that thrust generation in quiescent air requires the generation of a net flow along the wings as well. This allows us to define the angle of attack,  $\alpha$ , and plunge rate,  $\dot{h}$ , as we would for a pitching and plunging airfoil. A diagram of this is shown in Figure 5.8.

The calculation of  $\dot{h}(t)$  was straightforward. The plunge rate is defined in Equation 5.9. It was estimated at the points where the deflections were measured. An example of  $\alpha_{tip}(t)$ ,  $\alpha_{root}(t)$ ,  $\dot{h}_{tip}(t)$  and  $\dot{h}_{root}(t)$  for a flapping cycle at a flapping frequency of 11Hz for the stiff wing is shown in Figures 5.9 and 5.10.

$$\dot{h}(y) = \dot{\Gamma}y \quad (5.9)$$

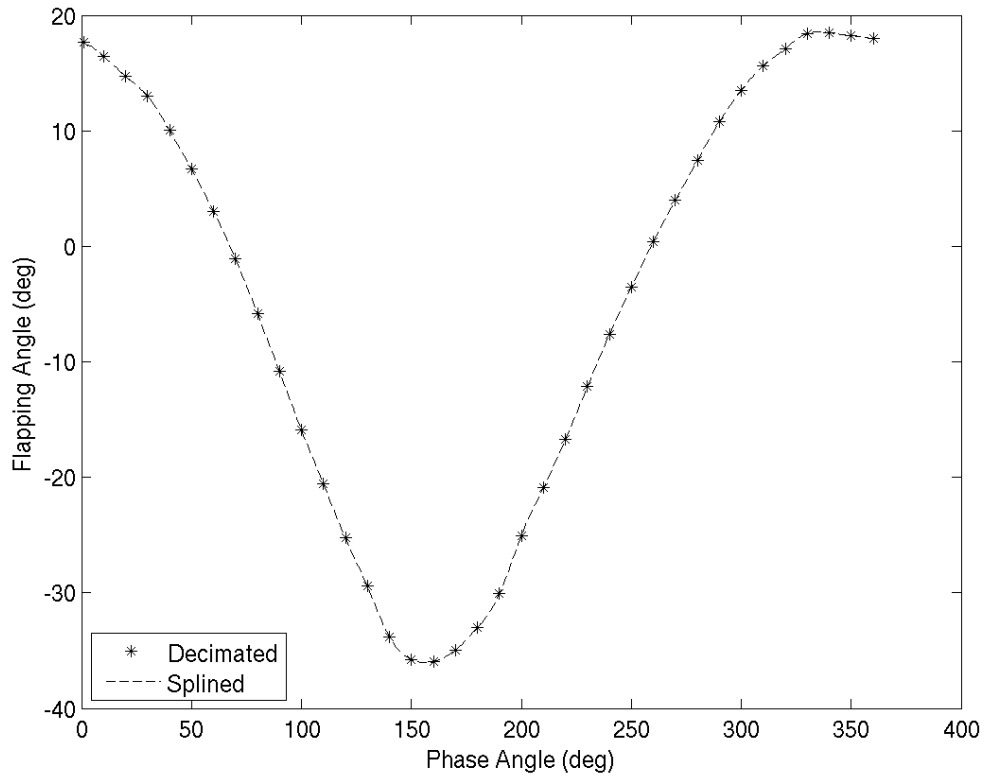


Figure 5.6. Plot of the simplified time series and spline fit for the stiff wing at an 11Hz flapping frequency.

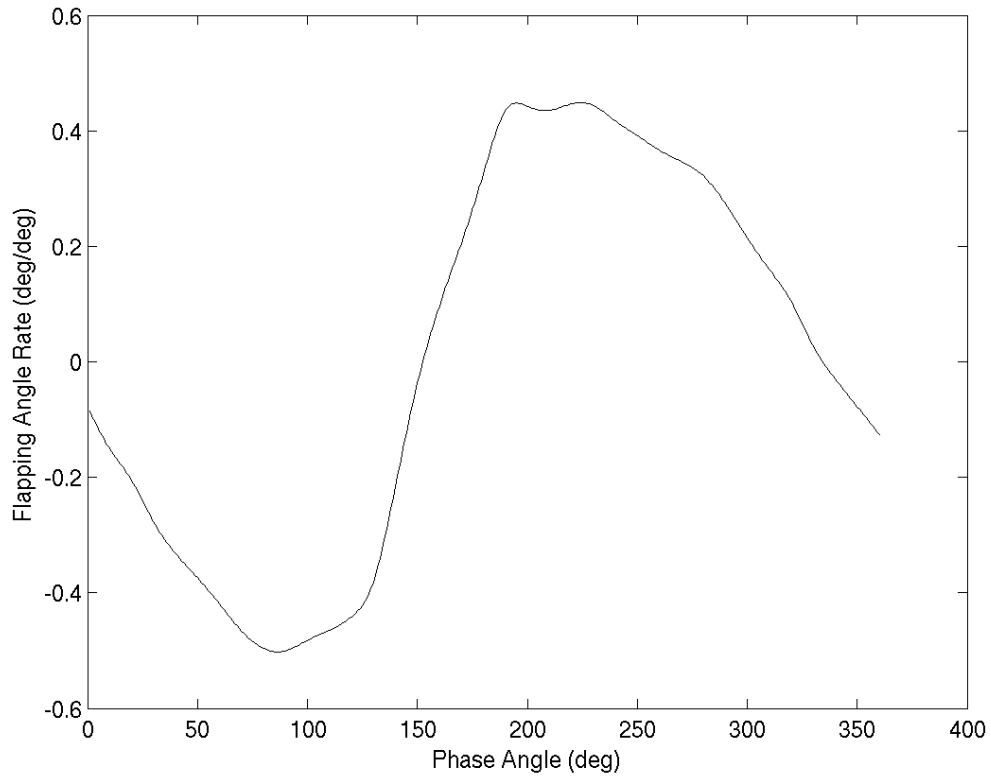


Figure 5.7. Plot of  $\dot{\Gamma}(t)$  for the time series in Figure 5.6.

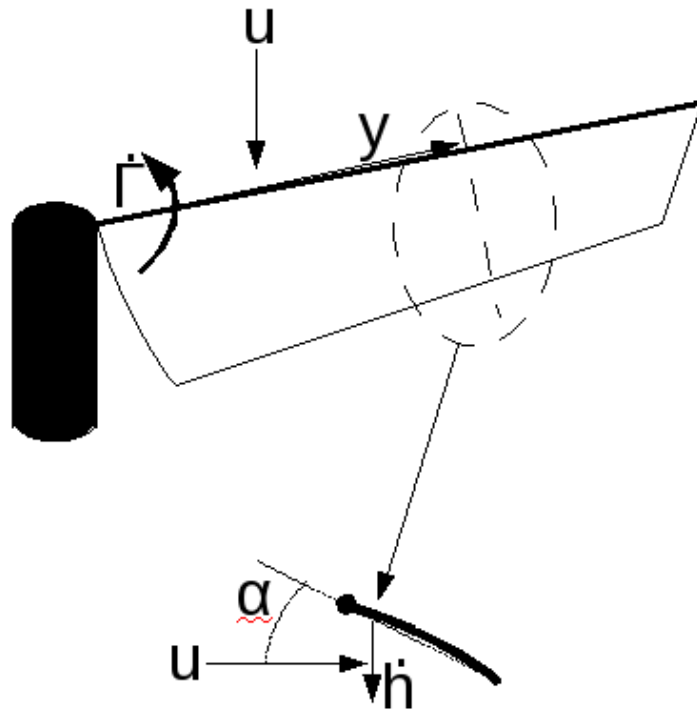


Figure 5.8. Diagram showing how  $\alpha$  and  $\dot{h}$  were computed.

#### 5.4.4 Construct long time series

Once smooth signals for a single period of the thrust  $T(t)$ , angle of attack  $\alpha(t)$  and plunge rate  $\dot{h}(t)$  were found, long time series were generated by concatenating ten flapping periods. The longer data sets allowed start up time for the model generation process. This improved the numerical accuracy.

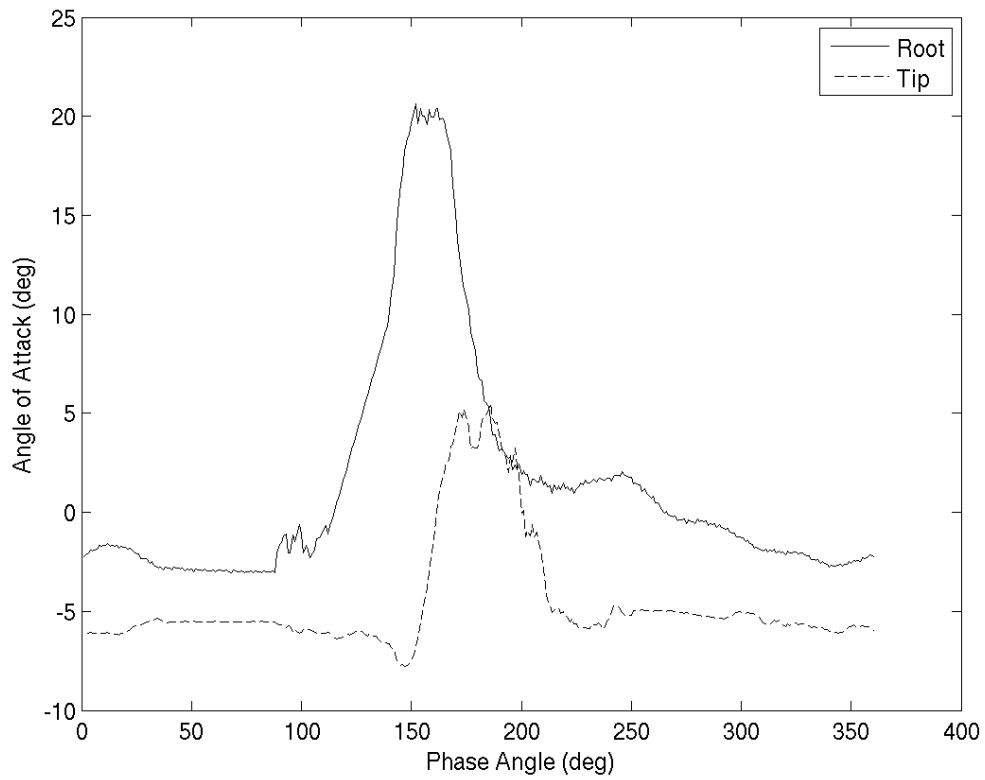


Figure 5.9. Estimate of  $\alpha_{tip}(t)$  and  $\alpha_{root}(t)$  for the stiff wing at a flapping frequency of 11Hz.

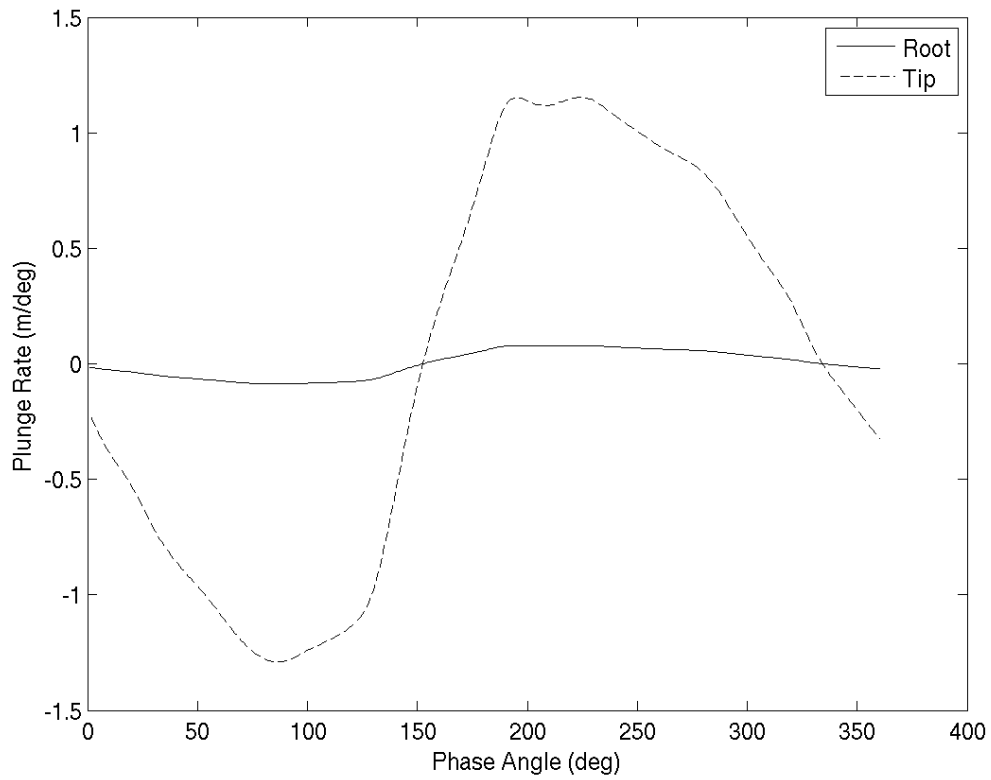


Figure 5.10. Estimate of  $\dot{h}_{tip}(t)$  and  $\dot{h}_{root}(t)$  for the stiff wing at a flapping frequency of 11Hz.

## 5.5 Model Generation

### 5.5.1 Stiff Wing

An example of the application of Equations 4.3 through 5.9 for the stiff wing at a flapping frequency of 11Hz is shown in Figures 5.9 and 5.10. This utilized the filtered phased averaged series that were shown in Figures 5.4 and 5.5.

Figure 5.11 shows a comparison between the measured thrust and the output from the simulation based on the wing deflection time series. In general the model captured the basic features of the thrust cycle. It shows the peak thrust began at the start of the down-stroke of the wing. The peak thrust that occurred at  $\phi = 216^\circ$  was underestimated by the model by approximately 50%.

This model does capture the period of negative thrust that occurs before the downstroke of the wing. The magnitude is similar between the two although the simulation exhibits oscillations that do not precisely match in amplitude. Over all, the quality of the fit is similar to that of the complex nonlinear model of flapping aircraft wings at this scale developed Ansari *et al.* [4]. However, in this case there is significantly less computation required, and the generation of models of similar quality for different cases is largely automated.

Figures 5.12 through 5.15 show the results of this modeling approach applied to the stiff wing at flapping frequencies of 10.5Hz, 9.5Hz, 8Hz and 6Hz. Given the similarities in wing motion and thrust measurements for this wing, it is not surprising that the model generated at other flapping frequencies produce similar results. In each case, there is a small negative thrust segment shortly before the peak thrust at the beginning of the down-stroke. Also as before, the model under-predicts the peak thrust by approximately 50%.

Figure 5.16 shows the mean-squared error of the model estimate of the thrust,  $T(t)$ , that is normalized by the variance of the measured thrust. This provides a

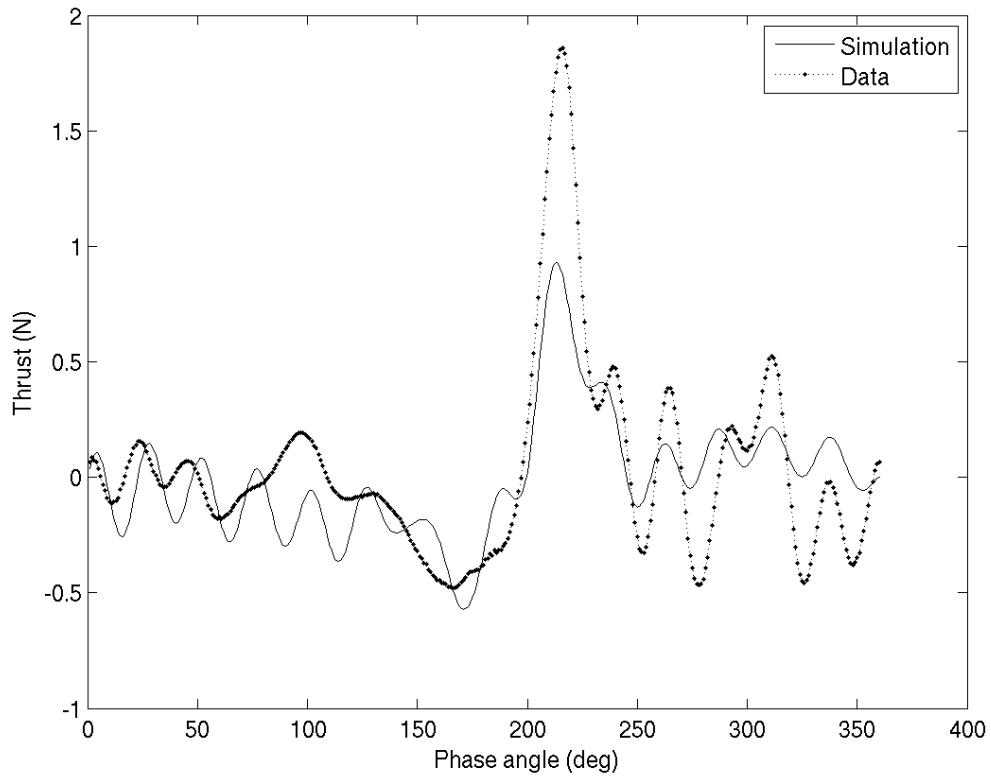


Figure 5.11. Comparison between the linear model and measured thrust for the stiff wing at a flapping frequency of 11Hz.

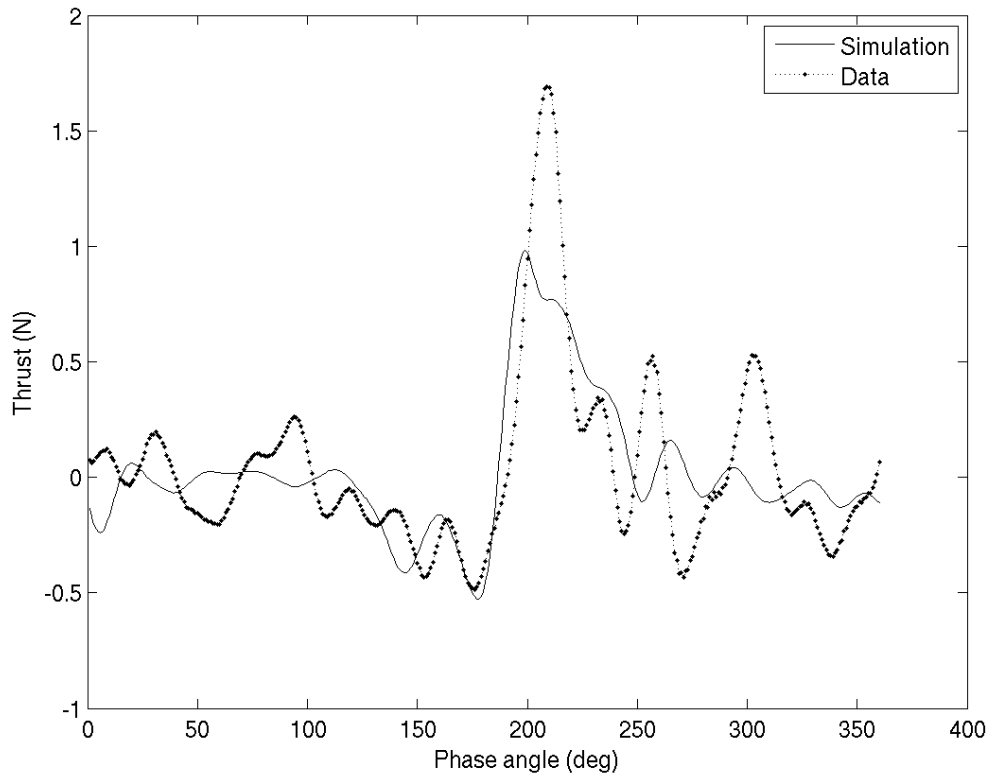


Figure 5.12. Comparison between the linear model and measured thrust for the stiff wing at a flapping frequency of 10.5Hz.

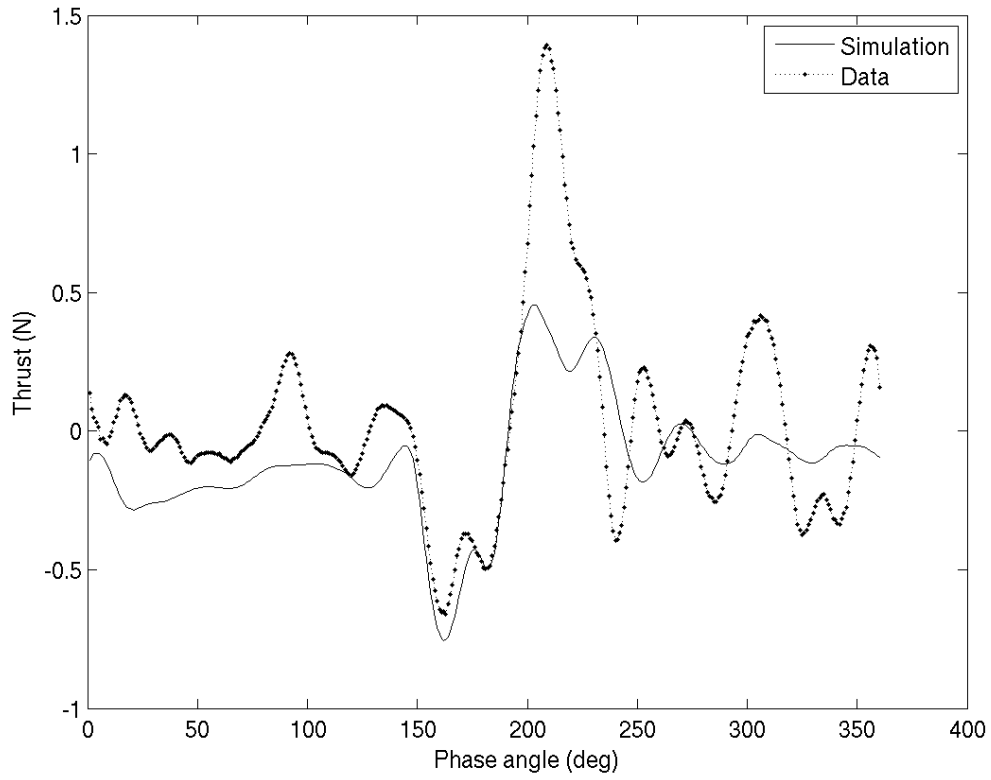


Figure 5.13. Comparison between the linear model and measured thrust for the stiff wing at flapping frequency 9.5Hz.

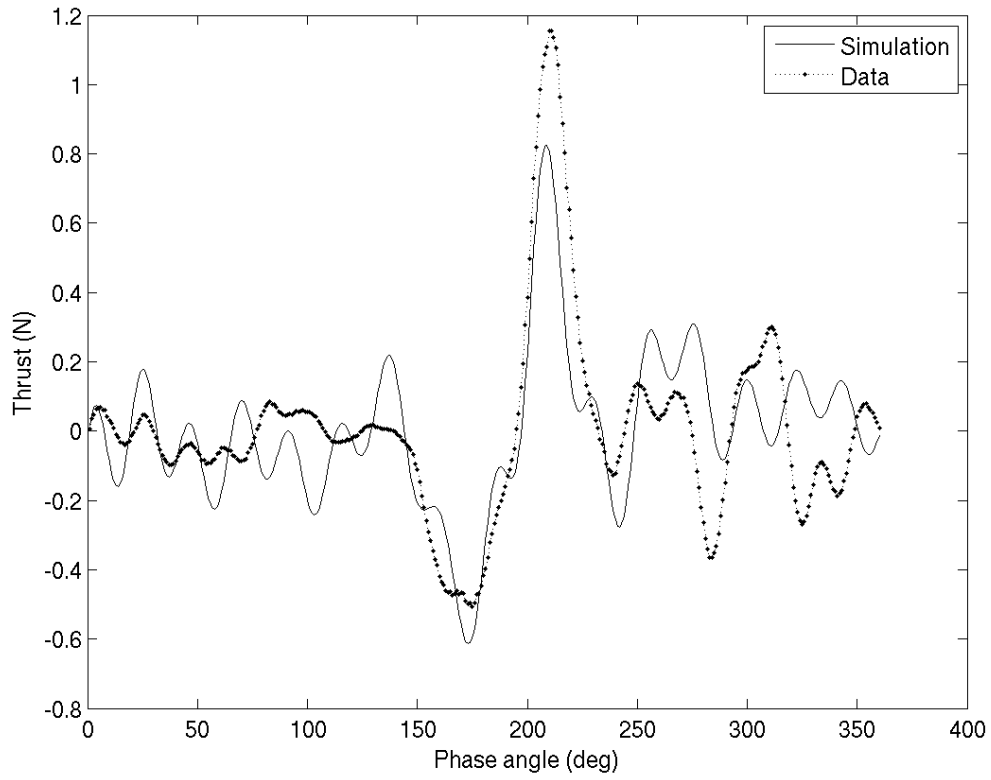


Figure 5.14. Comparison between the linear model and measured thrust for the stiff wing at a flapping frequency of 8Hz.

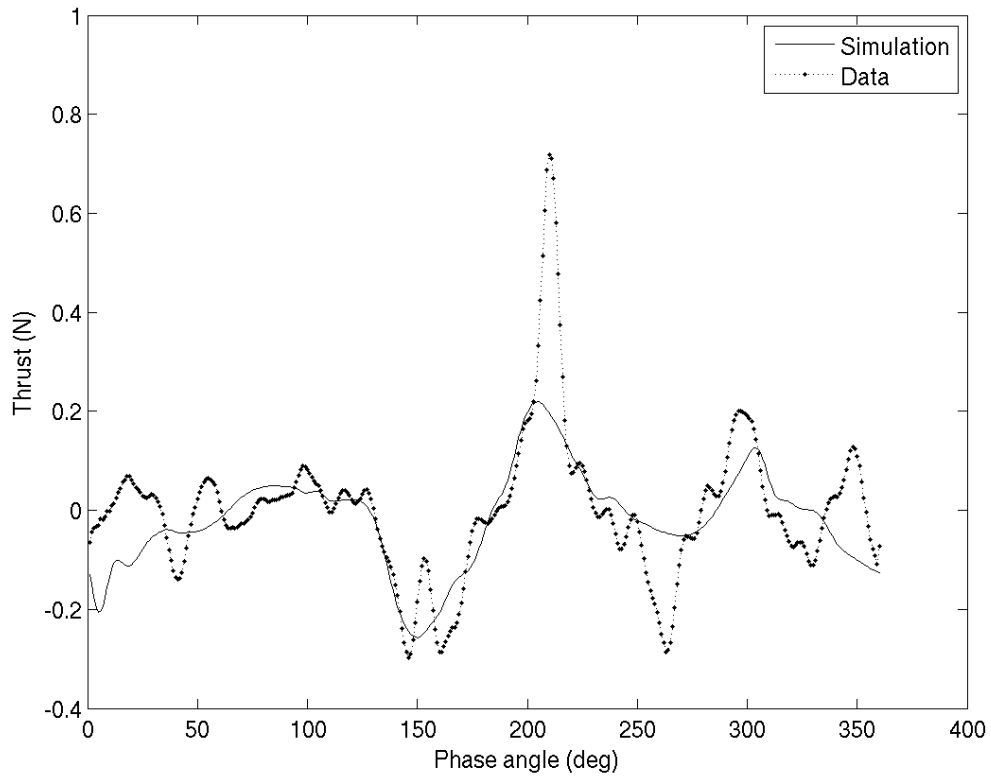


Figure 5.15. Comparison between the linear model and measured thrust for the stiff wing a flapping frequency of 6Hz.

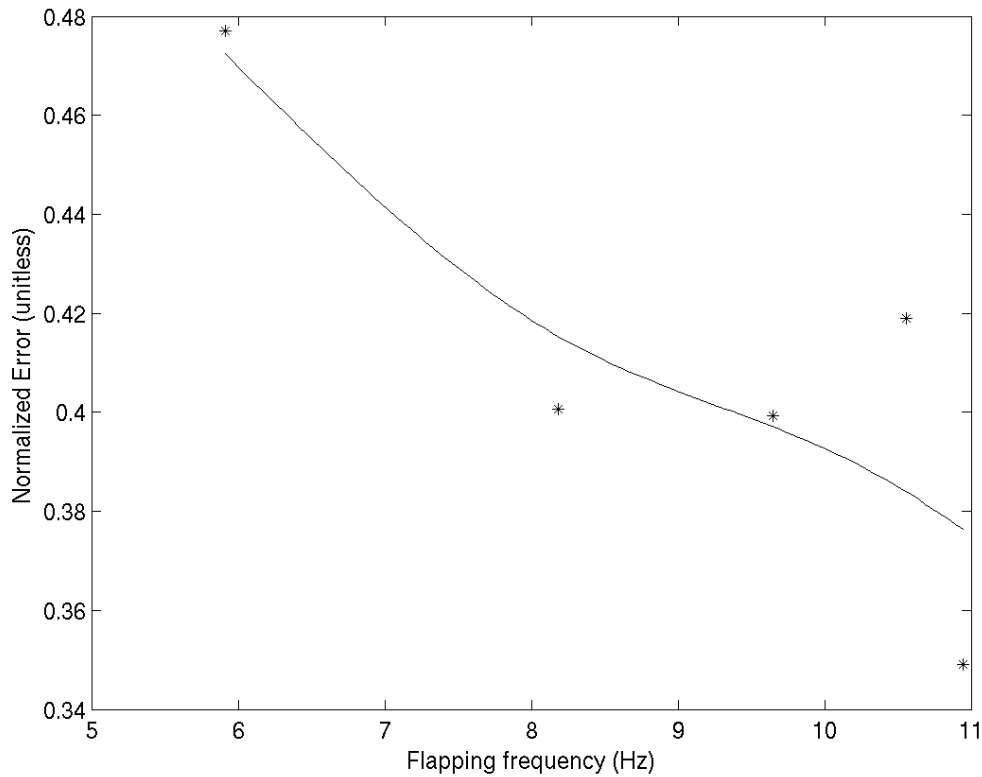


Figure 5.16. Normalize mean-squared error in the model estimated thrust for the stiff wing as a function of flapping frequency.

measure of the quality of the model for the different flapping frequencies. It shows a trend of generally decreasing normalized error. This might indicate that the thrust generation process becomes more linear as the flapping frequency increases, where we would expect that the acceleration effects come to dominate the wing motion.

While a simple procedure to generate a fairly good model of a wing is a significant step forward, it is important to understand the range over which the model is valid. Figures 5.17 through 5.20 shows plots of the thrust predicted using the model generated for the stiff wing at at a flapping frequency of 11Hz that used

inputs from the other flapping frequencies. At the higher flapping frequencies, the model prediction is qualitatively as good as that generated with the models at their respective flapping frequencies. However, the peak of the predicted thrust is slightly out of phase with the measured peak thrust. At a flapping frequency of 6Hz, where both inertial loads and aerodynamic loads play a role in structure deformation, the 11Hz flapping frequency model does not produce a good result. An estimate of the overall error in the model prediction is shown in Figure 5.21, with the data above 8Hz shown in Figure 5.22. The mean squared error normalized by the variance in the measured thrust at the corresponding flapping frequency is shown in Figure 5.21.

### 5.5.2 Flexible Wing

The input time series for the flexible wing at a flapping frequency of 11.5Hz are shown in Figures 5.23 and 5.24. These show significantly more motion than that of the stiff wings, which could possibly reduce the inherent linearity of the thrust generating system. A comparison between the predicted thrust and measured thrust time series based on those inputs is shown in Figure 5.25. Qualitatively, the prediction is as good as that for the stiff wing. As with the stiff wing it predicts a prominent thrust peak at the start of the down-stroke of the flapping cycle.

In contrast to the stiff wing, we expect that the flexible wing is more influenced by aeroelastic loads as the flapping frequency increases. As a result, its thrust characteristics should be more linear at lower flapping frequencies. Figures 5.26 through 5.29 show a comparison between the model estimated thrust at flapping frequencies of 11Hz, 10Hz, 8.5Hz and 6Hz. Qualitatively, the results at the higher flapping frequencies are comparable to that at a 11.5Hz flapping frequency. However, the normalized mean square error shown in Figure 5.30 indicates a clear trend of

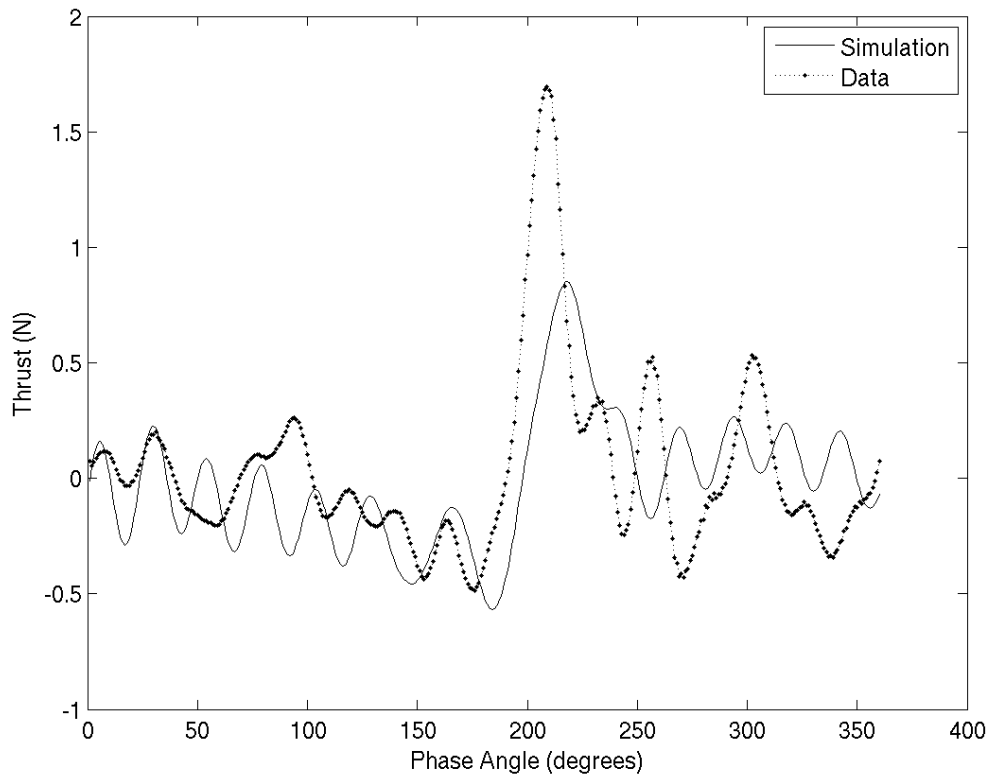


Figure 5.17. Comparison between the measured thrust and predicted thrust at flapping frequency of 10.5Hz for the model coefficients estimated for the stiff wing at an 11Hz flapping frequency.

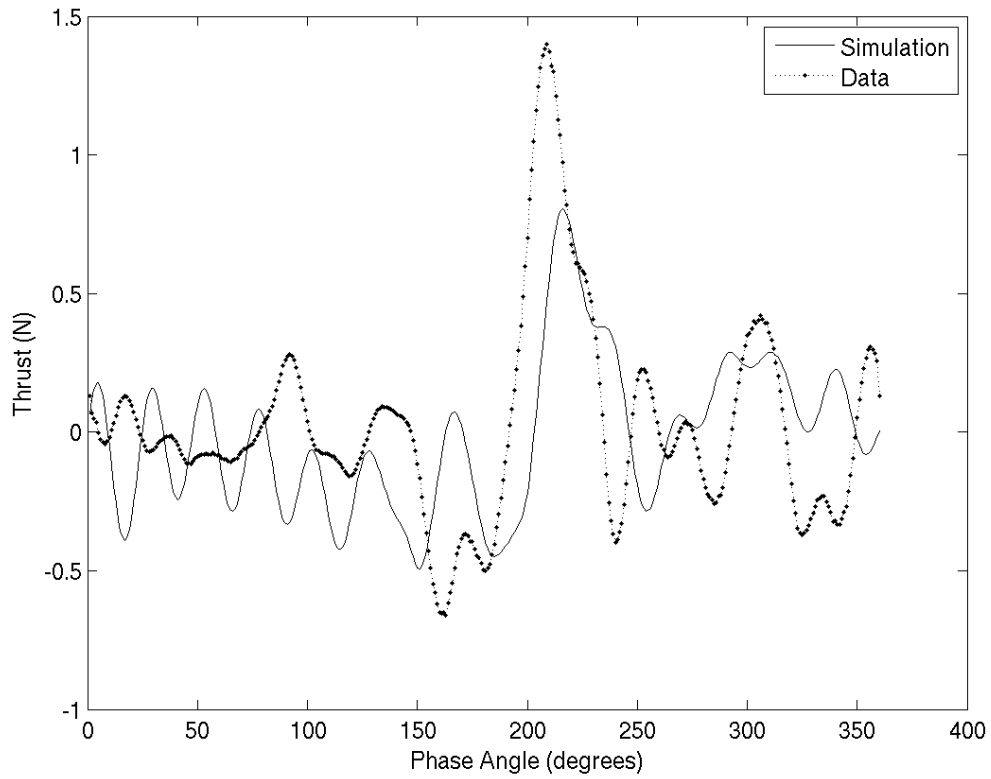


Figure 5.18. Comparison between the measured thrust and predicted thrust at flapping frequency 9.5Hz for the model coefficients estimated for the stiff wing at an 11Hz flapping frequency.

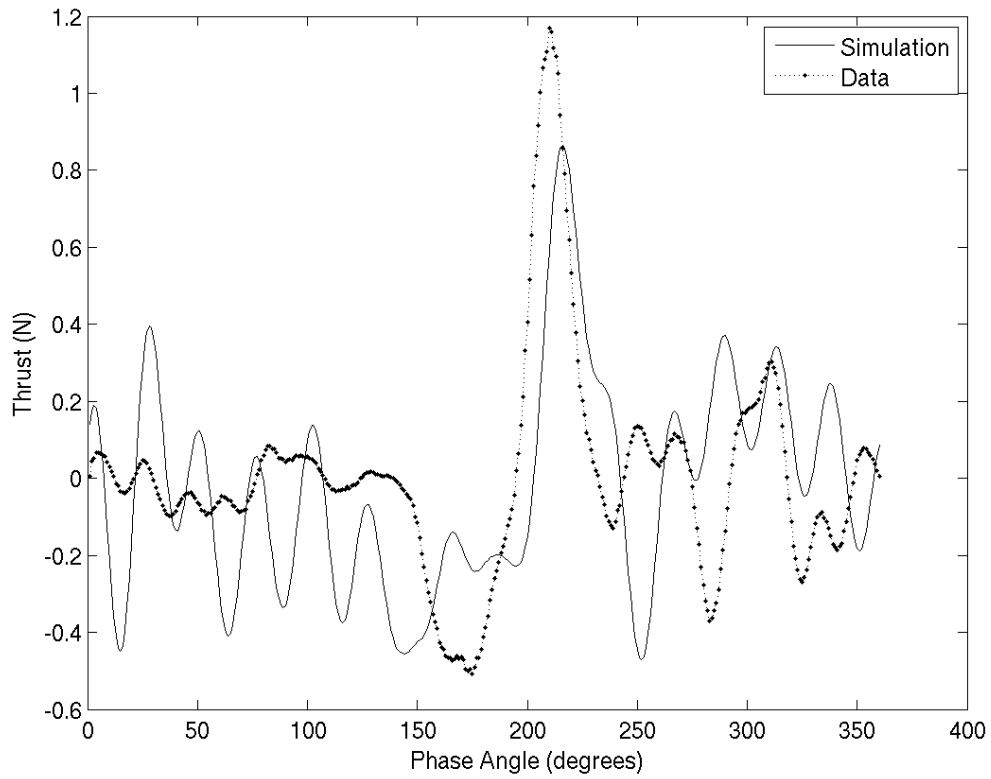


Figure 5.19. Comparison between the measured thrust and predicted thrust at a flapping frequency of 8Hz for the model coefficients estimated for the stiff wing at an 11Hz flapping frequency.

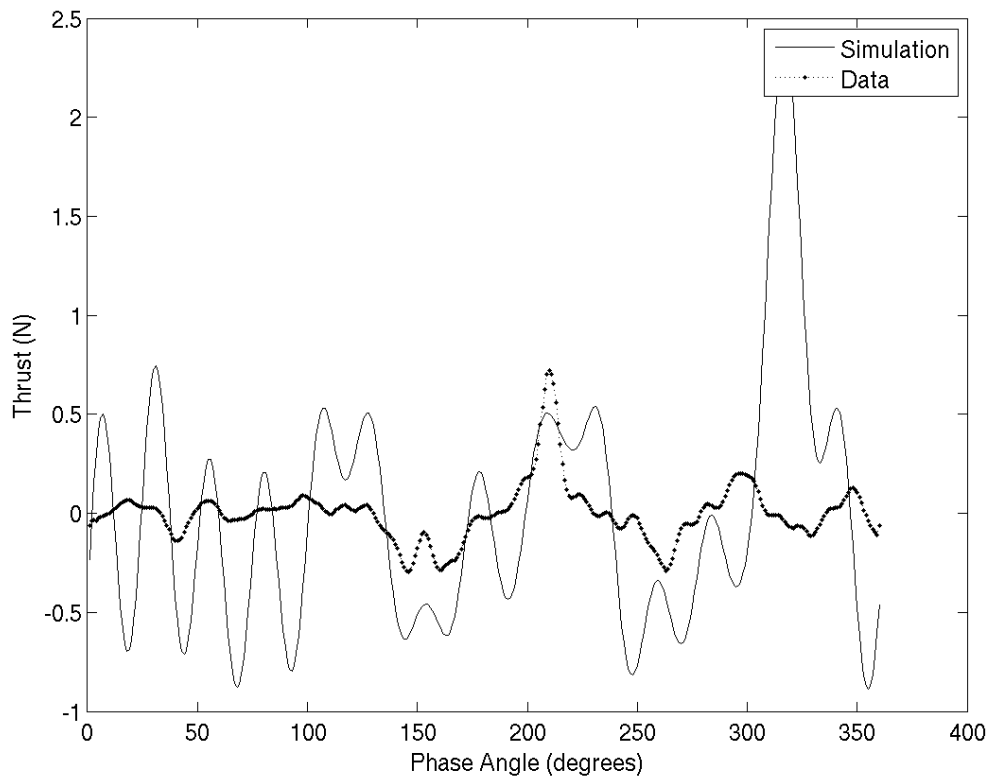


Figure 5.20. Comparison between the measured thrust and predicted thrust at a flapping frequency of 6Hz for the model coefficients estimated for the stiff wing at an 11Hz flapping frequency.

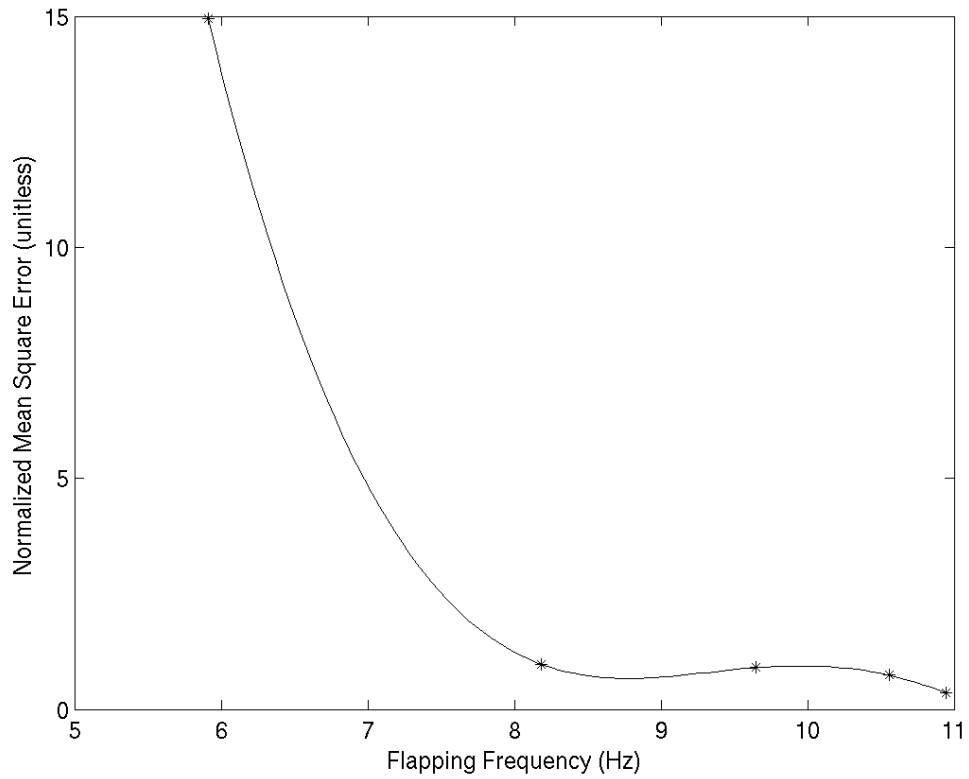


Figure 5.21. Normalized mean-squared error in the model estimate of the thrust for the stiff wing obtained using the 11Hz flapping model coefficients for conditions of the other flapping frequencies.

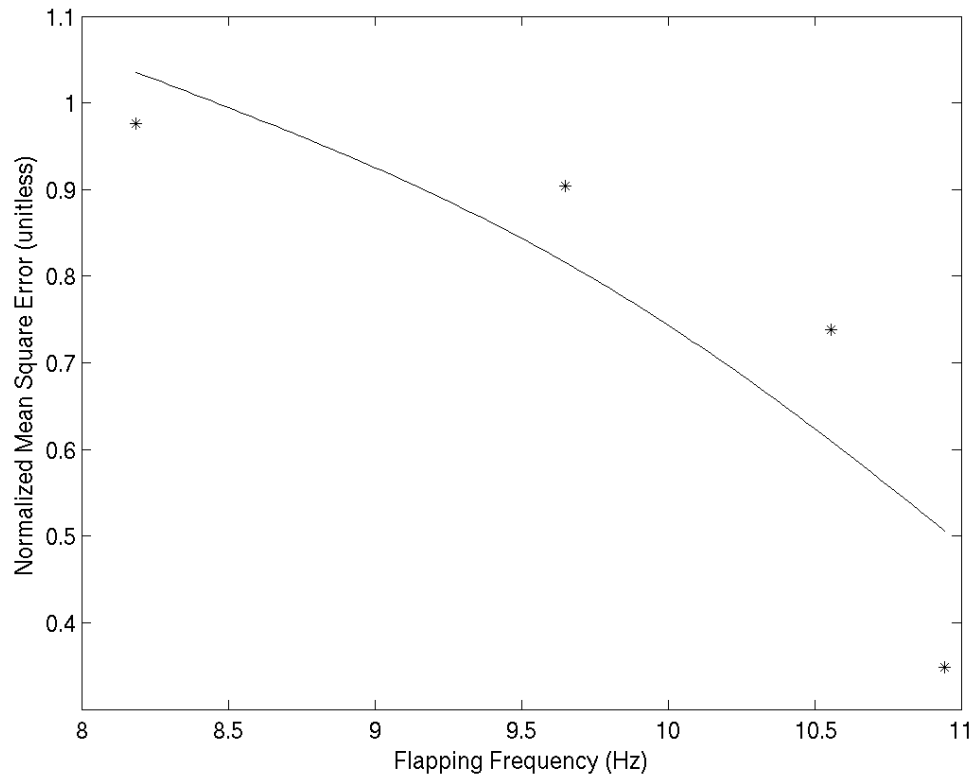


Figure 5.22. Plot of the data presented in Figure 5.21 above 8Hz.

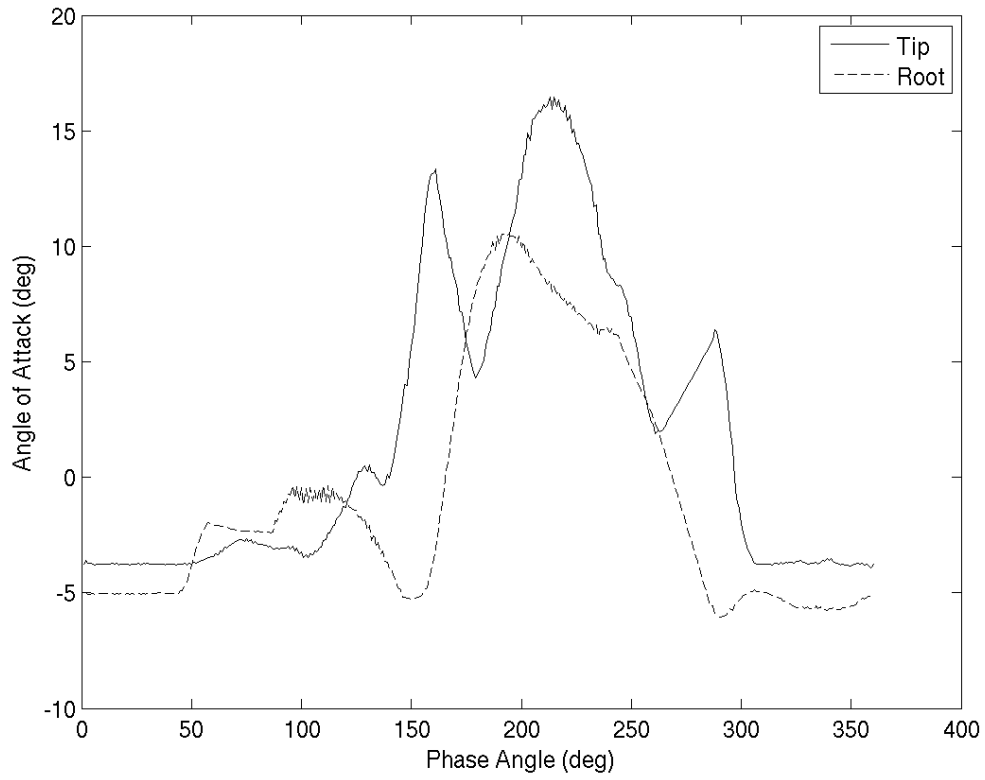


Figure 5.23. Input  $\alpha(t)$  for the flexible wing at a flapping frequency of 11.5Hz.

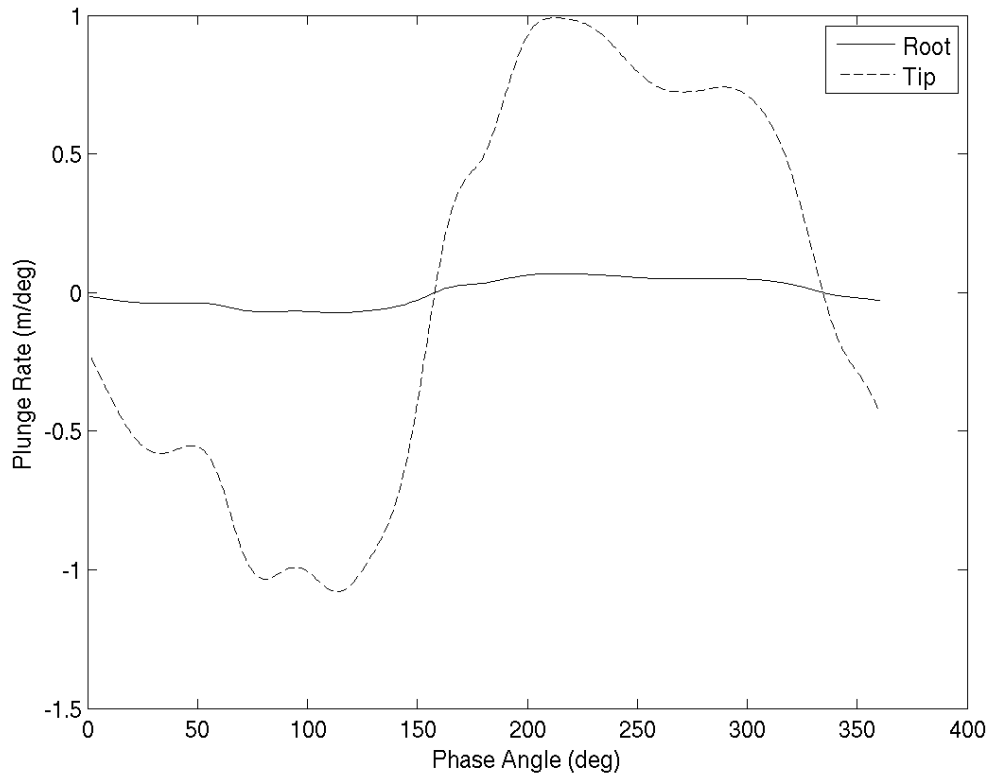


Figure 5.24. Input  $\dot{h}(t)$  for the flexible wing at a flapping frequency of 11.5Hz.

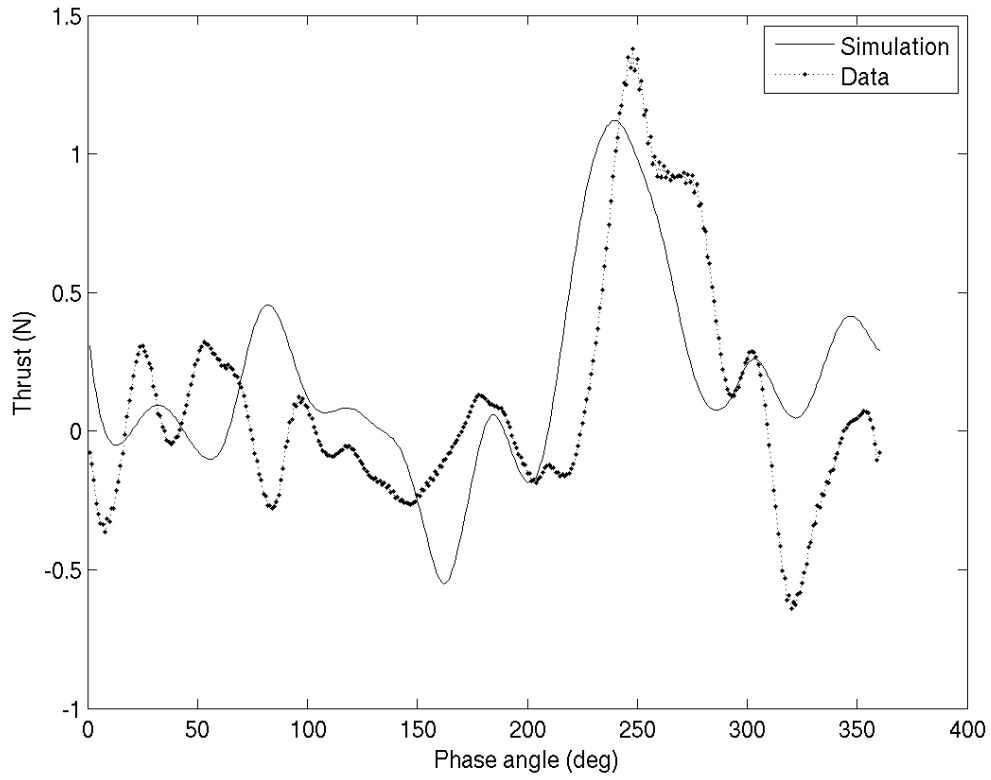


Figure 5.25. Comparison of the linear model and measured thrust for the flexible wing data at flapping frequency 11.5Hz.

lower model error at the lower flapping frequencies that would suggest the linear model is more appropriate there.

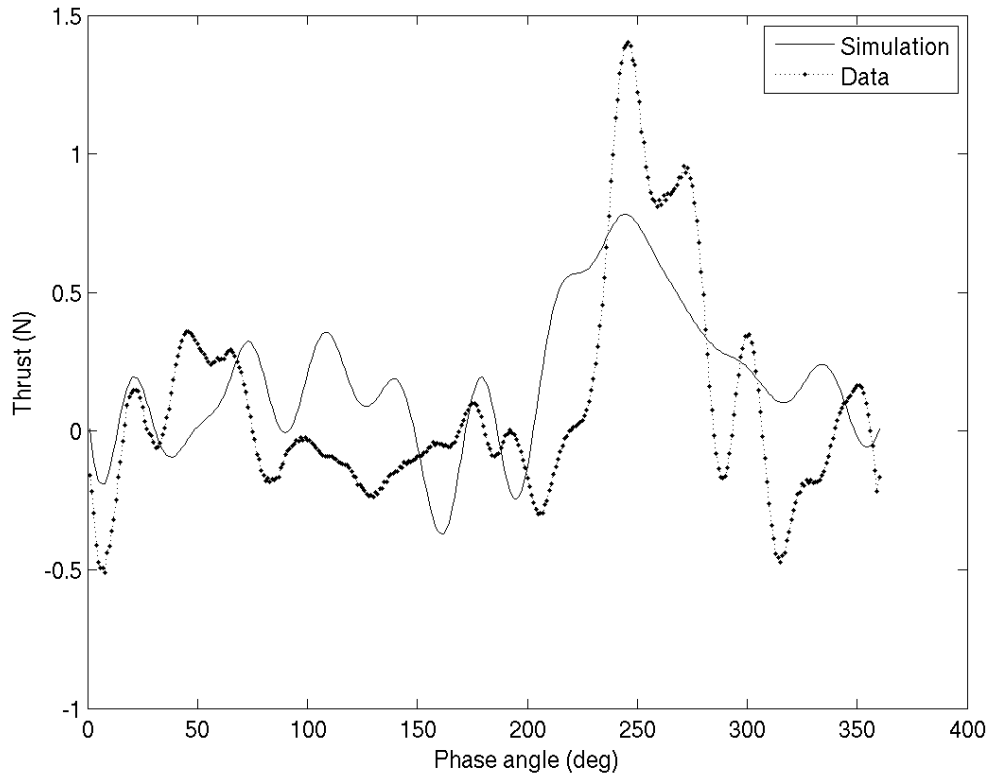


Figure 5.26. Comparison of the linear model and measured thrust for the flexible wing at a flapping frequency of 11Hz.

Figures 5.31 through 5.34 show the result of using the inputs from flapping frequencies of 11Hz, 10Hz, 8.5Hz, and 6Hz with the model coefficients generated with the data collected at an 11.5Hz flapping frequency. For flapping frequencies of 10Hz and 11Hz, the model gives qualitatively similar thrust time series compared to the experimental measurements. This indicates that the underlying physics are similar over this higher range of flapping frequencies. The mean square error between the predicted and measured time series for the linear model as a function of the flapping

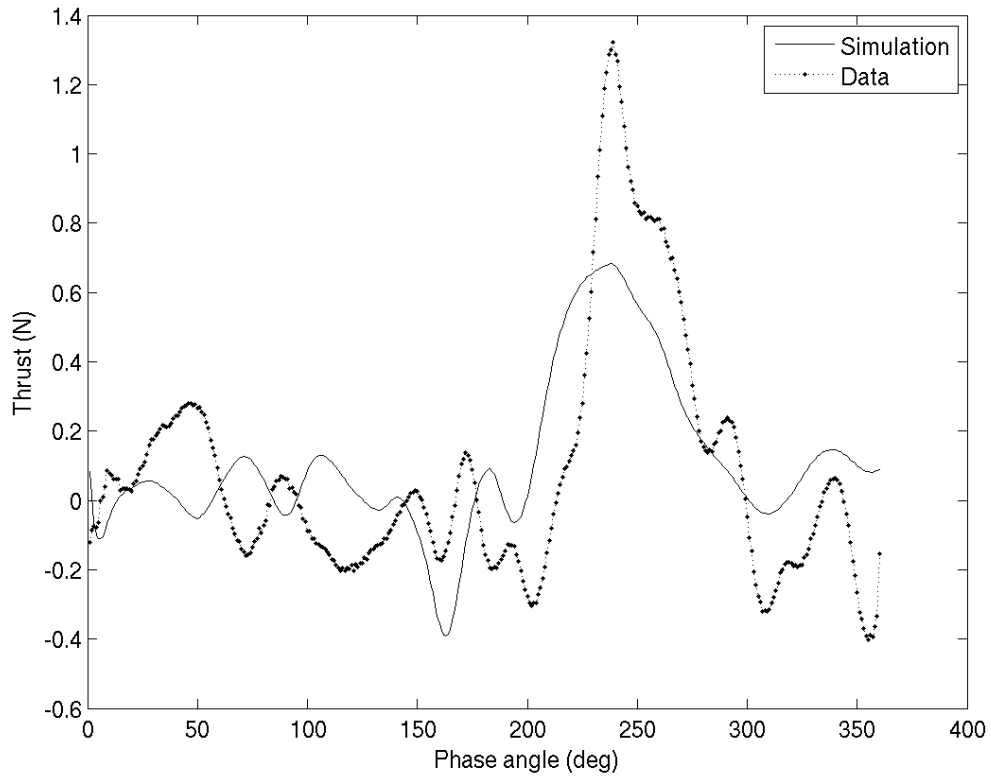


Figure 5.27. Comparison of the linear model and measured thrust for the flexible wing at a flapping frequency of 10Hz.

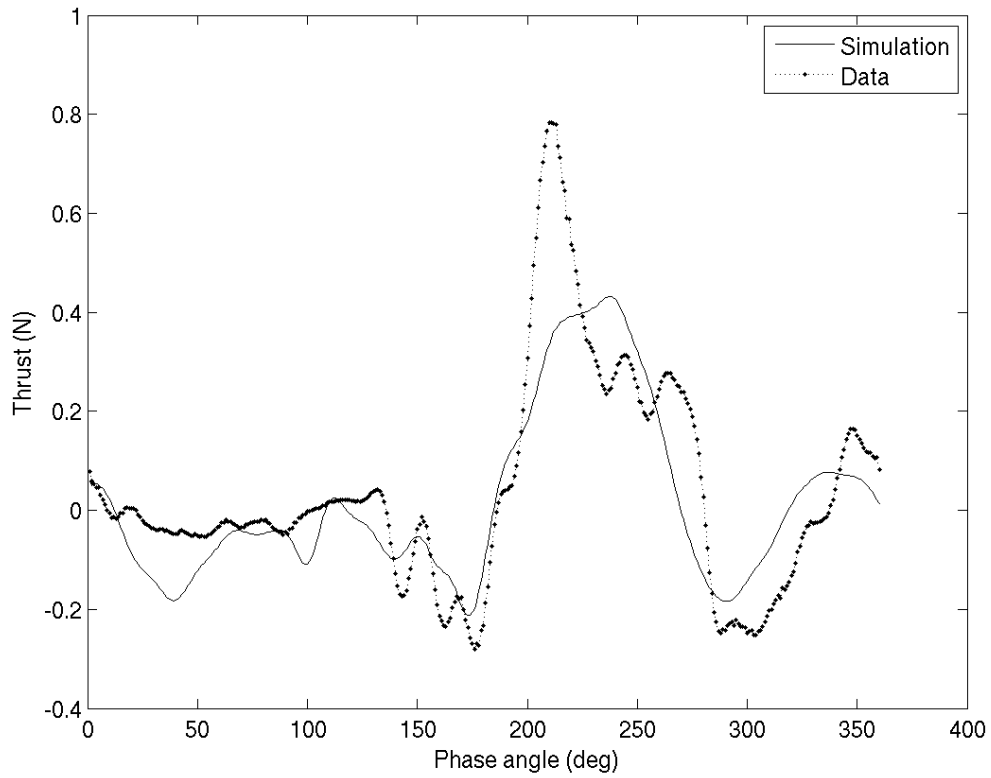


Figure 5.28. Comparison of the linear model and measured thrust for the flexible wing data at a flapping frequency of 8.5Hz.

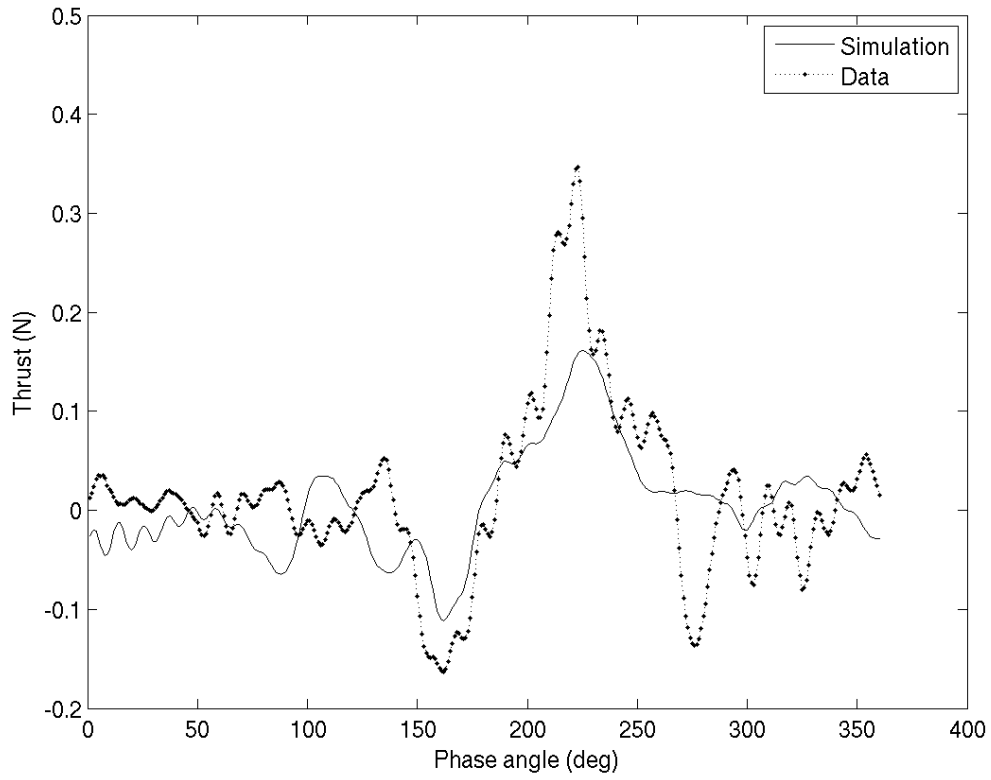


Figure 5.29. Comparison of the linear model and measured thrust for the flexible wing data at a flapping frequency of 6Hz.

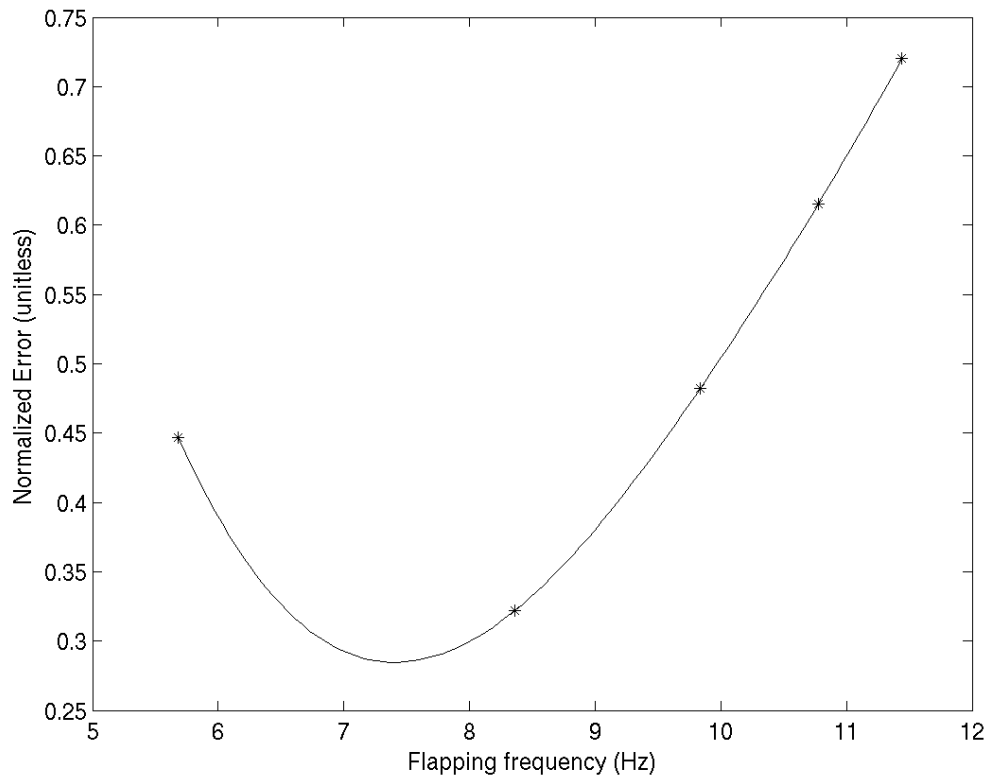


Figure 5.30. Normalized mean square prediction error versus flapping frequency for the flexible wing.

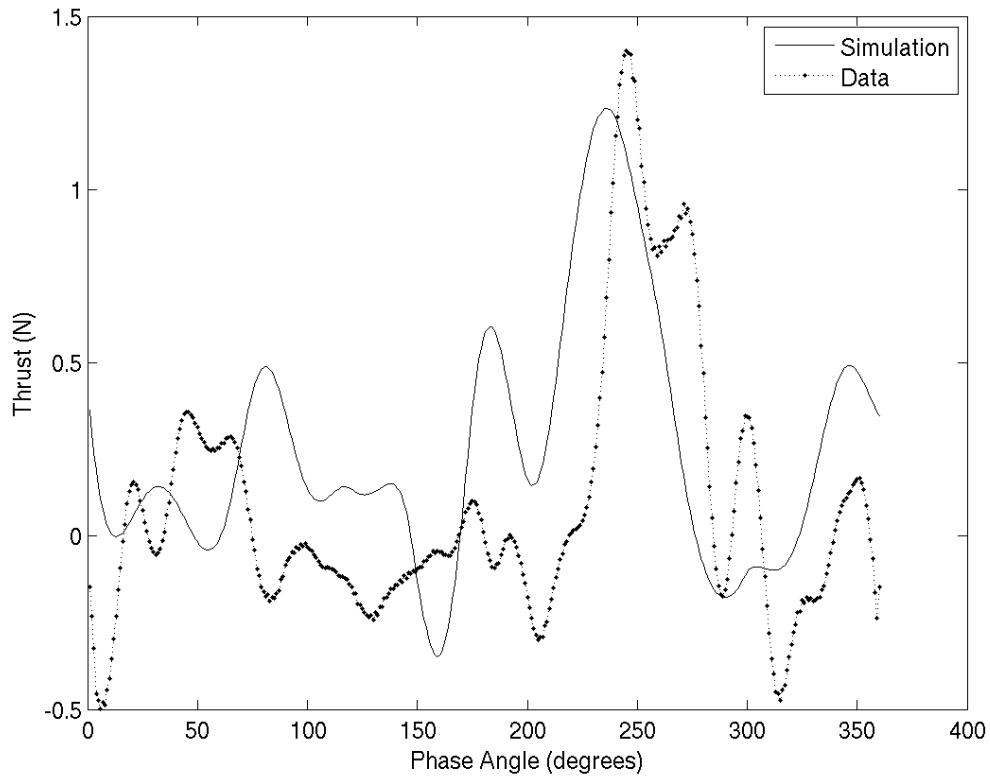


Figure 5.31. Comparison between the measured thrust and predicted thrust at a flapping frequency of 11Hz using the model coefficient's for the flexible wing at an 11.5Hz flapping frequency.

frequency is shown in Figure 5.35, with results for the higher flapping frequencies shown in Figure 5.36. When the coefficients for the 11.5Hz flapping case were used at other flapping frequencies it a comparable error down to a flapping frequency of about 8Hz.

### 5.5.3 Drumhead Wing

The drumhead wing provided an opportunity to study the response of the flapping wing thrust with high frequency motion inputs. These inputs are shown for a

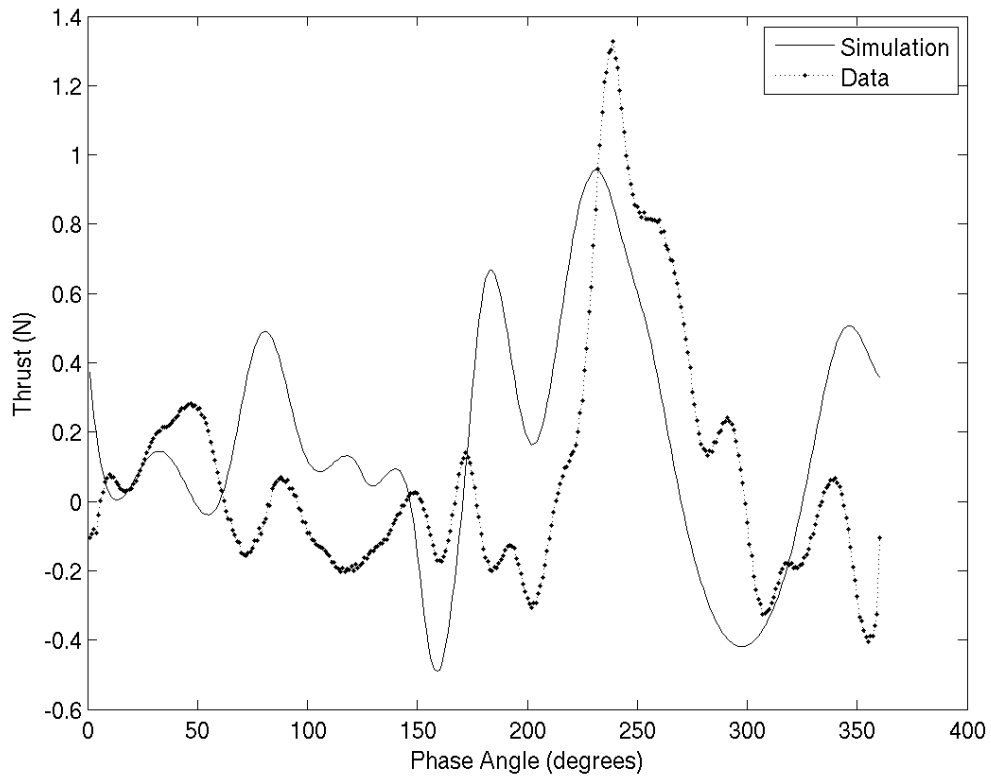


Figure 5.32. Comparison between the measured thrust and predicted thrust at a flapping frequency of 10Hz using the model coefficient's for the flexible wing at an 11.5Hz flapping frequency.

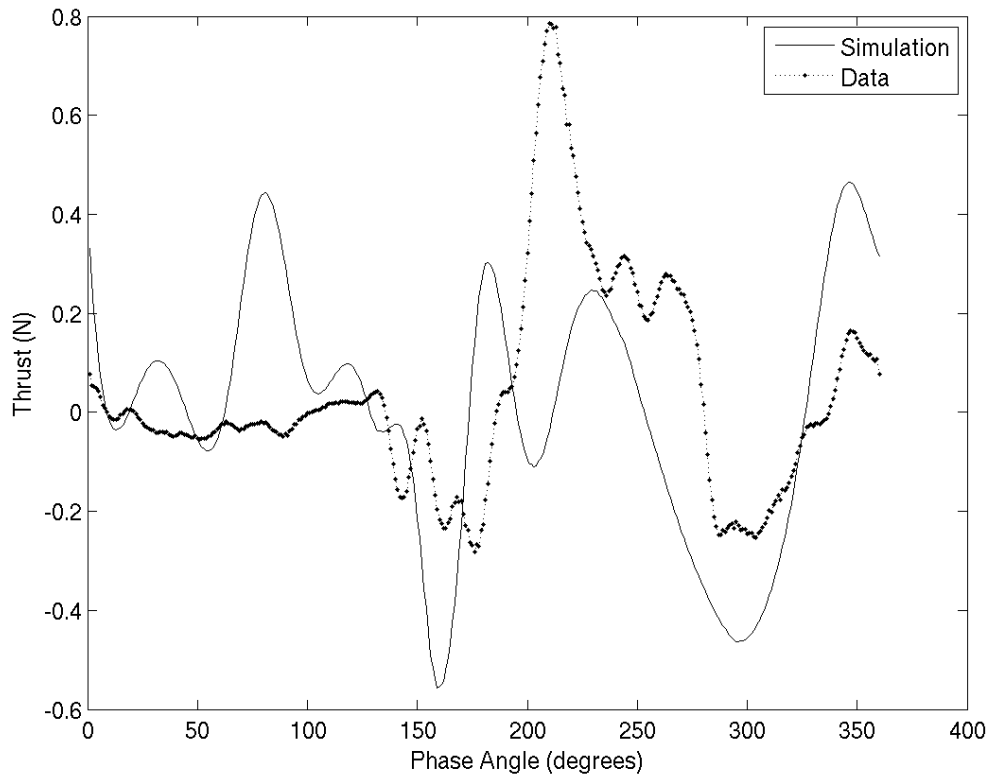


Figure 5.33. Comparison of measured thrust and predicted thrust at a flapping frequency of 8.5Hz using the model coefficients for the flexible wing at an 11.5Hz flapping frequency.

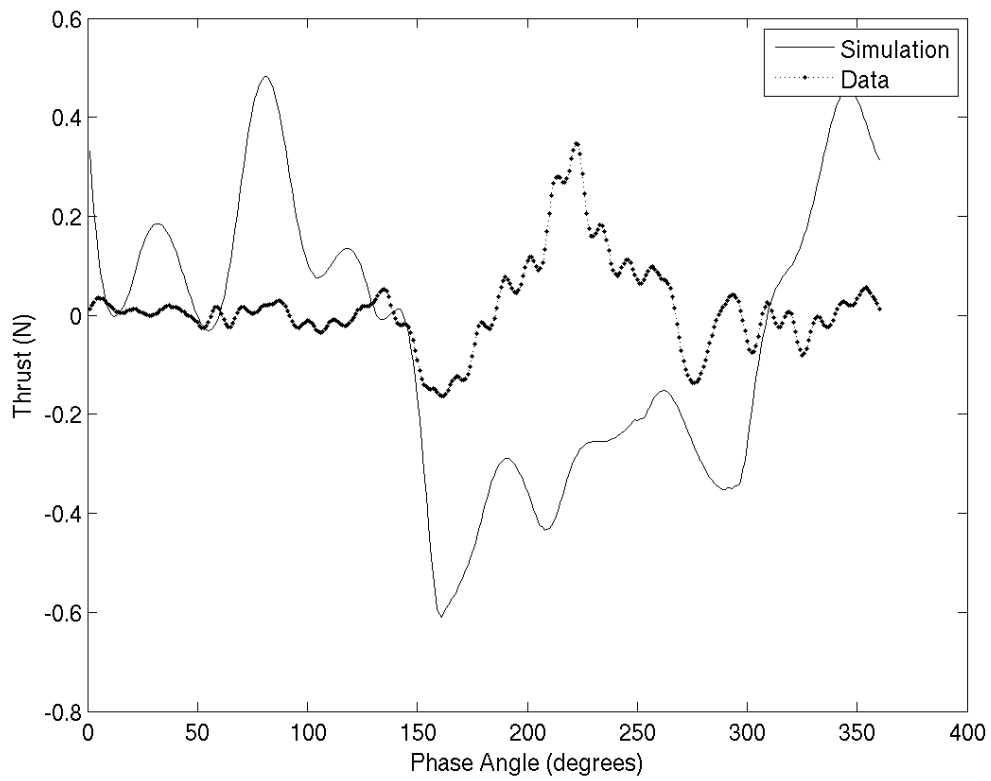


Figure 5.34. Comparison of measured thrust and predicted thrust at flapping frequency of 6Hz using the model coefficients for the flexible wing at an 11.5Hz flapping frequency.

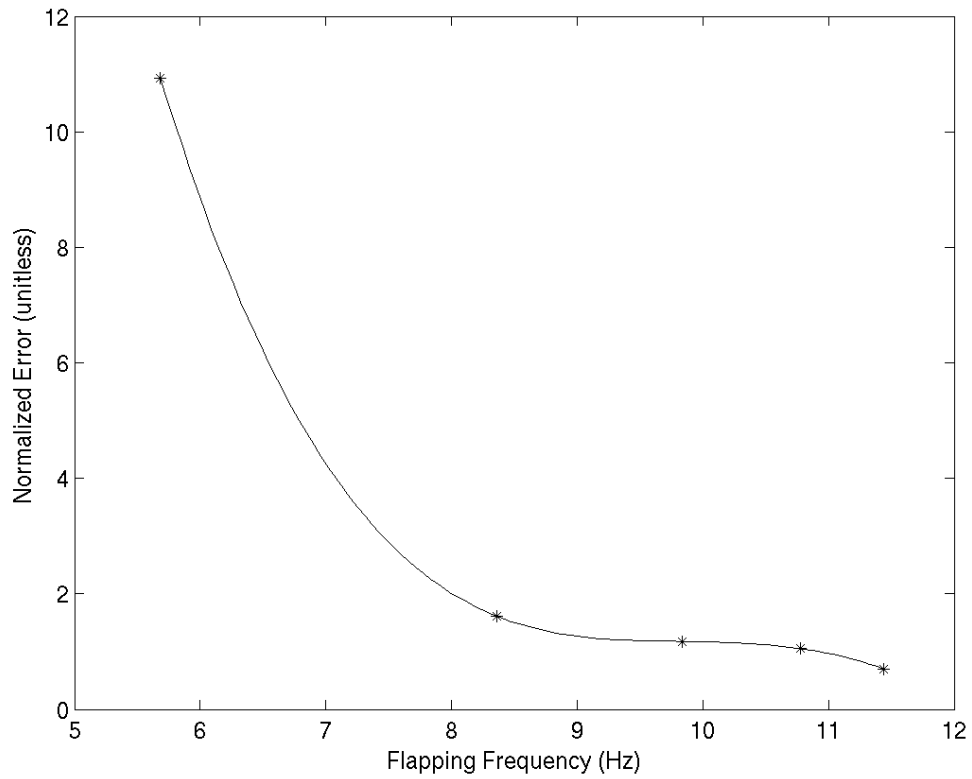


Figure 5.35. Normalized mean-squared error in the model estimate of the thrust for the flexible wing obtained using the 11.5Hz flapping model coefficients for conditions at the other flapping frequencies.

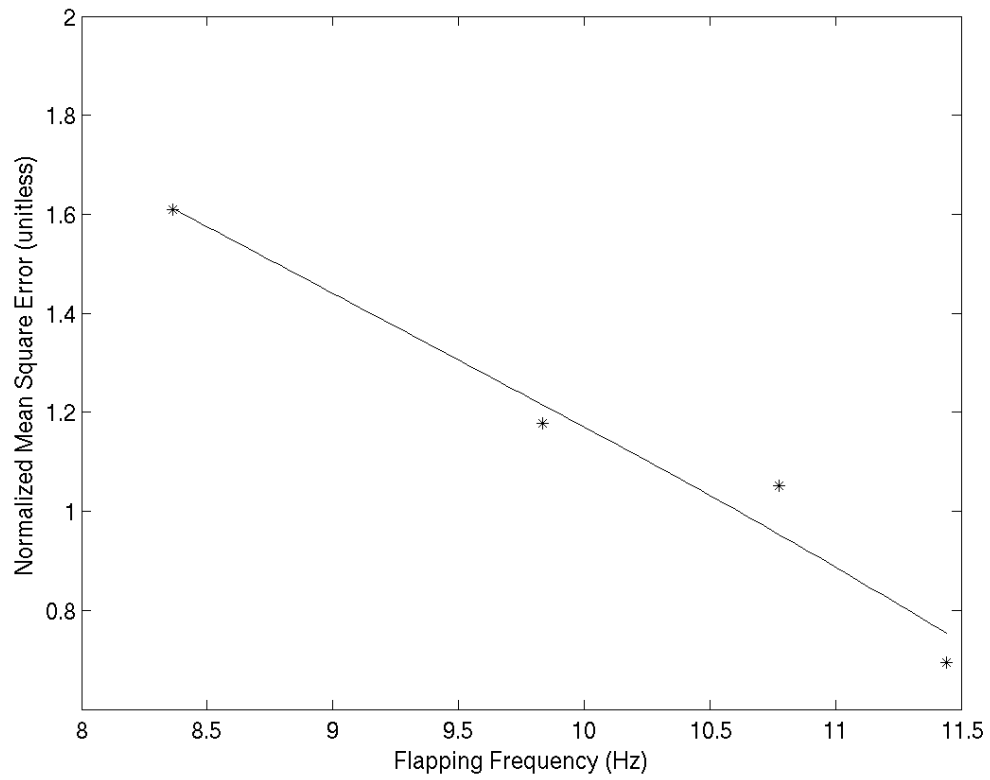


Figure 5.36. Plot of the data presented in Figure 5.35 above 8Hz.

flapping frequency of 11Hz in Figures 5.37 and 5.38. Using these input time series, the output from the model is compared to the experimental thrust in Figure 5.39. In this case, the thrust model prediction is satisfactory although the thrust peak at the down-stroke of the flapping is broader than exhibited in the experimental data series.

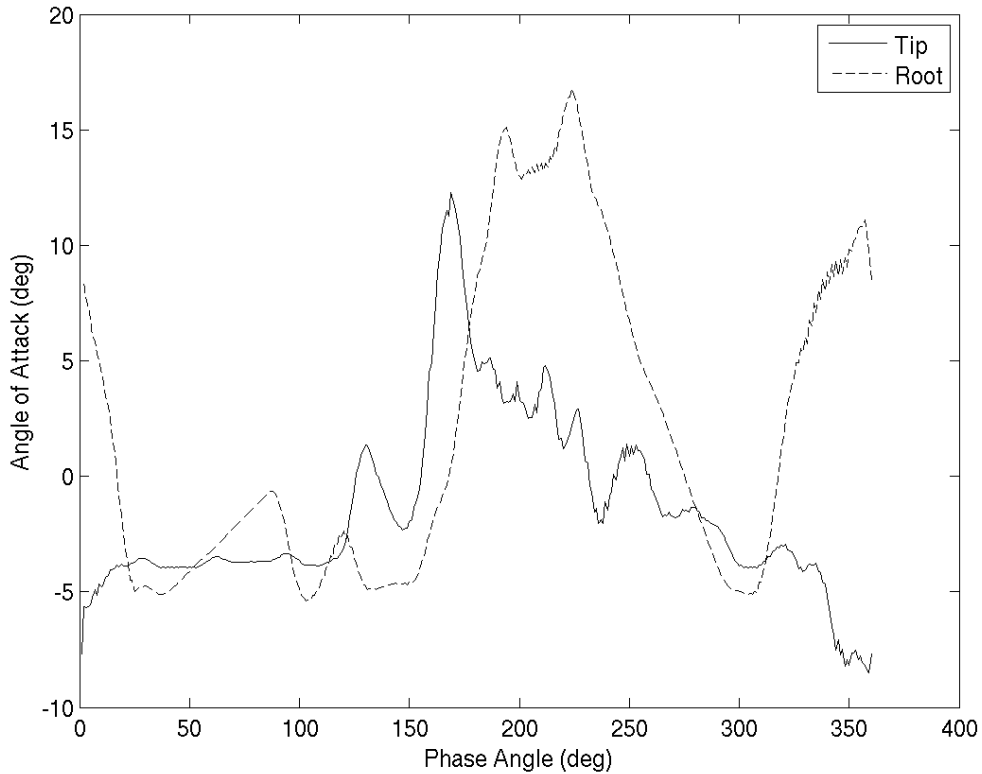


Figure 5.37. Estimates of  $\alpha$  for the drumhead wing at an 11Hz flapping frequency.

At lower flapping frequencies the wing motion is somewhat less erratic. This is illustrated in Figures 5.40 and 5.38, which shows the angle of attack and plunge rate time series for the wing at an 10.5Hz flapping frequency. The model thrust prediction for this input is shown in Figures 5.42. This indicates a significant improvement in

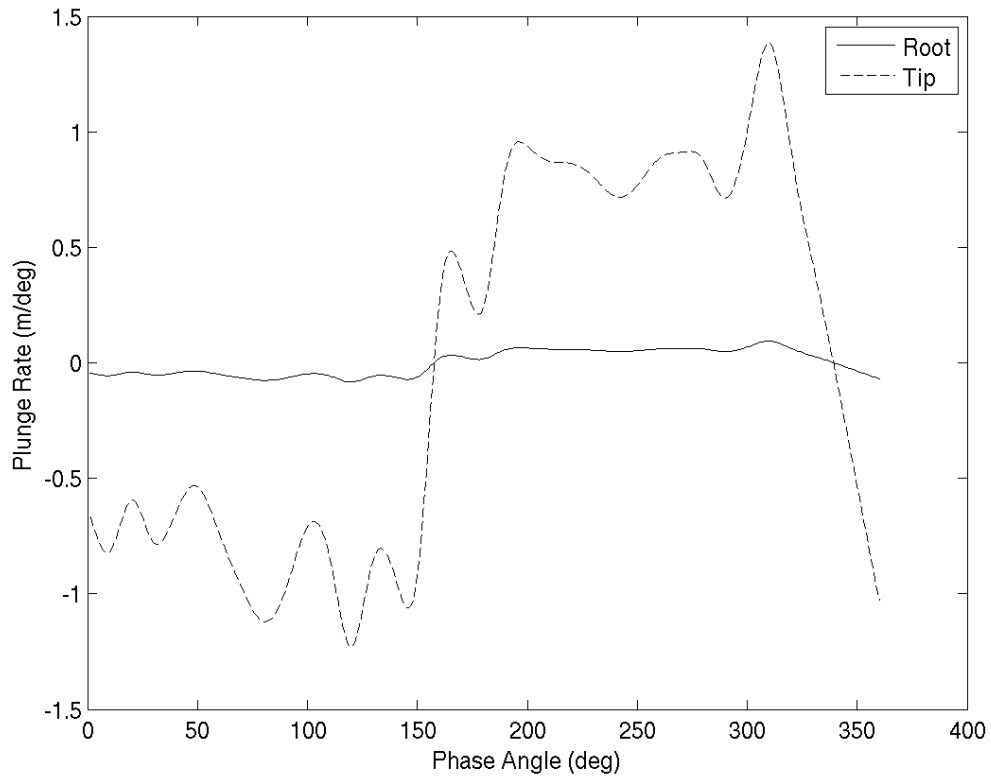


Figure 5.38. Estimates of  $\dot{h}$  for the drumhead wing at an 11Hz flapping frequency.

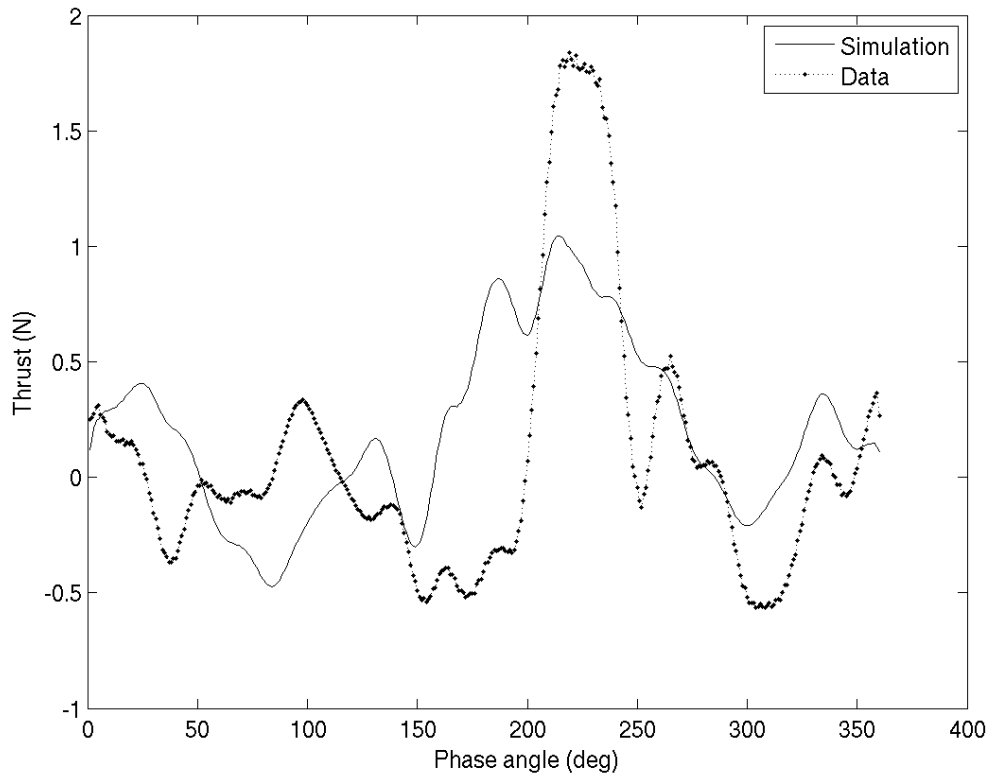


Figure 5.39. Comparison between the linear model output thrust,  $T(t)$ , and the measured thrust for the drumhead wing at a flapping frequency of 11Hz.

the model thrust estimate. A comparison of the model and experimental thrust time series for flapping frequencies of 8.5Hz and 6Hz are shown in Figures 5.44 and 5.45. The agreement is good at an 8.5Hz, but not as good at a 6Hz. This is confirmed by the normalized mean squared prediction error for each of these cases that is shown in Figure 5.46.

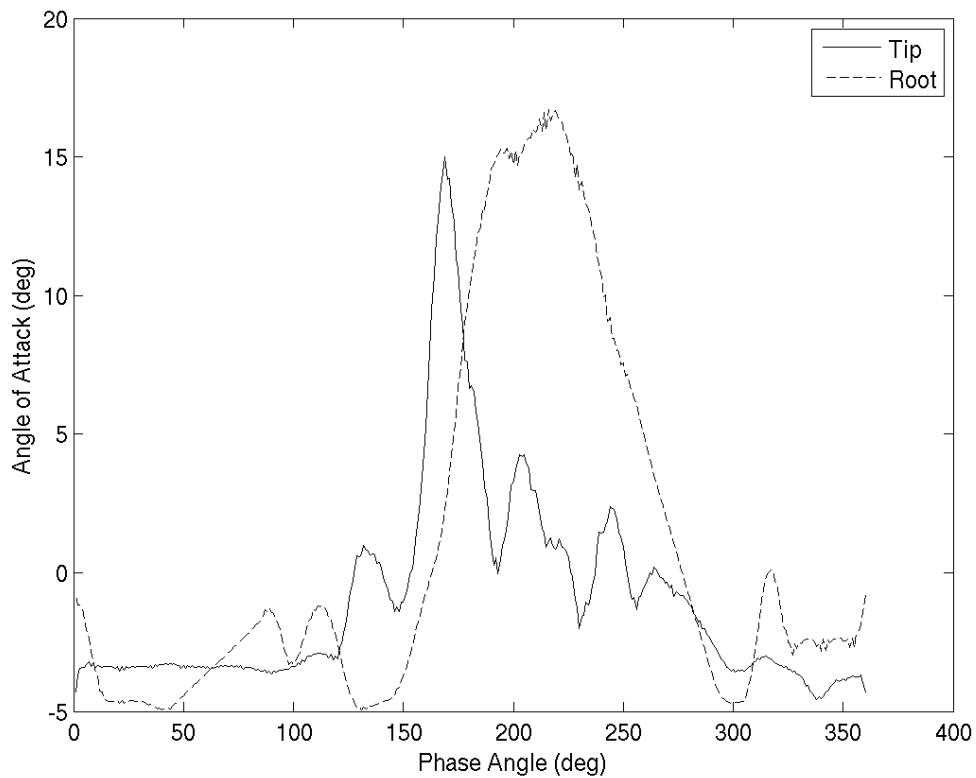


Figure 5.40. Estimate of  $\alpha$  for the drumhead wing at a flapping frequency of 10.5Hz.

## 5.6 Model trend analysis

Qualitatively, this approach captures the dominant features and phasing of the measured thrust. The utility and physicality of this approach, however, depends on

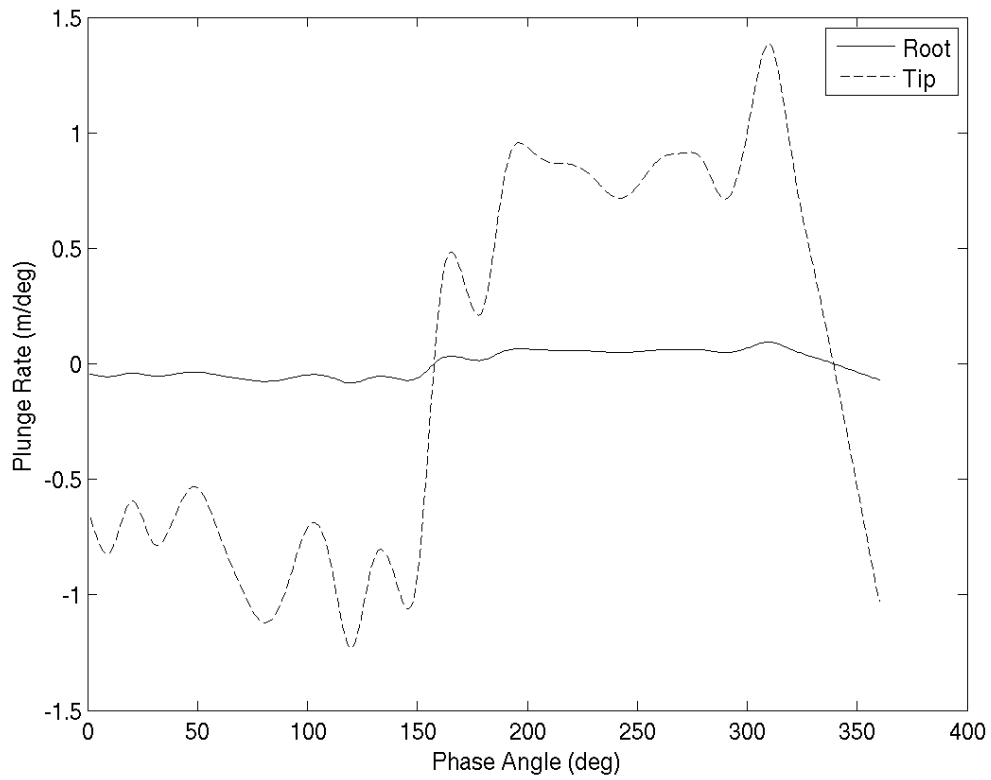


Figure 5.41. Estimate of  $\dot{h}(t)$  for the drumhead wing at a flapping frequency of 10.5Hz.

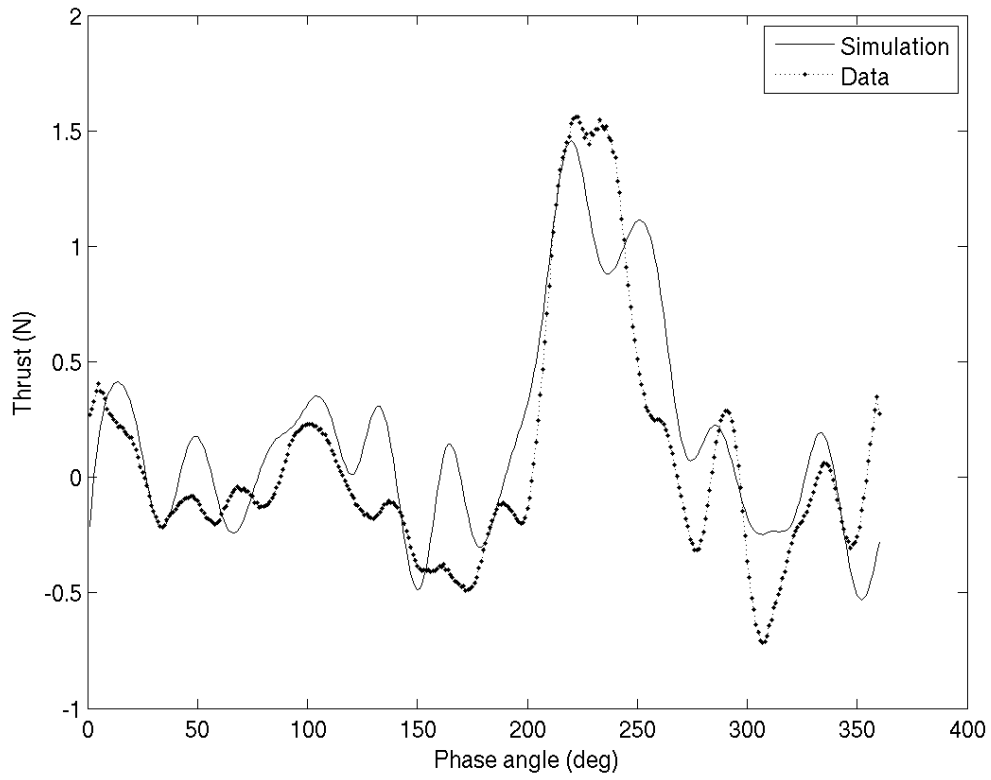


Figure 5.42. Comparison between the linear model and the measured thrust for the drumhead wing at a flapping frequency of 10.5Hz.

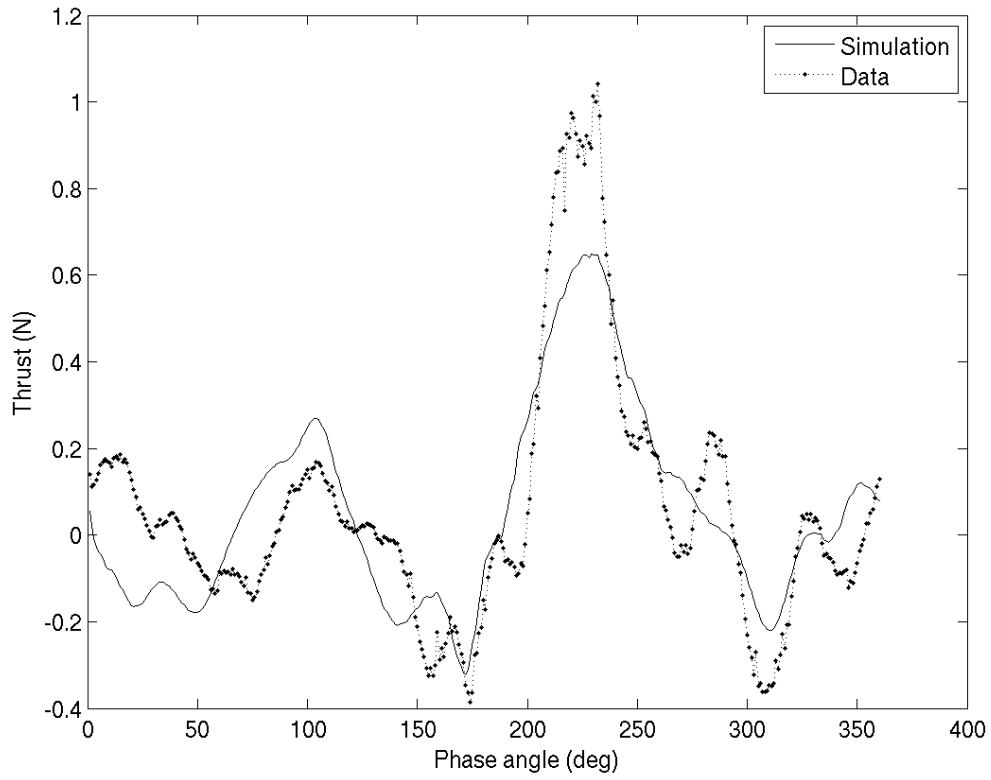


Figure 5.43. Comparison between the linear model and the measured thrust for the drumhead wing at a flapping frequency of 9.5Hz.

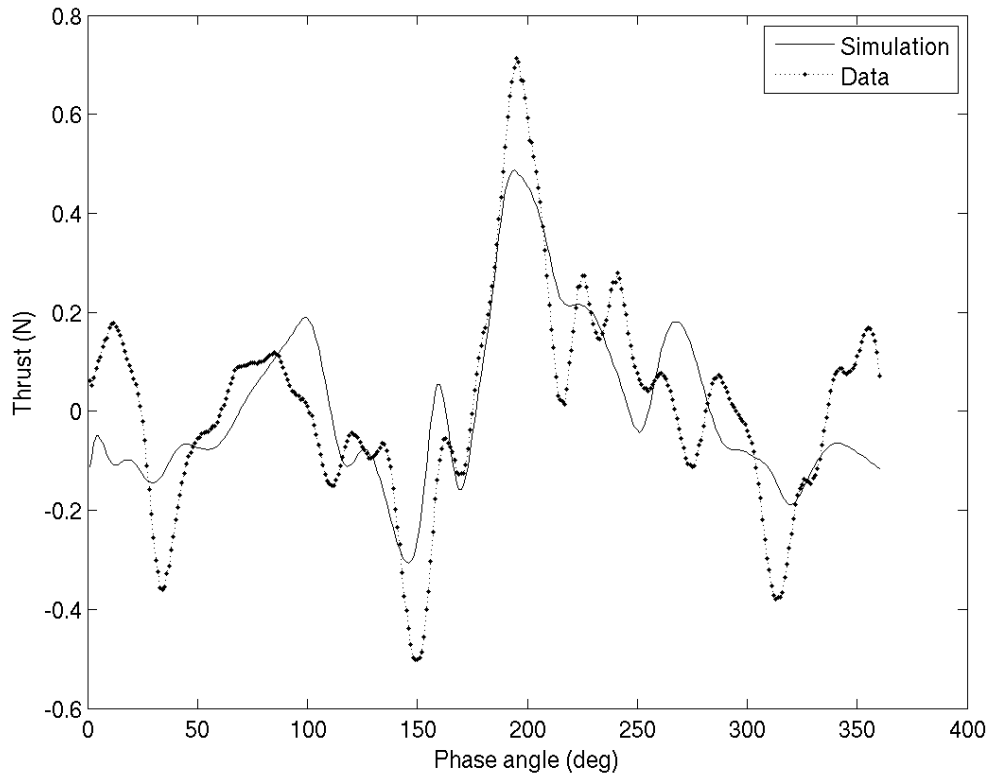


Figure 5.44. Comparison between the linear model and the measured thrust for the drumhead wing at a flapping frequency of 8.5Hz.

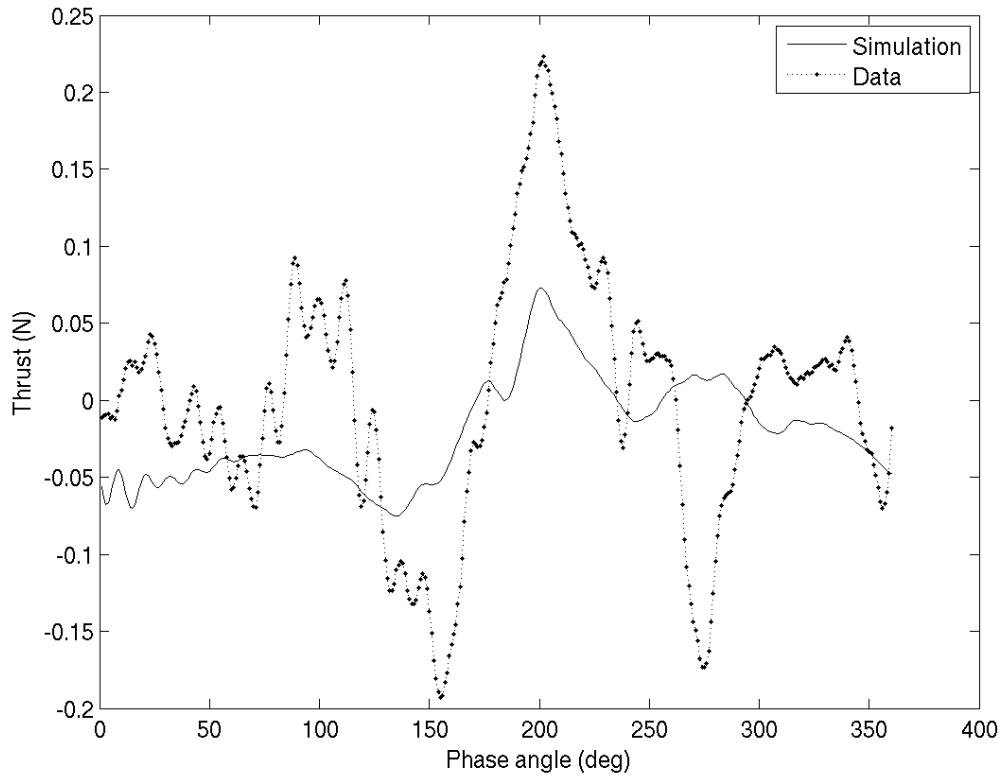


Figure 5.45. Comparison between the linear model and the measured thrust for the drumhead wing at a flapping frequency of 6Hz.

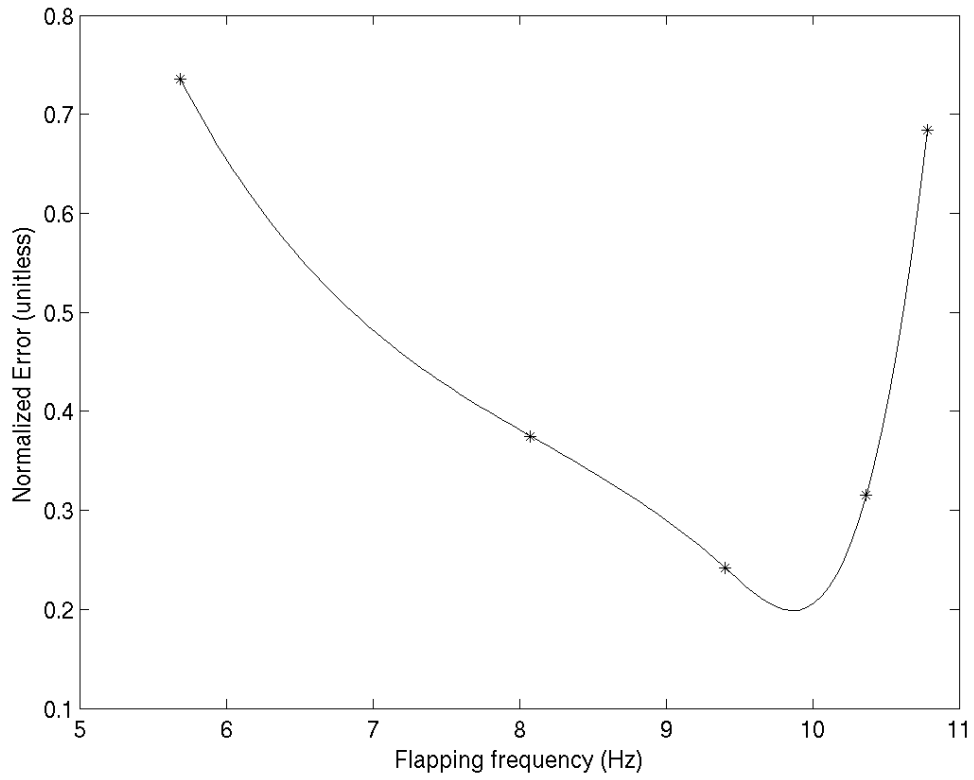


Figure 5.46. Normalized mean square error in the estimate of the thrust for the drumhead wing as a function of flapping frequency.

the ability of the linear model to capture trends in the mean and peak thrust. Figure 5.47 shows the expected power law relationship between the flapping frequency and average thrust reported in Zdunich *et al.* [70], Wu *et al.* [67], and for the stiff, flexible and drumhead wings.

### 5.6.1 Stiff wing

The stiff wing models did a poor job of capturing the trend in mean thrust with changing flapping frequency, however it did a good job of capturing the physical scaling trend of the maximum thrust. This is shown in Figure 5.48 for the mean thrust and Figure 5.50 for the maximum thrust. Figure 5.49 shows that the estimated mean thrust does not follow the power law observed in the experiment. However, Figure 5.51 shows that the maximum thrust does follow the square of the flapping frequency. The correct physical scaling of the maximum thrust was expected, given that stiff wing had the lowest mean squared error in its force prediction. This suggests that a linear model captures the unsteady component of the thrust very well, but must be coupled with a nonlinear function to determine the mean thrust. A block diagram of this approach is shown in Figure 5.52, where  $\hat{T}$  represents the zero-mean unsteady thrust component and  $\bar{T}$  represents the mean thrust.

### 5.6.2 Flexible wing

Despite having significantly larger mean square error when computing the unsteady thrust, this approach captures the physical scaling trends of the flexible wing experimental data quite well. The mean thrust appears to follow the scaling law of observed in the experiment as shown in Figure 5.53. A log-log plot suggests that the estimated mean thrust actually increases slight faster than the cube of the flapping frequency, as shown in Figure 5.54. The maximum thrust appears to be following a

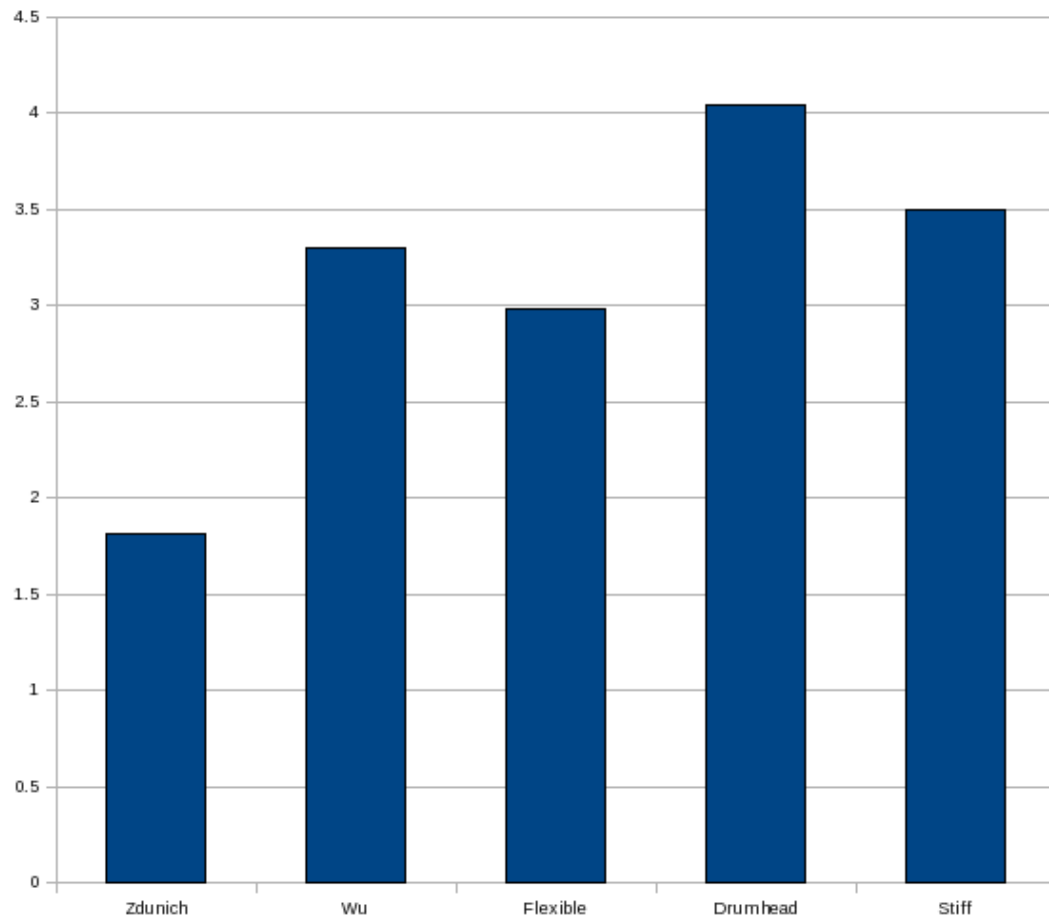


Figure 5.47. Histogram of power law relationship observed between mean thrust and flapping frequency in Zdunich *et al.* [70], Wu *et al.* [67] and the wings used in this study.

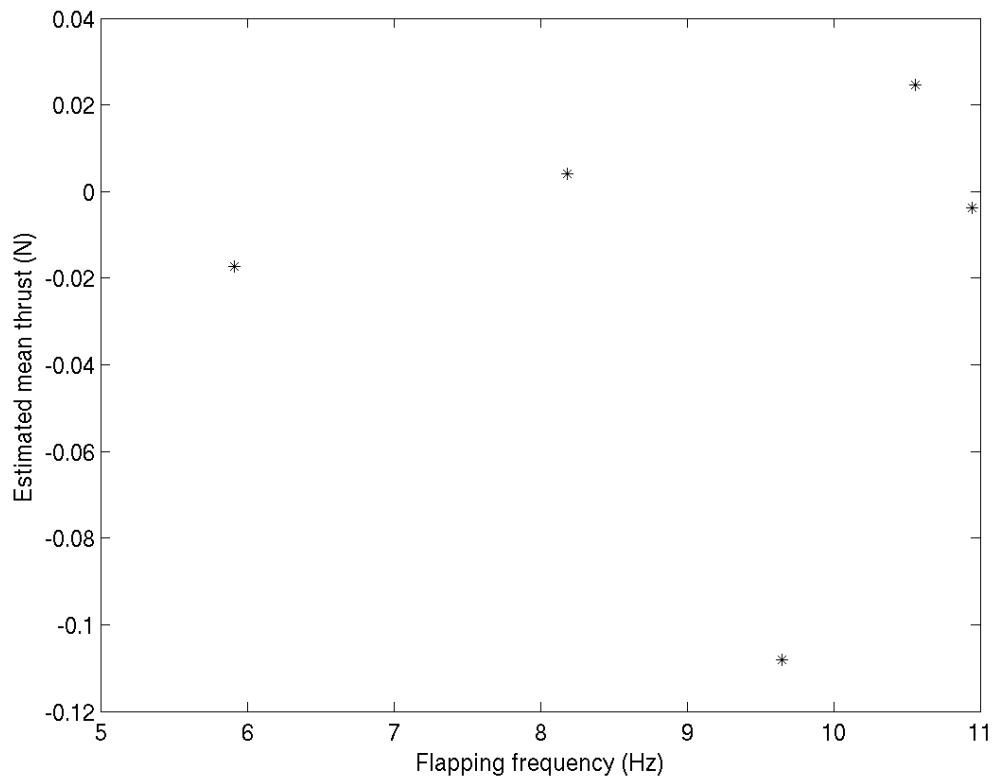


Figure 5.48. Plot of the model estimate of mean thrust for the stiff wing.

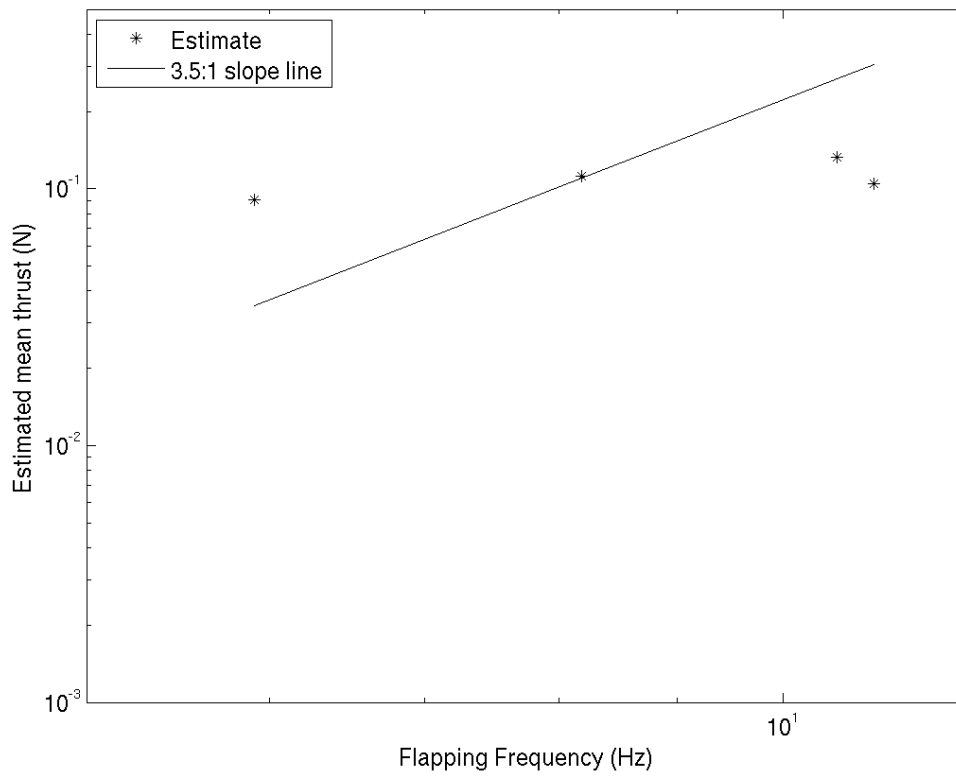


Figure 5.49. Log-log plot of the mean thrust presented in Figure 5.48 after a constant was added to each point to make the minimum value  $10^{-6}$ .

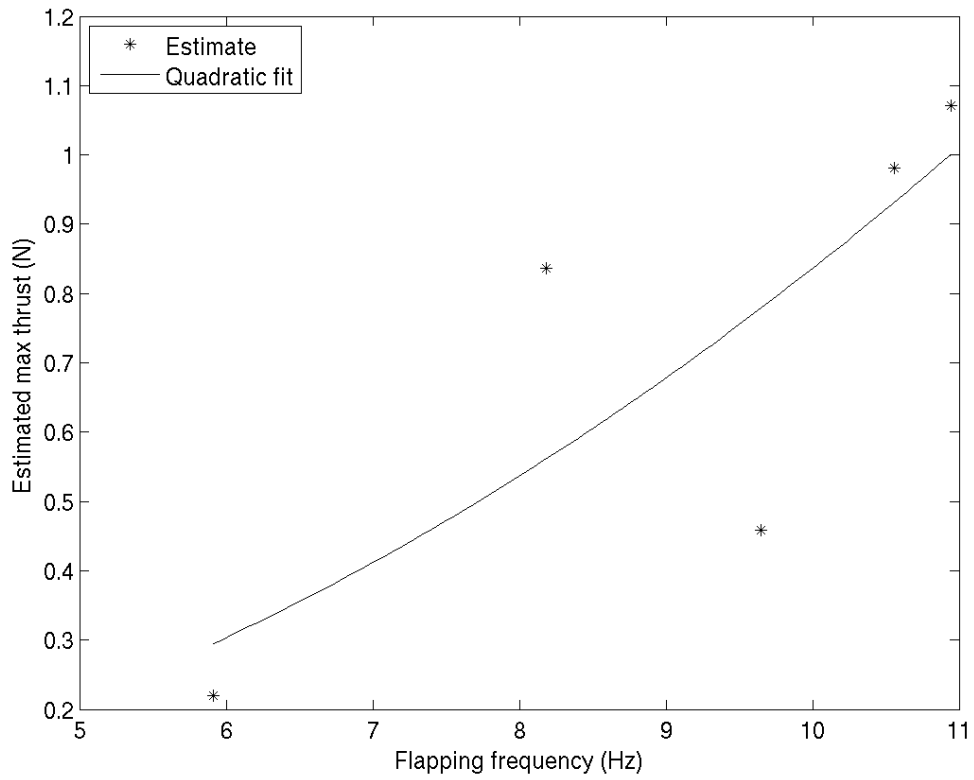


Figure 5.50. Plot of the model estimate of maximum thrust for the stiff wing.

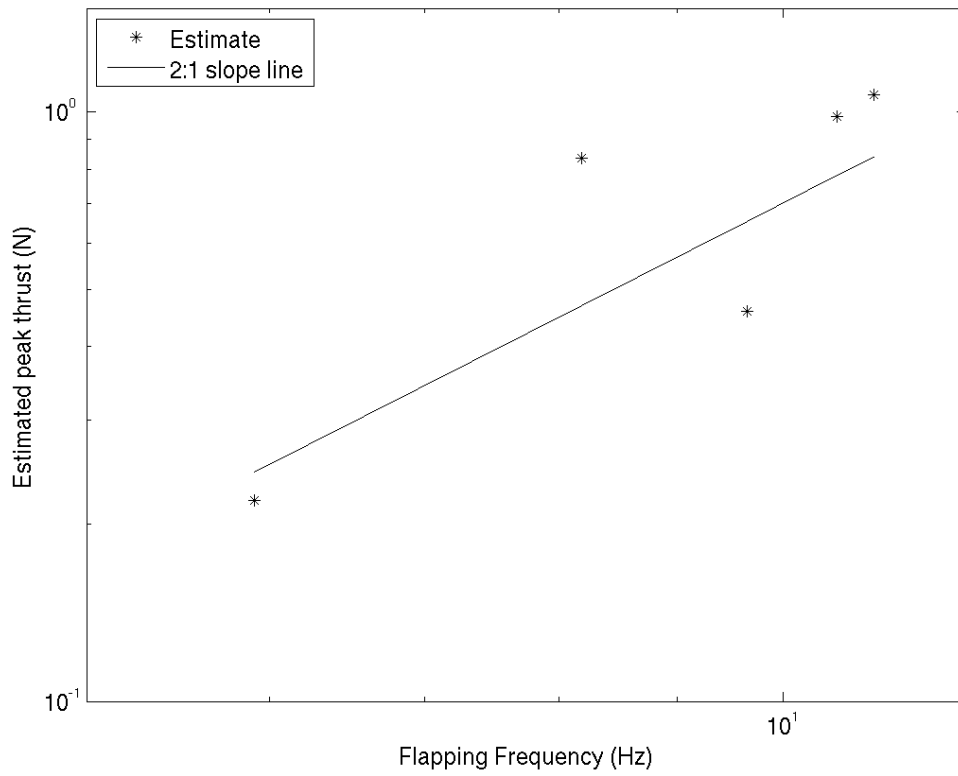


Figure 5.51. Log-log plot of the maximum thrust presented in Figure 5.50

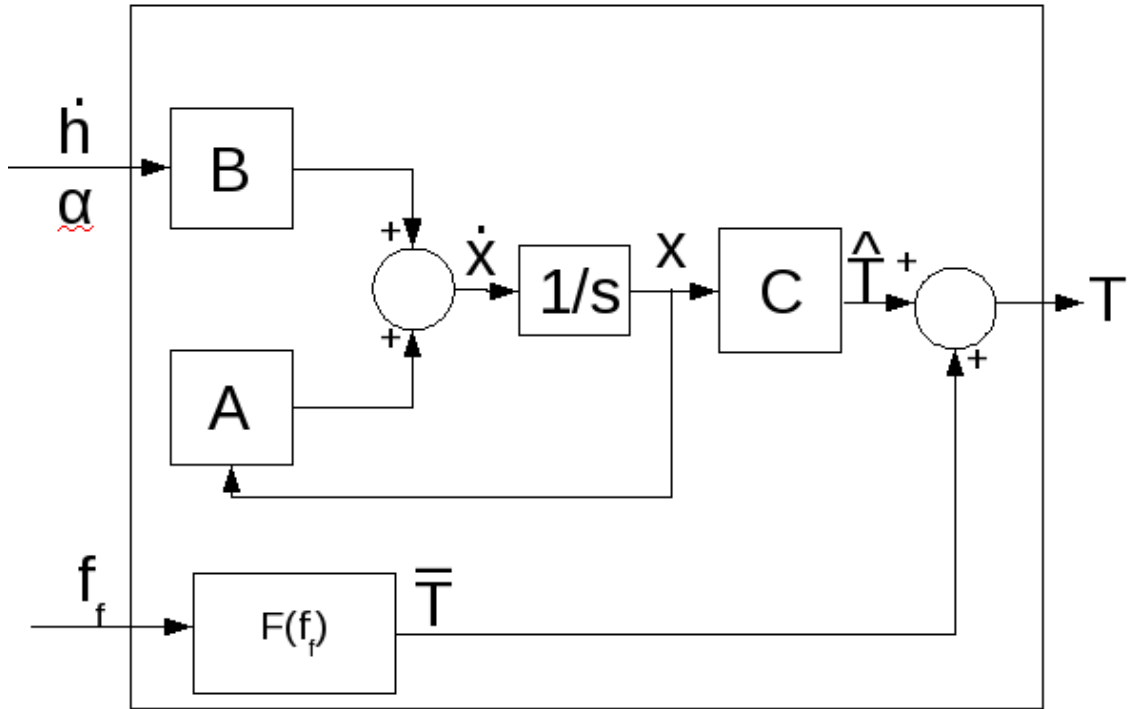


Figure 5.52. Block diagram showing a decoupled mean,  $\bar{T}$ , and unsteady,  $\hat{T}$ , thrust model.

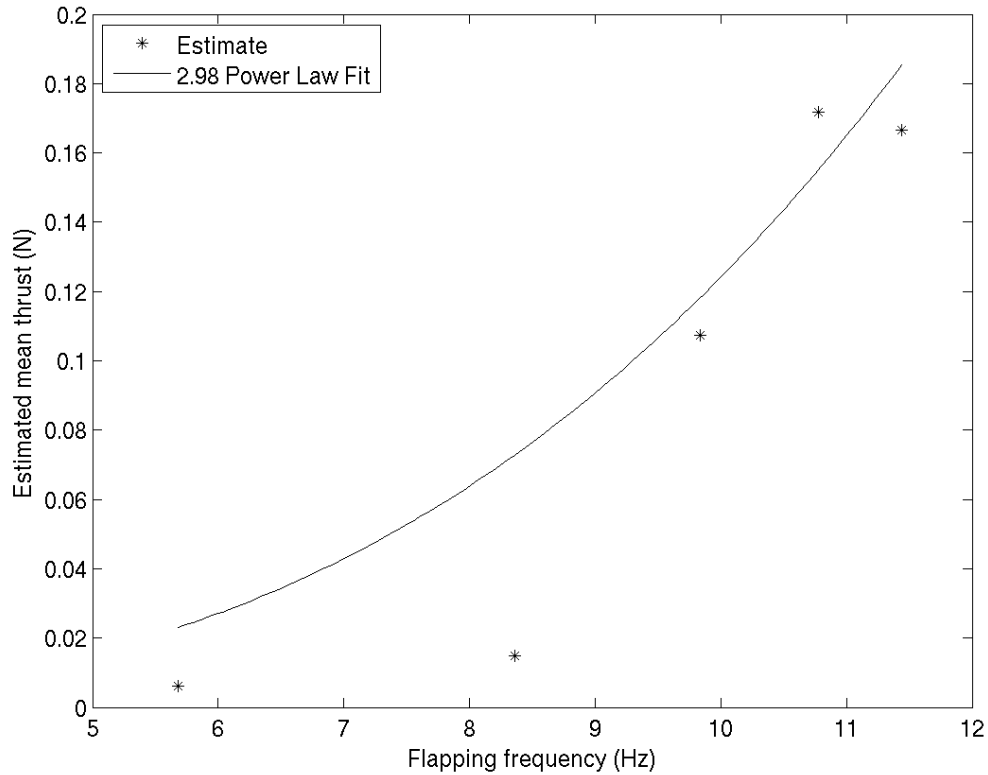


Figure 5.53. Plot of the model estimate of mean thrust for the flexible wing.

quadratic trend, as is the case with the physical wing. This is shown in Figure 5.55 and as a log-log plot in Figure 5.56.

These results and those for the stiff wing suggest that there is a threshold value of the ratio between maximum and average thrust that allows the linear model to capture the physical scaling trends. Data collected for the stiff wing, with a maximum thrust of 2N and mean thrust of .05N, suggest that a value of 40 is too large. The flexible wing data, with maximum thrust 1.5N and mean thrust of .12N suggest that a ratio of 12.5 is acceptable. These data also suggest that there is a trade-off between accuracy of the trends and the mean squared error as a function of this ratio.

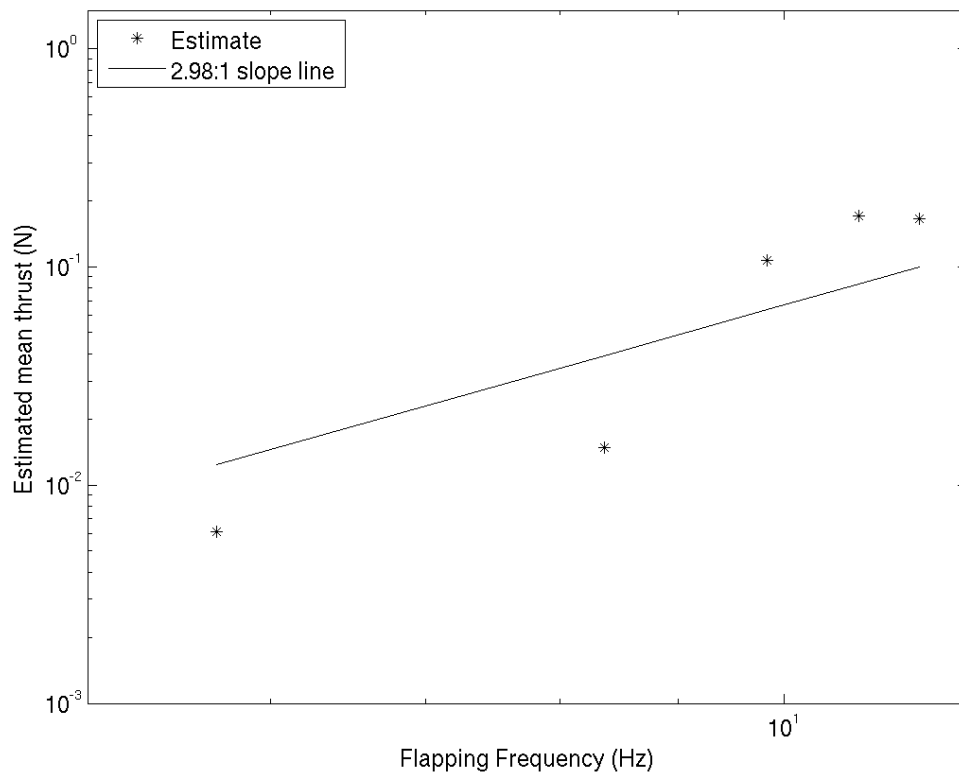


Figure 5.54. Log-log plot of the mean thrust presented in Figure 5.53.

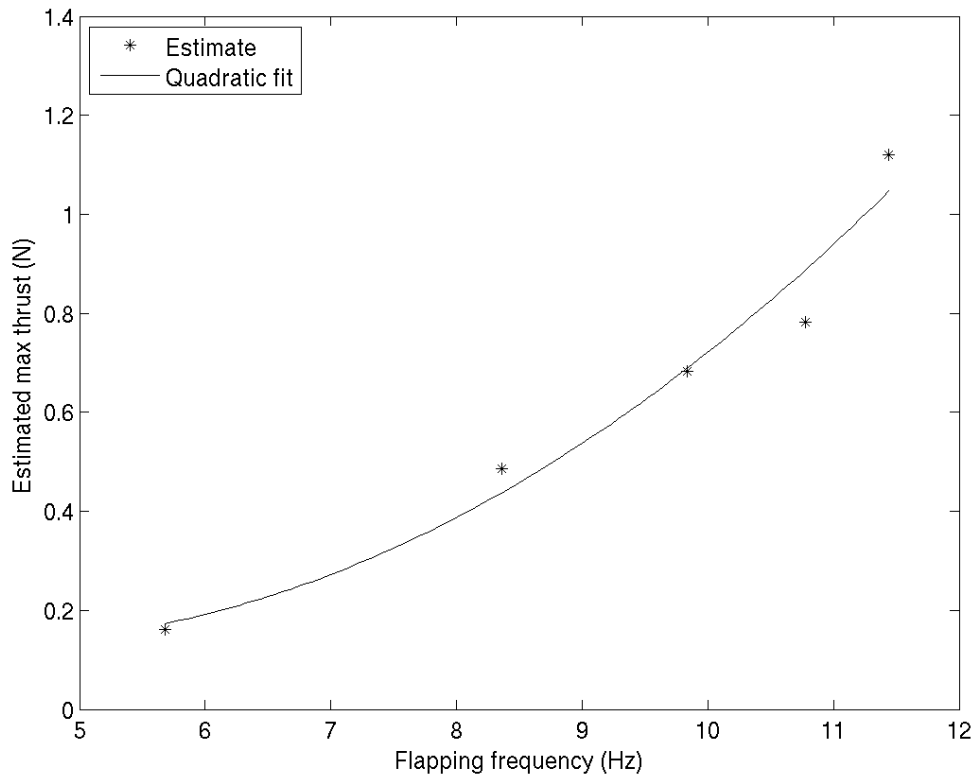


Figure 5.55. Plot of the model estimate of maximum thrust for the flexible wing.

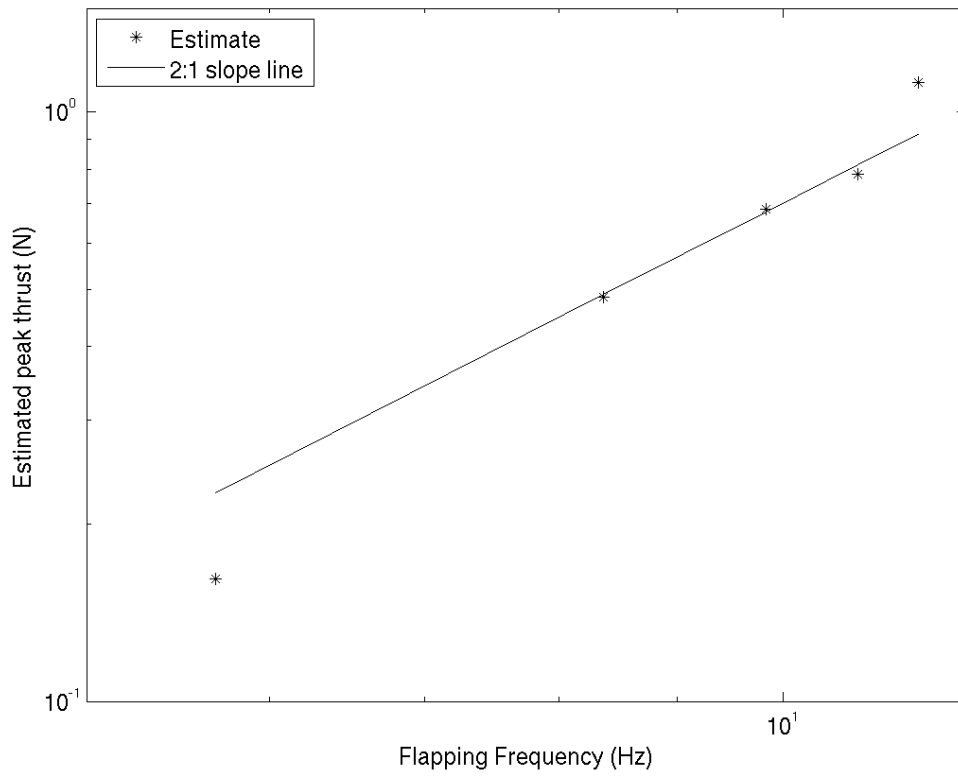


Figure 5.56. Log-log plot of the maximum thrust presented in Figure 5.55

### 5.6.3 Drumhead wing

The drumhead wing had a mean thrust of  $.11N$  and a maximum thrust of  $2.7N$ . This corresponds to a ratio of 24.5. The mean thrust does appear to follow the correct cubic scaling trend in Figure 5.57. Figure 5.59 indicates that the mean thrust is increasing with the scaling law observed for the drumhead wing. Additionally, the maximum thrust plotted in Figure 5.59 does generally follow a quadratic trend, but with more scatter than for the flexible wing. This trend can be seen more clearly as a log-log plot as shown in Figure 5.60.

These results, together with the other wings, suggest that the ratio between maximum and mean thrust provides a good indicator of how well linear models will capture physically important trends. For the flexible wing and drumhead wing the model scaled reasonably well with flapping frequency. The model for the stiff wing, however, did not scale well. As a result, a more complicated model that separates the mean and dynamic effects is required.

## 5.7 Chapter discussion

Several interesting conclusions came from this analysis:

1. The stiff wing, with its relatively separate structure and aerodynamics, was the most easily and reliably modeled over the range of flapping frequencies examined.
2. Linear models consistently under predicted the peak thrust, implying that the dynamic stall leading to maximum thrust is an inherently nonlinear process.
3. The model developed at the highest flapping frequency examined for the flexible wing more accurately captured the behavior at lower flapping frequencies.
4. The thrust generation appeared to be band-limited since high frequency motion of the drumhead wing did not translate into the thrust time series.
5. The ratio between the maximum and mean thrust provides a good indicator of how well a linear model will capture physical trends. In general, the smaller the ratio the better the physical trends are matched.

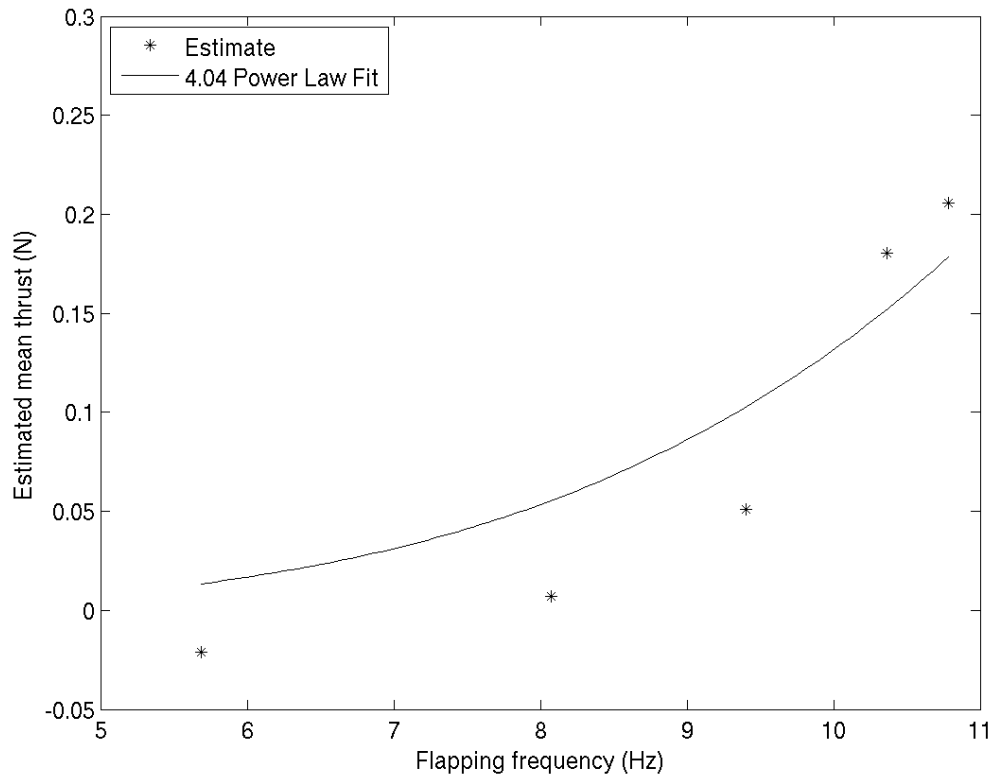


Figure 5.57. Plot of the model estimate of mean thrust for the drumhead wing.

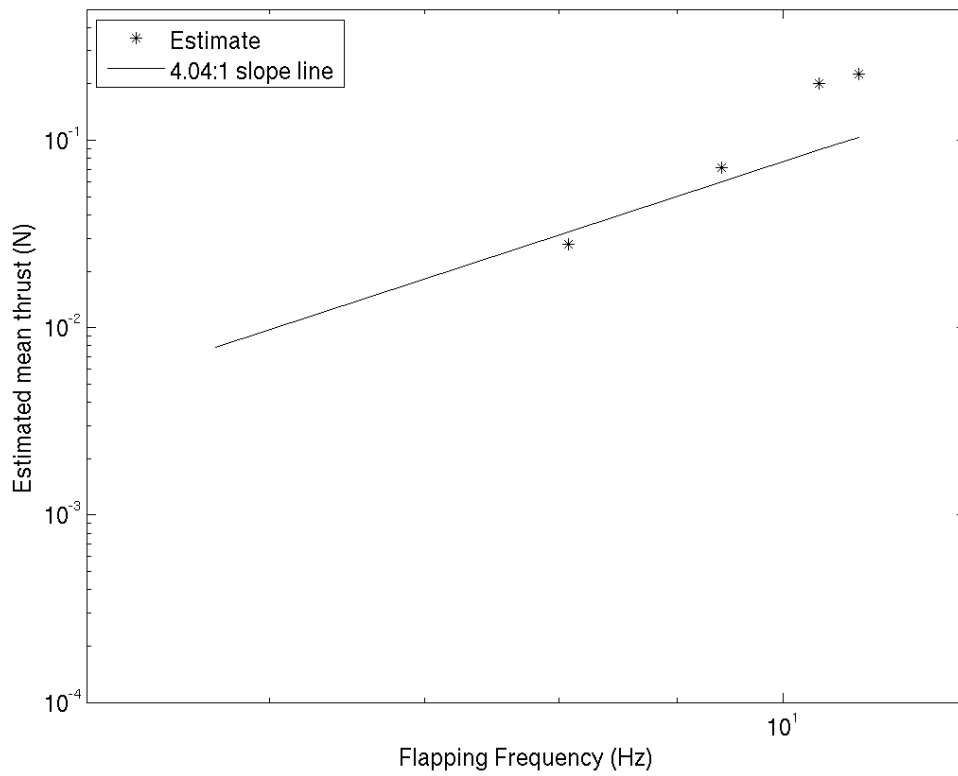


Figure 5.58. Log-log plot of the mean thrust presented in Figure 5.57 after a constant was added to each point to make the minimum value  $10^{-6}$ .

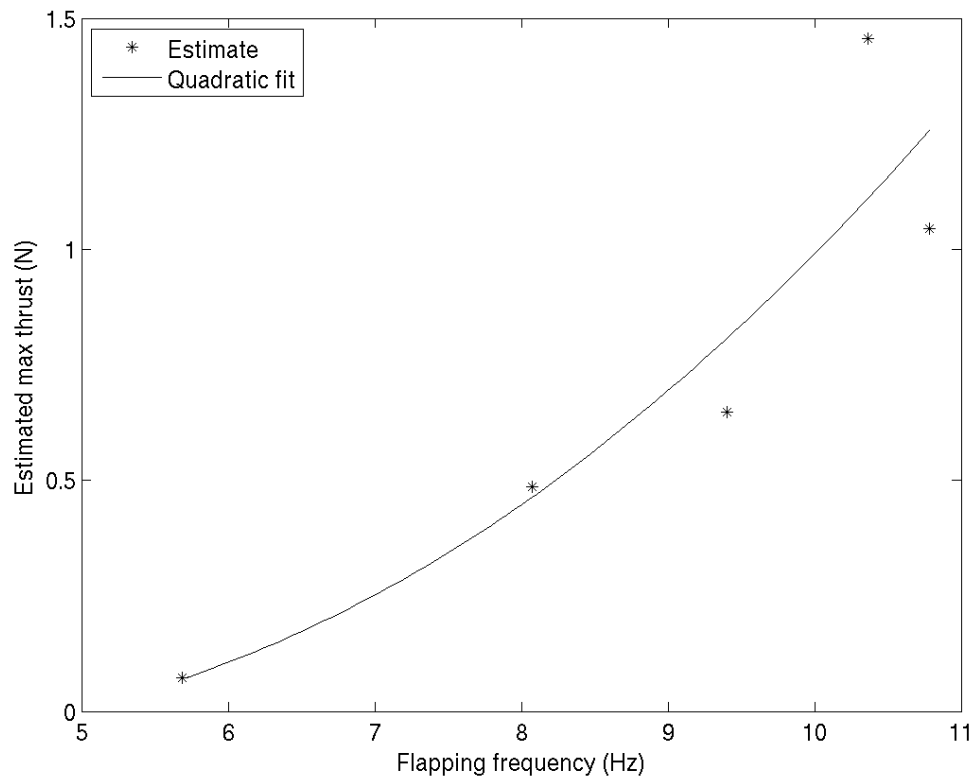


Figure 5.59. Plot of the model estimate of maximum thrust for the drumhead wing.

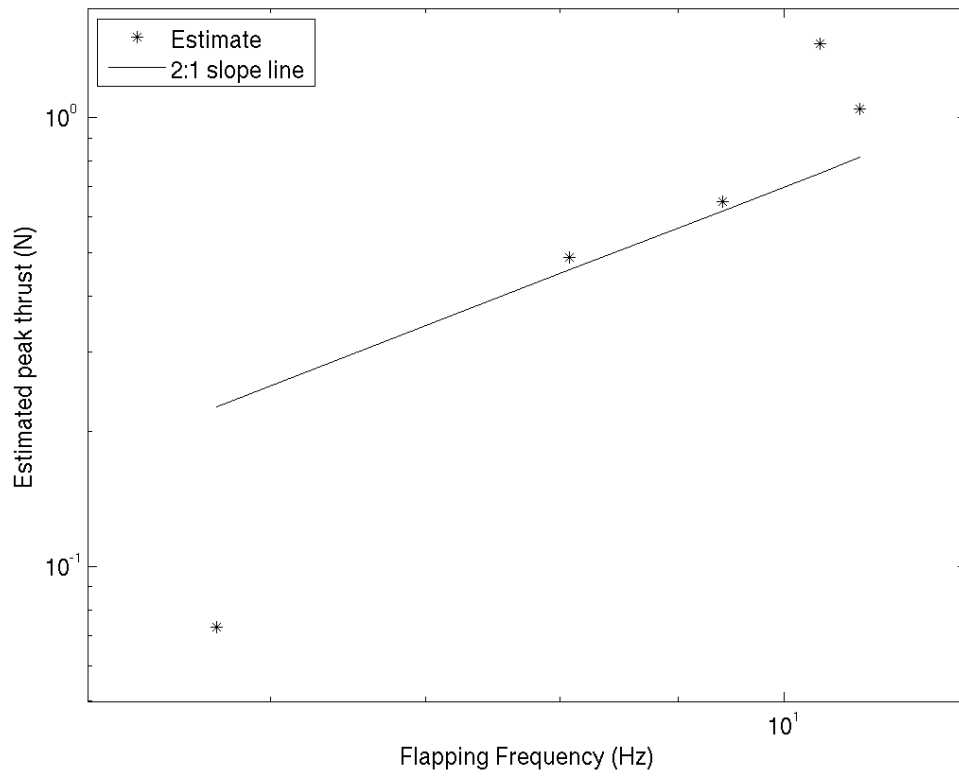


Figure 5.60. Log-log plot of the maximum thrust presented in Figure 5.59

This analysis demonstrated that for fairly stiff root-flapped wings, an approximate linear model could capture the unsteady behavior of the thrust cycle based on simple flapping wing inputs. If coupled with a nonlinear function to provide the mean thrust as a function of flapping frequency, these models are accurate enough for flight dynamics simulations.

For more flexible wings, the linear model performed reasonably well in capturing the unsteady behavior and trends in mean thrust. It appears that the ratio between maximum and mean thrust determines how well the physical trends are captured, with the best results seen at the lowest value tested.

These results suggest that sensors in the wings would probably work to provide a real-time indication of the thrust production as proposed by this author in [5] and [6].

## CHAPTER 6

### Conclusion and Future Work

#### 6.1 Conclusions

Returning to the open questions at the end of Chapter 1, it is now possible to provide answers.

Question 1: What are properties of the time-resolved thrust generated by mechanical flapping wings in air?

The thrust produced by flapping wings is closely correlated with the flapping wing phase angle when any oscillations in the structure occur at a much higher rate than the flapping frequency. The average thrust grows with a power law relationship to the flapping frequency between 2.98 and 4.04 for the cases studied. The maximum thrust grows with the square of the tip speed, consistent with other vorticity-dominated flows such as propellers and helicopter rotors.

The phase resolved thrust curve for the cases studied is characterized by a large thrust peak, small negative thrust region and small amplitude oscillations over the rest of the phase. The large thrust peak always occurs after the beginning of the downstroke, before the wing reaches its greatest linear speed, implying that this effect is driven by a dynamic stall vortex. The negative thrust occurred shortly before the peak thrust, as the wing transitioned from the upstroke to the downstroke. The oscillations through the rest of the flapping cycle do not correlate with the

structure motion, and so likely indicate the shedding of smaller vortices during the transition from the initial motion and towards a quasi-steady flow.

Question 2: What effect does changing the wing structure, and hence motion of the wing, have on thrust generation?

This study investigated three wing structures with different properties. The first was a relatively stiff wing that deflected smoothly in response to the acceleration loads imposed during each flapping period. The magnitude of the deflection was constant above a flapping frequency of 9Hz, resulting in phase-resolved thrust curves that looked very similar and a peak thrust that grew with the square of the flapping frequency. The lift generation process was well approximated by a linear model based on the measured deflection.

The flexible wing appeared to respond significantly to the aerodynamic loads acting on it. The peak thrust reached a maximum at a flapping frequency of 10Hz, although the mean thrust continued to grow with flapping frequency. This is likely due to the fact that the wing moved to a smaller “angle of attack” relative to the flapping plane as the linear speed of the wing increased. This weakened the dynamic stall vortex effect, but it allowed for more fully attached flow during the transition from dynamic stall to quasi-steady flow. The result was that this wing had the largest average thrust of the three cases tested. However, because of the strong effect of the fluid on the structure in this case, it was difficult to establish a linear relationship between the motion of the wing and the thrust.

The drumhead wing demonstrated that the thrust generation process is inherently band limited. It exhibited multiple sharp motions during the flapping cycle, and had the largest maximum thrust of the three cases tested. However, this extra motion did not translate into a larger average thrust. This wing appeared to reach a maximum average thrust at 11Hz, although its maximum thrust continued to grow.

Given that much of the thrust is generated by these sharp motions, resulting in a nonlinear dynamic stall behavior at several points in the flapping cycle, it was not possible to fit a linear dynamic model to the the relationship between its motion and thrust.

Question 3: What is the bandwidth and magnitude required of controls, sensors and navigation filters to maintain a stable hover?

For the situation studied in this work, the frequency content of the thrust signal extended to roughly 15 times the flapping frequency for all wings. This defines when the power in the thrust time series dropped below  $-20\text{dB}$ , and suggests that the minimum sampling rate for a state estimator or simulation should be 30 times the flapping frequency. Since this is a phenomenological observation rather than based on a fluid dynamic theory, the most important contribution of this work is that it provides a means of determining these values for any flapping wing system.

The net moment generated by the flapping wings is effectively zero, and in general the flapping period is much shorter than the time required for any maneuver. As a result, the control actuators only need to be as fast as required for other parts of the vehicle's mission.

Question 4: What components must be included in a flapping wing aerodynamics model?

This study has shown that a phenomenological linear model based on the flapping motion and wing deflection provides an adequate model for flight dynamics simulation and controller design in certain cases. When the ratio between the maximum thrust and mean thrust is small, these models capture physical trends in mean and maximum thrust well. At a ratio of 40, no physical trends are observed, despite very low mean squared error. Going from 24.5 to 12.5 appears to substantially increase the ability of the linear model to capture trends in both mean and max-

imum thrust. For high-ratio scenarios, it would be necessary to break the model into steady and unsteady components to use for flight dynamics simulation. In either case, producing such a model for wings similar to those tested here requires measurements of the angle of attack of the wing near the root and tip for flapping frequencies close to the desired operating frequency.

Any physics-based model must allow for interaction between spanwise segments of the wing. This suggests that a linearized vortex panel method should work, but a Blade Element Theory model similar to that used for propellers and helicopters will not work for small flapping wings.

Finally, this study determined that the flexible wing is the best design for hovering flapping wing aircraft. It exhibited the largest average thrust. It also exhibited the smallest maximum thrust, which allows the smoothest flight.

## 6.2 Future Work

### 6.2.1 Clap and Fling

Many hobbyists and researchers have demonstrated that paired clap-fling flapping is a more effective way of generating thrust with flapping wings than single flapped wings. It would be interesting to run experiments like those presented here to see how the results compare to the single wing flapping.

### 6.2.2 Fluid dynamics measurements

While there have been many studies of flapping wing fluid dynamics, it is now possible to directly correlate the thrust and fluid motion. Since the force generation is periodic, it is reasonable to assume the fluid motion is as well. Ideally, these measurements should be of the fluid along the span of the wing, to investigate spanwise flow effects such as dynamic stall vortex stabilization and the spread of unsteady circulation along the span of the wing.

### 6.2.3 Wing membrane strain measurements

The results of the present experiment show that knowledge of the dynamics of the structure provides enough information to determine a good approximation the thrust. This suggests that it is possible to use some technique that measures the strain in the wing membrane itself to estimate the thrust, and thus acceleration, of a flapping wing vehicle.

### 6.2.4 Gust and cross-wind response

This study focused on the phase-averaged thrust of flapping wings in quiescent air, but real vehicles will encounter gusts and crosswinds. This line of research will allow study of the stability and robustness of the thrust generation process. Additionally, it will allow researchers to address one of the critical issues preventing practical use of flapping wing vehicles.

### 6.2.5 Three axis measurements

Simultaneous measurements of lift, thrust and pitching moment are possible if the vehicle is free to make small deflections in these directions. A design that might accomplish this would use a long rod that runs through a journal bearing mounted in a ball and socket joint. As with the balance beam used in this study, a counterweight and inertial measurement unit placed at the other end would measure the steady and unsteady force and moment contributions, respectively.

## APPENDIX A

### FLUID MEASUREMENTS

#### A.1 Purpose and Objective

The purpose of the experiment described in this appendix is twofold:

- provide fluid data that can be used to produce an unsteady measurement of flapping wing thrust,
- provide insight into the fundamental fluid dynamics of flapping wings.

##### A.1.1 Thrust Measurement

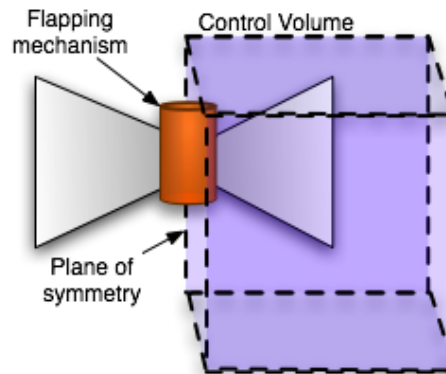


Figure A.1. Schematic of the control volume planned for force measurement. Flow symmetry is assumed based on the literature.

As described earlier, conventional load cells and other force measurement tools cannot measure the time-resolved forces generated by flapping wings. By assuming

that the flow, and hence thrust production, is periodic, it is possible to use a control volume approach to estimate the phase-resolved thrust,  $T(\phi)$ .

The data required for this approach is a sequence of cross-sections of the flow-field. At each slice, a sequence of vector fields captured at multiple phase angles can be used to compute the contribution of that segment to the phase-resolved thrust. The total thrust can then be estimated with the sum of each slice at a given phase angle.

### A.1.2 Fundamental Physics

While many studies have sought to understand the fundamental physics of flapping wing flight using detailed fluid velocity measurements, the goal of this study was more modest. Rather than ask why flapping wings generate lift and thrust, the work described in this appendix only seeks to answer three important questions that arise when attempting to design or simulate a flapping wing aircraft:

1. Can the flow be described as locally two dimensional at the surface of the wing, like a helicopter rotor, or is it fully three dimensional, like a canoe paddle?
2. Is the flow vortex dominated, or can other prominent flow structures be observed?
3. What is the effect of the flapping motion on the flow over an aerodynamic tail?

The first two questions determine how to approach the modeling of flapping wing force generation. The first determines if 2D simplifications can be made to describe the flow over sections of the wing using techniques such as blade element or lifting line theory. The second determines the required complexity of the 2D or 3D model, since a vortex dominated flow implies one that can be treated as largely inviscid, and thus linear in nature. Together, these questions will also determine how controllable a flapping wing aircraft will be using modern control design techniques

which trade bandwidth, and thus maneuverability, for robustness when applied to nonlinear systems.

Question three is import to both vehicle designers and biologists. Currently, there are no vehicles that use biological-style wings to hover, and all examples built to date use standard or v-tail empennage controls. However, there is no published data on the effect of flapping wing flow on the control authority of an aerodynamic tail. Understanding this may also reveal why biological fliers typically do not have aerodynamic tails, despite their relative simplicity and light weight [38].

## A.2 Experimental setup

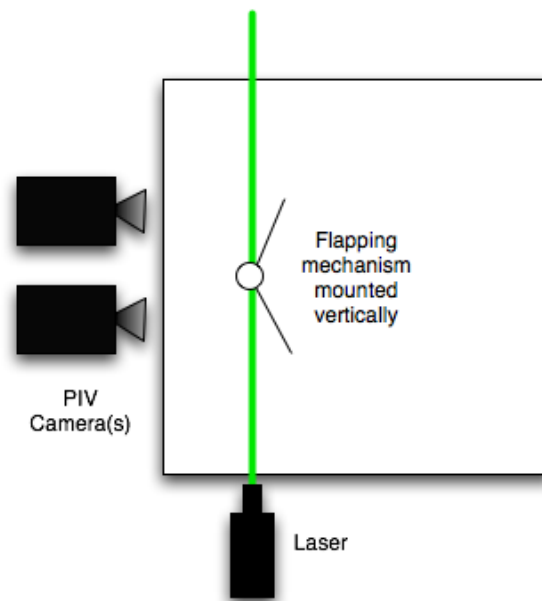


Figure A.2. Diagram showing arrangement of PIV camera, laser and flapping mechanism.

This study looked at the spanwise flow induced by the flapping wings in the plane of the wing at  $\Gamma = 0$ . Figure A.2 shows a schematic view of the arrangement

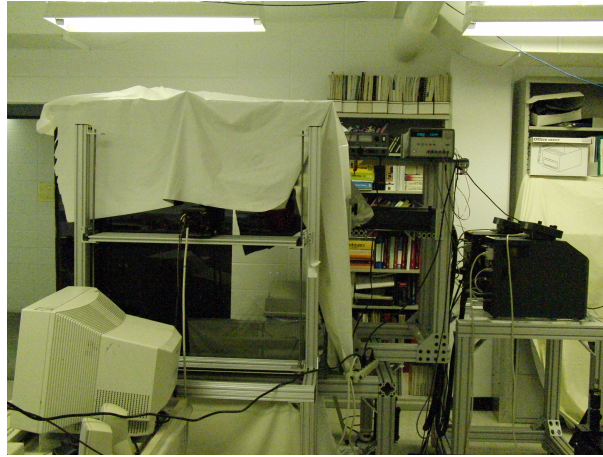


Figure A.3. Photograph of the camera and laser mounted outside the measurement box

of the laser sheet, flapping mechanism and camera.

The wings were mounted in a 4ft×4ft (1.23m<sup>2</sup>) box having an open top and bottom to allow airflow. A 2ft (.66m) section of the “back” wall was left open to provide access to the interior of the box for seeding and servicing the flapping mechanism. Opaque fabric was draped over the top and open section of the box to contain the seeding particles. The box itself sat on top of a 2ft high stand constructed of 80/20 brand slotted beams. Two sides were constructed of Plexiglas to allow the laser to shine in a plane normal to the camera’s field of view. This is shown in Figure A.3.

The flapping mechanism itself was mounted on an aluminum rectangular tube 1in×1.5in (2.54cm ×3.81cm) spanning the interior of the box approximately 1ft (.3m) below the top. Holes drilled at .5in (1.27cm) intervals allowed the short rectangular aluminum tube holding the mechanism and tachometer to be placed precisely and securely at many locations within the box. The 1in×2in (2.54cm×5.08cm) section of aluminum tube holding the wings was secured with a pair of 1/4in bolts

at the top, while the mechanism itself is attached to a custom-machined adapter block with a single #6 machine screw allowing small adjustments in the distance between the optical sensor and reflective spot. The tachometer was positioned such that the photo-detector would produce a pulse as the small piece of reflective tape passed in front of the sensor once per rotation.

All of the aluminum was painted black to limit specular reflections and reduce noise in the image. Parts that received frequent handling, such as the bolts holding the smaller tube in place, were covered with black electrical tape. A piece of tape was placed between the laser and motor to prevent the steel can from becoming a light source without adding a coat of paint that may have limited the motor's ability to cool properly.

The flapping was driven by a Cybird gearbox driven by a Great Planes Speed 280 brushed direct current (DC) motor. A Tenma regulated DC power supply, model number 72-630A, drove the motor at approximately  $9V$ , resulting in a flapping rate of 10Hz, the rate determined to be optimal by Liu *et al* [36] for a micro flapping vehicle. The tachometer was driven by the lower voltage side of an Aligent E3631A three-level DC power supply. The pair of high voltage rails powered an Analog Devices OP07 operational amplifier (op-amp) wired as a voltage follower. The output of the op-amp was directed to the "external trigger" of a TSI PIV Synchronizer and a LaCroix oscilloscope to provide feedback on the flapping frequency. Figure A.4 shows the schematic layout of the power and tachometer circuit.

The seeding particles consisted of very small ( $1 - 10\mu\text{ m}$ ) droplets of olive oil produced by a TSI seeding generator. The regulator on the generator was adjusted to produce the minimum velocity of the particles as they entered the box. The generator was pressurized by a building air supply connected via a standard pressure hose. The system is pressurized by opening a ball valve between the building

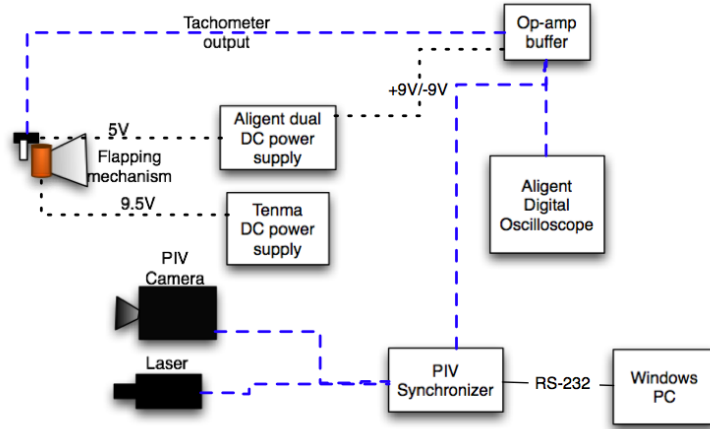


Figure A.4. Circuit diagram of the experiment

pressure supply and the hose to the generator.

An ND-YaG laser illuminated the particles with green laser light in separate pulses. The laser is spread into a  $45^\circ$  sheet using a combination of spherical and cylindrical lenses. A TSI PIV-CAM 10-30 captured the motion of the particle on its interlaced CCD; it was calibrated using a calibration plate in the frame to measure the field of view. TSI's Insight software, version 1.3, was used to control the Synchronizer and process the image pairs into vectors.

### A.3 Image collection procedure

1. Set both laser 1 and laser 2 to "Low" (Q-switch delay of  $75\mu$  s) .
2. Acquire an image, confirm that there is no saturation. If not, gradually increase the power on each laser until particles are visible but no regions are overexposed. Adjust the f-stop if necessary.
3. Process the image and observe the resulting vector field.
4. Adjust the time between pulses  $\Delta t$  to find the one that results in a good vector field in three shots in a row.
5. Open the valve to charge the seeder for approximately 3s, then wait approximately one minute for it to disperse. Capture a sequence of 1000 image pairs to the disk.

6. Adjust the camera trigger delay to the next scheduled phase angle and repeat from step 1 onward, being careful not to overwrite previously saved images.
7. Once all phase angles have been sampled, process the images to produce vector fields and move the flapping mechanism to the next position.

#### A.4 Problems Encountered

There were two problems that led to the decision to suspend this experiment. The first was incomplete vector fields over significant portions of the flapping periods at most wake slices. The second more critical problem was specular reflection off of the wings. The first problem could potentially be solved by making a composite image with multiple times between laser flashes. The second could not be solved, and further experimentation risked damage to the camera.

##### A.4.1 Incomplete Vector Fields

Most of the vector fields collected had substantial missing portions in which no vectors were detected. There are two likely reasons for this. The first is that the motion of the wing is normal to the plane of the image. The second is that the box may have been too small, and flow reflected off the walls may have contribute to a highly turbulent environment.

#### A.5 Specular reflection mitigation attempts

The most significant problem encountered was the inability to limit the reflection of the laser light off of the wings. Black paint, rhodamine and finally matte black cloth glued to the wings were each tried to reduce the amount of laser light reflected directly from the source to the camera. However, as shown in Figure A.5, it was not possible to reduce this to a level that would not risk damage to the camera, while also allowing a good vector field.



Figure A.5. Images captured by the PIV camera with the laser at low power showing specular reflections off the wing. The top image shows the reflection off black and rhodamine paint, the bottom matte black fabric

## A.6 Successful measurements

While it was not possible to compute the thrust based on PIV images, there were some measurements that yielded interesting results for the study of flapping wing fluid dynamics. When good measurements could be taken, a large vortical structure seemed to dominate the flow field. Two examples are shown in Figure A.6.

The most instructive frame was taken immediately after the wing had passed through the laser plane. The passage of the wing left a very clear “shadow” on the fluid, and gives the best view of the fluid environment around the wing itself. Figure A.7 shows this measurement, which provide the information needed to answer the questions posed in Chapter 1. These answers are enumerated below.

1. The flow appears to be fully three dimensional, like a canoe paddle.
2. There appears to be a single large vortex that dominates the flow environment, implying that a linear singularity model might be appropriate.
3. In hover, the wings can draw air towards them from below, implying that conventional aerodynamic control surfaces won't work.

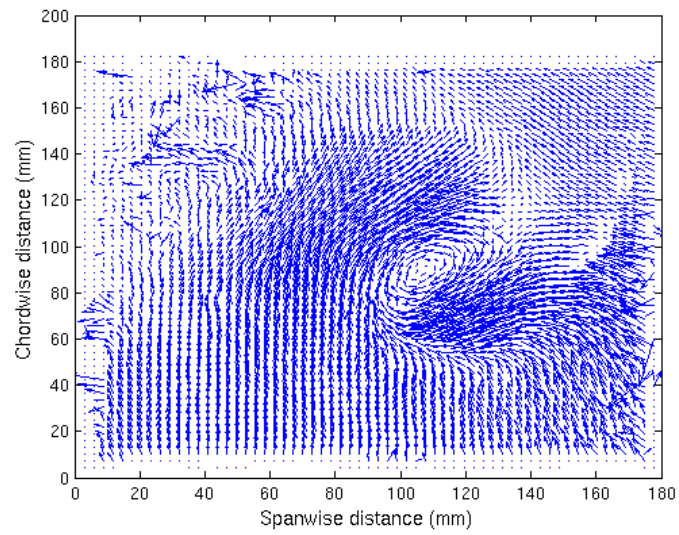
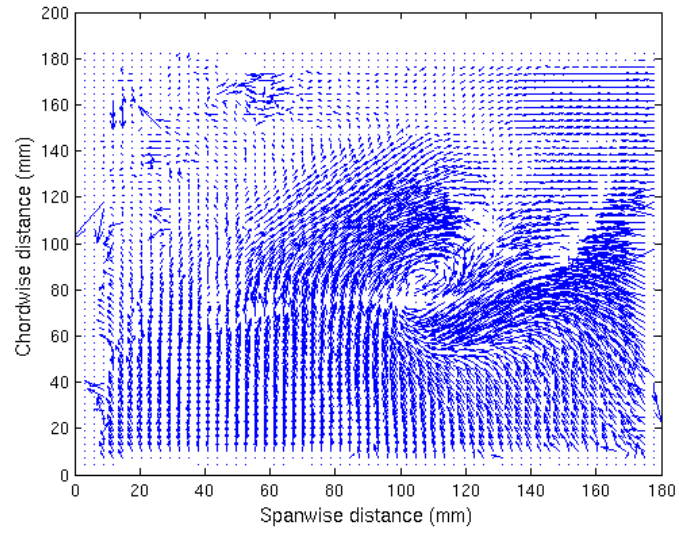


Figure A.6. Phase-averaged flow images at two phase angles showing a vortex dominated flow.

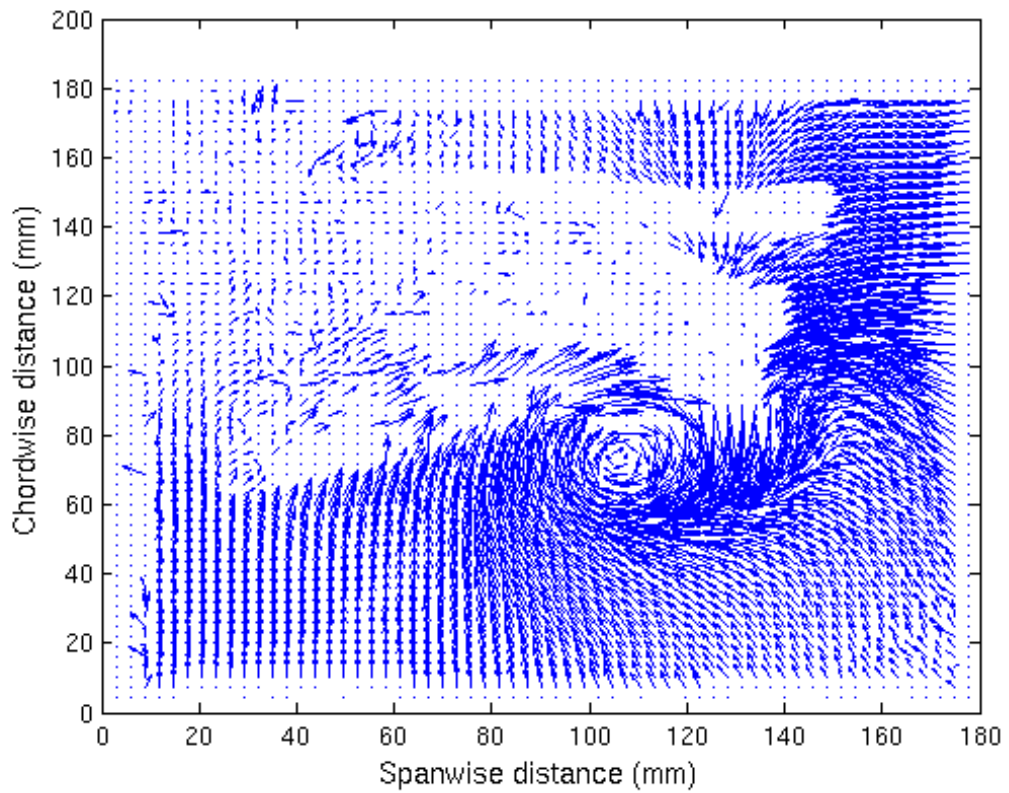


Figure A.7. Measurements of the flow immediately after the wing has passed on its downward plunge.

## BIBLIOGRAPHY

- [1] M. Abdulrahim and R. Lind. Using avian morphology to enhance aircraft maneuverability. In *AIAA Guidance, Navigation and Control Conference and Exhibit, Keystone, CO*, 2006.
- [2] K. Aditya and V. Malolan. Investigation of strouhal number effect on flapping wing micro air vehicle. In *AIAA Aerospace Sciences Meeting and Exhibit*, 2007.
- [3] A. Anderson, U. Pesavento, and Z. Jane Wang. Unsteady aerodynamics of uttering and tumbling plates. *Journal of Fluid Mechanics*, 541:65–90, 2005.
- [4] S A Ansari, R Zbikowski, and K Knowles. Non-linear unsteady aerodynamic model for insect-like flapping wings in the hover. part 1: methodology and analysis. *Institution of Mechanical Engineers – Part G – Journal of Aerospace Engineering*, 220:61–83, 2006.
- [5] Thomas B. Apker. Simulation of an ornithopter with active flow control and aeroelastic energy harvesting. In *AIAA Modeling and Simulation Technologies Conference and Exhibit, Keystone, CO*, 2006.
- [6] Thomas B Apker. Piezoelectric flapping wings as self-powering navigation sensors. In *AIAA Guidance, Navigation, and Control Conference 2007, Hilton Head, SC*, 2007.
- [7] B. Bandyopadhyay, T. Manjunath, and M. Umopathy. *Modeling, control and implementation of smart structures : a FEM-state space approach*. Springer, 2007.
- [8] Domenico Campolo, Ranjana Sahai, and Ronald S. Fearing. Development of piezoelectric bending actuators with embedded piezoelectric sensors for micromechanical flapping mechanisms. *Proceedings of the 2003 IEEE International Conference on Robotics and Automation*, 2003.
- [9] A T Conn, S C Burgess, and C S Ling. Design of a parallel crank-rocker flapping mechanism for insect-inspired micro air vehicles. *Journal of Mechanical Engineering Science*, 221:1211–1222, 2007.
- [10] James Kellogg David Cylinder, Donald Snull. Biomorphic approaches to micro air vehicles. In *UAV Asia-Pacific Conference*, 2003.
- [11] James D. DeLaurier. Ornithopter wing design. *Canadian Aeronautics and Space Journal*, 40(1):10–18, 1994.

- [12] J.D. DeLaurier. An aerodynamic model of flapping wing flight. *Aeronaughtical Journal*, pages 125–130, April 2003.
- [13] J.D. DeLaurier. The development of an efficient ornithopter wing. *Aeronaughtical Journal*, pages 153–161, May 1993.
- [14] William B. Dickson, Andrew D. Straw, Christian Poelma, and Michael H. Dickinson. An integrative model of insect flight control. In *Collection of Technical Papers - 44th AIAA Aerospace Sciences Meeting*, volume 1, pages 431 – 449, Reno, NV, United states, 2006. Ball joints;Drosophila melanogaster;Flight speed control;Rigid-body simulation;.
- [15] M. Ericka, D. Vasic, F. Costa, G. Poulin, and S. Tliba. Energy harvesting from vibration using a piezoelectric membrane. *Journal de Physique IV*, 128:187–193, 2005.
- [16] Flight gear source code. <http://www.flightgear.org/>, 2007.
- [17] Tracy E. Fritz and Lyle N. Long. A parallel, object-oriented unsteady vortex lattice method for flapping flight. *AIAA Paper No. 2004-0039, Aerospace Sciences Meeting*, Jan., 2004.
- [18] I. E. Garrick. Propulsion of a flapping and oscillating airfoil. Report 567, National Advisory Committee for Aeronautics, 1936.
- [19] Steven Ho, Hany Nassef, Nick Pornsinsiriak, Yu-Chong Tai, and Chih-Ming Ho. Unsteady aerodynamics and flow control for flapping wing flyers. *Progress in Aerospace Sciences*, 39:635–681, 2003.
- [20] Peter G. Ifju, David A. Jenkins, Scott Ettinger, Yongsheng Lian, Wei Shyy, and Martin R. Waszak. Flexible wing micro air vehicles. In *AIAA Aerospace Sciences Meeting and Exhibit, 40th, Reno, NV, 2002*.
- [21] Eric N. Johnson, Alison A. Proctor, Jincheol Ha, and Yoko Watanabe. Recent flight test results of active-vision control systems. *IEEE American Control Conference*, 2005.
- [22] Anya R. Jones and Holger Babinsky. Three-dimensional waving wings at low reynolds numbers. In *Collection of Technical Papers - 47th AIAA Aerospace Sciences Meeting*, 2009.
- [23] Eric J. Jumper and Ronald J. Hugo. Loading characteristics of finite wings undergoing rapid unsteady motions: A theoretical treatment. *Journal of Aircraft*, 31(3), 1994.
- [24] Joseph Katz and Allen Plotkin. *Low-Speed Aerodynamics, Second Edition*. Cambridge University Press, 2001.
- [25] James Kellogg, Christopher Bovais, Richard Foch, David Cylinder, Ravi Ramamurti, William Sandberg, John Gardner, Donald Scrull, George Piper, Peter Vaiana, and Aaron Kahn. Development and testing of unconventional micro air vehicle configurations. *AIAA Journal*, 2003.

- [26] P. Konstadinopoulos, D. F. Thrasher, D. T. Mook, A. H. Nayfeh, and L. Watson. A vortex-lattice method for general, unsteady aerodynamics. *Journal of Aircraft*, 22(1), 1985.
- [27] Roman Y. Krashanitsa, Dmitro Silin, Serey V. Shkarayev, and Gregg Abate. Flight dynamics of a flapping-wing air vehicle. *International Journal of Micro Air Vehicles*, 1(1), 2009.
- [28] Ali T. Kutay, John R. Culp, Jonathan A. Muse, Daniel P. Brzozowski, Ari Glezer, and Anthony J. Calise. A closed-loop flight control experiment using active flow control actuators. In *AIAA Aerospace Sciences Meeting and Exhibit*, 2007.
- [29] Rambob F. Larigani and James D. DeLaurier. A nonlinear aeroelastic model for the study of flapping wing flight, 1995.
- [30] C. K. Lee and T. C. O’Sullivan. Piezoelectric strain rate gages. *Journal of the Acoustic Society of America*, 90(2):945–953, 1991.
- [31] E. Lefeuvre, A. Badel, A. Benayad, L. Lebrun, C. Richard, and D. Guyomar. A comparison between several approaches of piezoelectric energy harvesting. *Journal De Physique*, 128:177–186, 2005.
- [32] Fritz-Olaf Lehmann, Sanay P. Sane, and Michael Dickinson. The aerodynamics effects of wing-wing interaction in flapping insect wings. *The Journal of Experimental Biology*, 208:3075–3092, 2005.
- [33] Gordon J. Leishman. *Principles of helicopter aerodynamics*. Cambridge University Press, 2000.
- [34] Sir Lighthill, M. J. *Mathematical biofluidynamics*. Society for Industrial and Applied Mathematics, 1975.
- [35] Ling Liu and Shuming Du. A computationally efficient particle-puff model for concentration variance from steady releases. *Environmental Modelling and Software*, 18(1):25–33, 2003.
- [36] Tianshu Liu, K. Kuykendoll, R. Rhew, and S. Jones. Avian wing geometry and kinematics. *AIAA Journal*, 44(5):954–63, 2006.
- [37] Lennart Ljung. *System Identification: Theory for the User*. Prentice Hall, Inc., 1999.
- [38] K. Loh, M. Cook, and P. Thomasson. An investigation into the longitudinal dynamics and control of a flapping wing micro air vehicle at hovering flight. *The Aeronautical Journal*, 2004.
- [39] Nathan Lunsford and Jamey D. Jacob. High speed videogrammetry of flexible wings in flapping flight. In *Collection of Technical Papers - 47th AIAA Aerospace Sciences Meeting*, 2009.
- [40] [http://www.et.byu.edu/groups/wwwmav/Tenth\\_MAV\\_Site/Rules/general.htm](http://www.et.byu.edu/groups/wwwmav/Tenth_MAV_Site/Rules/general.htm), 2006.

- [41] J. L. Meriam and L. G. Kraige. *Engineering Mechanics, Dynamics*. Wiley, 1997.
- [42] Laura A. Miller and Charles S. Peskin. A computational fluid dynamics of ‘clap and fling’ in the smallest insects. *The Journal of Experimental Biology*, 208:195–212, 2005.
- [43] F. O. Minoti. Unsteady two-dimensional theory of a flapping wing. *Physical Review E*, 66, 2002.
- [44] Wael A. Mokhtar, Xu D. Zheng, Ilteris Koc, and Kursat Kara. Aerodynamics and flow control of flapping wings. In *44th AIAA Aerospace Sciences Meeting and Exhibit*, 2006.
- [45] Thomas J. Mueller and James D. DeLaurier. Aerodynamics of small vehicles. *Annual Review of Fluid Mechanics*, 35:89–111, 2003.
- [46] W. Nitsche, P. Mirow, and J. Szodruch. Piezo-electric foils as a means of sensing unsteady surface forces. *Experiments in Fluids*, 7, 1989.
- [47] Dmitry Orlov. *MODELLING AND SIMULATION OF SINGLE DIELECTRIC BARRIER DISCHARGE PLASMA ACTUATORS*. PhD thesis, University of Notre Dame, 2006.
- [48] K. Parker, K. D. von Ellenrider, and J. Soria. Using stereo multigrid dpiv (smdpiv) measurements to investigate the vortical skeleton behind a finite-span flapping wing. *Experiments in Fluids*, 39:281–298, 2005.
- [49] P. J. Philips, R. A. East, and N. H. Pratt. An unsteady lifting line theory of flapping wings with application to the forward flight of birds. *Journal of Fluid Mechanics*, 112, 1981.
- [50] Martiqua L. Post. *Plasma Actuators for Separation Control on Stationary and Oscillating Airfoils*. PhD thesis, University of Notre Dame du Lac, 2004.
- [51] Sergio Preidikman. *Numerical Simulations of Interactions Among Aerodynamics, Structural Dynamics, and Control Systems*. PhD thesis, Virginia Tech, 1998.
- [52] Jeremy M. V. Rayner. Mathematical modelling of the avian flight power curve. *Mathematical Methods in the Applied Sciences*, 24:14851514, 2001.
- [53] <http://www.realflight.com/>, 2006.
- [54] Erik Sallstrom and Lawrence Ukeiley. Three-dimensional averaged flow around rigid flapping wings. In *AIAA Fluid Dynamics Conference*, 2008.
- [55] William Rees Sears. *A systematic presentation of the theory of thin airfoils in non-uniform motion*. PhD thesis, California Institute of Technology, 1938.
- [56] J.S. Shang, S.T. Surzhikov, R. Kimmel, D. Gaitonde, J. Menarta, and J. Hayes. Mechanisms of plasma actuators for hypersonic flow control. *Progress in Aerospace Sciences*, 41:642668, 2005.

- [57] Wei Shyy, Mats Berg, and Daniel Ljungqvist. Flapping and flexible wings for biological and micro air vehicles. *Progress in Aerospace Sciences*, 35:455–505, 1999.
- [58] Bret Stanford, Roberto Albertani, Drago Viieru, Wei Shyy, and Peter Ifju. Static aeroelastic model validation of membrane micro air vehicle wings. In *AIAA Aerospace Sciences Meeting and Exhibit*, 2007.
- [59] B.L. Stevens and F.L. Lewis. *Aircraft Control and Simulation*. Wiley, 2003.
- [60] Mao Sun and Xin Yu. Aerodynamic force generation in hovering flight in a tiny insect. *AIAA Journal*, 44(7):1532–1540, 2006.
- [61] Erik W. M. Swanton, Blake A. Vanier, and Kamran Mohseni. Leading edge vortex stability in a flapping model hummingbird wing. In *38th AIAA Fluid Dynamics Conference and Exhibit*, 2008.
- [62] Mathew J. Tarascio, Manikandan Ramasamy, Inderjit Chopra, and J. Gordon Leishman. Flow visualization of micro air vehicle scaled insect-based flapping wings. *Journal of Aircraft*, 42(2):385–390, 2005.
- [63] X. Tian, J. Iriarte-Diaz, K. Middleton, R. Galvao, E. Israeli, A. Roemer, A Sullivan, A Song, S Swartz, and K. Breuer. Direct measurements of the kinematics and dynamics of bat flight. *Bioinspiration and Biomimetics*, 1:S10–S18, 2006.
- [64] James R. Usherwood, Tyson L. Hendrick, Craig P. McGowan, and Andrew A. Biewener. Dynamic pressure maps for wings and tails of pigeons in slow, flapping flight, and their energetic implications. *Journal of Experimental Biology*, 208:355–369, 2005.
- [65] T. Weis-Fogh. Quick estimates of flight fitness in hovering animals, including novel mechanism for lift production. *J. Exp. Bio.*, 59:169231, 1973.
- [66] Alexander P. Willmott, Charles P. Ellington, and Adrian L. R. Thomas. Flow visualization and unsteady aerodynamics in the flight of the hawkmoth. *Philosophical Transactions of the Royal Society of London B*, 1997.
- [67] Pin Wu, Bret Stanford, and Peter Ifju. Passive bending and twisting motion during the flapping stroke of a micro elastic wing for thrust production. In *Collection of Technical Papers - 47th AIAA Aerospace Sciences Meeting*, 2009.
- [68] Yonliang Yu and Binggang Tong. A flow control mechanism in wing flapping with stroke asymmetry during insect forward flight. *Acta Mechanica Sinica*, 21:218–227, 2005.
- [69] Rafal Zbikowski. On aerodynamic modelling of an insect-like flapping wing in hover for micro air vehicles. *Philosophical Transactions of the Royal Society of London*, 360:273–290, 2002.
- [70] P. Zdunich, D. Bilyk, M. MacMaster, D. Loewen, and J. DeLaurier. Development and testing of the mentor flapping-wing micro air vehicle. *Journal*

*of Aircraft*, 44(5):1701 – 11, Sept.-Oct. 2007. flapping-wing micro air vehicle;portable surveillance systems;clap-fling phenomenon;mechanical simulation;hummingbird flight;internal-combustion engine;electric motor;rotary shaft motion;.